Study of polarization of light through a stack of metallic metamaterials

Xavier Romain

UBFC
UNIVERSITÉ
BOURGOGNE FRANCHE-COMTÉ

UFC
UNIVERSITÉ
DE FRANCHE-COMTÉ

THÈSE DE DOCTORAT DE L'ÉTABLISSEMENT UNIVERSITÉ BOURGOGNE FRANCHE-COMTÉ

PRÉPARÉE À L'UNIVERSITÉ DE FRANCHE-COMTÉ

École doctorale n°37
Sciences Pour l'Ingénieur et Microtechniques

Doctorat d'Optique & Photonique

par

XAVIER ROMAIN

Study of the polarization of light through a stack of metallic metamaterials

Thèse présentée et soutenue à Besançon, le 8 Novembre 2018

Composition du Jury :

BERNAL MARIA-PILAR	Directeur de recherche CNRS, Femto-ST	Président
MOREAU ANTOINE	Maitre de conférences, Université Clermont Auvergne	Rapporteur
LETARTRE XAVIER	Directeur de Recherche CNRS, INL	Rapporteur
FEHREMBACH ANNE-LAURE	Maitre de conférences, Université d'Aix-Marseille	Examinateur
BOYER PHILIPPE	Maitre de conférences, Université Bourgogne Franche-Comté	Co-encadrant de thèse
BAIDA FADI	Professeur, Université Bourgogne Franche-Comté	Directeur de thèse

N° | X | X | X |

SPIM

école doctorale **sciences pour l'ingénieur et microtechniques**

UBFC
UNIVERSITÉ
BOURGOGNE FRANCHE-COMTÉ

Université Bourgogne Franche-Comté
32, avenue de l'Observatoire
25000 Besanon, France

ACKNOWLEDGEMENTS

I would like to express my sincere gratitude to all those who helped me to complete my Ph.D. thesis in Femto-ST. I would like to thank especially Aline, Sarah, Valérie and Joëlle who are always available and ready to help.

I would like to thank Anne-Laure Fehrembach, Antoine Moreau, Xavier Letartre and Maria-Pilar Bernal for serving as my thesis committee, for their encouraging remarks and fruitful discussion concerning my work.

Working in Femto-ST has been a very pleasant, stimulating and enriching experience. I would like to thank the whole Optics department and in particular the nano-optics team for this great working environment. During these years, I have shared the office with Ali, Alexis, Wentao, Zhihua and Mengjia and I thank you all for the nice mood and the good moments we had together.

The time I have spent in Besançon has been a wonderful experience thanks to the friends I have met in Femto-ST. Writing your names brings back many memories! Many thanks to Guoping, Venan, Gautier, Phong, Anurupa, Stefania, Luca, Vincent, Séverine, Raya, Etienne Coffy, Etienne Vaillant, Guillaume, Joel, Souleymane, Xiaolong, Shanti, Bicky, Alok, Rémi, Charles-Louis, Ravinder, Beatrice and... those I forgot! I wish the best for all of you in the future.

I wish to acknowledge my gratitude to my thesis director, Fadi Baida. Despite the number of students visiting his office, he always had time for guiding me. I also thank him for his many precious advices and his warm encouragements during my thesis. Each visit to his office has always been very fruitful and efficient.

I am much indebted to Philippe Boyer, my thesis co-advisor. Through countless conversations with him, I have learned more than I could hope and imagine. During these inspiring moments, I have learned a lot about physics and much more. His constant support has helped to improve myself in many aspects. I am also deeply grateful for his very valuable aid at the very last moments of my PhD thesis.

I would like to renew my acknowledgements to both my supervisors, they have been an example for me and I hope I could reach their scientific level in my future career.

My most heartfelt thanks goes to Tintu. Her presence was more than necessary in many occasions, especially towards the end! She gave me the strength and the courage to finish this PhD.

I would also like to thank my parents without whom - needless to say - I wouldn't have reached here. It is with a lot of love and gratitude that I dedicate my thesis to them.

CONTENTS

1

INTRODUCTION

1.1/ GENERAL REMARKS ON OPTICS AND ARTIFICIAL MATERIALS

From antique ray model to modern quantum physics, optics has accumulated, through the last centuries, several ways to describe and understand the nature of light and its properties such as polarization. It is however not before the last decades - especially with the development of lasers (serving as stable and coherent light sources) and optical fibers (serving as low-loss waveguides) - that optics and light-based technologies have considerably grown and attracted researcher's attention. Optics is now essential in a large diversity of scientific domains, such as in astronomy [1], telecommunications [2,3] and medicine [4]. More recently, optics is increasingly entangled to another very active research area called nanotechnology. Indeed, the many breakthroughs in modern physics, and notably in optical imaging, has fostered nanosciences.

The great potential and fast growth of nanotechnology was perfectly represented by Moore's law [5], which states that the number of components in an integrated circuit doubles every 24 months. In other words, the dimensions of individual components in integrated circuits such as electronic transistors have considerably shrunk. Such breakthrough has of course led to constant and important improvements in computer technology and embedded devices. In return, nanotechnology has therefore greatly helped other sciences. For example, it has led to super-fast computers which are essential for simulation and modelling. Nanotechnology also serves now as a platform for the study of light at the nanoscale which forms the domain of nano-optics [6].

The traditional optical components such as lenses, fibers, polarizers etc., usually rely on the specific properties of bulk materials. However, nano-optics and nano-fabrication techniques have facilitated the growth of artificially engineered materials like photonic crystals (i.e., periodic dielectric media) [7] and more recently metamaterials. When carefully designed such structured materials can exhibit very specific properties that are not achiev-

able with conventional bulk materials. For example, photonic crystals featuring photonic bandgaps can be used for designing mirrors at specific wavelength range [7]. Photonic crystals also find use in many other applications such as waveguides with low-loss sharp bends [7], narrow band filters [7] or sensors [8, 9]. In this thesis, we are interested in the latter mentioned artificial materials, i.e., metamaterials.

The field of metamaterials has rapidly gained in popularity and has reached a very broad scientific community over the past 20 years. Such rapid developement is due to the unique and exotic features of metamaterials including negative refraction [10], cloaking [11, 12], epsilon near-zero materials [13] perfect absorption [14], optical activity [15] and many more. Figure 1.1 shows popular example of metamaterials. Given its diversity, it is not so trivial to give a simple and clear definition of metamaterials that could satisfy the whole ”metamaterial community”. Nonetheless, a widely used definition for

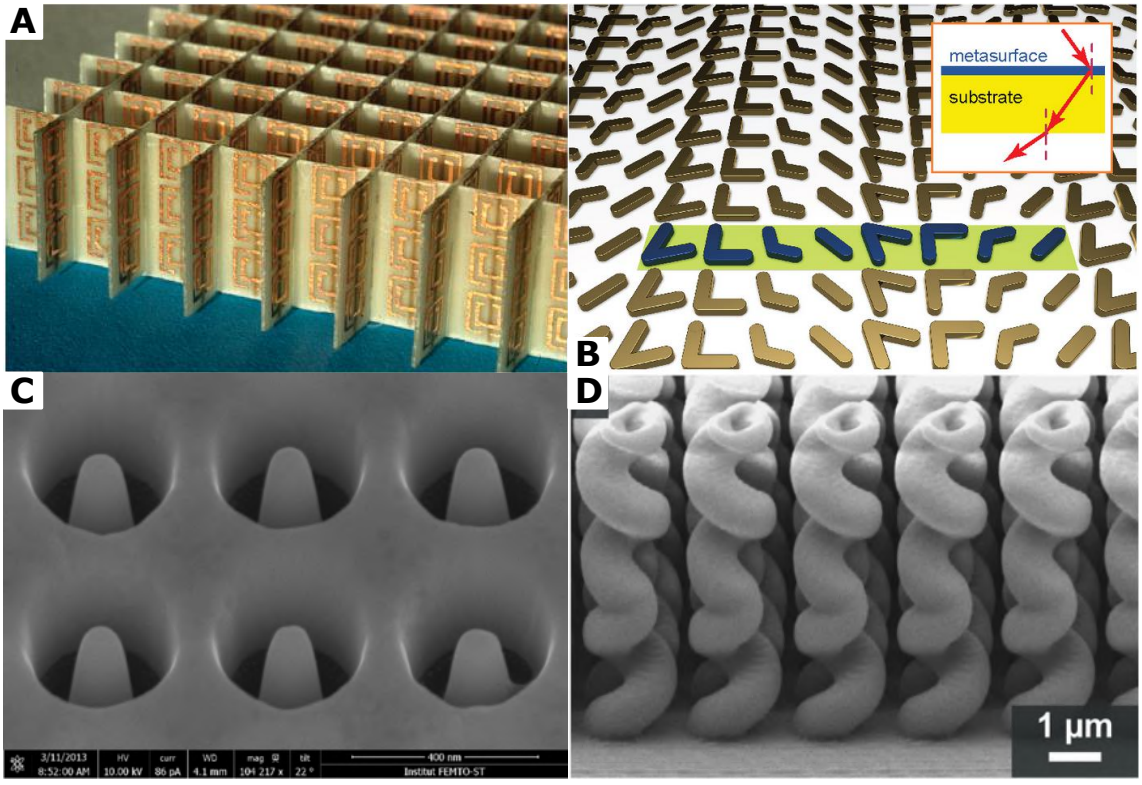

Figure 1.1: Examples of typical metamaterials for different applications. **(a)** Image of a metamaterial that combines double split rings with cut wires for achieving negative refraction index used in superlenses design [10]. **(b)** 3D scheme example of a metasurface that demonstrates generalised Snell's law of refraction [18] that can be applied for the design of ultra-thin lenses [19]. **(c)** SEM image of a metallic metamaterial with slanted annular aperture unit-cell - developed by the Femto-ST nano-optics team - that achieves the enhanced optical transmission of the transverse electromagnetic mode. **(d)** Subwavelength helix based chiral metamaterial for broadband polarization conversion, essential in telecommunications. Images A, B C and D taken from [20], [21], [22] and [23] respectively.

metamaterials is the following: Artificially (or man-made) structured materials consisting of periodic subwavelength unit-cells [16]. Furthermore, the properties of the whole metamaterial is dictated by the characteristics of its subwavelength unit-cell (or subwavelength pattern) [16]. More recently, similar structures called ”metasurfaces” are also extensively studied [17]. The main difference lies in the structure thickness. For metasurfaces, the unit-cell as well as the thickness are smaller than the wavelength. Metasurfaces are sometimes referred to as the ”2D counterpart” of metamaterials due to their subwavelength thickness.

Metamaterials can be either made of dielectric or metallic materials. In the context of this PhD thesis, we are interested in metallic metamaterials because they can offer Extraordinary Optical Transmission (EOT). As we will see throughout the thesis, such EOT phenomenon is beneficial to maintain a high transmission in the stacked structures we are studying. In the next section, we focus on the development of metallic metamaterials. Therein, we briefly discuss the historical background and development of metallic metamaterials and EOT as well as the research conducted by the nano-optics team of the Femto-ST Institute, Besançon. Then, in Sec. 1.3 we provide a brief overview on the different possibilities to describe and model metallic metamaterials. In Sec. 1.4, we focus on the state of the art of polarization properties of metallic metamaterials and their limitations. In Sec. 1.5 we detail the context of this PhD thesis and the main contributions. Finally, the organization of the thesis is presented in Sec. 1.6.

1.2/ HISTORICAL DEVELOPMENT OF METALLIC METAMATERIALS

In 1998, Ebbesen *et al.* reported EOT in the visible range using a metallic film pierced by periodic subwavelength holes [24]. They coined the term EOT because of the unusually high transmission of 6% observed at the wavelength of 326 nm. Indeed, their observations were in total contradiction with the normalized transmission $T = \left(\frac{r}{\lambda}\right)^4$ predicted by Bethe in 1944 [25] for a single subwavelength hole with a radius r. Ebbesen *et al.* advanced two points for explaining the EOT phenomenon. Firstly, the holes array play an active role via the 0^{th} order of diffraction to increase the transmission. Secondly and more importantly, the incident light excites surface plasmons at the metamaterial interfaces [26] and therefore enhances the transmitted light. This pioneering study has not only participated to the rise of metamaterials, but it has also renewed the area of plasmonics and plasmonic materials [27].

Soon after, some other theoretical and physical explanations for the EOT were proposed.

More specifically, the EOT behaviour of metamaterials was suggested either by guided mode resonances in the subwavelength holes array [28–30], or by Fabry-Perot resonances along the metamaterials thickness [31]. These preliminary studies were considering either monoperiodic lamellar gratings or biperiodic lamellar gratings patterned by circular/square holes. It is worth mentionning that EOT can also be referred to as "Enhanced Optical Transmission" to differentiate the plasmon-based transmission ("extraordinary") from the resonance-based transmission ("enhanced"). In the meantime, the nano-optics team of Femto-ST has theoretically proposed other biperiodic geometries for the subwavelength holes arrays to achieve EOT, namely the Annular Aperture Array (AAA) [32–34] and the square coaxial aperture array [35]. Such geometries have the particularity to support TEM guided modes with no cut-off frequency in the desired spectral domain [32]. Further, the enhanced transmission through AAA metamaterials was experimentally demonstrated by the same team [36, 37] with measured transmission value up to 90%. Note that, it was the first experiment to report such a high transmission through a metallic metamaterial. More recently, our team has also proposed a study on the origin of the resonance in planar metallic metamaterials [38]. In the following section, we present several modelling methods that are used for describing metallic metamaterials.

1.3/ OVERVIEW ON METALLIC METAMATERIALS MODELLING

As we can notice from Fig. 1.1, the metamaterial designs can be drastically different depending on the desired properties (chirality, negative refractive index and so on). Consequently, several independent theories and simulation techniques have emerged to model metamaterials. Each modelling technique is used for particular designs and applications such as, transformation optics (also known as C-method) for cloaking metamaterials [12, 39]. It is however not the aim of this section to give an exhaustive list of modelling and simulation techniques for every kind of metamaterials. In this section, we specifically focus on metallic metamaterials modelling.

Some particular metallic unit cells such as split ring resonators can be well analysed by using the transmission line theory [40]. This theory originates from the microwave and radio frequency domain and it was used to model electrical devices with size that are not negligible compared to the working wavelength, such as coaxial cable. Principally, the transmission line theory consists in modelling an infinitely small electrical wire with an equivalent electrical circuit made of basic lumped components (resistor, inductance, capacitance and conductance). Such technique is currently applied to describe metallic metamaterial unit cells. Figure 1.2 gives classic examples of equivalent circuit modelling

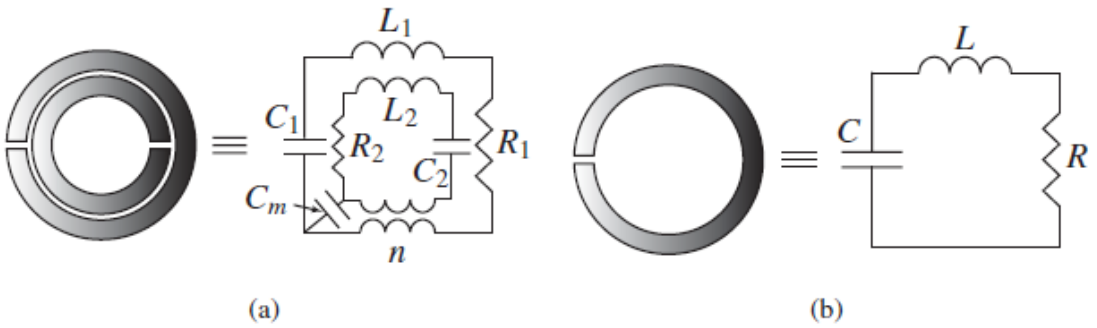

Figure 1.2: **(a)** Double split ring resonator and its equivalent electrical circuit based on lumped L,C and R components. **(b)** Equivalent counterpart for a single split ring. Image taken from [40].

for double split rings in Fig. 1.2**(a)** and a single split ring in Fig. 1.2**(b)**. However, this theory is restricted to particular unit cell shape such as split rings and it is only valid if the homogeneity conditions are satisfied [41] (i.e. wavelength much larger than the unit-cell dimension).

Full wave simulations such as the Finite Difference Time Domain (FDTD) [42] or the Finite Element Method (FEM) [43] are also very popular for modelling metallic metamaterials because they are especially powerful to model any kind of geometry while taking into account complex phenomena or structures imperfections. Both methods consist in, first, meshing - (or subdividing) the considered metamaterial geometry and second, locally solving sets of equations for each subdivided volume. These class of simulation methods are, in a sense, more ”natural” since they empirically solve electromagnetic problems based on the Maxwell’s equations in differential form. The FDTD considers discretized equations where the derivatives are replaced by finite differences while the FEM considers approximate form (finite elements) of the derivatives [44]. Even though such simulation technique can be used for any kind of unit cell shape, they can cost a large amount of computer resources and computation time, for example, if the wavelength is much smaller than the entire structure of interest).

Metallic metamaterials also encompass the group of structure called subwavelength metallic gratings. Metallic diffraction grating have been studied for centuries and are well described by several theories. Probably the most popular technique for modelling diffraction gratings is the Rigorous Coupled Wave Analysis (RCWA) [45] which is now also known as the Fourier Modal Method (FMM) [42]. This method considers expansions of the electromagnetic fields into (Floquet-)Fourier series and the structure permittivity into Fourier series but the FMM is restricted to the modelling of thickness-invariant grating such as lamellar gratings. More mathematically involving methods such as the

integral [46] and differential methods [47] are also popular for modelling gratings or metamaterials. Even though these methods can be ”computation intensive”, they have the advantage of rigorously modelling gratings made of any arbitrary shape.

For some particular unit-cell shapes, metallic metamaterials can be described by modal methods where the electromagnetic fields is expanded into series of modes for any region of space, including the unit-cell [48]. The electromagnetic problem is then simply solved by matching the different modal expansions. Such technique has the advantage to reduce the electromagnetic problem to a set of linear equations where the only unknowns are the amplitudes of the electromagnetic modes. In some cases, the solution of the problem even becomes analytical and it leads to very fast computation time. These analytical solution also enables precise physical investigations to further get new insights into metamaterials. The modal method is the basis of the theoretical formalism used in this PhD thesis and we present it in more details later in this chapter.

1.4/ POLARIZATION PROPERTIES OF METALLIC METAMATERIALS

In addition to the EOT phenomenon introduced in section 1.2, different groups focused on the polarization properties of metallic metamaterials. As an example, linear polarization properties were analysed for rectangular holes array [49–51] and for elliptical holes array [52,53]. Metamaterials were further designed to exhibit special polarization properties such as anisotropy [54, 55], asymmetric transmission [56] and polarization rotation [57]. The Femto-ST nano-optics team has also contributed to the development of anisotropic metamaterials by proposing compact and efficient waveplates [58, 59]. Recently, metamaterials and metasurfaces are further engineered for various polarization applications such as high efficiency polarizers [60], polarization-selective multispectral imaging [61] or linear/circular to vector bessel beam converters [62]. Specific models are currently proposed to describe the polarization properties of metamaterials where the shape and the symmetry of the unit cell are analysed [63,64]. In particular, this PhD thesis is based on a custom Jones formalism extended to metallic metamaterials made of specific symmetry unit cell [65] which will enable the design of metallic metamaterials with polarization effect together with high transmission.

Nevertheless, single metamaterials suffer the intrinsic limitations imposed by their own subwavelength unit cell. As an example, Fig. 1.3**(a)** shows the linear polarization rotation principle used in [57] where the polarization rotation is due to the chirality of the gammadion unit cell. As we can remark in Fig. 1.3**(b)** the transmitted beam is rotated by only

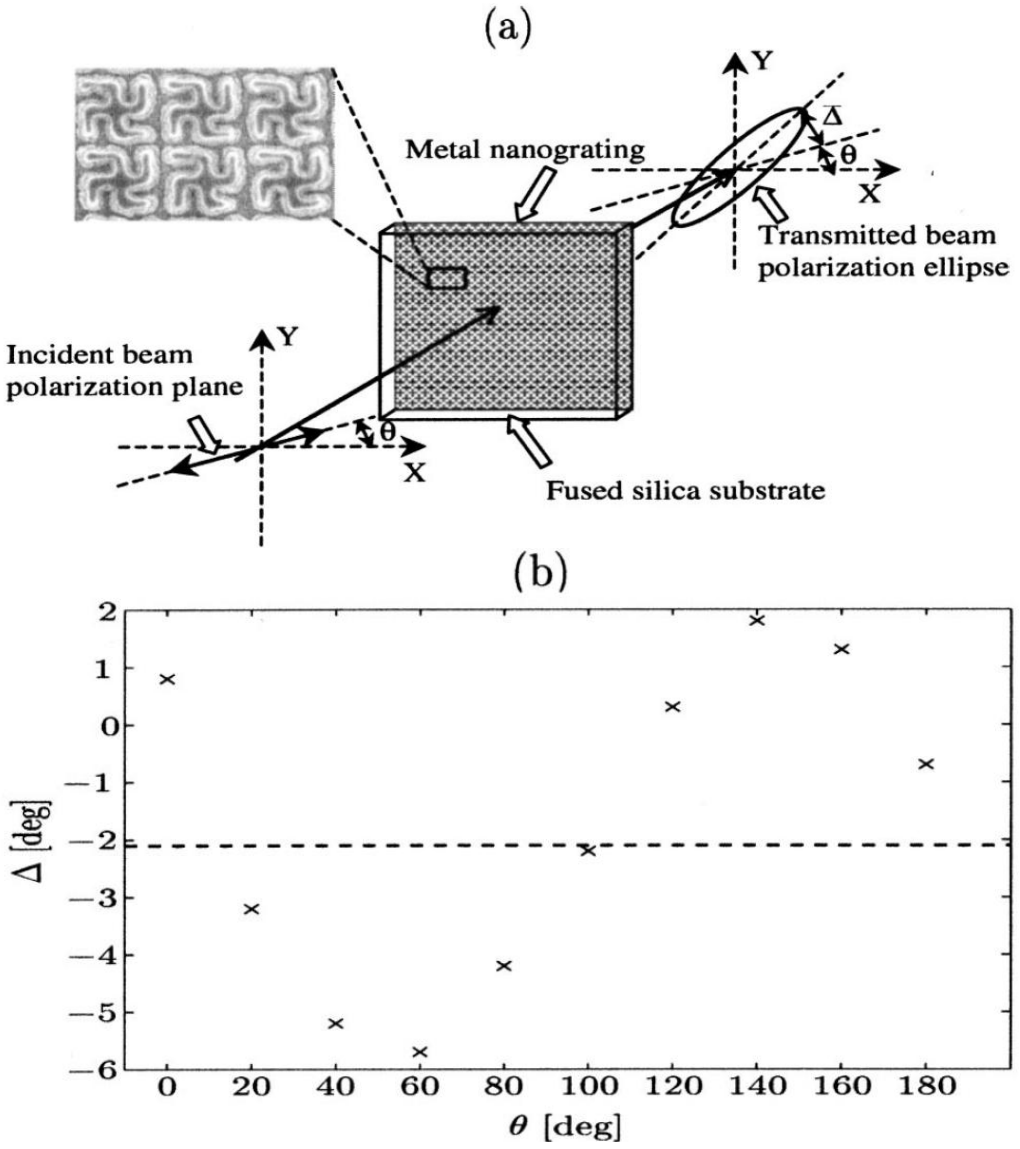

Figure 1.3: **(a)** Schematic principle of an incident linearly polarized light oriented along θ in the transverse (x-y) plane and rotated by an angle Δ after passage through the metallic nano-grating. **(b)** Measured rotation angle Δ as a function of the orientation of the linear input beam given by θ. Images taken from [57].

few degrees. In addition, such rotation was reported for a single wavelength ($\lambda = 633nm$). The authors also reported a larger polarization rotation effect for a wavelength $\lambda = 540nm$ but it was accompanied by a decrease in the transmitted intensity. This issue then leads to a compromise between polarization rotation effect and the transmission efficiency of the structure.

As another example, the efficient metallic waveplates studied by the Femto-ST nano-optics team [58, 59] undergo similar kind of problem. The structure studied in [58] is depicted in Fig. 1.4**(a)**. The objective was to design a metallic half-wave plate with a high

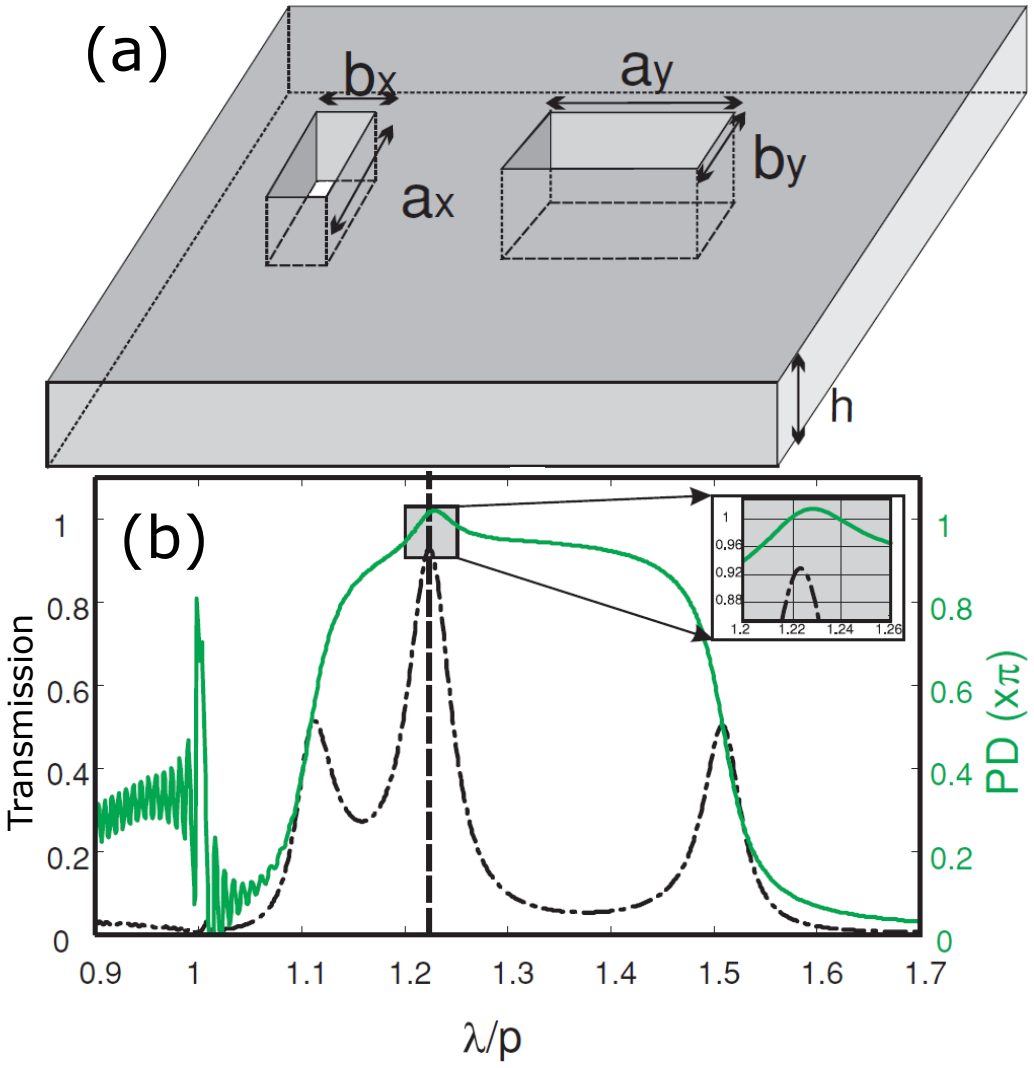

Figure 1.4: **(a)** Scheme of the metallic half-wave plate unit cell composed of two rectangular holes. **(b)** Transmission spectrum of the half-wave plate in dashed black line. The phase difference between the two orthogonally polarized transmissions is given by the green solid curve. Image taken from [58].

transmission value. For that, two conditions has to be fulfilled:

- the Phase Difference (PD) between the two orthogonally polarized transmission has to be $PD = \pi$.
- the transmission should be close to one.

As we can see in Fig. 1.4**(b)**, these two conditions are satisfied only for $\lambda/p = 1.223$ where p is the period of the structure. The working spectral band is rather limited and it thus makes the structure performances very sensitive to fabrication imperfections.

To overcome the intrinsic limitations imposed by the unit cell of single metamaterials, two options can be considered. The first option is to develop more complex unit cell and/or

to optimize the unit cell design in order to improve the metamaterial performances. The second option is to use stacks of metamaterials instead of single metamaterials. As we will see in the next section, we choose the stacked metamaterials alternative as it features some unique advantages over single metamaterials.

1.5/ CONTEXT AND CONTRIBUTIONS OF THIS PHD THESIS

As we have seen in Sec. 1.4, single metamaterials or single metasurfaces can be used to efficiently manipulate the polarization of light for a large diversity of applications. In addition, many specialized theories are available to efficiently design metamaterials for specific polarization applications. However, single metamaterials are innately limited by the properties of their own subwavelength unit cell. Therefore, achieving complex properties together with low losses can lead to the design of complex unit cells. Such complex patterns can be difficult to fabricate and time-consuming to be simulated. These issues may finally lead to unnecessarily heavy and costly development process.

In order to overcome the issues and limitations associated with single metamaterials, stacked (or cascaded) metamaterials are currently proposed [66]. Indeed, stacking metamaterials enables additional degrees of freedom and it features two main advantages. First, the additional degree of freedom can drastically reduce the complexity of the basic subwavelength unit cells. Second, the combination of several metamaterials can lead to exotic effects that can not be obtained by single metamaterials. For example, the nano-optics team has proposed in 2012 a structure based on two anisotropic metallic metamaterials which exhibits an EOT-based tunable optical activity [67].

From the numerical point of view, even though such stacking may allow for simpler metamaterial unit cell, the stacked structure itself can remain challenging to model. Indeed, if we consider a same unit cell, a stacked structure made of several metamaterials is innately more time consuming to model than a single metamaterial. Then, the goal is to find unit cells that can be simple to analyze and to model and that can lead to interesting effects in stacked structure. From the experimental point of view, each metamaterial may be simpler to fabricate but the precise stacking and/or alignment of each metamaterial inevitably requires more fabrication and/or experimental steps than for a single metamaterial. Finally, modelling exotic effects or new functionalities in stacked metamaterials requires the development of original models that properly take into account such new effects.

As a consequence, there is a current need of efficient models - in terms of computa-

tion time and results accuracy - that can take into account the properties arising from the stacking, and that can physically or qualitatively describe the properties of the whole structure. Presently, much efforts are being made to describe and engineer stacked metamaterials. Models based on Floquet analysis [68], scattering matrices [69] and wave matrices [70] have been recently proposed. Stacked metamaterials or stacked metasurfaces currently find use in asymmetric transmission [71], polarization conversion [72], angular insensitive metalenses [73] and leaky wave pattern synthesis [74].

This PhD thesis takes place within this framework of modelling and studying the polarization properties of stacked metallic metamaterials. In this work, we develop a simple and analytical formalism in order to model and describe the polarization properties of stacked metallic metamaterials. The developed model is extracted from a monomodal method which restricts our theoretical model to particular unit cell geometries and to a limited spectral range. As we will see throughout this manuscript, the analytical expressions derived from the theoretical formalism will allow us to study with more details the polarization properties of stacked metallic metamaterials. With our model, we will further explore, describe and understand new possibilities that arises from the stacking and that have not been reported yet. Mainly, we will see that the multiple reflections of light inside the stacked structure can lead to Fano resonances. In fact, the model we use will also enables us to establish a simple model based on a Fabry-Perot-like approach that clearly shows that the Fano resonance in the stacked structures originates from the specific polarization properties of the metamaterials. It is crucial to remind that such polarization-based Fano resonances can not be obtained by using single metallic metamaterials. These Fano and Fabry-Perot-like resonances will allow us to design and to propose various applications for filtering, sensing as well as polarization rotation. Our new insights into stacked metamaterials will also be of great help to identify and apprehend the critical points for fabrication and experiments.

Basically, during this thesis, we explore and reveal original phenomena that are based on the specific polarization properties of metallic metamaterials. We think that the overall contribution of this PhD thesis enlarges the perspectives and the range of applications of stacked metallic metamaterials and/or stacked metallic metasurfaces.

1.6/ THESIS OUTLINE

In the first chapter, we mainly focus on the modelling aspect of single metallic metamaterials. For this entire thesis, we focus on monoperiodic metallic metamaterials made of

subwavelength lamellar grooves, and biperiodic metamaterials consisting subwavelength rectangular holes array. First, we introduce the basic concept of the modal method which is the starting point of our theory. This method is especially well suited for such geometries as it leads to simple and analytical expressions for the transmission and polarization properties of the metallic metamaterials. Given few assumptions that are commonly permitted for such structures (negligible evanescent modes), we use a monomodal method to establish an Extended Jones Formalism (EJF) which takes into account the polarization properties for single metallic metamaterials in view of modelling stacked metamaterials in the next chapters. Further, we use the EJF to study monoperiodic and biperiodic metamaterials in order to highlight the common points and the differences between them. We also compare and validate this preliminary results with the multimodal method using a scattering matrix formalism which takes into account evanescent modes in the metamaterials. We finally emphasize that the metallic metamaterials play the role linear polarizers with enhanced transmission.

In the second chapter, we make an analytical and numerical study for the smallest stack possible, i.e., a stack of two metamaterial polarizers only. Such simple structure resembles the well known polarizer-analyzer configuration which is typically obtained with a pair of anisotropic bulk plates. We combine the EJF with a simple analytical algorithm that accounts for the stacking and it allows us to derive an analytical expression for the transmission through the entire structure: the extended Malus' Law. We further compare this extended Malus' law with the transmission expression obtained for the classical polarizer-analyzer configuration (i.e., the classical Malus' Law) and we further highlight their discrepancies. Therein, we show that the difference originates from the multiples reflections that arise only in the stacked metallic metamaterials. With the appropriate design, we show that this additional effect gives us the opportunity to turn our structure into an electro-optically sensitive detector. We also discuss some limiting aspects such as absorption and substrate's refractive index that needs to be considered for potential fabrication and experimental measurements. Finally, we remark that the spectral signature we use for the sensing application is very similar to Fano resonance line shape and it leads us to the next chapter where we give a physical explanation of the origin of Fano resonances in stacked metamaterials.

The third chapter is devoted to the analysis of the physical process that leads to Fano resonances in the polarizer-analyzer configuration. This study is of great importance since Fano resonances have not been reported or described yet in stacked metallic metamaterials. It is however interesting to note that Fano resonances have been extensively studied for single metamaterials with specific geometry unit cells. For this in-depth study,

we keep the same structure made of two identical metallic polarizers and we take advantage of our analytical EJF together with a circulating field approach to develop a polarized Fabry-Perot cavity model. This new viewpoint helps us to identify and discuss the key points that are involved in the formation of Fano resonances. We reveal that the Fano resonances in stacked metamaterials are induced by the specific polarization properties of the each metamaterial. Such way of exciting Fano resonances has not been reported to date. We further illustrate the potential of Fano resonances in stacked structures by demonstrating multiple and independently tunable Fano resonances.

In the fourth chapter, we finally study the transmission property for stacked structures made of an arbitrary number N of metallic metamaterials ($N \geq 3$). We especially make our numerical study in view of polarization rotation applications. We show that some parameters play a crucial role in the spectral tunability of our structures. For example, we show that a same initial structure can achieve either broadband cross-polarization rotation or an ultra-narrow band filtering by simply playing with the arrangement of the structure (the metamaterials position and rotation). We also show the intrinsic limitations of such structure and we discuss the compromises that have to be considered for practical design and fabrication. In addition, we also propose polarization rotation based on the excitation of a Fano-like resonance using only two metamaterial polarizers. To our knowledge, such concept of polarization rotation combining stacked metallic metamaterials and Fano-like resonances has not been reported yet.

The conclusion summarizes the thesis contributions and develop an overview of the several possibilities offered by stacked metallic metamaterials. We especially emphasize on the realization and control of Fano resonances, which could open new and promising opportunities using stacked metamaterials. Some intriguing and unexplained results due to the multiple reflections are also addressed in the perspectives. We also discuss some issues and key points that should be taken into account for the fabrication and the experimental counterpart. Finally, we consider more general implications concerning the polarized Fabry-Perot cavity aspect of such structures which could open new possibilities in sensing and filtering for stacked metallic metamaterials.

2

THEORETICAL BACKGROUND AND MODELLING

This chapter presents the theory involved for modelling the polarization properties of metallic metamaterials. Firstly, we describe the opto-geometrical parameters of the considered metamaterial, which is a metallic plate patterned with subwavelength apertures. We note that such kind of structures have been extensively studied in the past years [75] and can bear different names according to the specific scientific community or the desired applications. For example, it can be named as frequency selective surface, or periodic surface or slot arrays which are mainly used for radomes, filters or reflectors [76]. This kind of structure can also be regarded as a subwavelength diffraction grating [42, 48, 77], i.e. a diffraction grating with a periodicity smaller than the wavelength. For example, the diffraction gratings find applications in spectrometry, wavelength division multiplexing or chirp pulse amplification [77]. In this manuscript, we simply refer to this structure as metallic metamaterial. Secondly, we present the modal method which constitutes the general framework of our theory. Principally, this method (based on modal expansions) gives a description of the electromagnetic field in the metamaterial apertures and in the regions surrounding the metamaterial (substrate and superstrate). Then, we briefly give more details on the modal expression of the electromagnetic fields in the surrounding regions (using Floquet modes) and in the metamaterials (using waveguide modes). We will derive from it the scattering matrix (S-matrix) of the considered metamaterial that takes into account its polarization properties. With the appropriate assumptions on the electromagnetic field in the metamaterial apertures, we will show that an Extended Jones Formalism (EJF) can be extracted from the S-matrix. The advantage of such model is that it efficiently describes the polarization properties of single metamaterials using analytical Jones matrices.

In the last section of this chapter, we will illustrate the EJF to present the specific polar-

ization properties of the metamaterials of interest. We will also compare the polarization properties of our structure with the ones of conventional dichroic polarizers. The linear polarization selection is achieved differently for metallic metamaterials than for dichroic polarizers. Such polarization selectivity with metallic metamaterials will lead to exotic effects in stacked structures, that will serve to propose several applications such as polarization rotation or ultra-sensitive detection.

The EJF will allow us to further explore and describe interesting phenomena (such as Fano resonances) occurring in stacked structure that originates from the specific metamaterial polarization properties. Furthermore, the simplicity of this formalism will greatly help to develop a simple polarized Fabry-Perot model later in the manuscript which qualitatively explains exotic Fano resonances in stacked structures. We also mention that the extended Jones formalism can be applied to more complex unit cells with particular symmetry such as C_{1v} or C_{4v}. We briefly show that it can be used for designing anisotropic metamaterials. Finally, we conclude this chapter by outlining the main polarization properties of the studied metamaterials.

2.1/ DESCRIPTION OF THE STRUCTURE

In the thesis introduction, we have shown a wide variety of designed metamaterials. We now introduce in detail the type of metamaterial that we specifically wish to study. We consider in this work a metallic plate of thickness h which is periodically structured, in the $(x-y)$ plane, with an array of rectangular apertures with z-invariant opto-geometrical parameters, as shown in Fig. 2.1 **(a)**. We note however that the theory allows for other aper-

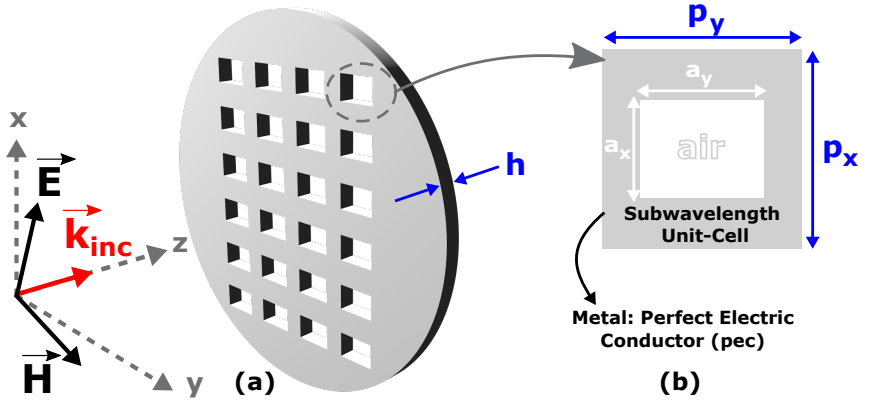

Figure 2.1: Example of a metallic metamaterial composed of a repeating unit cell with dimensions p_x and p_y that are shorter than the incident light wavelength λ. The unit-cell is made of rectangular holes where the width is denoted by a_x and the length by a_y. The thickness of the metamaterials is represented by h.

tures geometries - such as circles - but are not considered for the rest of this manuscript. Indeed, the considered rectangular aperture possesses a $C_{2,y}$ symmetry which leads to specific linear polarization properties (see section 2.4). The periodicity of the structure is following a rectangular Bravais lattice. We mention that it is possible to generalize the theory for other Bravais lattices with arbitrary nonorthogonal coordinates [78, 79]. In this manuscript, we consider a unit-cell comprising only one aperture, as depicted in Fig. 2.1**(b)**. The particularity is that the unit-cell dimensions along the x and y axis - p_x and p_y respectively - are smaller than the wavelength λ of the incident electromagnetic field. This ensures an enhanced optical transmission [34] which will allow us to design stacked structures with very high transmission. We will refer to this kind of pattern as subwavelength aperture for the rest of this manuscript. For this whole thesis, we consider the metal as a perfect electric conductor (pec).

For the most part of this manuscript, when the periods p_x and p_y are kept equal, we note $p_x = p_y = p$. The surface of the unit-cell is denoted by S and $S = p_x p_y$. The width of the rectangular holes is given by a_x and its length by a_y. The cross-section of the rectangular aperture is given by $\Omega = a_x a_y$. The structure is surrounded by two semi-infinite, lossless, isotropic, linear and homogeneous regions. We simply refer to these surrounding media as homogeneous regions. If not mentioned, the apertures and the homogeneous regions are filled with air. It is worth noting that monoperiodic metamaterials are also considered since they follow the same theoretical treatment. The single and double periodicities are shown in Fig. 2.2**(a)** and **(b)** respectively. Figure 2.2 **(a)** shows a monoperiodic (or 1D-periodic) pattern composed of one invariant axis and one periodicity axis. Figure 2.2

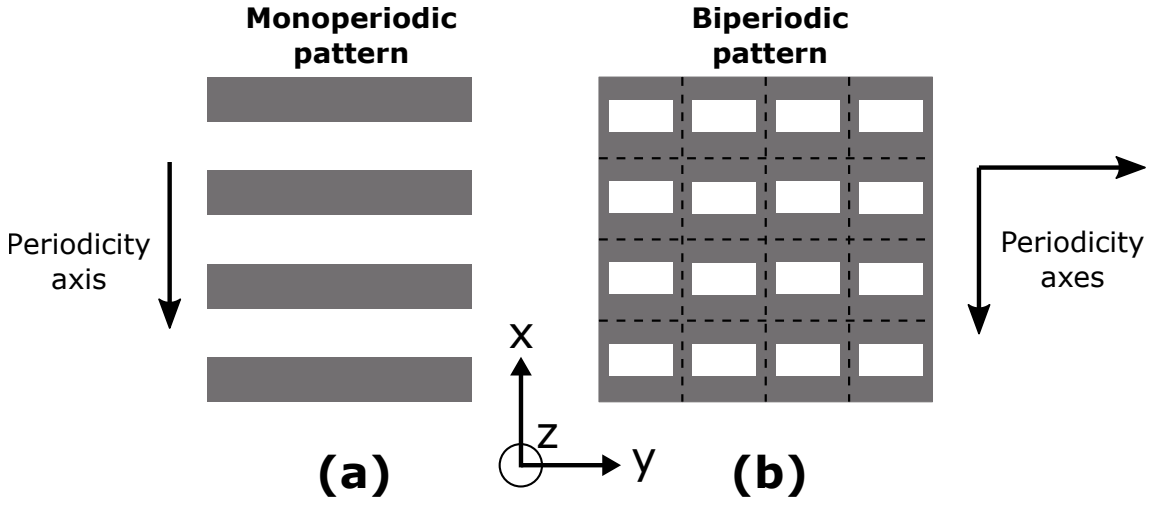

Figure 2.2: **(a)** Monoperiodic pattern featuring a single periodicity axis and a single invariant axis. **(b)** Example of a biperiodic pattern. In this case, there are two orthogonal periodicity axes and no invariant axis.

(b) depicts a biperiodic (or 2D-periodic) rectangular Bravais lattice made of rectangular apertures.

In this section, we have described the basic geometry that will be used to design metallic metamaterials with linear polarization properties. In the next section, we will theoretically describe the metamaterials and we will focus only on the general case of the biperiodic metamaterial with subwavelength rectangular apertures, as shown in Fig. 2.1 and Fig. 2.2**(b)**.

2.2/ THE MODAL METHOD

We have established an EJF to model the polarization properties of stacked metallic metamaterials. It involves the combination of various theories such as the Floquet theory for periodic structure, the electromagnetic (EM) theory of metallic waveguide, the modal method and the fundamentals of Jones matrices. It is therefore necessary to give brief reminders of all these elements before describing the Jones formalism extended to metallic metamaterials. We remind that we present the biperiodic case only, which is characterized by the period p along the x and y axes and the surface of the periodic unit-cell $S = p^2$.

2.2.1/ PRINCIPLE OF THE MODAL METHOD

The fundamental principle of the Modal Method originates from the method of moment [80] which has been extensively used in microwave engineering for solving a large variety of electromagnetic problems [81], including periodic metallic structures [82–84]. Basically, the method of moment approximates the response of a studied structure as a series of basis functions with their associated expansion coefficients. In our case, these functions satisfy boundary conditions imposed by the metallic metamaterial. The basis functions are thus called modes and the expansion coefficients are the amplitudes associated to these modes. We consider modal expansion in the homogeneous regions and in the apertures (we detail later in section 2.2.3 and section 2.2.4 the specific properties of such modes). The expanded EM field is then projected on the two orthogonal basis vectors $\vec{e}_x$ and $\vec{e}_y$ which define the transverse plane. The modal projection on the transverse (x, y) plane allows us to directly apply the continuity of the transverse EM field at the metamaterial interfaces. By matching the modal expansions and applying Galerkin operators, we will be able to extract Jones matrices giving the polarization properties of the metamaterials.

In this configuration, these EM modes can be given by a general expression, regardless of the considered region j with $j \in \{1, 2, 3\}$ where $j = 2$ for the metallic metamaterial and $j = 1$ or $j = 3$ for the surrounding homogeneous regions. The EM field in harmonic regime for any propagative or evanescent modes τ is expressed as follows:

$$\vec{U}_\tau^{(j)}(\vec{r}, t) = \vec{U}_\tau^{(j)}(\vec{r}_t) e^{i\gamma_\tau^{(j)} z} e^{-i\omega t} \tag{2.1}$$

where $\vec{U}$ denotes either the electric or the magnetic field: $\vec{U} \in (\vec{E}, \vec{H})$, $\vec{r} = x\vec{e}_x + y\vec{e}_y + z\vec{e}_z$ and $\vec{r}_t = x\vec{e}_x + y\vec{e}_y$. The term $\gamma_\tau^{(j)}$ denotes the propagation constant of the mode τ in region j. The components of the field that depend only on the transverse coordinates is denoted by $\vec{U}_\tau^{(j)}(\vec{r}_t)$. The subscript τ is a super-index which consists of the mode orders (resulting from the application of boundary conditions) and the polarization state of the mode. For this manuscript, we refer to the polarization state of the modes with the following terms: Transverse Electric (TE) with $E_z = 0$, Transverse Magnetic (TM) with $H_z = 0$ and Transverse Electromagnetic (TEM) with $E_z = H_z = 0$. By convention, we consider that $j = 1$ corresponds to the incident region. In addition, we split the transverse components and the z-component of the field so that

$$\vec{U}_\tau^{(j)} = \vec{U}_{\tau,t}^{(j)} + U_{\tau,z}^{(j)} \vec{e}_z \tag{2.2}$$

where $\vec{U}_{\tau,t}$ and $U_{\tau,z}$ are respectively the transverse and the z components of the mode τ.

We mention that such harmonic EM modes feature general properties that are essential in the modal method. First, the transverse components of the electric field verify the following orthogonality relation:

$$\iint_\zeta \vec{E}_{\tau,t}^{(j)*}(\vec{r}_t) . \vec{E}_{q,t}^{(j)}(\vec{r}_t) dxdy = \delta_{\tau,q} \tag{2.3}$$

where $*$ denotes the complex conjugate, ζ is the periodic surface (either S in homogeneous regions, or Ω in apertures) and δ is the Kronecker delta function. Note that the left hand side of Eq. (2.3) is the inner product of $\vec{E}_{\tau,t}^{(j)*}(\vec{r}_t)$ with $\vec{E}_{q,t}^{(j)}(\vec{r}_t)$. In Sec. 2.2.3 and Sec. 2.2.4, we will detail the expression of ζ according to the considered region. The orthogonality relation simply means that two different modes ($\tau \neq q$) do not couple to each other during their propagation along the z-axis, in the region j. However, we will see later that the modes couple to each other at the metamaterials interfaces.

Second, it is important to mention that for any transverse electric component $\vec{E}_{\tau,t}^{(j)}(\vec{r}_t)$ we

can deduce its corresponding transverse magnetic component $\vec{H}^{(j)}_{\tau,t}(\vec{r}_t)$ with the following relationship:

$$\vec{H}^{(j)}_{\tau,t}(\vec{r}_t) = \eta_0 \eta^{(j)}_{\tau} \vec{e}_z \wedge \vec{E}^{(j)}_{\tau,t}(\vec{r}_t) \tag{2.4}$$

where $\eta_0 = \sqrt{\frac{\varepsilon_0}{\mu_0}}$ is the optical admitance of vacuum with ε_0 and μ_0 being respectively the permittivity and permeability of vacuum. The term $\eta^{(j)}_{\tau}$ is the relative optical admittance of the mode τ in region j which is also referred to as the modal admittance [79]. This relation is crucial since it allows to deduce the expansion of the transverse magnetic field from the expansion of transverse electric field. For all regions j, the optical admittances of any mode τ is expressed by

$$\begin{aligned}
\eta^{(j)}_{\tau} &= \frac{\varepsilon^{(j)}_r k_0}{\gamma^{(j)}_{\tau}} \quad : \text{TM mode} \\
\eta^{(j)}_{\tau} &= \frac{\gamma^{(j)}_{\tau}}{k_0 \mu^{(j)}_r} \quad : \text{TE mode} \\
\eta^{(j)}_{\tau} &= \frac{\varepsilon^{(j)}_r k_0}{\gamma^{(j)}_{\tau}} = \frac{\gamma^{(j)}_{\tau}}{k_0 \mu^{(j)}_r} = \sqrt{\frac{\varepsilon^{(j)}_r}{\mu^{(j)}_r}} \quad : \text{TEM mode}
\end{aligned} \tag{2.5}$$

where $\varepsilon^{(j)}_r$ and $\mu^{(j)}_r$ are respectively the relative permittivity and relative permeability of the region j and $k_0 = 2\pi/\lambda$. Furthermore, we define $\vec{k}^{(j)}_{\tau}$ as the wave vector of the mode τ in region j such that

$$\vec{k}^{(j)}_{\tau} = \vec{k}^{(j)}_{\tau,t} + \gamma^{(j)}_{\tau} \vec{e}_z \tag{2.6}$$

where $\vec{k}^{(j)}_{\tau,t}$ is the transverse wave vector of the mode and $\left\|\vec{k}^{(j)}_{\tau}\right\|^2 = k_0 n_j$ (with n_j the refractive index of the considered region j). Since we consider lossless homogeneous regions, the propagation constant can be written as

$$\gamma^{(j)}_{\tau} = \begin{cases} \sqrt{\left\|\vec{k}^{(j)}_{\tau}\right\|^2 - \left\|\vec{k}^{(j)}_{\tau,t}\right\|^2} & \text{for propagative modes} \quad (\gamma^{(j)}_{\tau} \in \mathbb{R}) \\ i\sqrt{\left\|\vec{k}^{(j)}_{\tau,t}\right\|^2 - \left\|\vec{k}^{(j)}_{\tau}\right\|^2} & \text{for evanescent modes} \quad (\gamma^{(j)}_{\tau} \in \mathbb{C}) \end{cases} \tag{2.7}$$

We also define $\lambda^{(j)}_{\tau}$ as the cut-off wavelength of the mode for which $\gamma^{(j)}_{\tau} = 0$. Such wavelength indicates the transition between propagative and evanescent regime of the mode, as shown in Fig. 2.3.

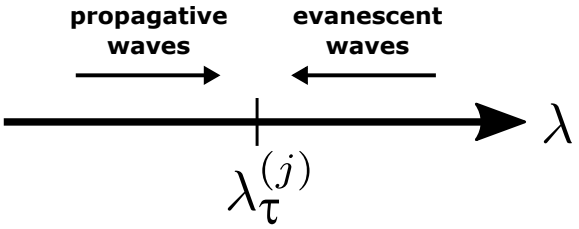

Figure 2.3: The first cut-off wavelength $\lambda_\tau^{(j)}$ separating the propagative regime and the evanescent regime of a mode τ in region j.

With this additional consideration, the general expression of the propagation constant $\gamma_\tau^{(j)}$ can be written as

$$\gamma_\tau^{(j)} = k_0 n_j \sqrt{1 - \frac{\lambda}{\lambda_\tau^{(j)}}} \tag{2.8}$$

so that $\gamma_\tau^{(j)} \in \mathbb{R}$ for $\lambda < \lambda_\tau^{(j)}$ and $\gamma_\tau^{(j)} \in \mathbb{C}$ for $\lambda > \lambda_\tau^{(j)}$. Finally, for any region, the modal expansion of the total transverse electric field $\vec{E}_t^{(j)}(\vec{r},t)$ is given by the same expression shown below:

$$\vec{E}_t^{(j)}(\vec{r},t) = e^{-i\omega t} \sum_\tau \left[A_\tau^{(j)} e^{i\gamma_\tau^{(j)}\left(z - z_A^{(j)}\right)} + B_\tau^{(j)} e^{-i\gamma_\tau^{(j)}\left(z - z_B^{(j)}\right)} \right] \vec{E}_{\tau,t}(\vec{r}_t) \tag{2.9}$$

where $A_\tau^{(j)}$ and $B_\tau^{(j)}$ are the amplitudes of the forward and backward modes, respectively, and $z_A^{(j)}$ and $z_B^{(j)}$ denotes their arbitrary phase origins. We note that the arbitrary phase origins z_A and z_B are optional when writing the modal expansion. Nonetheless, we will see later that making explicit the phase origin in the modal expansion is very useful as it finally simplifies the expression of the equation to be solved. Equation (2.9) suggests that the total transverse electric field in any region j is a sum of forward and backward modes τ with their respective amplitude $A_\tau^{(j)}$ and $B_\tau^{(j)}$. Note that the transverse EM components $\vec{E}_{\tau,t}^{(j)}$ are not defined for the moment since the EM conditions imposed in each region are not specified yet. More details will be given in section 2.2.3 and section 2.2.4 where we present the modes satisfying conditions imposed by the structure. From a more mathematical point of view, the right hand side of Eq. (2.9) is the projection of the total transverse electric field on the transverse plane using the basis functions $\vec{E}_{\tau,t}(\vec{r}_t)$.

From the modal expansion of the total transverse electric field given in Eq. (2.9), we deduce the expansion of the total transverse magnetic field $\vec{H}_t^{(j)}(\vec{r},t)$ using Eq. (2.4) and it leads to

$$\vec{H}_t^{(j)}(\vec{r},t) = e^{-i\omega t} \sum_\tau \left[A_\tau^{(j)} e^{i\gamma_\tau^{(j)}\left(z - z_A^{(j)}\right)} - B_\tau^{(j)} e^{-i\gamma_\tau^{(j)}\left(z - z_B^{(j)}\right)} \right] \vec{H}_{\tau,t}(\vec{r}_t) \tag{2.10}$$

A comparison of Eq. (2.10) with Eq. (2.9) highlights a "−" sign in Eq. (2.10)) instead of a "+" sign (as in Eq. (2.9) for the backward modes amplitudes $B_\tau^{(j)}$. This is due to the relative optical admittance $\eta_\tau^{(j)}$ in Eq. (2.4) and given by Eq. (2.5) which involves the propagation constant of the mode $\gamma_\tau^{(j)}$. For the backward modes, the propagation constant is $-\gamma_\tau^{(j)}$ and therefore causes the "−" sign in Eq. (2.10).

The studied metallic metamaterial is a periodic array of rectangular apertures which may be seen as sections of metallic waveguides. Therefore, the projected modes, in region $j = 2$, correspond to waveguide modes. The metamaterial transverse bi-periodicity also imposes the same transverse bi-periodicity on the homogeneous regions $j = 1$ and $j = 3$. Consequently, the projected modes in these periodic homogeneous regions are Floquet modes. Basically, the metamaterial imposes a periodic unit-cell in the whole space, as shown in Fig. 2.4**(a)**. To summarize, the EM fields is described as an expansion of

- Floquet modes that satisfy the transverse periodic condition of the unit-cell in homogeneous regions ($j = 1$ and $j = 3$).
- waveguide modes satisfying the boundary condition on the walls of the subwavelength apertures ($j = 2$).

More details on Floquet modes and waveguide modes are given later in this chapter in section 2.2.3 and section 2.2.4. The modal expansion is illustrated in Fig. 2.4**(b)** showing the field expansion for each regions. The terms $A^{(1)}$, $A^{(3)}$ and $B^{(1)}$, $B^{(3)}$ schematically

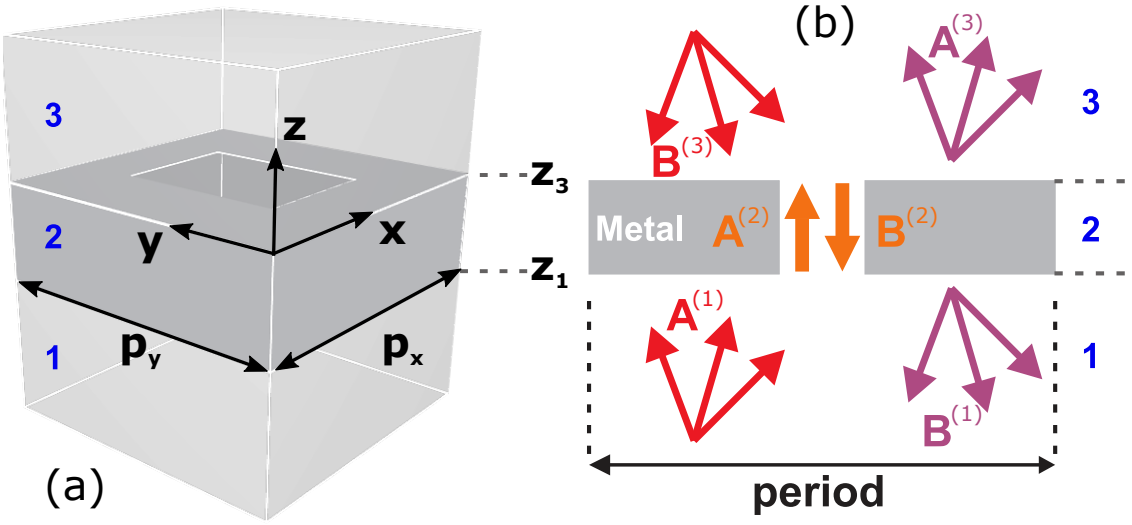

Figure 2.4: **(a)** Schematic view of a bi-periodic unit-cell of the considered EM problem. **(b)** Schematic summary of the Modal Method principle. The fields in the homogeneous regions 1 and 3 consist in a sum of incident and scattered Floquet modes and the field in the aperture is seen a sum of TE and TM waveguide modes. For monoperiodic metamaterials the sum also includes the TEM waveguide mode.

denote the amplitudes of forward and backward Floquet modes in the homogeneous regions while $A^{(2)}$ and $B^{(2)}$ are the amplitude of forward and backward waveguide modes respectively. We note that for an infinite number of modes, both the Floquet and the waveguide expansions form complete sets. In other words, the infinite modal expansion in each region gives the exact solution for the total transverse EM field.

We now want to establish the fundamental equations of the modal method which links the Floquet modes amplitudes with waveguide modes amplitudes. The key step for obtaining these fundamental equations is to match the modal expansion in the homogeneous regions with the one in the waveguides at the interfaces z_1 and z_3. For that, we first precise the values of the phase origins $z_A^{(j)}$ and $z_B^{(j)}$. For the incident region ($j = 1$), we impose the phase origins at the interface $z = z_1$, i.e. $z_A^{(1)} = z_B^{(1)} = z_1$. Likewise, for the homogeneous region 3 we choose $z_A^{(3)} = z_B^{(3)} = z_3$. For the region 2 containing the metamaterial, the phase origin of the forward modes is $z_A^{(2)} = z_1$ while the origin for the backward modes is $z_B^{(2)} = z_3$. As we will see in the following page, such phase origin values will allow us to get simple expressions of the modal expansion matching (see Eq. (2.13 to Eq. (2.17)). We remind that in region 2, the unit cell is composed of a pec rectangular waveguide with a cross-section $\Omega = a_x a_y$ (with $\Omega \in S$). In order to realize the modal expansion matching at the metamaterials interfaces, we use the continuity relation [85] of the EM field on the unit cell surface S at the metamaterials interfaces $z = z_1$ and $z = z_3$. The transverse electric field is continuous at the interfaces for $\vec{r}_t \in S$. However, for $\vec{r}_t \notin \Omega$, the pec metallic surface imposes the condition $\vec{E}_t = 0$. Thus, at the interfaces $z = z_1$ and $z = z_3$ we respectively have

$$\begin{aligned} \vec{E}_t^{(1)}(x, y, z = z_1, t) &= \vec{E}_t^{(2)}(x, y, z = z_1, t), \quad \forall \vec{r}_t \in \Omega \\ \vec{E}_t^{(3)}(x, y, z = z_3, t) &= \vec{E}_t^{(2)}(x, y, z = z_3, t), \quad \forall \vec{r}_t \in \Omega \end{aligned} \tag{2.11}$$

For the transverse magnetic field, the continuity of the transverse magnetic field can be applied only on the cross section Ω, so that

$$\begin{aligned} \vec{H}_t^{(1)}(x, y, z = z_1, t) &= \vec{H}_t^{(2)}(x, y, z = z_1, t), \quad \forall \vec{r}_t \in \Omega \\ \vec{H}_t^{(3)}(x, y, z = z_3, t) &= \vec{H}_t^{(2)}(x, y, z = z_3, t), \quad \forall \vec{r}_t \in \Omega \end{aligned} \tag{2.12}$$

Replacing the transverse fields in Eq. (2.11) and Eq. (2.12) by their modal expansion expressed in the right hand side of Eq. (2.9) and Eq. (2.10) respectively, we obtain the matching of the modal expansions at both interfaces of the metamaterials. Now, to clarify the notation for the equations, we differentiate the waveguide modes by the specific index ν (instead of τ).

For the transverse electric field, the modal expansion matching at $z = z_1$ gives

$$\sum_{\tau} \left[A_{\tau}^{(1)} + B_{\tau}^{(1)}\right] \vec{E}_{\tau,t}^{(1)}(\vec{r}_t) = \sum_{\nu} \left[A_{\nu}^{(2)} + B_{\nu}^{(2)} u_{\nu}^{(2)}\right] \vec{E}_{\nu,t}^{(2)}(\vec{r}_t), \quad \forall \vec{r}_t \in \Omega \tag{2.13}$$

and at the interface $z = z_3$ it yields

$$\sum_{\tau} \left[A_{\tau}^{(3)} + B_{\tau}^{(3)}\right] \vec{E}_{\tau,t}^{(3)}(\vec{r}_t) = \sum_{\nu} \left[A_{\nu}^{(2)} u_{\nu}^{(2)} + B_{\nu}^{(2)}\right] \vec{E}_{\nu,t}^{(2)}(\vec{r}_t), \quad \forall \vec{r}_t \in \Omega \tag{2.14}$$

with

$$u_{\nu}^{(2)} = e^{i\gamma_{\nu}^{(2)}(z_3 - z_1)} = e^{i\gamma_{\nu}^{(2)} h} \tag{2.15}$$

where $u_{\nu}^{(2)}$ is the propagation term of the waveguide mode ν in the aperture, along the metamaterial's thickness $h = z_3 - z_1$. We can now see that writing the optional arbitrary phase in Eq. (2.9) and Eq. (2.10) finally gives simple expressions for the modal expansions matching. For the transverse magnetic field, the modal expansion matching at $z = z_1$ gives

$$\sum_{\tau} \left[A_{\tau}^{(1)} - B_{\tau}^{(1)}\right] \vec{H}_{\tau,t}^{(1)}(\vec{r}_t) = \sum_{\nu} \left[A_{\nu}^{(2)} - B_{\nu}^{(2)} u_{\nu}^{(2)}\right] \vec{H}_{\nu,t}^{(2)}(\vec{r}_t), \quad \forall \vec{r}_t \in \Omega \tag{2.16}$$

and at $z = z_3$ we have

$$\sum_{\tau} \left[A_{\tau}^{(3)} - B_{\tau}^{(3)}\right] \vec{H}_{\tau,t}^{(3)}(\vec{r}_t) = \sum_{\nu} \left[A_{\nu}^{(2)} u_{\nu}^{(2)} - B_{\nu}^{(2)}\right] \vec{H}_{\nu,t}^{(2)}(\vec{r}_t), \quad \forall \vec{r}_t \in \Omega \tag{2.17}$$

Now that we have matched the modal expansions in regions 1 and 3 with the modal expansion in region 2, we realize the modal projections at each interface. For that, we use the inner product as defined by the left hand side of Eq. (2.3). We apply on both sides of Eqs. (2.13) and (2.14) the following inner product

$$\iint_{S} [\cdot].\vec{E}_{q}^{(j)*}(\vec{r}_t).dS, \ \forall q \in \mathbb{Z}^3 \tag{2.18}$$

where $\vec{E}_{q}^{(j)}(\vec{r}_t)$ are Floquet modes, q is the index identifying these modes and the symbol $[\cdot]$ denotes the equation to operate on. In the method of moments, such function $(\vec{E}_{q}^{(j)}(\vec{r}_t))$ is generally referred to as the "testing" or "weighting" function. Since, the "testing" function is chosen in the same set as the basis functions - i.e. Floquet modes - the technique is called the Galerkin method [81].

Remark: Strictly speaking, we do not apply a true Galerkin method since the operation (2.18) using Floquet mode is also applied on the waveguide mode basis given by the right hand side of Eqs. (2.13) and (2.14).

Using the orthogonality relation given by Eq. (2.3), the modal projection directly gives

$$\forall\tau,\ A_\tau^{(1)} + B_\tau^{(1)} = \sum_\nu \left[A_\nu^{(2)} + B_\nu^{(2)} u_\nu^{(2)}\right] g_{\nu,\tau}^{(1)} \tag{2.19}$$

and

$$\forall\tau,\ A_\tau^{(3)} + B_\tau^{(3)} = \sum_\nu \left[A_\nu^{(2)} u_\nu^{(2)} + B_\nu^{(2)}\right] g_{\nu,\tau}^{(3)} \tag{2.20}$$

where $g_{\nu,\tau}^{(j)}$ is the overlap integral of a Floquet mode τ in region j (1 or 3) with a waveguide mode ν on the waveguide cross-section Ω. It is given by

$$g_{\nu,\tau}^{(j)} = \iint_\Omega \vec{E}_{\nu,t}^{(2)}(\vec{r}_t)\vec{E}_{\tau,t}^{(j)*}(\vec{r}_t)d\Omega \tag{2.21}$$

In other words, the overlap integral $g_{\nu,\tau}^{(j)}$ is the coupling, at the metamaterial interfaces, between a waveguide mode and a Floquet mode in region j. Note that the we have written the index τ instead of q in the overlap integral expression since the index q was only necessary to make the difference between the testing Floquet modes and the basis Floquet modes. For the Eqs. (2.16) and (2.17), we apply another special operator defined by

$$\iint_\Omega \left([\cdot] \wedge \vec{E}_{\mu,t}^{(j)}(\vec{r}_t)\right).\vec{e}_z d\Omega \tag{2.22}$$

where $\vec{E}_\mu^{(j)}$ are the "testing" waveguide modes defined by the index μ. Here, the modal projection is not as straightforward as the one given before. After some derivations, we obtain

$$\forall\tau, \sum_\tau \left[\ A_\tau^{(1)} - B_\tau^{(1)}\right] \eta_\tau^{(1)} g_{\nu,\tau}^{*} = \sum_\nu \left[A_\nu^{(2)} - B_\nu^{(2)} u_\nu^{(2)}\right] \eta_\nu^{(2)} \tag{2.23}$$

and

$$\forall\tau, \sum_\tau \left[\ A_\tau^{(3)} - B_\tau^{(3)}\right] \eta_\tau^{(3)} g_{\nu,\tau}^{*} = \sum_\nu \left[A_\nu^{(2)} u_\nu^{(2)} - B_\nu^{(2)}\right] \eta_\nu^{(2)} \tag{2.24}$$

This set of four equations (Eqs. (2.19), (2.20), (2.23) and (2.24)) links the amplitude of the modes τ in the homogeneous regions to the amplitude of the modes ν inside the aperture. They correspond to the fundamental equations of the modal method.

With this set of 4 equations, it is possible to derive a general scattering matrix S which links the Floquet modes scattered by the metamaterial to the incident Floquet modes. However, our aim is to extract from the S-matrix an analytical and compact Jones formalism to describe efficiently the polarization properties of stacked metallic metamaterials.

To do so, we first have to use a simpler version of the modal method by considering only one propagative mode inside the aperture, i.e., the monomode modal method.

2.2.2/ MONOMODE MODAL METHOD

The Monomode Modal Method (MMM) consists in considering only a single propagative (guided) mode in the metamaterials apertures. The first successful attempt to model metallic metamaterials with the MMM was achieved by Lalanne *et al.* in 2000 [86] to predict the transmission and absorption properties of a monoperiodic grating made of real metal. However, considering only one mode in the apertures could lead to important errors compared to a multi-modal method. In order to minimize the error induced by the MMM approximation, we have to make sure that the EM field in the apertures is (almost) totally carried by a single mode. For that, we have to discuss two important points.

First Point: For the MMM validity, we have to ensure that one waveguide mode, at most, can be propagative along the aperture. To verify this, we impose:

$$\lambda > \lambda_2^{(2)} \tag{2.25}$$

where $\lambda_2^{(2)}$ is the cut-off wavelength of the second waveguide mode. Figure 2.5 gives a simple representation of the first hypothesis.

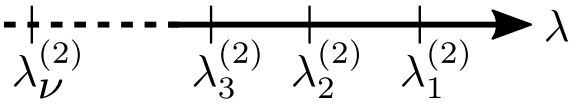

Figure 2.5: Cut-off wavelength chart of the fundamental mode $\lambda_1^{(2)}$ and the next higher order waveguide modes.

With such condition, all the higher order modes are evanescent so that only the mode with the highest cut-off wavelength is propagative and carries with no losses the EM field in the waveguide. Basically, the higher order modes exponentially decay from the interfaces along the metamaterial thickness. The mode with highest cut-off wavelength $\lambda_1^{(2)}$ is called the fundamental mode or the dominant mode. Note that when $\lambda > \lambda_1^{(2)}$, the fundamental mode is also evanescent but we then have $\lambda >> \lambda_2^{(2)}$ and it does not challenge the MMM validity. We emphasize that this condition is mandatory because the presence of a second guided mode (or more guided modes) would drastically modify the polarization and spectral properties of the studied structure. In such case, using the MMM would make no sense.

Second Point: Even if all the higher order waveguide modes are evanescent, they can still influence the MMM accuracy because of the evanescent modes coupling that can occur between the metamaterials interfaces (z_1 and z_3) through the apertures (tunnel-like effect). The importance of this effect involving the evanescent modes is directly influenced by the metamaterials thickness $h = z_3 - z_1$ and the cut-off wavelength of the higher order modes (dictated by the apertures geometry). Contrary to the first point of discussion, there is no absolute criterion for the value of h (or for the apertures dimensions) that allows to definitely neglect the evanescent coupling effect and we will discuss in detail this second point later in Sec. 2.3.4. Therein we compare the results obtained by the extended Jones formalism - which neglects the evanescent mode and the tunnel-like effect - with the results computed by the multimodal method - which takes into account the evanescent modes - for different values of h and a_x. Finally, we conclude that the error acceptability strongly depends on the targeted application based on broadband or narrow band resonances.

If we have only one guided mode and negligible evanescent modes in the apertures, then we can use the MMM and the notation simplifies. Since there is now only one mode to consider inside the aperture, we can get rid of the waveguide mode index ν so that

$$\begin{aligned} A_\nu^{(2)} &\rightarrow A^{(2)} \\ B_\nu^{(2)} &\rightarrow B^{(2)} \\ g_{\tau,\nu}^{(j)} &\rightarrow g_\tau^{(j)} \\ u_\nu^{(2)} &\rightarrow u_{(2)} \end{aligned} \tag{2.26}$$

With such a notation, we can rewrite the set of the 4 fundamental equations that links the Floquet modes amplitudes with the fundamental guided mode amplitudes:

$$A_\tau^{(1)} + B_\tau^{(1)} = \left[A^{(2)} + B^{(2)} u_{(2)}\right] g_\tau \ , \ \forall \tau \tag{2.27}$$

$$A_\tau^{(3)} + B_\tau^{(3)} = \left[A^{(2)} u_{(2)} + B^{(2)}\right] g_\tau \ , \ \forall \tau \tag{2.28}$$

$$\sum_\tau \left[A_\tau^{(1)} - B_\tau^{(1)}\right] \eta_\tau^{(1)} g_\tau^* = \left[A^{(2)} - B^{(2)} u_{(2)}\right] \eta^{(2)} \ , \ \forall \tau \tag{2.29}$$

$$\sum_\tau \left[A_\tau^{(3)} - B_\tau^{(3)}\right] \eta_\tau^{(3)} g_\tau^* = \left[A^{(2)} u_{(2)} - B^{(2)}\right] \eta^{(2)} \ , \ \forall \tau \tag{2.30}$$

The goal is now to obtain the scattering matrix S with this set of 4 equations:

$$\begin{pmatrix} A^{(3)} \\ B^{(1)} \end{pmatrix} = S \begin{pmatrix} A^{(1)} \\ B^{(3)} \end{pmatrix}. \tag{2.31}$$

where the terms inside brackets are the reduced notation for the corresponding column vectors containing all the Floquet modes τ. For example:

$$A^{(j)} \equiv \begin{pmatrix} \vdots \\ A_\tau^{(j)} \\ \vdots \end{pmatrix}; \quad B^{(j)} \equiv \begin{pmatrix} \vdots \\ B_\tau^{(j)} \\ \vdots \end{pmatrix} \tag{2.32}$$

for $j \in (1, 3)$.

Remark: After examination of Eq. (2.31) and Eq. (2.32), we see that for a number N_F of Floquet modes, the scattering matrix S has a $(2N_F \times 2N_F)$ dimension. Thus, it seems that the S matrix does not take into account the polarization properties of the Floquet modes but only their forward and backward propagation. However, as we have introduced in Eq. (2.1), we remind that the index τ takes into account the modes order and their polarization state (TE or TM). More details on the polarization properties of Floquet modes are given in Sec. 2.2.3 and especially in Eq. (2.54) and Eq. (2.55).

To derive the S matrix, we first specify the important step that consists in determining the matrix M that links the amplitude of incident Floquet modes to the amplitude the single guided mode. We first start by substituting Eq. (2.27) in Eq. (2.29) which leads to

$$\sum_\tau \left\{2A_\tau^{(1)} - \left[A^{(2)} + B^{(2)}u_{(2)}\right] g_\tau\right\} \eta_\tau^{(1)} g_\tau^* = \left[A^{(2)} - B^{(2)}\right] \eta^{(2)} \tag{2.33}$$

$$2\sum_\tau \eta_\tau^{(1)} g_\tau^* A_\tau^{(1)} - \left[A^{(2)} + B^{(2)}u_{(2)}\right] \sum_\tau \eta_\tau^{(1)} g_\tau g_\tau^* = \left[A^{(2)} - B^{(2)}\right] \eta^{(2)} \tag{2.34}$$

and we note that $g_\tau g_\tau^* = |g_\tau|^2$. We now introduce the coupling coefficient $C^{(j)}$ so that

$$C^{(j)} = \sum_\tau \eta_\tau^{(j)} |g_\tau|^2 \tag{2.35}$$

We remind that g_τ is the overlap integral between a Floquet mode τ and the fundamental waveguide mode. Therefore, the coupling coefficient $C^{(j)}$ can be regarded as the average optical admittance in region j of the Floquet modes with the fundamental guided mode which is weighted by the overlap integral. With this notation, Eq. (2.34) becomes

$$A^{(2)}\left[\eta^{(2)} + C^{(1)}\right] + B^{(2)}u_{(2)}\left[C^{(1)} - \eta^{(2)}\right] = 2\sum_\tau \eta_\tau^{(1)} g_\tau^* A_\tau^{(1)} \tag{2.36}$$

Equation (2.36) expresses $A^{(2)}$ and $B^{(2)}$ as a function of $A_\tau^{(1)}$ only. We follow the same technique by substituting Eq. (2.28) in Eq. (2.30) and we obtain

$$A^{(2)}u_{(2)}\left[C^{(3)}-\eta^{(2)}\right]+B^{(2)}\left[C^{(3)}+\eta^{(2)}\right]=2\sum_\tau \eta_\tau^{(3)}g_\tau^* B_\tau^{(3)} \tag{2.37}$$

where $A^{(2)}$ and $B^{(2)}$ are expressed as a function of $B_\tau^{(3)}$ only. With Eq. (2.36) and Eq. (2.37) we build the M matrix so that:

$$\begin{pmatrix} 2\sum_\tau \eta_\tau^{(1)}g_\tau^* A_\tau^{(1)} \\ 2\sum_\tau \eta_\tau^{(3)}g_\tau^* B_\tau^{(3)} \end{pmatrix} = M \begin{pmatrix} A^{(2)} \\ B^{(2)} \end{pmatrix} \tag{2.38}$$

where

$$M=\begin{pmatrix} C^{(1)}+\eta^{(2)} & u^{(2)}\left[C^{(1)}-\eta^{(2)}\right] \\ u^{(2)}\left[C^{(3)}-\eta^{(2)}\right] & C^{(3)}+\eta^{(2)} \end{pmatrix} \tag{2.39}$$

Even though the modes are orthogonal by propagation (see Eq. (2.3)), Eq. (2.38) suggests that the waveguide modes are coupled to each other via the Floquet modes. Finally, the amplitudes $A^{(2)}$ and $B^{(2)}$ of the fundamental waveguide mode are given by inversion of the matrix M

$$A^{(2)}=\frac{2}{\det(M)}\sum_\tau \left[C^{(3)}+\eta^{(2)}\right]\eta_\tau^{(1)}g_\tau^* A_\tau^{(1)}+u_{(2)}\left[\eta^{(2)}-C^{(1)}\right]\eta_\tau^{(3)}g_\tau^* B_\tau^{(3)} \tag{2.40}$$

$$B^{(2)}=\frac{2}{\det(M)}\sum_\tau \left[C^{(1)}+\eta^{(2)}\right]\eta_\tau^{(3)}g_\tau^* B_\tau^{(3)}+u_{(2)}\left[\eta^{(2)}-C^{(3)}\right]\eta_\tau^{(1)}g_\tau^* A_\tau^{(1)} \tag{2.41}$$

We can now replace the updated expressions of $A^{(2)}$ and $B^{(2)}$ in Eq. (2.27), and it leads to

$$\begin{aligned} B_\tau^{(1)} &= \frac{2g_\tau}{\det(M)}\sum_q \left[C^{(3)}+\eta^{(2)}\right]\eta_q^{(1)}g_\tau^*+u_{(2)}^2\left[\eta^{(2)}-C^{(3)}\right]\eta_q^{(1)}g_q^*A_q^{(1)}-\delta_{\tau,q}A_q^{(1)} \\ &+\frac{2g_\tau}{\det(M)}\sum_q \left[\eta^{(2)}-C^{(1)}\right]\eta_q^{(3)}g_\tau^*+u_{(2)}\left[\eta^{(2)}+C^{(1)}\right]\eta_q^{(3)}g_\tau^*B_\tau^{(3)} \end{aligned} \tag{2.42}$$

Likewise, we substitute Eq. (2.40) and Eq. (2.41) in Eq. (2.28) and we obtain

$$\begin{aligned} A_\tau^{(3)} &= \frac{2g_\tau u_{(2)}}{\det(M)}\sum_q \left[C^{(3)}+\eta^{(2)}\right]\eta_q^{(1)}g_q^*+u_{(2)}^2\left[\eta^{(2)}-C^{(3)}\right]\eta_q^{(1)}g_q^*A_q^{(1)}-\delta_{\tau,q}B_q^{(3)} \\ &+\frac{2g_\tau u_{(2)}}{\det(M)}\sum_q u_{(2)}^2\left[\eta^{(2)}-C^{(1)}\right]\eta_q^{(3)}g_\tau^*+\left[\eta^{(2)}+C^{(1)}\right]\eta_q^{(3)}g_\tau^*B_\tau^{(3)} \end{aligned} \tag{2.43}$$

With Eq. (2.42) and Eq. (2.43) we relate the amplitude of the scattered Floquet modes $A_\tau^{(3)}$ and $B_\tau^{(1)}$ to the amplitudes of the incident waves $A_\tau^{(1)}$ and $B_\tau^{(3)}$ from which we can build the scattering matrix S:

$$S = \begin{pmatrix} (S_{11})_{\tau,q} & (S_{12})_{\tau,q} \\ (S_{21})_{\tau,q} & (S_{22})_{\tau,q} \end{pmatrix} \tag{2.44}$$

where the expression of the (2×2) scattering matrix sub-blocks $(S)_{\tau,q}$ are given by

$$\begin{aligned} (S_{11})_{\tau,q} &= f^T \eta_q^{(1)} g_\tau g_q^* \quad ; \quad (S_{12})_{\tau,q} = f_1^R \eta_q^{(3)} g_\tau g_q^* - \delta_{\tau,q} \\ (S_{21})_{\tau,q} &= f_3^R \eta_q^{(1)} g_\tau g_q^* - \delta_{\tau,q} \quad ; \quad (S_{22})_{\tau,q} = f^T \eta_q^{(3)} g_\tau g_q^*. \end{aligned} \tag{2.45}$$

and each sub-block is arranged as

$$(S)_{\tau,q} = \begin{pmatrix} S_{\tau,\tau} & S_{\tau,q} \\ S_{q,\tau} & S_{q,q} \end{pmatrix}. \tag{2.46}$$

The metamaterial transmission factor is denoted by f^T while the reflection factors, in region 1 or region 3, are denoted by f_j^R. Their respective expressions are given by:

$$f^T = \frac{4u_{(2)}\eta^{(2)}}{[C^{(1)} + \eta^{(2)}][C^{(3)} + \eta^{(2)}] - u_{(2)}^2 [C^{(1)} - \eta^{(2)}][C^{(3)} - \eta^{(2)}]} \tag{2.47}$$

$$f_j^R = \frac{2\left\{C^{(j)} + \eta^{(2)} + u_{(2)}^2 \left[\eta^{(2)} - C^{(j)}\right]\right\}}{[C^{(1)} + \eta^{(2)}][C^{(3)} + \eta^{(2)}] - u_{(2)}^2 [C^{(1)} - \eta^{(2)}][C^{(3)} - \eta^{(2)}]}. \tag{2.48}$$

which feature an Airy-like form. It is important to note that the transmission factor f^T does not depend on the considered region. However, the reflection terms f_j^R depend on the considered region j. It means that, for $n_1 \neq n_3$, the metallic plates are reciprocal in transmission, but not in reflection.

We have now set up the basis for extracting a Jones formalism that can be extended to metallic metamaterials. However, before diving into the EJF, we give more details on the Floquet modes in homogeneous regions and the fundamental guided mode in the rectangular apertures.

2.2.3/ Elements on Floquet analysis for metallic metamaterials

The Floquet analysis is extensively used in the domain of phased array for designing antennas [75] or frequency selective surfaces [87]. More generally, the Floquet theory can be applied for modelling any periodic structure.

Remark: The Floquet analysis for periodic structures strongly resembles the theory of diffraction gratings in optics. In fact, the two approaches only differ from the adopted vocabulary and the physical interpretation. While in optics we consider the "grating problem" [48] to determine and analyse diffraction orders, in phased array we consider Floquet modes that satisfy the periodicity condition imposed by the studied structure.

First of all, we define the monochromatic plane wave incident on the biperiodic structure. The EM field for an incident monochromatic plane wave is given by:

$$\vec{U}_{inc}(\vec{r},t) = \vec{U}_0 e^{i\vec{k}^{(inc)}.\vec{r}} e^{-i\omega t} \tag{2.49}$$

with $\vec{U}_0$ its amplitude vector and $\vec{k}^{(inc)} = k_x\vec{e}_x + k_y\vec{e}_y + k_z\vec{e}_z$ its wave vector. We rewrite the wave vector in order to split its transverse component $\vec{k}_t^{(inc)} = k_x\vec{e}_x + k_y\vec{e}_y$ from the propagation constant k_z. We obtain

$$\vec{k}^{(inc)} = \vec{k}_t^{(inc)} + k_z\vec{e}_z \tag{2.50}$$

We also define

$$k^{(inc)} = ||\vec{k}^{(inc)}|| = k_0 n^{(inc)} = \omega^2\mu_0\varepsilon_0. \tag{2.51}$$

where $k^{(inc)}$ is the incident wave vector norm.

Basically, the Floquet theorem states that the EM field is the same in the periodic unit-cells , except that it comprises an additional exponential multiplier from one unit-cell to the adjacent one. The application of Floquet theorem to periodic structure is demonstrated in [88]. For the studied bi-periodic case, the Floquet theorem can be expressed by

$$\vec{U}_\tau(\vec{r}+\vec{p}_t) = \vec{U}_\tau(\vec{r})e^{i\vec{k}_{\tau,t}.\vec{p}_t} \tag{2.52}$$

where τ is the index of the modes which takes into account the corresponding Floquet modes orders ($(n,m) \in \mathbb{Z}^2$) and their polarization state ($\sigma \in$ TE, TM, TEM) so that $\tau = (n,m,\sigma)$, $\vec{U}_\tau(\vec{r})$ is a Floquet mode, $e^{i\vec{k}_{\tau,t}.\vec{p}_t}$ is the exponential multiplier and $\vec{p}_t = p_x\vec{e}_x + p_y\vec{e}_y$ is the bi-periodic shift corresponding to the metamaterials bi-periodicity. Because of this exponential multiplier in Eq. (2.52), the function $\vec{U}_\tau(\vec{r})$ is called a pseudo-periodical function. The transverse component of the wave vector $\vec{k}_{\tau,t}$ as previously introduced in Eq. (2.6) is now given by

$$\vec{k}_{\tau,t} = \vec{k}_t^{(inc)} + n\frac{2\pi}{p_x}\vec{e}_x + m\frac{2\pi}{p_y}\vec{e}_y = \vec{k}_t^{(inc)} + n\vec{G}_x + m\vec{G}_y \tag{2.53}$$

where $\vec{G}_x$ and $\vec{G}_y$ are the primitive vectors of the reciprocal Bravais lattice [89]. The expression of the transverse profile of a Floquet mode τ in region j is given by

$$\vec{U}_{\tau,t}^{(j)} = \frac{1}{\sqrt{S}} e^{i\vec{k}_{\tau,t}.\vec{r}_t} \vec{e}_\tau \tag{2.54}$$

where $\vec{e}_\tau$ is the unit vector associated to the Floquet mode and account for its polarization state which is given by

$$\vec{e}_\tau = \begin{cases} \dfrac{\vec{k}_{\tau,t}}{||\vec{k}_{\tau,t}||} & \forall \tau \in \{n, m, TM\} \\ \vec{e}_z \wedge \dfrac{\vec{k}_{\tau,t}}{||\vec{k}_{\tau,t}||} & \forall \tau \in \{n, m, TE\} \\ \cos\varphi_{inc}.\vec{e}_x + \sin\varphi_{inc}.\vec{e}_y & \forall \tau \in \{0, 0, TM\} \text{ or } \{TEM_1\} \\ -\sin\varphi_{inc}.\vec{e}_x + \cos\varphi_{inc}.\vec{e}_y & \forall \tau \in \{0, 0, TE\} \text{ or } \{TEM_2\} \end{cases} \tag{2.55}$$

Note that, for $\varphi_{inc} = 0°$, we have the TEM_1 and TEM_2 Floquet modes polarized along the x and y axes, respectively. The Floquet modal expansion is written as

$$\vec{U}_t(\vec{r}, t) = e^{-i\omega t} \sum_\tau \left[A_\tau^{(j)} e^{i\gamma_\tau^{(j)} z} + B_\tau^{(j)} e^{-i\gamma_\tau^{(j)} z} \right] \vec{U}_{\tau,t}^{(j)} \tag{2.56}$$

which suggests that the total scattered transverse field in region j is the sum of forward and backward Floquet modes. The separation between the propagative and evanescent regime is at $\gamma_\tau^{(j)} = 0$ and it occurs when $\lambda = \lambda_\tau^{(j)}$ which is called the Floquet mode cut-off wavelength. It is expressed by

$$\lambda_\tau^{(j)} = \frac{2\pi n_j}{||\vec{k}_{\tau,t}^{(j)}||} \tag{2.57}$$

To be precise, the separation between propagative and evanescent regime is at the first Floquet modes cut-off $\lambda_\tau^{(j)}$. Furthermore, we remind that for this manuscript, the periods p_x and p_y are kept equal so that $p_x = p_y = p$. In addition, as we will see later in this chapter, we always consider a normally incident light. In such way, the first cut-off is at $\lambda = \lambda_\tau^{(j)} = n_j p$. Then, we have $k_0 n_j = ||\vec{k}_{\tau,t}^{(j)}||$ which marks the transition between the propagative and the evanescent regime, and the propagation constant γ_τ vanishes.

Remark: In optics - particularly in the diffraction gratings area - such phenomenon is known as the Rayleigh-Wood anomaly [90, 91].

In the next section, we give more details on the waveguide modes located in the metamaterial's apertures. In the framework of the MMM, we especially pay attention to the

fundamental waveguide mode.

2.2.4/ MODES IN THE SUBWAVELENGTH RECTANGULAR WAVEGUIDE MADE OF PERFECT ELECTRIC CONDUCTOR

In this part, we now give some elements of metallic waveguide theory to describe the modes in the metamaterials apertures. The theory of metallic waveguide is well known and it is the basis of telecommunication engineering in the microwave domain [92].

As for the previous section, we focus on the waveguide modes for the biperiodic metamaterial made of rectangular waveguides, as previously depicted in Fig. 2.1. In the framework of the modal method, we associate the Maxwell's equations with Eq. (2.1) and we write the following reduced Helmoltz equation

$$\left(\nabla_t^2 + k_c^2\right) U_z(x,y) = 0, \text{ with } U_z = \begin{cases} E_z \text{ for TM} \\ H_z \text{ for TE} \end{cases} \tag{2.58}$$

where $k_c = \sqrt{k_0^2 - \gamma^2}$ is the cutoff wavenumber, γ is the propagation constant and ∇_t^2 is the transverse Laplacian operator. After some derivations, we obtain the solution for $H_z(x,y)$ in TE polarization ($E_z = 0$) and the solution for $E_z(x,y)$ in TM polarization ($H_z = 0$). For the TE polarization, the solution for $H_z(x,y)$ is given by

$$H_z^{(n'm')} = H_0^{(n'm')} \cos(n'\frac{\pi}{a_x}x)\cos(m'\frac{\pi}{a_y}y) \tag{2.59}$$

from which we deduce, by using Eq. (2.4), all the transverse components:

$$\begin{aligned} E_x^{(n'm')} &= -E_0^{(n'm')}\frac{m'}{a_y}\cos(n'\frac{\pi}{a_x}x)\sin(m'\frac{\pi}{a_y}y) \\ E_y^{(n'm')} &= E_0^{(n'm')}\frac{n'}{a_x}\sin(n'\frac{\pi}{a_x}x)\cos(m'\frac{\pi}{a_y}y) \\ H_x^{(n'm')} &= -H_0^{(n'm')}\frac{n'}{a_x}\sin(n'\frac{\pi}{a_x}x)\cos(m'\frac{\pi}{a_y}y) \\ H_y^{(n'm')} &= H_0^{(n'm')}\frac{m'}{a_y}\cos(n'\frac{\pi}{a_x}x)\sin(m'\frac{\pi}{a_y}y) \end{aligned} \tag{2.60}$$

where (n', m') are the indices denoting the waveguide modes order and $E_0^{(n'm')}$ and $H_0^{(n'm')}$ are the waveguide modes amplitudes. The transverse wave vector $\vec{k}_\nu$ of a waveguide mode ν is given by

$$\vec{k}_\nu = n'\frac{\pi}{a_x}\vec{e}_x + m'\frac{\pi}{a_y}\vec{e}_y = k_\nu^x\vec{e}_x + k_\nu^y\vec{e}_y \tag{2.61}$$

With such notation, the expression of the transverse profile of the electric field of a waveguide mode ν can be written in the general and compact form

$$\vec{E}_{\nu}^{(2)} = \frac{\epsilon_{\nu}}{\sqrt{\Omega}} \vec{f}(\vec{r}_t) \otimes \vec{e}_{\nu} \tag{2.62}$$

with

$$\vec{f}(\vec{r}_t) = \cos(k_{\nu}^{x} x) \sin(k_{\nu}^{y} y) \vec{e}_x + \sin(k_{\nu}^{x} x) \cos(k_{\nu}^{y} y) \vec{e}_y \tag{2.63}$$

and

$$\vec{e}_{\nu} = \begin{cases} \dfrac{\vec{k}_{\nu}}{||\vec{k}_{\nu}||}, \ \forall \nu \in \{n', m', TM\} \\ \vec{e}_z \wedge \dfrac{\vec{k}_{\nu}}{||\vec{k}_{\nu}||}, \ \forall \nu \in \{n', m', TE\} \end{cases} \tag{2.64}$$

and

$$\epsilon_{\nu} = \begin{cases} 2, \ \text{for } n' \neq 0 \text{ and } m' \neq 0 \\ \sqrt{2}, \ \text{for } n' = m' = 0 \end{cases} \tag{2.65}$$

where the operator $\otimes$ is defined such that $\vec{u} \otimes \vec{v} = u_x v_x \vec{e}_x + u_y v_y \vec{e}_y$. Furthermore, the cut-off wavelength of each $\mathrm{TE}_{(n'm')}$ mode can be expressed in the same way as the cut-off wavelength for the Floquet modes in Eq. (2.57). Now, we have $\lambda_{\nu} = \dfrac{2\pi n_2}{||\vec{k}_{\nu}||}$ and for each $\mathrm{TE}_{(n'm')}$ modes, the cut-off wavelength is given by

$$\lambda_{\nu} = \frac{2 a_x a_y}{\sqrt{(n'.a_y)^2 + (m'.a_x)^2}} \tag{2.66}$$

For our structure, we have considered $a_y > a_x$ by convention. Furthermore, in the framework of the MMM and the EJF, we consider only a single propagative mode (guided mode). Equation (2.66) suggests that the mode with the highest cutoff wavelength λ_{ν} is for $n = 0$ and $m = 1$, i.e. the TE_{01} mode and $\lambda_{01} = 2a_y$. Usually in microwave engineering, the mode corresponding to the highest λ_{ν} is called the dominant mode or the fundamental mode of the waveguide [92, 93]. Following Eq. (2.62), the expression of the transverse profile of the electric field the fundamental TE_{01} mode ($n' = 0$, $m' = 1$) is written as

$$\vec{E}_{\nu}^{(2)} = \sqrt{\frac{2}{\Omega}} \sin\left(\frac{\pi}{a_y} y\right) \vec{e}_x \tag{2.67}$$

We can directly see that the TE_{01} mode is linearly polarized along the x-axis only, i.e. along the rectangle's width as depicted in Fig. 2.6.

We will see in the sections below that the properties of this "dominant" mode will a major role in the metamaterial's properties. It is called dominant mode because it dictates

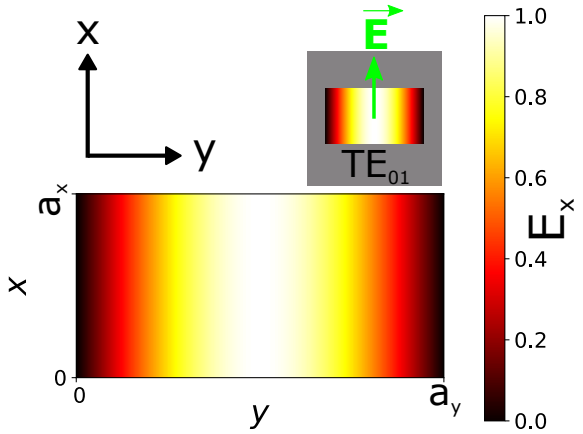

Figure 2.6: Distribution of the normalized electric field E_x in the rectangular apertures for the TE_{01} mode polarized along the x-axis.

the field pattern in the far-field region [93]. Indeed, the polarization and transmission properties of the metamaterial originates from this dominant mode. To be precise, the monomodal approximation is perfectly relevant because, for the considered spectral region (more details in next section), the dominant mode have preponderant weight in the waveguide mode expansion. Therefore, neglecting the evanescent higher order mode in the aperture will not lead to important discrepancies.

In the previous section, we have described the electromagnetic field in the homogeneous regions with the use of the Floquet modes expansion (2.56). In this section, we have continued by describing how the light propagates inside the subwavelength metallic waveguides thanks to a waveguide mode expansion. The next step is then to make the connection between the field in homogeneous region and the field guided in the aperture for establishing a Jones formalism extended our metamaterials.

2.3/ EXTENDED JONES FORMALISM FOR METALLIC METAMATERIALS

So far, we have derived the scattering matrix from the MMM. In this section, we want to extract the EJF from the scattering matrix. For that, we first have to mention two important conditions in order to preserve a valid model.

First Condition: The incoming light is in normal incidence to the metamaterial. This is typical from the classical Jones formalism and it is not intrinsic to our model. In addition, it is relevant to use such hypothesis in the framework of stacked structures.

Second Condition: **a)** In order to correctly use the Jones formalism, we have to make sure that only only one Floquet mode is propagative in the homogeneous regions. For that, we impose that only the Floquet mode with the highest cut-off wavelength can propagate while all the other Floquet modes are evanescent. For that, we set

$$\lambda > n_{max}^{(j)} p_{max} : \quad \text{TEM Floquet modes 1 and 2} \tag{2.68}$$

In fact, the highest cut-off modes are two degenerate TEM Floquet modes. They still respect the orthogonality relationship given by Eq. (2.3) because they are orthogonally polarized to each other.

b) To enforce the condition given in **a)**, we further decrease the influence of the evanescent modes by considering a far-field propagation only. Thus, we consider that the evanescent Floquet modes are negligible after a propagation of $\lambda/2$ from the interfaces. In other words, we consider

$$z < z_1 - \frac{\lambda}{2} \text{ and } z > z_3 + \frac{\lambda}{2}. \tag{2.69}$$

The far-field approximation will be further discussed in chapter 3 where we consider a stack of two metamaterials. It is very important to specify the second hypothesis because it is not needed in the classical Jones formalism. Indeed, the Jones formalism is usually applied to bulk structures where the diffraction of light does not occur or can be neglected.

The condition 2.**b)** also implies that the polarization state is carried only by the degener-

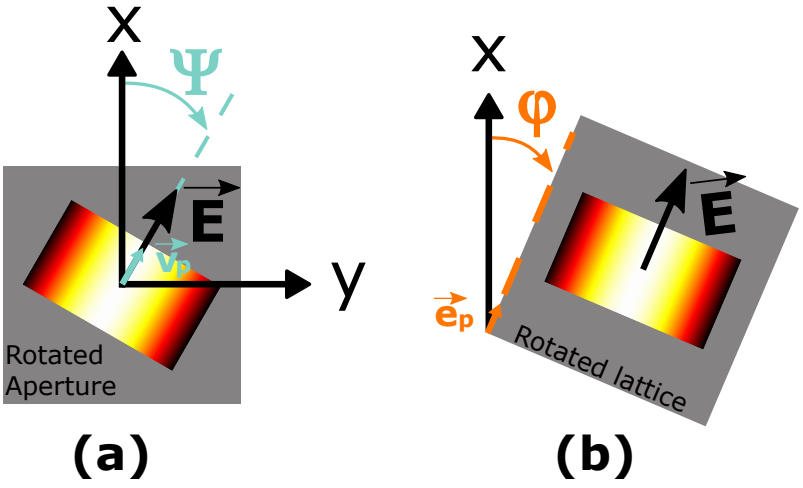

Figure 2.7: **(a)** Aperture rotated by an angle Ψ inside the lattice where $\vec{v}_p$ is the polarization unit vector giving the orientation of the electric field $\vec{E}$. **(b)** Lattice rotated by an angle φ and $\vec{e}_p$ the unit vector associated to this rotation.

ated TEM Floquet modes (the specular order). Then, rotating the polarization state of the normally incident TEM Floquet modes by an angle φ_{inc} is equivalent to rotate by an angle $-\varphi_{inc}$ the orientation of the metallic plate. We introduce the metamaterial rotation angle φ such that

$$\varphi = -\varphi_{inc} \tag{2.70}$$

as shown in Fig. 2.7**(b)**. The equivalence between the metamaterials orientation and the TEM Floquet modes polarization allows us to rewrite the polarization unit vector $\vec{e}_\tau$ (given by Eq. (2.55)) such that

$$\vec{e}_{0,0,\sigma} = \begin{cases} \cos\varphi.\vec{e}_x - \sin\varphi.\vec{e}_y & (\mathrm{TEM}_1) \\ \sin\varphi.\vec{e}_x + \cos\varphi.\vec{e}_y & (\mathrm{TEM}_2) \end{cases} \tag{2.71}$$

We also note that, for a rectangular aperture rotated by an angle Ψ in its Bravais lattice (as shown in Fig. 2.7)**(a)**), the distribution of the transverse electric field inside the rotated waveguide is unchanged. The only difference is the orientation of the electric field in the x-y plane. The unit vector $\vec{v}_p$ takes into account the rotation of the polarization state of the TE_{01} and it is given by

$$\vec{v}_p = \cos\Psi\vec{e}_x + \sin\Psi\vec{e}_y \tag{2.72}$$

With this new notation, it allows us to establish metamaterials Jones matrices that are independent of the incident EM field orientation - as it is classically the case when using Jones matrices. If the conditions are verified, we can now rewrite the notation so that it is adapted to the usual Jones notation. We propose that the amplitudes of TEM Floquet

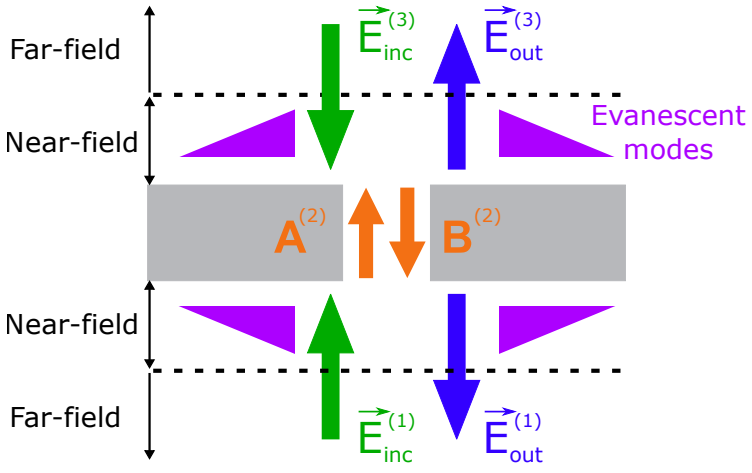

Figure 2.8: Schematic configuration of the extended Jones formalism. The incident/outward field in the homogeneous region is normal to the interfaces and is only considered in far-field region. The near-field region is still taken into account for evaluating the coupling between the fundamental guided mode and the Floquet modes.

modes are now rearranged as

$$\begin{aligned} A^{(1)}_{0,0,TE}\vec{e}_{0,0,TE} + A^{(1)}_{0,0,TM}\vec{e}_{0,0,TM} &\rightarrow \vec{E}^{(1)}_{inc} \\ B^{(3)}_{0,0,TE}\vec{e}_{0,0,TE} + B^{(3)}_{0,0,TM}\vec{e}_{0,0,TM} &\rightarrow \vec{E}^{(3)}_{inc} \\ B^{(1)}_{0,0,TE}\vec{e}_{0,0,TE} + B^{(1)}_{0,0,TM}\vec{e}_{0,0,TM} &\rightarrow \vec{E}^{(1)}_{out} \\ A^{(3)}_{0,0,TE}\vec{e}_{0,0,TE} + A^{(3)}_{0,0,TM}\vec{e}_{0,0,TM} &\rightarrow \vec{E}^{(3)}_{out} \end{aligned} \tag{2.73}$$

where $\vec{E}^{(j)}_{inc}$ and $\vec{E}^{(j)}_{out}$ respectively denote the incident and outward TEM Floquet modes in region j. This configuration is summarized in Fig. 2.8.

In this section, we have discussed the necessary conditions to establish a Jones formalism that can be applied to metallic metamaterials. In the next section, we will extract the transmission and reflection Jones matrices of the structure.

2.3.1/ General notation and Jones matrices extraction

Before extracting the metamaterials Jones matrices from the scattering matrix, we give a reminder on the general notation for the Jones formalism. The incident and outward electromagnetic fields, respectively $\vec{E}_{inc}$ and $\vec{E}_{out}$ are described by their transverse component along the x and y axes so that:

$$\vec{E}^{(j)}_{inc} = \begin{pmatrix} E^{(j)}_{inc,x} \\ E^{(j)}_{inc,y} \end{pmatrix} \quad \text{and} \quad \vec{E}^{(j)}_{out} = \begin{pmatrix} E^{(j)}_{out,x} \\ E^{(j)}_{out,y} \end{pmatrix} \tag{2.74}$$

where the component along the x and y axes are respectively the TEM_1 and TEM_2 Floquet modes. In the far-field configuration, as depicted in Fig. 2.8, it now becomes clear that

$$\begin{aligned} \vec{E}^{(1)}_{out} &= J^R_1 \vec{E}^{(1)}_{inc} + J^T_3 \vec{E}^{(3)}_{inc} \\ \vec{E}^{(3)}_{out} &= J^R_3 \vec{E}^{(3)}_{inc} + J^T_1 \vec{E}^{(1)}_{inc} \end{aligned} \tag{2.75}$$

where $J^T_{(j)}$ and $J^R_{(j)}$, are the (2×2) transmission and reflection Jones matrices of the metallic metamaterials. In fact the Jones matrices $J^T_{(j)}$ and $J^R_{(j)}$ are simply the scattering matrices $S_{\tau,q}$ (introduced in Eq. (2.45)) reduced the TEM Floquet mode so that we have S_{TEM_1,TEM_2}:

$$\begin{aligned} J^T_1 &= (S_{11})_{TEM_1,TEM_2} \; ; \quad J^R_3 = (S_{12})_{TEM_1,TEM_2} \\ J^R_1 &= (S_{21})_{TEM_1,TEM_2} \; ; \quad J^T_3 = (S_{22})_{TEM_1,TEM_2} \end{aligned} \tag{2.76}$$

In matrix notation, we obtain

$$\begin{pmatrix} \vec{E}^{(3)}_{out} \\ \vec{E}^{(1)}_{out} \end{pmatrix} = \begin{pmatrix} J_1^T & J_3^R \\ J_1^R & J_3^T \end{pmatrix} \begin{pmatrix} \vec{E}^{(1)}_{inc} \\ \vec{E}^{(3)}_{inc} \end{pmatrix} = J_M \begin{pmatrix} \vec{E}^{(1)}_{inc} \\ \vec{E}^{(3)}_{inc} \end{pmatrix} \tag{2.77}$$

where J_M is the (4×4) Jones matrix of the metamaterial. When the homogeneous regions (1) and (3) are filled with the same material - for example air - the structure is then reciprocal. In this case $J_1^T = J_3^T$ and $J_1^R = J_3^R$ (see discussion on Eqs. (2.47)) and (2.48).

Remark: The Jones formalism is usually applied in systems composed of reciprocal polarizing plates, and where the reflection can be neglected, so that only a (2×2) transmission Jones matrix is needed (e.g. Jones matrix of dichroic polarizers) to properly describe the whole system. For metallic metamaterials, the reflection can not be ignored and the reflection Jones matrices are needed.

2.3.2/ POLARIZATION PROPERTIES OF THE OVERLAP INTEGRAL

So far, we first have seen how to express the scattering matrix of a metallic plate. Then, we have matched the reduced S-matrix - composed of two degenerate TEM Floquet mode only - to Jones matrices. Now, we specifically give the overlap integral g_0 of the TEM Floquet modes in homogeneous regions (TEM_1 and TEM_2) with the fundamental TE_{01} guided mode in apertures. This overlap integral lets appear the metamaterial polarization properties. Following the Eqs. (2.54) and (2.67), we have

$$g_0 = \sqrt{\frac{2}{S\Omega}} \iint_{\Omega} \sin\left(\frac{\pi}{a_y} y\right) \vec{v}_p \vec{e}_{0,0,\sigma} d\Omega \tag{2.78}$$

On the one hand, the vectors $\vec{e}_{0,0,\sigma}$ ($\vec{e}_{TEM}$) give the polarization orientation of the TEM Floquet modes along x and y with the angle φ. On the other hand, the vector $\vec{v}_p$ gives the orientation of the rectangular aperture in its Bravais lattice with the angle Ψ, as shown in Fig. 2.7. Following Eq. (2.72) and Eq. (2.71), we obtain

$$\vec{v}_p \cdot \vec{e}_{0,0,\sigma} = \begin{cases} \cos(\varphi + \Psi); \ p = \{TEM_1\} \\ \\ \sin(\varphi + \Psi); \ p = \{TEM_2\} \end{cases} \tag{2.79}$$

which gives compact terms for the polarization orientation for both TEM Floquet modes. We finally write

$$g_0 = \tilde{g}_0 \vec{v}_p \vec{e}_{0,0,\sigma} \tag{2.80}$$

where $\tilde{g}_0 = \iint_{\Omega} \sin\left(\frac{\pi}{a_y} y\right) d\Omega$ is the scalar part of the overlap integral.

In this section, we have detailed the analytical expression of the overlap integral which reveals the general polarization properties of our considered structure. In the next section, we finally re-arrange the present notation to build transmission and reflection Jones matrices which allow for a compact and efficient description of the metamaterials polarization properties as well as its spectral properties.

2.3.3/ ANALYTICAL EXPRESSIONS OF JONES MATRICES

In the previous subsection, we have expressed the overlap integral and we have chosen a notation that explicitly shows the polarization properties of the overlap integral. After re-arranging the expression of the overlap integral by separating the polarization properties from the spectral properties, we can finally write:

$$J^T = \begin{pmatrix} J^T_{x,x} & J^T_{x,y} \\ J^T_{y,x} & J^T_{y,y} \end{pmatrix} = f^T |\tilde{g}_0|^2 \underbrace{\begin{pmatrix} \cos^2(\Psi+\varphi) & \cos(\Psi+\varphi)\sin(\Psi+\varphi) \\ \cos(\Psi+\varphi)\sin(\Psi+\varphi) & \sin^2(\Psi+\varphi) \end{pmatrix}}_{\text{classical Jones matrix of polarizer rotated by an angle } \Psi+\varphi \implies J^{(pol,\vec{e}_x)}_{\Psi+\varphi}} \tag{2.81}$$

and

$$J^R_{(j)} = \begin{pmatrix} J^R_{x,x} & J^R_{x,y} \\ J^R_{y,x} & J^R_{y,y} \end{pmatrix} = f^R_{(j)} |\tilde{g}_0|^2 \begin{pmatrix} \cos^2(\Psi+\varphi) & \cos(\Psi+\varphi)\sin(\Psi+\varphi) \\ \cos(\Psi+\varphi)\sin(\Psi+\varphi_p) & \sin^2(\Psi+\varphi) \end{pmatrix} - \underbrace{\begin{pmatrix} 1 & 0 \\ 0 & 1 \end{pmatrix}}_{I_d\text{: (2×2) identity matrix}} \tag{2.82}$$

We introduce the following terms

$$\alpha_T = f^T |\tilde{g}_0|^2 \tag{2.83}$$

and

$$\alpha^{(j)}_R = f^R_{(j)} |\tilde{g}_0|^2 \tag{2.84}$$

that respectively correspond to the transmission and reflection coefficient of the metamaterial. For most of the results presented in this manuscript, we consider that the aperture dimension are oriented along the x and y axes, i.e. $\Psi = 0°$. We will focus only on φ, the rotation angle of the metallic metamaterials. Besides, we mainly consider the metama-

terials to be surrounded by air so that the metamaterials are reciprocal in reflection so that

$$\alpha_R^{(j)} \rightarrow \alpha_R. \tag{2.85}$$

We can now express the transmission and reflection Jones matrix in a more compact form given by

$$J^T = \alpha_T J_\varphi^x \tag{2.86}$$

and

$$J_{(j)}^R = \alpha_R J_\varphi^x - I_d \tag{2.87}$$

where J_φ^x corresponds to the classical Jones matrix of a linear polarizer rotated by an angle φ and $-I_d$ is the term accounting for the reflection on the pec metal. In other words, when $\varphi = 0°$, the structure is linearly polarizing the transmitted light along the x axis. We remind that:

$$J_\varphi^x = R(-\varphi)J^x R(\varphi) = \begin{pmatrix} \cos\varphi & -\sin\varphi \\ \sin\varphi & \cos\varphi \end{pmatrix}\begin{pmatrix} 1 & 0 \\ 0 & 0 \end{pmatrix}\begin{pmatrix} \cos\varphi & \sin\varphi \\ -\sin\varphi & \cos\varphi \end{pmatrix} \tag{2.88}$$

where the matrix $R(-\varphi)$ denotes the rotation of the plate in the transverse plane. This expression corresponds to the classical rotation of an linear polarizer along the x-axis. For $\varphi = 0°$, we have

$$J^T = \begin{pmatrix} \alpha_T & 0 \\ 0 & 0 \end{pmatrix} \text{ and } J^R = \begin{pmatrix} \alpha_R - 1 & 0 \\ 0 & -1 \end{pmatrix} \tag{2.89}$$

As we can remark, the expression of the transmission and reflection Jones matrices aligned along the x axis are quite simple. Apart from its elegance, the Jones formalism will proves very useful and and handy to understand the properties and additional effect that emerges from the stack. The Extended Jones Formalism has been established in 2014 by Philippe Boyer [65].

2.3.4/ EXAMPLE OF EXTENDED JONES FORMALISM FOR A SINGLE PLATE

In the previous section, we have finally established an extended Jones formalism to describe the polarization properties as well as the spectral behavior of the metamaterial of interest. In this last chapter's section, we propose to illustrate our theoretical model with two different structures. First, a biperiodic metamaterial patterned with rectangular holes (Fig. 2.2**(a)**) and second, a monoperiodic metamaterial (Fig. 2.2**(b)**). This study high-

lights the main polarization properties of such metamaterials and outline the difference between monoperiodic and biperiodic geometries.

We consider the two structures to be aligned on the x axis so that the transmitted light is linearly polarized on the x axis. First, we focus on the metamaterial with rectangular pattern. The transmission T of the metallic plates is given by:

$$T = |J^T_{x,x}|^2 + |J^T_{y,x}|^2 \tag{2.90}$$

For structures aligned along the x axis, the term $|J^T_{y,x}|^2 = 0$. The term $|J^T_{y,x}|^2$ is however necessary since it takes into account any possible transverse rotation of the plate. First, we consider a biperiodic metamaterial with $h/p = 1.0$, $a_x/p = 0.3$, $a_y/p = 0.9$ and $\Psi = \varphi = 0°$. The Floquet modes orders (for both x and y axes) taken into account for the computation are in the range $[-F : F]$ and we take $F = 5$ for the computations.

Figure 2.9 **(a)** gives the transmission spectrum of the rectangular aperture metamaterial. The first characteristic we can notice is the 100 % transmission for the wavelength highlighted by the dashed purple lines. It denotes the resonant properties of the metamaterial which are attributed to the resonances of the fundamental guided mode in the rectangular cavities. For such a geometry, the fundamental guided mode is the TE_{01} mode as presented in Sec. 2.2.4. We observe 3 distinct resonances. We have 2 Fabry-Perot (FP) resonances, the first and second harmonic respectively located at $\lambda/p \approx 1.45$ and $\lambda/p \approx 1.1$. To be more specific, these FP resonances occur along the thickness h of the

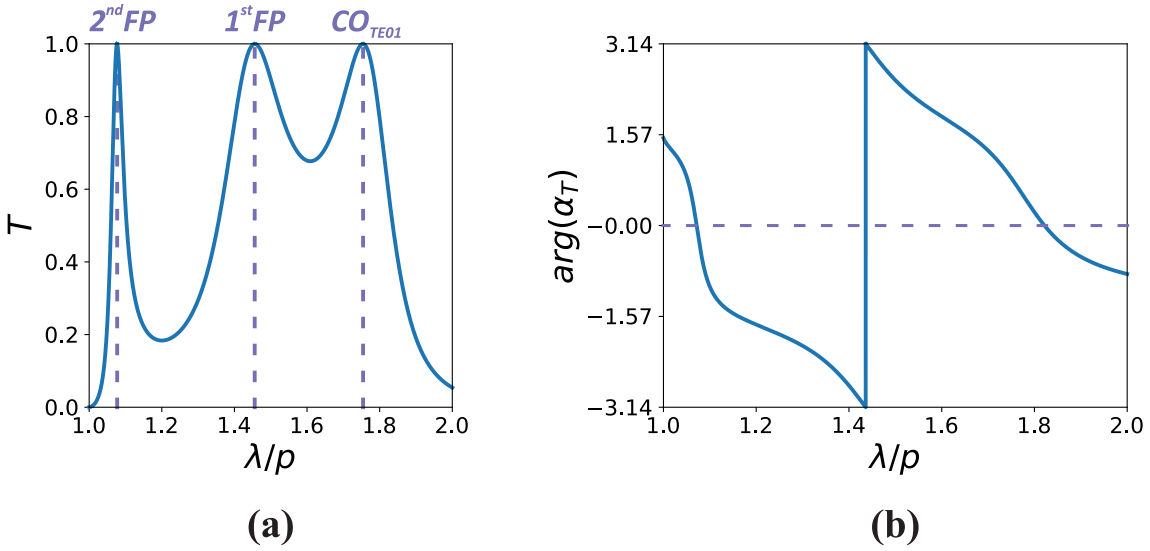

Figure 2.9: **(a)** Transmission spectrum of a metamaterial with rectangular pattern. The vertical dashed lines highlight the multiple resonance of the structure. The parameters are $a_x/p = 0.3$, $a_y/p = 0.9$ and $h/p = 1.0$. **(b)** The corresponding phase of the transmission coefficient α_T

metamaterial. In addition, we have a third resonance located at $\lambda/p \approx 1.75$ corresponding to the cut-off wavelength of the TE_{01} guided mode. As we have seen in Sec. 2.2.4, this resonance should be located exactly at $\lambda/p = 2a_y = 1.8$. This wavelength shift is explained by the coupling of the cut-off resonance with the first harmonic FP resonance. Figure 2.9**(b)** gives the spectral phase of the transmission coefficient α_T. The horizontal dashed purple line correspond to $\arg(\alpha_T) = 0$ and also gives us an indications of the resonances positions and is in agreement with Fig. 2.9 **(a)**.

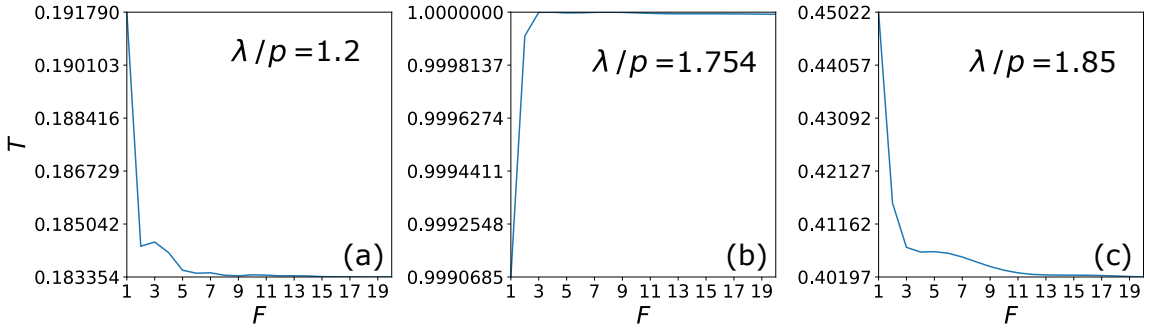

Figure 2.10: Transmission value as a function of F, giving the number of Floquet mode orders, at different wavelengths **(a)** $\lambda/p = 1.2$, **(b)** $\lambda/p = 1.754$ and **(a)** $\lambda/p = 1.85$.

Now that we have obtained the transmission spectrum for a biperiodic metamaterial, we make convergence tests by computing the transmission as a function of F at some wavelength of interest: at a local minimum ($\lambda/p = 1.2$), at resonance (local maximum at $\lambda/p = 1.754$) and at a steep part of the spectrum ($\lambda/p = 1.85$), as shown in Fig. 2.10. Such test is made in order to validate the chosen value of F ($= 5$) for the computations. As we can see, at the local minimum and maximum of transmission ($\lambda/p = 1.2$ and $\lambda/p = 1.754$), the transmission values rapidly converge with F while for $\lambda/p = 1.85$ the convergence is slower. For the three tests, it appears that $F = 5$ is a good compromise between computation time and results accuracy. For $F = 5$, the error $\Delta T = |T_{F=20} - T_{F=5}|$ is $\Delta T < 10^{-3}$ at $\lambda/p = 1.2$, $\Delta T < 10^{-4}$ at $\lambda/p = 1.754$ and $\Delta T = 5 \times 10^{-3}$ at $\lambda/p = 1.85$. Therefore, we keep $F = 5$ for the computation of biperiodic metamaterials.

Figure 2.11**(a)** gives the transmission spectrum as a function of the rectangle width a_x/p where $h/p = 1.0$. For $a_x/p = 0.1$ we can clearly see that the TE_{01} mode cut-off wavelength is exactly located at $\lambda/p = 1.8$. As a_x/p increases, the cut-off wavelength progressively couples to the first FP resonance and we can simultaneously observe the shift of both resonances. One advantage of such coupling is the broad transmission band that occurs for $a_x/p > 0.3$ where the two resonance merge to form a larger transmission peak.

Figure 2.11**(b)** gives the transmission spectrum as a function of the metamaterials thickness h/p where $a_x/p = 0.3$. Here, we can remark that the FP harmonics only are affected

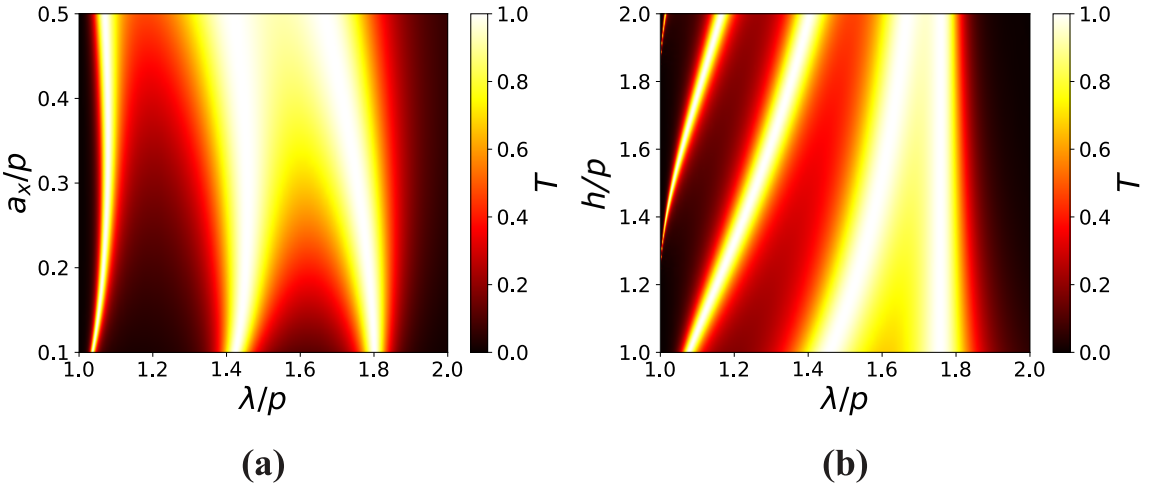

Figure 2.11: **(a)** Evolution of the transmission spectrum when the rectangle width a_x/p vary from 0.1 to 0.5 for $h/p = 1.0$. It shows the progressive coupling of the cut-off resonance with the first harmonic FP resonance. **(b)** Transmission spectrum as a function of the thickness h/p showing the FP resonances shift for $a_x/p = 0.3$.

by the thickness variations while the TE_{01} mode cut-off wavelength remains constant. This result is in accordance with the theory since the FP harmonics location is directly proportional to the thickness h/p while the TE_{01} cut-off wavelength is given by $\lambda_{TE_{01}} = 2a_y$ and does not depend on the thickness. The overall results of Fig. 2.11 demonstrate that it is possible to tailor the transmission spectrum of the metamaterial by carefully choosing the thickness and the rectangle width.

We now focus on the second structure, a monoperiodic metamaterial with $a/p = 0.3$ and

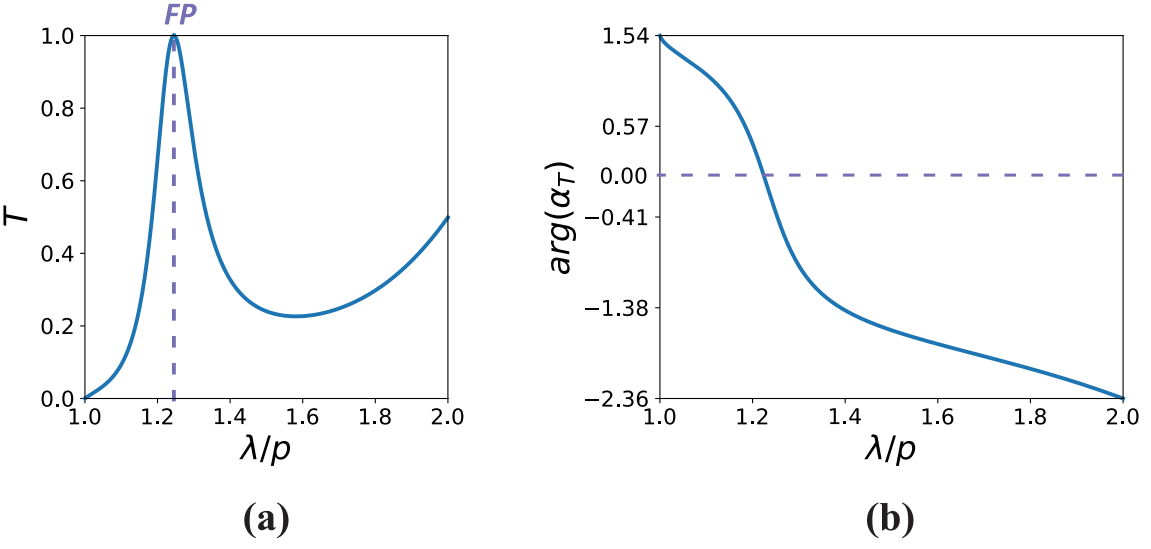

Figure 2.12: **(a)** Transmission spectrum of a metamaterial with a 1D pattern. The purple dashed line gives the location of the first FP resonance. The parameters are $a/p = 0.3$ and $h/p = 1.0$. **(b)** The corresponding phase of the transmission coefficient α_T.

$h/p = 1.0$ aligned on the x-axis. For the monoperiodic metamaterials, the Floquet modes orders taken into account for the calculus are in the range $[-50 : 50]$. Figure 2.12**(a)** gives its corresponding transmission spectrum. In contrast to the rectangular pattern, we only notice one resonance which is a FP resonance located at $\lambda/p \approx 1.25$. The fundamental guided mode is a TEM mode with a cut-off wavelength which is pushed to $\lambda/p \to \infty$. An intuitive way to understand it is to imagine the rectangular structure studied above where the length a_y/p is stretched to infinity. The cut-off wavelength being proportional to a_y, we thus obtain a cut-off wavelength which is pushed to infinity. Figure 2.12**(b)** gives the corresponding spectral phase $arg(\alpha_T)$. Again, for $arg(\alpha_T) = 0$ we can locate the resonance position.

Figure 2.13**(a)** shows the transmission spectrum of the monoperiodic metamaterial versus a/p. If we compare with Fig. 2.11**(a)**, we remark that the single FP resonance shift in a similar way with a/p. We can also notice a slight coupling with the TEM mode. This is however, not as evident as in Fig. 2.11**(b)** where the TE_{01} resonance is much closer to the FP resonance.

Figure 2.13**(b)** gives the spectrum as a function of h/p. We can clearly see the proportional FP resonance shift with h/p and the appearance of higher order FP harmonics. A careful comparison of Fig. 2.13**(b)** with Fig. 2.11**(b)** shows an interesting difference in the evolution of the FP resonances. In Fig. 2.11**(b)**, the FP harmonics seem to reach asymptotically the TE_{01} mode cut-off wavelength. In other word, they do not "cross" the cut-off wavelength. In Fig. 2.13**(b)** the FP harmonics location are linearly shifted for any value of h/p. The difference between the linear and asymptotic evolution is due to the TE_{01} mode

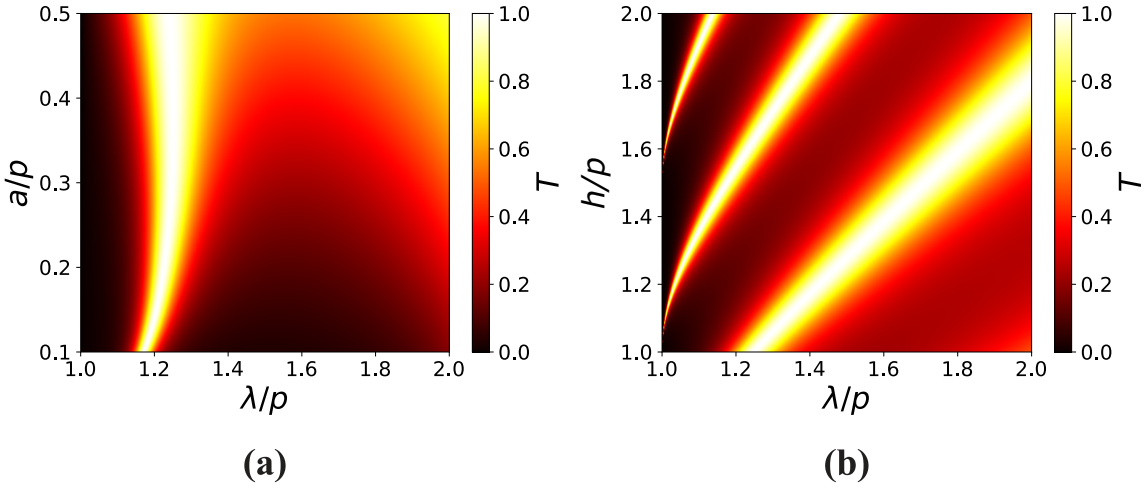

Figure 2.13: **(a)** Evolution of the transmission spectrum as a function of a/p for $h/p = 1.0$. We can observe the slight coupling of the TEM mode with the first harmonic FP resonance when a/p increase. **(b)** Transmission spectrum as a function of the thickness h/p showing the FP resonances linear shift for $a/p = 0.3$.

cut-off itself (see Fig. 2.9**(a)**). In the case of the rectangular apertures, for $\lambda/p < \lambda_c^{TE_{01}}$ the rectangular apertures carries a single propagative mode. For $\lambda/p > \lambda_c^{TE_{01}}$, this mode becomes evanescent and therefore it prevents the far-field propagation of all FP harmonics after this wavelength. For the monoperiodic pattern, the evanescent regime of the fundamental TEM mode cannot be reached since $\lambda_{TEM} \to \infty$. As a consequence, for any value of $\lambda/p > \lambda_r$ the apertures carry a propagative mode and the FP resonance steadily shift with h/p.

So far, we have described the spectral properties of monoperiodic pattern and rectangular pattern and highlighted the differences between them. We have not shown yet any element about the polarizing properties of our structures. We now propose a simple study to highlight the linear polarization properties that are common to both patterns.

Figure 2.14**(a)** shows the simple preliminary idea to study the polarizing properties of our metamaterials. It consist in sending a linearly polarized light along the x-axis and study the transmission and reflection responses when rotating by an angle φ the orientation of the structure. Figure 2.14**(b)** shows the transmission and reflection responses $|J^T_{x,x}|^2$ and $|J^R_{x,x}|^2$ along the x-axis as a function of φ, the orientation of the metamaterial. The transmission response of the structure is computed at the metamaterial resonance and it follows the well-known $\cos^2\varphi$ law which indicates that the metallic metamaterials act as classical linear x-polarizer. Such polarizers are usually achieved with dichroic polarizer in the optical domain where one transverse axis is transparent while the other transverse axis absorbs totally the electric field. However, our structure is assumed to be made of perfectly conducting metal so that the selection of the linear polarization is made by

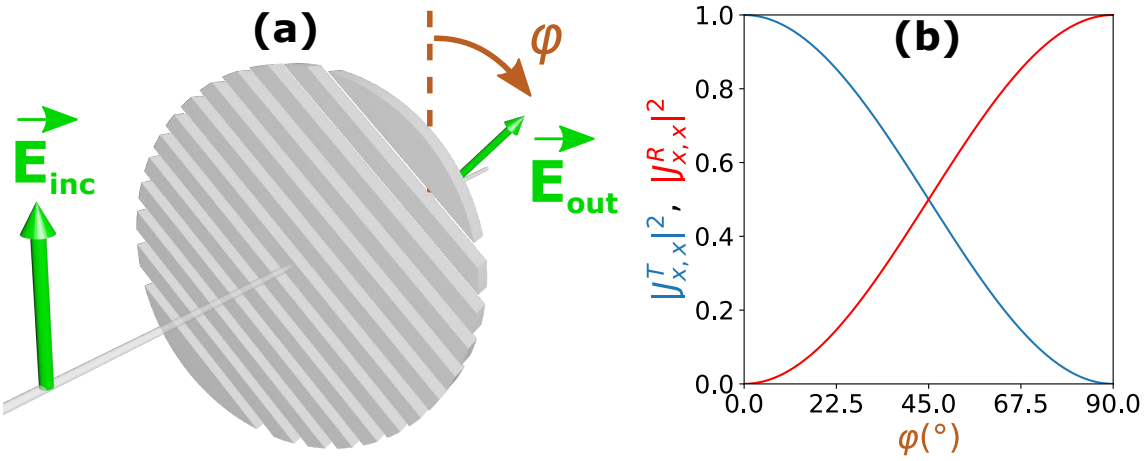

Figure 2.14: **(a)** Schematic principle of linearly polarized light incident on a metallic plate which is rotated by an angle φ. **(b)** Transmission curve - in red - and reflection curve - in blue - computed a the metamaterials resonance and confirming the classical Malus' Law and demonstrating the linear polarization properties of our structures.

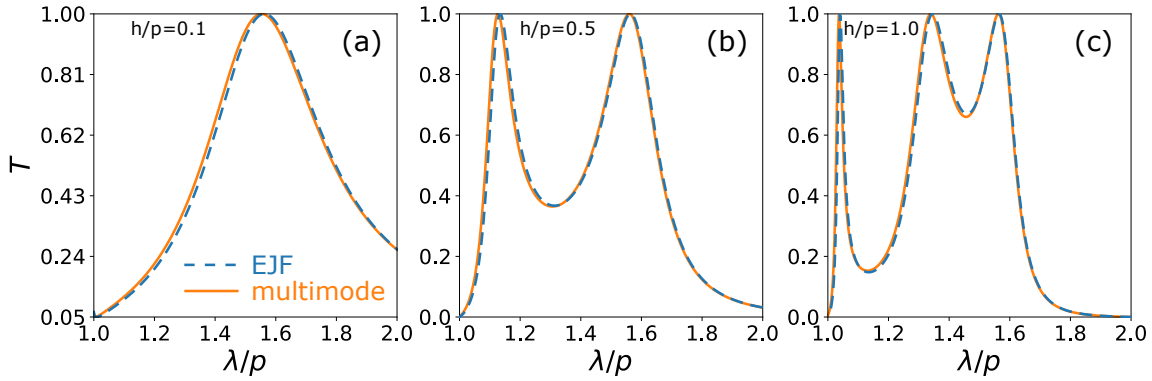

Figure 2.15: Transmission spectra for different values of h/p and with $a_y/p = 0.8$, $a_x/p = 0.3$. Each EJF transmission spectrum (in solid orange line) is compared with a scattering matrix computation which takes into account 8 waveguide modes in the apertures.

reflection, not by absorption, as indicated by the reflection response in red curve in Fig. 2.14**(b)**. It is then interesting to notice that, for $\varphi = 90°$, the studied metamaterials act perfect mirrors along the x-axis. It has to be noted that this angular transmission response is rigorously the same for the monoperiodic and biperiodic metamaterials.

Furthermore, we now compare the results produced by the EJF with results given by larger scattering matrices - which takes into account several waveguides modes - in order to discuss the validity of the EJF model. It has to be noted that, in near-field computation, the Bravais lattice has to be aligned along the x and y axes, so that φ is always kept null. We can only vary the angle Ψ. We propose to compare the EJF results and the multimodal method results for the following biperiodic structure where $a_y/p = 0.8$, $a_x/p = 0.3$ and $\Psi = 0°$. For the Fig. 2.15 to Fig. 2.18, we systematically vary the thickness h/p and another parameter (either Ψ or a_x) in order to discuss the influence of the evanescent waveguide modes.

Figure 2.15 gives the transmission spectrum computed with the EJF (in dashed blue curves) and compared with a multimodal method (in solid orange curves) which takes into account 8 waveguide modes. Figure 2.15 **(a)**, **(b)** and **(c)** give the transmission spectra respectively for $h/p = 0.1$, $h/p = 0.5$ and $h/p = 1.0$. For the thickness $h/p = 0.5$ and 1.0 we can observe that the evanescent modes have negligible effects over the transmission spectrum. For Fig. 2.15 **(a)** however, we can notice a slight shift on the entire spectrum because of the very small thickness that allows for a coupling of the exponentially decayed evanescent modes at the interfaces z_1 and z_3.

However, by choosing $\Psi = 0°$, the incident electric field polarized on the x-axis excites the evanescent modes polarized on the x-axis only. For example, the evanescent mode polarized along the rectangle length with the highest cut-off wavelength, i.e the mode

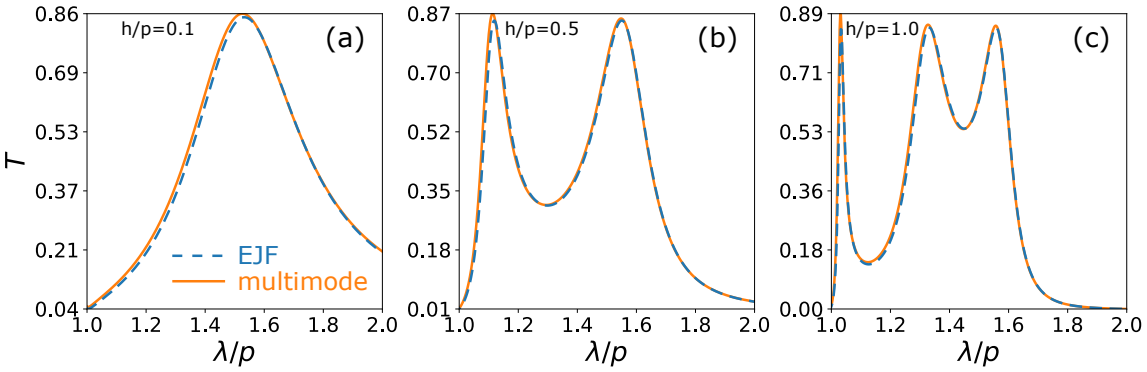

Figure 2.16: Same transmission spectrum comparison as in Fig. 2.15 except that $\Psi = 23°$.

TE_{10} (with a cut-off wavelength $\lambda_{\mathrm{TE}_{10}} = 2a_x$) is not excited by the incident x-polarized light. One could expect that those y-polarized evanescent modes also influence the transmission response, and especially the TE_{10} mode with a cut-off wavelength relatively close to the considered spectral region. We now study the same structure except that we choose an arbitrary angle $\Psi = 23°$ and Fig 2.16 shows the corresponding comparison between the multimodal method and the EJF. It is interesting to note that exciting the y-polarized evanescent modes leads to almost the same comparison shown in Fig. 2.15 between EJF results and multimodal results. The only difference is that the transmission peaks values are slightly larger for the multimode method, especially for the peak in Fig. 2.16**(a)** and the left peaks in Fig. 2.16**(b)** and **(c)**. This shows the coupling of the forward and backward TE evanescent modes through the metamaterials which leads to a slightly higher transmission peak values.

Another parameter is also playing a major role in the evanescent mode contribution: the width of the rectangular aperture a_x/p. Indeed, all the evanescent modes polarized along the rectangle's length have cut-off wavelength that depends on this parameter while the fundamental guided mode cut-off depends only on a_y. By varying the cut-off wavelength, we modify the exponential decay rate of all evanescent modes polarized along the rectangle's length, which can lead to substantial discrepancies in the compared spectra.

Figure 2.17 shows the comparison between EJF simulated results and multimode ones for $a_y/p = 0.8$, $\Psi = 23°$ and for $a_x/p = 0.45$. With this larger value of a_x/p the cut-off wavelengths of all evanescent mode are closer to considered spectral region (especially for the TE_{10} evanescent mode where $\lambda_{\mathrm{TE}_{10}}/p = 0.9$). Therefore, the exponential decay is much smaller so that the evanescent mode couples more easily. This is confirmed by the compared transmission spectra shown in Fig. 2.17 where the difference between EJF and multimode method becomes much larger, even for $h/p = 1.0$.

On the contrary, for smaller values of a_x/p, the evanescent modes cut-off wavelengths are

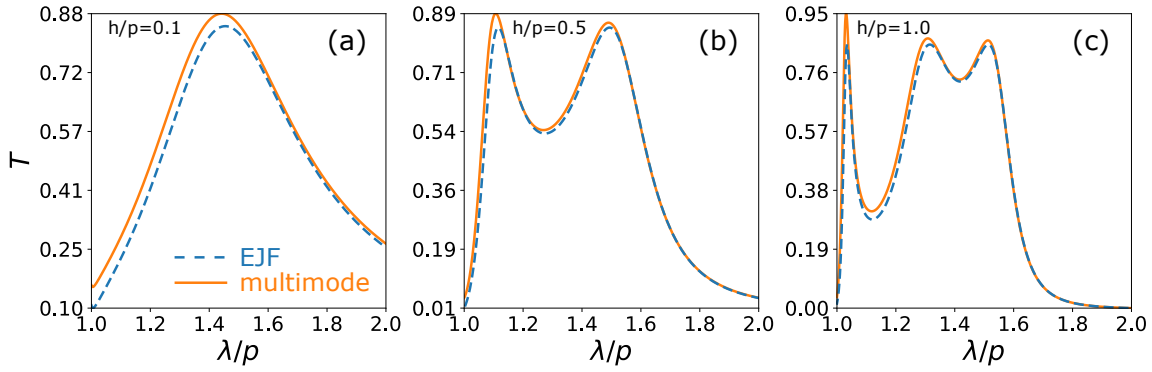

Figure 2.17: Same transmission spectrum comparison as in Fig. 2.16 except that $a_x/p = 0.45$

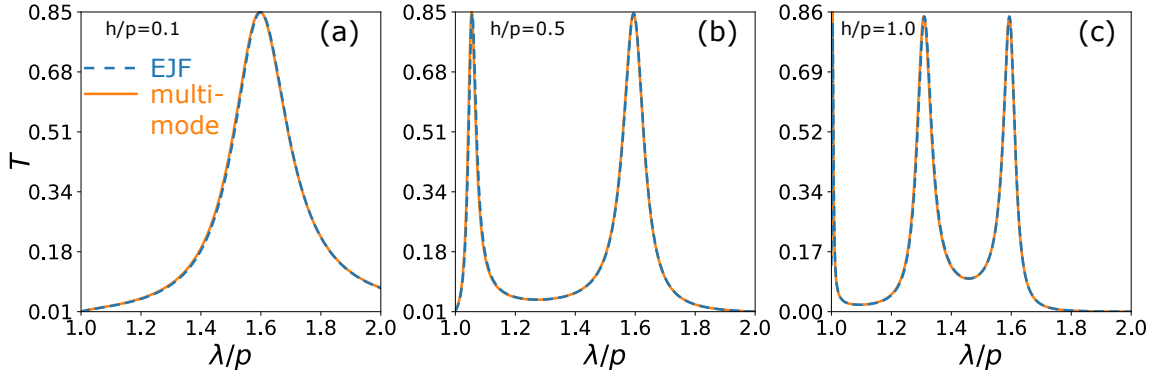

Figure 2.18: Same transmission spectrum comparison as in Fig. 2.17 except that $a_x/p = 0.1$

pushed toward smaller wavelength and the exponential decay of those modes becomes larger. Figure 2.18 shows the another comparison for the same metamaterial parameters except that $a_x/p = 0.1$ ($\lambda_{\mathrm{TE}_{10}}/p = 0.2$). As we can see, for such value of a_x/p, the EJF is in perfect agreement with the multimode method.

We can conclude that the EJF validity depends mainly on a set of three parameters: h/p, a_x/p and Ψ. As we already discussed earlier in this section, there are no absolute criteria to define the EJF validity. It rather depends on the structure parameters and the error tolerance, which mainly depends on the aimed application (i.e. applications based either on broadband or ultra-narrow band spectrum).

2.4/ EXTENSION TO A RENEWED JONES FORMALISM

So far, we have considered metamaterials with a single propagative mode inside the apertures. Nevertheless, the extended Jones formalism can be applied to other specific geometries. Indeed, subwavelength aperture featuring specific symmetries such as $C_{1,v}$,

$C_{2,v}$ or $C_{4,v}$ symmetry allows for the excitation of two propagative, orthogonal and uncoupled mode.

On one hand, the formalism for a single metamaterial can be extended to a subwavelength unit cell which consists of two uncoupled monomode apertures. Precisely, figure 2.19**(a)** shows one example of a dual rectangular aperture unit cell such that the modes excited by the two cavities are orthogonal. This condition is satisfied for structures respecting C_{1v} symmetry. Indeed, the two modes propagates independently inside the apertures and are not coupled by evanescent waves at the metamaterial interfaces. In this case, the dual cavity metamaterial is seen as a superimposition of two metamaterial patterned with a single monomode aperture. On the other hand, square or almost square apertures also support two propagative, degenerated and orthogonal modes, as shown in Fig. 2.19 **(b)**. In other word, for sufficiently large aperture width, the cut-off wavelength of the second propagative mode is above the Rayleigh wavelength. For the case of perfect square apertures - i.e. $a_x = a_y$, the metamaterial supports two orthogonal degenerate propagative mode. It has to be noted that for the C_{4v} symmetry, the corresponding metamaterial does not feature linear polarization properties. For the dual-cavity C_{1v} symmetry, the metamaterial may or may not show linear polarization properties or anisotropy. It mainly depends on the respective holes dimensions.

For both the dual-cavity and the square cavity, the overall Jones matrices is based on the expression given by Eq. 2.86 and Eq. (2.87). More specifically, the transmission Jones matrix J^T_{dual} of the dual cavity metamaterial is a linear superimposition of two monomodal

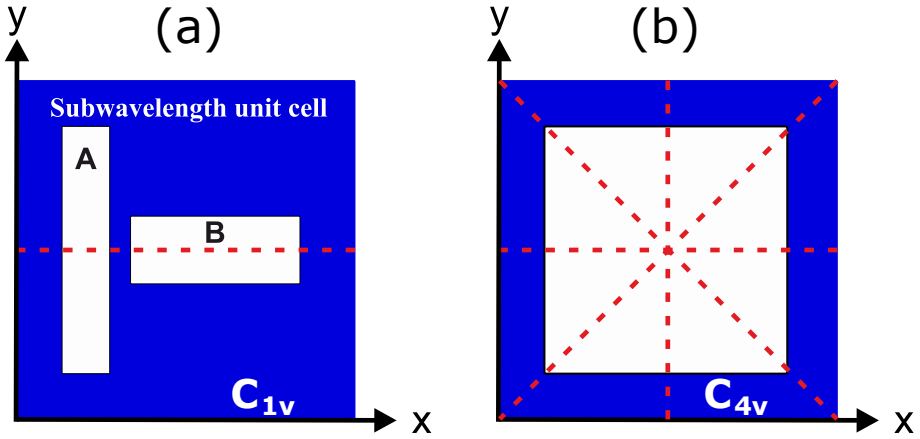

Figure 2.19: Two possible example of subwavelength unit-cell supporting two orthogonal propagative modes. **(a)** Subwavelength unit cell featuring a $C_{1,v}$ symmetry, where the $C_{1,v}$ symmetry axis is represented by the red dashed line. A and B denotes the two holes carrying the two uncoupled modes, polarized along the x and y axes, respectively. **(b)** Unit-cell with a square aperture which support two degenerated mode along the x and y axis.

Jones matrices on the x and y axes. The Jones matrix J^T_{dual} for such metamaterials is expressed as follows

$$J^T_{dual} = \begin{pmatrix} J^T_A & 0 \\ 0 & J^T_B \end{pmatrix} \tag{2.91}$$

where J^T_A and J^T_B are the transmission Jones matrices corresponding to the fundamental mode supported by A and B, respectively. As we can see, the transmission Jones matrix remains analitycal and rather simple. Such dual-cavity metamaterials can therefore present an artificial anisotropy based the effective refractive index difference between mode A and B. Breaking the aperture symmetry could lead to additional effect via the coupling between the two mode. This principle has been used for the design of efficient and compact metallic half-wave plates [58, 65].

2.5/ SUMMARY

In this chapter, we have presented some basics of electromagnetism, diffraction and metallic waveguides theories that allows us to describe the basic properties of our metamaterials. Then, we have used a modal method which combines the different theories and gives the scattering properties for our metallic structures. Under certain conditions, we have then extracted Jones matrices that analytically and efficiently describes the polarization and spectral properties. As a preliminary results of this thesis, we have used this extended Jones formalism to study the transmission and reflection properties of single metallic plates. We have concluded that they act as linear polarizers in transmission and they follow the classical $\cos^2\varphi$ law which is usually found for dichroic polarizer. We have noticed however, that the linear polarization selection is not achieved by absorption - as it is the case for dichroic polarizers - but by reflection at the metamaterial interfaces. As we will see in the next chapters, this difference will be exploited in stacks of metamaterials. We have also shortly discussed the other possibilities offered by the extended Jones formalism. Principally, we have seen that the EJF can also be used to model anisotropic metamaterials with expressions that are still analytical. This possibility is however not considered for the metamaterial stacking and is out of the manuscript's scope. We emphasize that it is thanks to this analytical Jones formalism presented in this chapter that we are able to efficiently model stacked metamaterials with short computation time.

In the next chapter, we will employ this extended Jones formalism for the simplest case of stacked metamaterials, i.e. a stack of two metamaterials. We will study this dual stack

structure in a polarizer-analyzer configuration to further show the differences with dichroic polarizers. This will also allow us to highlight interesting properties and phenomena that emerge from the stacking.

3

STACKING OF TWO METALLIC METAMATERIALS: EXTENDED MALUS' LAW

In the previous chapter, based on a renewed Jones formalism, we have highlighted the polarization properties of single metallic metamaterials. We have especially seen that they follow the usual $cos^2\varphi$ transmission response which demonstrates that they act as linear polarizers. Commonly, the $\cos^2\varphi$ law is referred to as the Malus' Law and it is used to study the polarization properties of material such as birefringence or optical activity. One popular method to obtain the Malus' Law is the polarizer-analyzer configuration where two dichroic polarizers are cascaded. This basic configuration is, for example, used in ellipsometry [94]. In this chapter, we would like to revisit the polarizer-analyzer configuration with metallic polarizers. This will allow us to underline the differences that arise between the polarizers either made of dichroic or metallic materials.

First, we will introduce the classical Malus' Law and the polarizer-analyzer configuration. We will then give some example of applications of the polarizer-analyzer configuration and some recent extensions of the Malus' Law. Second, we will review recent breakthroughs of the Malus' Law using metallic metamaterials. Third, we will focus on the the study of two metallic metamaterials in polarizer-analyzer configuration. We will briefly discuss the algorithm that accounts for the cascading of the two metamaterials. We will derive an analytical equation - the Extended Malus' Law (EML) - that gives the transmitted EM intensity through the structure. We will compare it to the classical Malus' Law. This will help us to get more insights into the physical process occurring in the structure and understand better the breakthroughs that are recently reported. Based on a particular configuration featuring a sharp transmission dip, we will further propose an applications for electro-optical sensing in the THz domain. We will also compare and confirm the

validity of the results with other methods such as FDTD and a multimodal method.

Finally, we will discuss further the very nature of this sharp transmission dip that will drive us to a complementary model to describe the complex behavior of the stacked structure - given in the next chapter. Principally, we conclude that the narrow transmission dip obtained by rotating the analyzer have the same feature than Fano resonances. Part of the work presented in this chapter has been published in 2016 [95].

3.1/ REMINDER ON THE CLASSICAL MALUS' LAW

The study of the polarization of light started much before the electromagnetic theory of light established by James Clerk Maxwell [96]. In 1690, Christian Huygens proposed an experiment of light passing through two cascaded calcites crystals and discovered the polarization of light [97]. More than hundred years later - in 1808 - Etienne Louis Malus proposed a similar experiment by sending a partially reflected light on a calcite crystal and gave the same conclusion as Huygens. It is in the same year that Malus first gave the transmission formula of the transmitted optical intensity - proportional to $\cos^2\theta$ - of the light beam passing through the polarizing calcite crystal - the well known Malus' Law [98]. Moreover, Malus was following Newton's corpuscular theory of light and proposed that the light corpuscles had "poles". He was the first to coin the term of "polarized" light.

3.1.1/ THE POLARIZER-ANALYZER CONFIGURATION

The Malus' Law is usually observed by using a pair of dichroic polarizers in a polarizer-analyzer configuration, as depicted in Fig. 3.1. The conventional principle is the following:

1) A normal incident arbitrary polarized light $\vec{E}_0$ falls on the first polarizer. The x-component $\vec{E}_{0,x}$ of the electric field is passing through the polarizer while the y-component $\vec{E}_{0,y}$ is totally absorbed by it (see Fig. 3.1).

2) After passing through this first polarizer, the linearly polarized light falls on the second polarizer rotated by an angle θ (called analyzer)

3) The partially transmitted intensity of the output beam is given by the Malus' Law $I = I_0 \cos^2\theta$. The other component of the beam is absorbed by the analyzer.

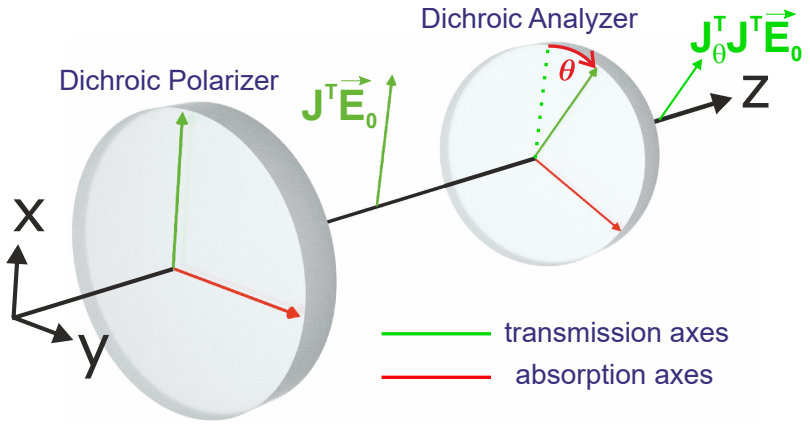

Figure 3.1: 3D render of the polarizer-analyzer configuration with polarizers made of dichroic bulk materials. The first polarizer is aligned along the x axis. The second polarizer (analyzer) is rotated by an angle θ from the x axis.

3.1.2/ Absorption of light by refringent material and Malus' Law

Following the principle of the polarizer-analyzer configuration mentioned above, we would like to give the basic calculus to retrieve the expression of the Malus' Law. This quick reminder will prove useful later, when compared to the EML. The Malus' Law can be easily retrieved using the classical Jones formalism. Assuming a total absorption of the dichroic polarizers along the y-axis, and an incident field $\vec{E}_0$, we have $\vec{E}_T = J_\theta^T J^T \vec{E}_0$ and it follows

$$\begin{aligned}\vec{E}_T &= \begin{pmatrix} \cos\theta & -\sin\theta \\ \sin\theta & \cos\theta \end{pmatrix}\begin{pmatrix} 1 & 0 \\ 0 & 0 \end{pmatrix}\begin{pmatrix} \cos\theta & \sin\theta \\ -\sin\theta & \cos\theta \end{pmatrix}\begin{pmatrix} 1 & 0 \\ 0 & 0 \end{pmatrix}\begin{pmatrix} E_{0,x} \\ E_{0,y} \end{pmatrix} \\ &= E_{0,x}\cos\theta \begin{pmatrix} \cos\theta \\ \sin\theta \end{pmatrix}\end{aligned} \tag{3.1}$$

and

$$T = \left|\frac{E_T}{E_{0,x}}\right|^2 \Rightarrow \boxed{T = \cos^2\theta} \qquad \text{(Classical Malus' Law)} \tag{3.2}$$

When $\theta = 0°$, the transmission axes of the two dichroic plates are aligned along the x-axis and it results in a full transmission along the x axis while the y component is totally absorbed. When $\theta = 90°$, the absorption axis of the analyzer is aligned on the transmission axis of the polarizer and light is totally absorbed. Note that the determinant of a dichroic polarizer Jones matrix $\det(J^T)$ is equal to zero. Indeed, this is due to the fact that the EM energy is not conserved because of the polarizer absorption.

The polarizer-analyzer configuration is used in a wide variety of experiments. For example, it can be used to accurately control the intensity level of a light beam which is particularly crucial for non-linear optics. As another example, a pair of crossed polarizer-analyzer - $\theta = 90°$ - allows for the accurate study of optically active media [99]. Such configuration can also be used for polarization-selective rotation of the incident light but it is however not efficient in terms of transmission efficiency due to the dichroic absorption. In this case, anisotropic wave plates would be preferred to manipulate the orientation of the electric field.

Furthermore, the Malus' Law can be used in more complex setup for a wide range of applications. For example a displacement sensor [100] has been realized by implementing an angular displacement-linear displacement converter. The principle is to convert a mechanical displacement into an angular value applied on the polarizer. Thus the information is retrieved by the light intensity variation measured after the fixed analyzer. The Malus' Law is also applied to quantum optics where the analyzer controls the probability of a photon to have a particular polarization state or its complementary polarization state [101].

It has to be noted that a device similar device called Malus Fabry-Perot interferometer was theoretically investigated in 1999 by Vallet *et al.* [102]. This device consisted of a Fabry-Perot interferometer between polarizer and analyzer made of crossed polarized beamsplitters as shown in Fig. 3.2. The two mirrors of that device produce similar multiple reflections to the ones generated by the metallic polarizers in our structure. However, the behaviors of these two kinds of polarizing resonators are different. For the Malus Fabry-Perot interferometer [102], the Fabry-Perot resonances and the polarization effects are

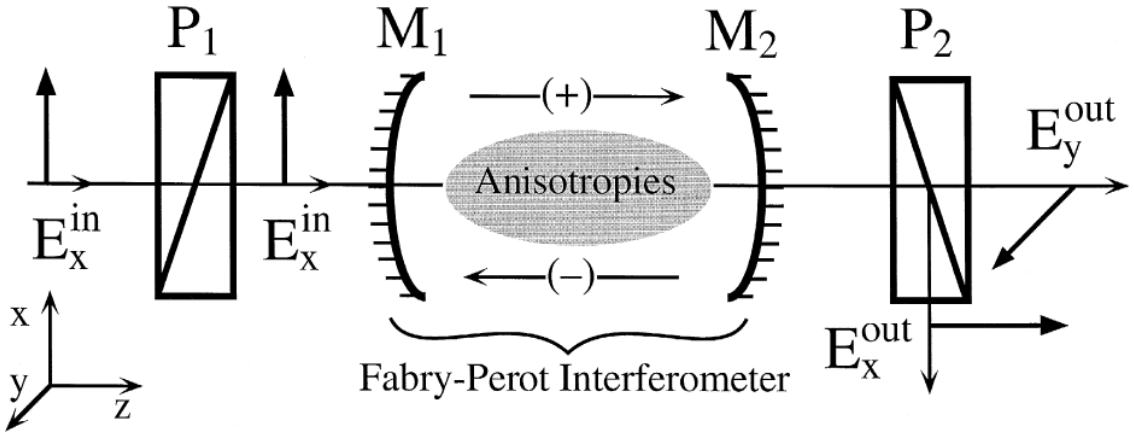

Figure 3.2: Principle scheme of the Malus-Fabry-Perot interferometer. P_1 and P_2 denotes the crossed polarized beam-splitters. M_1 and M_2 are the two mirrors that forms the FP cavity located between the crossed polarizers. Image taken from [102].

independent. For the metallic metamaterials stack, the metamaterials play the role of both polarizers and mirrors. In our study, the interdependency between the polarization and the reflection properties drastically change the transmission response of the structure. The unique transmission response we will observe will be the basis to propose the design of an electro-optical sensor.

3.2/ BREAKTHROUGH OF THE MALUS' LAW

Recently, some papers have reported Malus' Law breakthrough using metallic metamaterials. We can distinguish two main physical effects at the origin of the breakthrough. It can either involve plasmons at the metallic metamaterials interfaces or a "cavity effect" due to the stacking of metamaterials.

3.2.1/ WITH PLASMONS

For example, Huang *et al.* [103] have used a pair of metallic polarizers and shown a transmission response in complete disagreement with the classical Malus' Law. They have suggested the presence of an internal surface plasmon polariton (ISPP) located

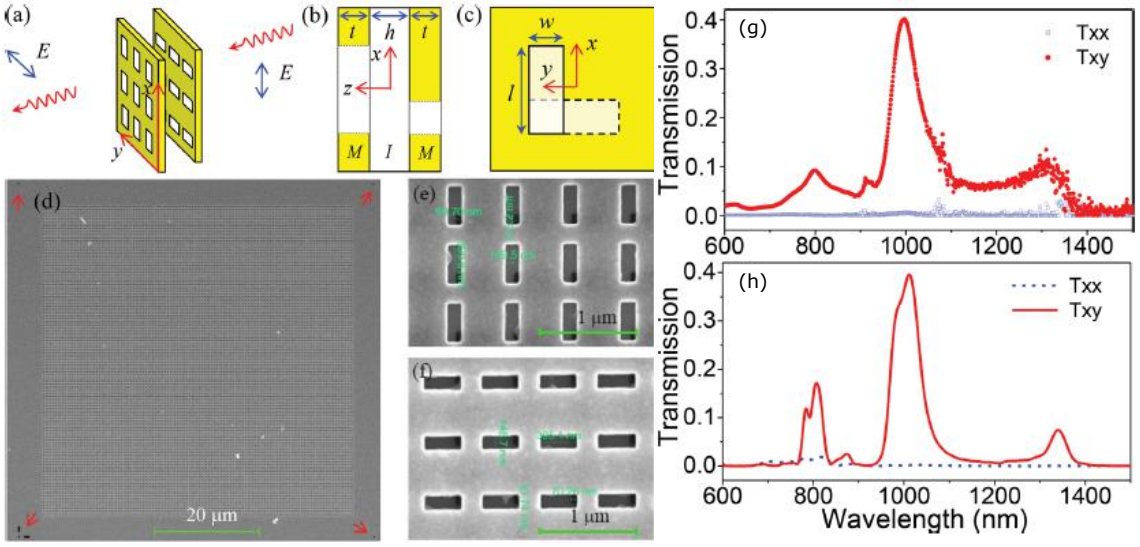

Figure 3.3: **(a)** Principle scheme of cross polarization conversion with two orthogonally oriented plasmonic polarizers. **(b)** x-z scheme of the structure where t is the thickness of the plasmonic polarizers and h the middle layer thickness. **(c)** x-y view of the polarizers where l and w respectively correspond to the length and width of the apertures milled in the metal. **(d)**, **(e)** and **(f)** SEM images of the fabricated structure. **(g)** Experimentally measured cross-polarization transmission in very good agreement with **(h)** the FDTD simulated cross-polarization transmission. Images taken from [103].

between the two polarizers. The discrepancies with the classical Malus' Law is due to the ISPP which couples with the cavity modes of the polarizers holes. For some particular configurations, they even show that a pair of crossed polarizers (as depicted in Fig. 3.3**(a)**) exhibit a high transmission. For such case, the classical Malus' Law predicts a 0 in transmission.

Figures 3.3**(g)** and **(h)** respectively show the measured and the FDTD simulated transmission spectra for $\theta = 90°$. We can especially notice that T_{xy} is 40% for the central wavelength around 1000 nm and therefore demonstrate a breakthrough of the Malus Law.

3.2.2/ WITH "CAVITY EFFECT"

Another example is given by Zhang *et. al* using a three-gold-layer structure as depicted in Fig. 3.4**(a)** [104]. The first polarizing layer is oriented along the x axis, the middle layer is rotated by 45° and the third one is oriented along the y axis. In other words, there is an angle of 45° between each layer and the classical Malus' Law predicts a maximum transmission of 25 %. Fig. 3.4**(b)** shows however the measured transmission spectrum of the x to y converted polarization $T_{yx} > 25\%$ for a very broad range. The authors suggest that a "cavity effect" between each gold layers leads to the enhanced transmission through the structure. Indeed, the stacking of three metallic layers provokes multiple reflections between them and the transmission response can be enhanced via Fabry-Perot-like resonances.

Recently, some others papers has also mentioned such Fabry-Perot-like enhanced trans-

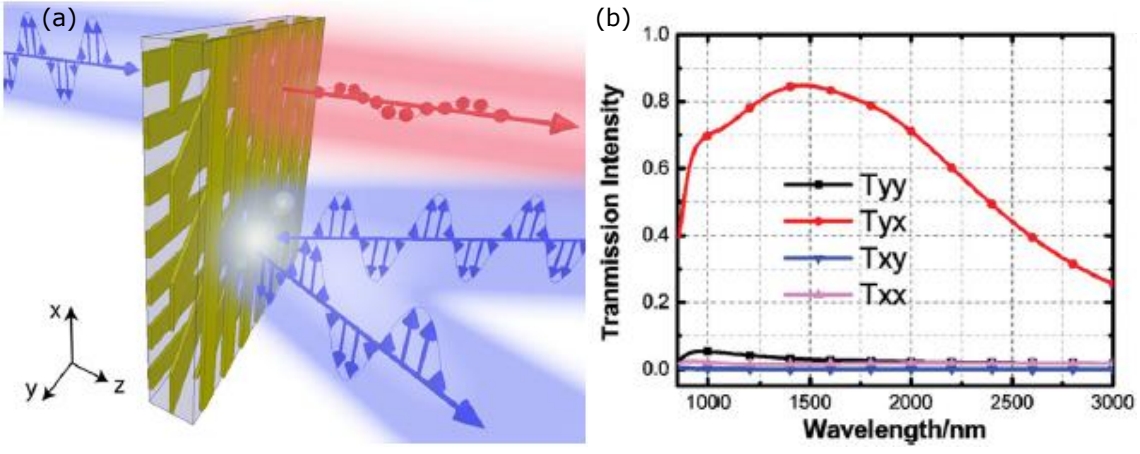

Figure 3.4: **(a)** Rendered view of the tri-layer structure with cross polarization conversion effect. **(b)** Measured cross polarization transmission spectrum in red curve. Images taken from [104].

mission with similar tri-layer structure [105–107]. None of these articles, however, gives an analytical treatment of the multi-layered structure they study.

In the next section, we make an analytical study which gives an accurate description of the structure's transmission response. This theoretical analysis enables us to study further the "cavity effect" suggested in recent papers. Furthermore, this original study will reveal some interesting transmission properties of the polarizer-analyzer structure. In fact, it will lead in Sec. 3.5 to an original setup for electro-optical sensing.

3.3/ ANALYTICAL STUDY OF THE POLARIZER-ANALYZER CONFIGURATION WITH METALLIC POLARIZERS

In this section, we propose to give an analytical treatment of the polarizer-analyzer configuration formed by two metallic polarizers. The EJF (introduced in the first chapter) gives the transmission and polarization properties of a single metamaterial while the S-matrix algorithm accounts for the stacked metamaterials with several Floquet modes orders. This will allow us to derive an analytical scattering matrix describing the whole stacked structure. From this matrix, we will extract an analytical formulae for the transmission response of the PAC - the Extended Malus' Law (EML). We will further give an in-depth description of this expression and highlight its main characteristics. We finally demonstrate the important role of the multiple reflections between both polarizers.

3.3.1/ HYPOTHESIS AND DESCRIPTION OF THE STRUCTURE

Before deriving the EML formulae, we recall the hypothesis for the EJF and we specify additional hypotheses concerning the stacked structure to preserve the validity of the model.

We remind that we consider a normal incident light on the structure and that only one propagative mode is excited in the subwavelength apertures. Since we consider rectangular apertures for this study, the single propagative mode corresponds to the fundamental TE_{01} guided mode since λ is assumed to be larger than the cut-off wavelength of the second waveguide mode (TE_{10} mode). We also assume that the polarizers thickness h is large enough to neglect the coupling of evanescent waveguide modes at the polarizers interface. Furthermore, we remind that the EJF is only valid for a far-field description. It implies that the distance between the polarizer and the analyzer has to be large enough in order to neglect evanescent field coupling between the polarizer and the analyzer.

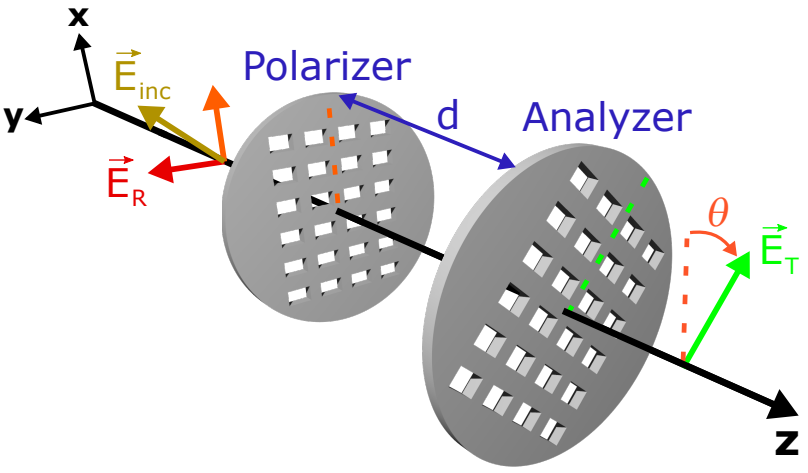

Figure 3.5: Principle schematic of the Polarizer-Analyzer Configuration (PAC)

For this study, we consider that the near-field coupling of the evanescent waveguide modes between polarizer and analyzer is negligible when the optical distance $L > \lambda/2$ with $L = n_{hom}d$ where n_{hom} is the refractive index of the homogeneous middle layer and d is the distance between both polarizers, as shown in Fig. 3.5. We also consider that the two metallic polarizers are perfectly parallel to each other in the (x-y) plane. We consider the whole structure to be free standing in air. This implies that the homogeneous regions, the middle region as well as the subwavelength apertures are filled with air ($n_{hom} = 1$ unless otherwise stated). We also precise that all homogeneous regions are linear and isotropic. For more simplicity, we consider that the polarizer and analyzer have common geometrical parameters (i.e. a_x, a_y, h and p).

3.3.2/ EXTENDED JONES CALCULUS FOR THE PAC: EXTENDED MALUS' LAW

In the first chapter, we have presented an EJF for the description of the polarization properties of single metamaterial structures. As we have seen, a single metamaterial features reflection properties that cannot be neglected. Therefore, to account for the stacking of metallic metamaterials, the direct multiplication of the transmission Jones matrices is not valid and the reflection Jones matrices has to be considered as well. We will now present the algorithm allowing us to model structures comprising two or more metamaterials. The algorithm is known as the scattering matrix propagation algorithm (S-matrix algorithm) given by Lifeng Li in 1996 [108]. It is an iterative process based on the Redheffer star product [109]. For this manuscript, we choose the "S-matrix algorithm" terminology. This algorithm consists in computing the scattering matrix of a whole structure by using the scattering matrix of its constituent layers. We mention that we use a derived version of the S-matrix algorithm as established in [110, 111].

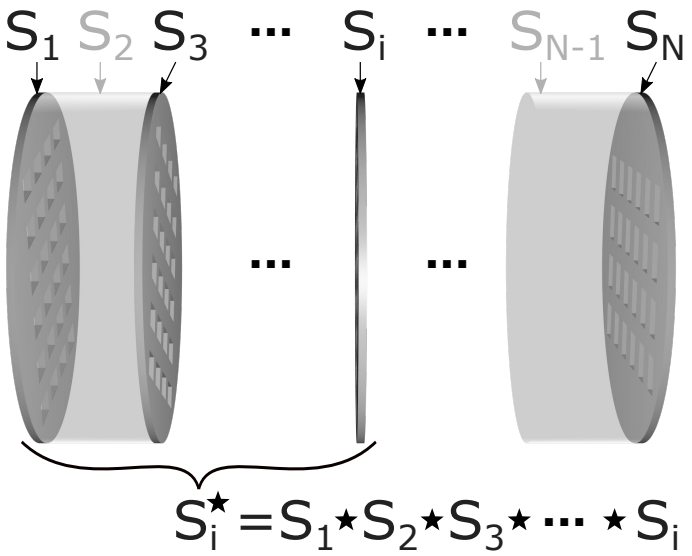

Figure 3.6: S-matrix algorithm principle. The overall structure S-matrix $S_N^{\bigstar}$ is obtained by iteratively "feeding" the S-matrix algorithm with the intermediate S-matrix structure $S_{i-1}^{\bigstar}$ with the next layer matrix S_i.

Let us consider an arbitrary structure made of N individual layers as depicted in Fig. 3.6. Each layer i (where $i \in \{1, N\}$) possesses its own scattering matrix denoted by S_i. The S-matrix algorithm consists in computing iteratively the scattering matrix of the partial structure $S_{i-1}^{\bigstar}$ with the scattering matrix of the next layer S_i in the structure, so that $S_i^{\bigstar} = S_{i-1}^{\bigstar} \bigstar S_i$. The term $\bigstar$ denotes the specific operator of the S-matrix algorithm. Finally, the S-matrix of the entire structure is computed by the last step $S = S_{N-1}^{\bigstar} \bigstar S_N$.

To present the S-matrix algorithm, let us consider two arbitrary scattering matrices denoted by $S^{(a)}$ and $S^{(b)}$. We note $S^{(c)}$, the scattering matrix resulting from the application of the S-matrix algorithm. Its expression is given by

$$S^{(c)} = S^{(a)} \bigstar S^{(b)} = \begin{pmatrix} S_{11}^{(c)} & S_{12}^{(c)} \\ S_{21}^{(c)} & S_{22}^{(c)} \end{pmatrix} \tag{3.3}$$

where $\bigstar$ is the S-matrix algorithm operator. The (2×2) sub-blocks of the resulting matrix $S^{(c)}$ are written as

$$\begin{aligned} S_{11}^{(c)} &= S_{11}^{(b)} \left\{ I_d + S_{12}^{(a)} Z S_{21}^{(b)} \right\} S_{11}^{(a)} \quad ; \quad S_{12}^{(c)} = S_{11}^{(b)} S_{12}^{(a)} Z S_{22}^{(b)} + S_{12}^{(b)} \\ S_{21}^{(c)} &= S_{22}^{(a)} Z S_{21}^{(b)} S_{11}^{(a)} + S_{21}^{(a)} \quad ; \quad S_{22}^{(c)} = S_{22}^{(a)} Z S_{22}^{(b)} \end{aligned} \tag{3.4}$$

with the matrix $Z = \left[I_d - S_{21}^{(b)} S_{12}^{(a)} \right]^{-1}$, as given in [110, 111].

In our case, the PAC is seen as a tri-layer system. The first and the third layers are

the polarizer and the analyzer, respectively. Since we consider the structure to be free standing in air, the polarizer and analyzer are reciprocal elements. We can then simplify the notation and we define $J^T = J^T_{11} = J^T_{22}$ and $J^R = J^R_{12} = J^R_{21}$. Therefore, the reduced S-matrix for each polarizer is given by:

$$S_{pol} = \begin{pmatrix} J^T & J^R \\ J^R & J^T \end{pmatrix} \text{ and } S_{ana} = \begin{pmatrix} R(-\theta)J^T R(\theta) & R(-\theta)J^R R(\theta) \\ R(-\theta)J^R R(\theta) & R(-\theta)J^T R(\theta) \end{pmatrix} = \begin{pmatrix} J^T_\theta & J^R_\theta \\ J^R_\theta & J^T_\theta \end{pmatrix} \tag{3.5}$$

where the matrices $J^{T,R}$ are given in the previous chapter by Eq. (2.89). The second layer S_{hom} denotes the S-matrix of homogeneous region between both polarizers and it is simply a propagation operator. Its expression is given by:

$$S_{hom} = S_{prop} = \begin{pmatrix} J_{prop} & 0 \\ 0 & J_{prop} \end{pmatrix} \text{ with } J_{prop} = \begin{pmatrix} u & 0 \\ 0 & u \end{pmatrix} \tag{3.6}$$

where

$$u = \exp(ik_0 L), \tag{3.7}$$

is the propagation term between the polarizer and the analyzer interfaces, with $k_0 = 2\pi/\lambda$.

For a tri-layer system, the S-matrix algorithm is applied twice on the reduced S-matrices in order to obtain the S-matrix of the entire structure. The first iteration of the S-matrix algorithm is:

$$S^\bigstar = S_{pol} \bigstar S_{hom} = \begin{pmatrix} uJ^T & u^2 J^R \\ J^R & uJ^T \end{pmatrix} \tag{3.8}$$

where $S^\bigstar$ is the S-matrix representing the partial system composed of the polarizer and the homogeneous region. Then, the reduced scattering matrix of the PAC, S_{PAC}, is obtained by the second iteration of the S-algorithm applied on $S^\bigstar$ and S_{ana}:

$$S_{PAC} = S^\bigstar \bigstar S_{ana} = \begin{pmatrix} J^T_{PAC} & J^R_{PAC} \\ J^R_{PAC} & J^T_{PAC} \end{pmatrix} \tag{3.9}$$

where $J^{T,R}_{PAC}$ are transmission and reflection Jones matrix of the PAM. The matrix J^T_{PAC} is given by

$$J^T_{PAC} = uJ^T_\theta \left[I_d - u^2 J^R J^R_\theta\right]^{-1} J^T \tag{3.10}$$

where the inversion of $\left[I_d - u^2 J^R J^R_\theta\right]$ give

$$\left[I_d - u^2 J^R J^R_\theta\right]^{-1} = \frac{1}{D}\begin{pmatrix} 1 - u^2(1 - \alpha_R \sin^2\theta) & -u^2(1-\alpha_R)\alpha_R \cos\theta \sin\theta \\ -u^2 \alpha_R \cos\theta \sin\theta & 1 - u^2(1-\alpha_R)(1 - \alpha_R \cos^2\theta) \end{pmatrix} \tag{3.11}$$

with

$$D = 1 + u^2(u^2 - 1)(1 - \alpha_R)(\alpha_R^2 \sin^2\theta - 1) \tag{3.12}$$

Substituting Eqs. 3.11 and 3.12 in Eq. 3.10 leads to:

$$J_{PAC}^T = \alpha\,(\theta, \lambda, L)\, J_\theta^T J^T \tag{3.13}$$

where the term α is expressed as

$$\alpha(\theta, \lambda, L) = \frac{\alpha_T^2(\lambda) u}{\gamma - u^2\,[1 - \alpha_R(\lambda)]^2} \tag{3.14}$$

with

$$\gamma = \frac{1 - u^2\left[1 - \alpha_R^2(\lambda)\sin^2\theta\right]}{1 - u^2} \tag{3.15}$$

It is interesting to compare the extended Jones formalism for metallic polarizers with the classical Jones formalism for dichroic polarizers. As for the classical Jones formalism, we find the typical multiplication of Jones matrices $J_\theta^T J^T$. However, we note the appearance of an additional term α in the extended Jones calculus for metallic polarizers. This term accounts for the reflection properties of the metallic plates.

The analytical expression of the EML is directly deduced from Eq. (3.13) by considering that the transmitted electric field is given by $\vec{E}_t = J_{PAC}^T \vec{E}_{inc}$. It leads to

$$T = |\alpha(\lambda, L, \theta)|^2 \cos^2\theta \qquad \boxed{\text{Extended Malus' Law}} \tag{3.16}$$

where T is the transmission coefficient of the polarizer-analyzer structure.

Compared to the classical Malus' Law ($T = \cos^2\theta$) the modulation term $|\alpha(\theta, \lambda, L)|^2$ in the EML expression, accounts for the additional properties of the two metallic metamaterials. First, it takes into account the spectrally resonant properties of the metallic plates (via λ dependency). It thus ensures a perfect transmission through the structure at those resonance wavelengths. Second, it takes into account the optical distance L between the polarizer and the analyzer (via the propagation term u). Indeed, the reflections induced by both polarizers implies that the entire structure acts as a resonant cavity. Therefore, the optical length L of the cavity is a parameter that plays an important role in the transmission response of the structure. We remind that, in the classical Jones formalism, the distance between polarizers is not taken into account because the reflection of the polarizers is negligible. Third, the modulation term α also depends on the angle θ and shows the interdependency between the polarization and reflection properties. Finally, the trans-

mission is also modulated by the classical term $\cos^2\theta$ that results from the classical Jones matrices multiplication ($J_\theta^T J^T$).

THE MULTIPLE REFLECTIONS INTERPRETATION

It is interesting to take a closer look at the analytical expression of α in Eq. (3.14). We can especially notice the term $\alpha_R(\lambda)$ representing the reflection properties of the plates. This means that the term α is accounting for the multiple reflections process that takes place between the polarizer and the analyzer. This implies that, unlike dichroic polarizers, there is an interaction between both metallic polarizers via the multiple reflections. Therefore, it makes senses that the distance L (via u in Eq. (3.14)) and the rotation angle θ (via $\sin\theta$ in Eq. (3.15)) play a role in the modulation of the transmission. Furthermore, the different modulation parameters λ, θ and L are interdependent. Indeed, in Eq. 3.15, we can notice the term $u^2\left[1-\alpha_R^2(\lambda)\sin^2\theta\right]$ in the numerator where the three parameters are linked to each other. This leads to a rather complex transmission response, as we will see below in the numerical investigation (see Sec. 3.4).

The EJF also allows us to compute the classical Malus' Law obtained with dichroic polarizing plates with perfect absorption. We first give the general expression of the reflection Jones matrix of a polarizer oriented along the x-axis:

$$J_d^R = \begin{pmatrix} \alpha_R - 1 & 0 \\ 0 & \beta \end{pmatrix} \tag{3.17}$$

where β is the reflection coefficient of one polarizer along the rectangle length axis, calculated in accordance with the absorption along this axis only. For metallic polarizers, $\beta = -1$ (no absorption), Eq. (3.17) becomes identical to Eq. (2.89). For dichroic polarizer, $\beta = 0$ (total absorption along the rectangle length axis) which means that the multiple reflections in the PAC are reduced to the ones oriented along the rectangle width axis (term $\alpha_R - 1$ in J_d^R). These reflections are weak for most of the natural dichroic plates. This leads to the expression of α_d (instead of α) in the case of the classical Malus' Law, when the multiple reflections are not neglected ($\beta = 0$ and $\alpha_R \approx 1$ with $\alpha_R \neq 1$):

$$\alpha_d(\theta,\lambda,L) = \frac{\alpha_T^2(\lambda)u}{1-u^2\left[1-\alpha_R(\lambda)\right]^2\cos^2\theta} \quad \underset{\alpha_R\to 1}{\longrightarrow} \alpha_T^2(\lambda)u \tag{3.18}$$

This equation highlights the discrepancies between the factor α_d found for a pair of dichroic polarizers and the modulation factor α previously obtained for a pair of metallic polarizers (Eqs. (3.14) and (3.15)). We see that α_d depends on θ, but the factor

$u^2\left[1-\alpha_R(\lambda)\right]^2$ relating to the multiple reflections may be neglected for the special case of highly absorbing dichroic polarizers ($\alpha_R \to 1$). On the contrary, for metallic polarizers, the term $u^2\left[1-\alpha_R^2(\lambda)\sin^2\theta\right]$ cannot be neglected in Eq. (3.15). Indeed, we know that $\alpha_R \approx 1$ when $|\alpha_T| = 1$ due to the energy balance criterion: $\left|\alpha_T^2-(\alpha_R-1)^2\right| = 1$ (see Fig. 3 in [65]). Consequently, and contrary to the EML for metallic polarizers, we can assume that α_d is independent of θ, as it is commonly accepted for dichroic polarizers. Therefore, the transmission expression for dichroic polarizer takes the form of the classical Malus' Law which corresponds to the single pass propagation through the PAC as shown in Eq. (3.18).

3.4/ NUMERICAL ANALYSIS OF THE POLARIZER-ANALYZER CONFIGURATION

To further study the properties of the polarizer-analyzer structure, we propose a numerical investigation of the transmission of the PAC. We will especially focus on the parameters L and θ that appear in the modulation term α. This will enable us to highlight the additional properties of the PAC due the reflection of the metallic polarizers. As we have mentioned in section 3.3.1, the rectangular apertures of the polarizer and the analyzer are kept identical. For this whole numerical investigation, we set the dimensions of the aperture's length $a_y/p = 0.9$ and aperture's width $a_x/p = 0.45$. These values are chosen such that, the radiative losses of the apertures are maximized in order to achieve a broadband transmission. Moreover, we remind that the width a_x/p value is such that only the fundamental mode can propagate in the apertures at wavelengths located above the Floquet mode cut-off in order to satisfy the monomode regime and the extended Jones formalism. In other words, we ensure that the cut-off wavelength of the second cavity mode is smaller than the first Floquet mode cut-off wavelength. The thickness is $h/p = 1$ so that $h > \lambda/2$ for the considered spectral region. This ensures that evanescent waveguide modes do not couple to each other through the apertures. The transmission coefficient of the structure T is given by

$$T = \left|J_{PAC}^{T,x,x}\right|^2 + \left|J_{PAC}^{T,y,x}\right|^2 \tag{3.19}$$

First, we compute the transmission spectrum for $d/p = 1.0$ and $\theta = 0°$, as shown in Fig. 3.7**(a)** by the red curve. It is interesting to compare it with the dashed blue curve which gives the transmission spectrum for a single metallic polarizers. We notice that we retrieve the transmission maxima that are due to the resonance of one metallic polarizer. We also remark additional transmission maxima that are due to the multiple reflections between both polarizers. In fact, such additional peaks confirms the "cavity effect" discussed in

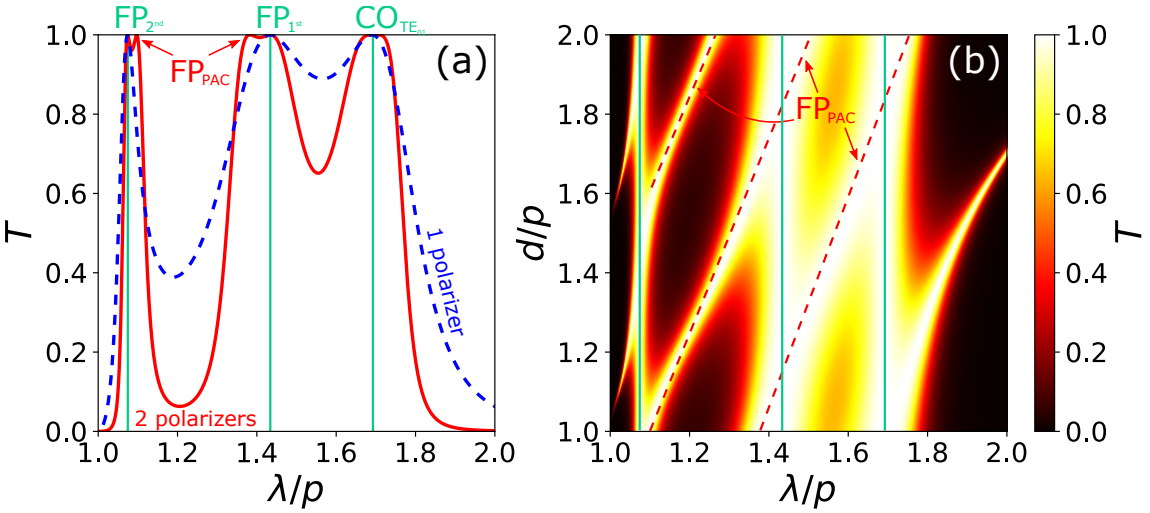

Figure 3.7: **(a)** Comparison of the transmission spectrum of a single metamaterial - in dashed blue curve - and a polarizer analyzer stack - in red curve. **(b)** Normalized transmitted electric intensity spectra of the PAC versus d/p for $\theta = 0°$. The parameters are: $a_x/p = 0.45$, $a_y/p = 0.9$ and $h/p = 1.0$. Vertical lines show resonances of $|\alpha|$ ($T = 1$). The resonance at $\lambda/p = 1.434$ is related to the first harmonic of the Fabry-Perot resonance of the fundamental mode guided inside the rectangular apertures (FP_{1st}). The other resonance at $\lambda/p = 1.69$ corresponds to the cut-off of the same mode (CO). The FP_{PAC} branches, in dashed red line, denotes the Fabry-Perot resonances located between the polarizer and the analyzer.

the previous section and in [104] that are FP-like resonances. Then, we calculate the spectrum of the electric intensity transmitted through the entire structure as a function of the distance d/p for $\theta = 0°$ ($T = |\alpha|^2$) as shown in Fig. 3.7**(b)**, in order to study further the FP-like resonances of the PAC. On the one hand, we see that the polarizers FP harmonics and the cut-off resonance of the TE_{01} mode (highlighted by the vertical dashed lines)

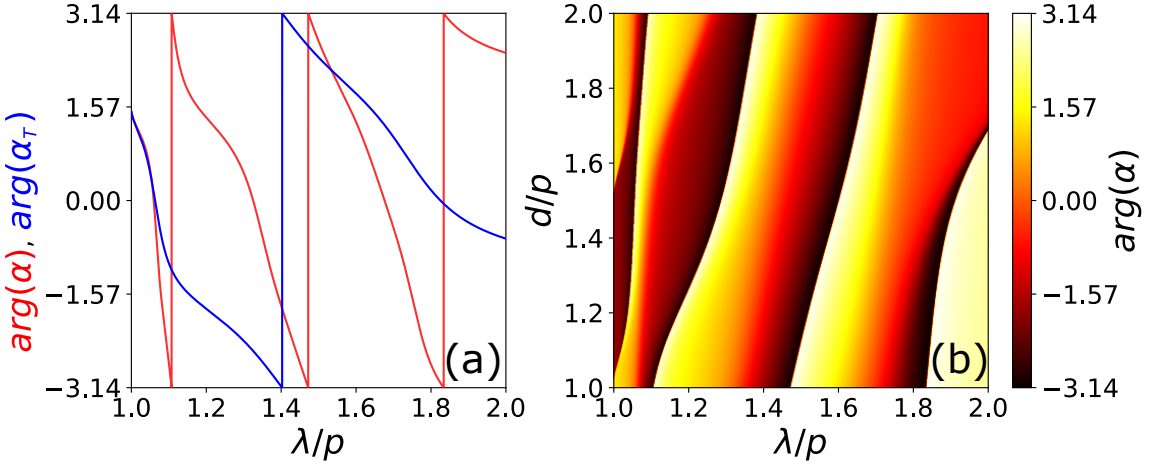

Figure 3.8: **(a)** Spectral phase of the modulation term α for a distance $d/p = 1.0$ and for $\theta = 0°$. **(b)** Evolution of the spectral phase as a function of the distance d/p for $\theta = 0^{0°}$

are not affected by the distance d between polarizer and analyzer. On the other hand, the additional FP-like resonances (FP_{PAC}, in oblique dashed lines) spectral location are linearly proportional to the distance d, as it is expected for FP-like resonances. Figure 3.8**(a)** gives - in red curve - the phase $arg(\alpha)$ of the modulation term α for $\theta = 0°$ and $d/p = 1.0$ which confirms the FP-like resonance location (for $arg(\alpha) = 0 \mod \pi$). It is compared with the phase of α_T given by the blue curve. Inspection of Fig. 3.8**(b)** reveals the FP_{PAC} branches highlighted in Fig. 3.7 for $arg(\alpha) = 0$ and $arg(\alpha) = -\pi$.

Figure 3.9**(a)** shows the transmission spectra as a function of θ for $L/p = 1$. It reveals that the wavelengths of transmission maxima are affected by the variation of θ (dashed lines). Figure 3.9**(b)** shows the transmission at fixed resonance wavelengths (taken for $\theta = 0°$), marked as solid lines in Fig. 3.9 **(a)**. It is interesting to compare the two transmission responses, in Fig. 3.9**(b)**, with the classical Malus' Law (in dashed black line). It shows that the multiple reflections strongly modifies the PAC transmission as a function of θ. The results obtained with our analytical model are in good agreement with results obtained with homemade FDTD code [32] given by the circles. The FDTD simulations were done with a uniform spatial mesh of $p/200$ along the x, y and z axes, and a temporal resolution respecting the stability criterion.

As mentioned earlier, the distance d/p can drastically modulate the transmission response of the PAC. More importantly, θ and d are two interdependent parameters, as clearly shown in Eq. (3.14) and Eq. (3.15). Now, we would like to vary both θ and d/p, while λ is fixed, in order to explore further the interdependency of θ and d. We now fix λ at

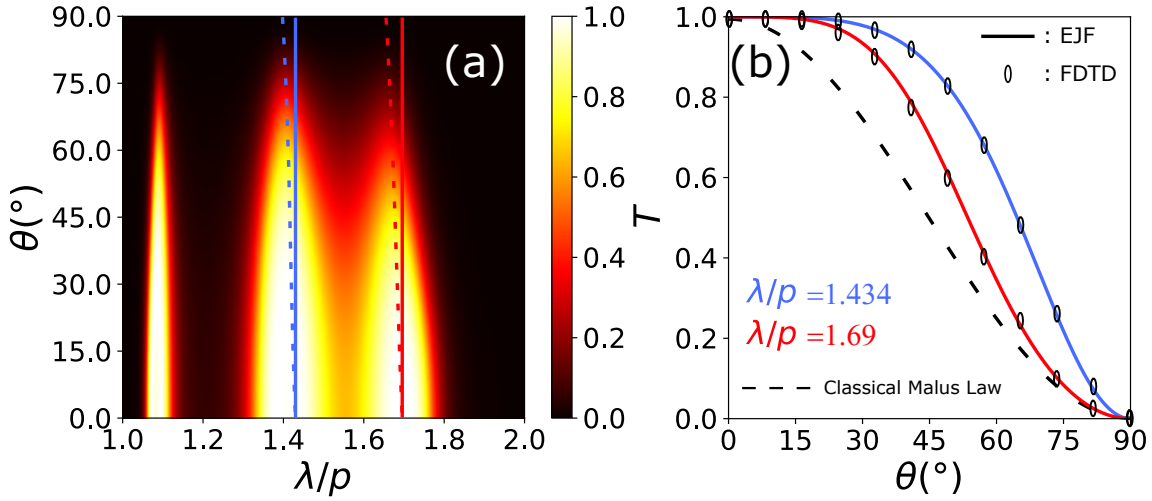

Figure 3.9: **(a)** Normalized transmission spectra versus θ for $d/p = 1$ (see fig. 3.7 for other parameters). The curved dashed lines represent the trajectories of the resonance of α ($|\alpha| = 1$). **(b)** Normalized transmission computed for fixed values of λ/p (blue and red vertical solid lines in (a)) and compared with the classical Malus Law (dashed black line).

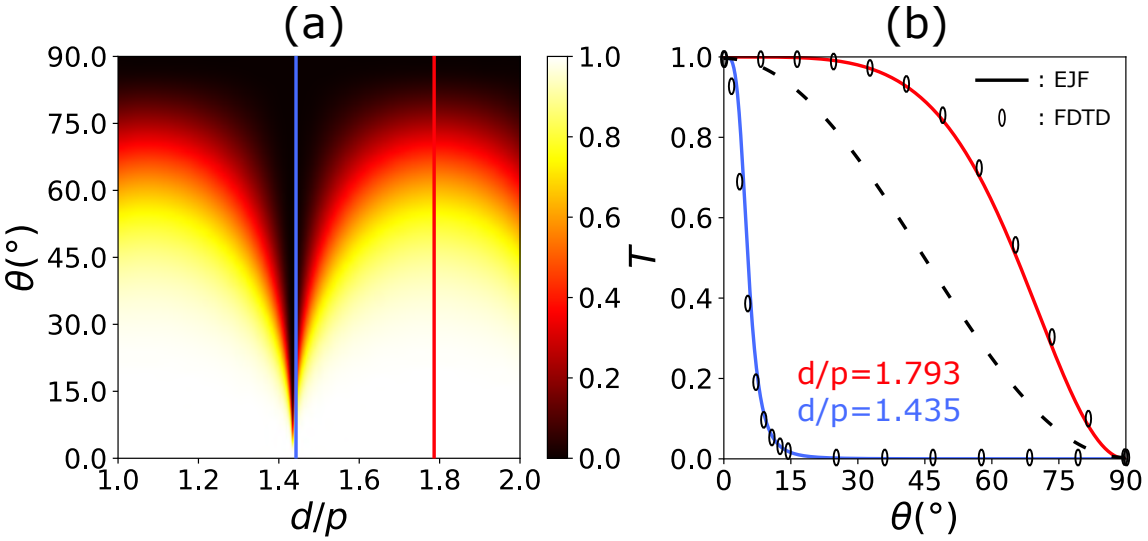

Figure 3.10: **(a)** Normalized transmitted intensity versus L/p and θ for $\lambda/p = 1.434$ (see fig. 3.7 for other parameters). **(b)** Normalized transmission computed for fixed values of L/p (blue and red vertical dashed lines in **(a)**) by comparison with the classical one (dashed black line).

a resonance wavelength $\lambda/p = 1.434$ and we plot the transmission response as a function of both θ and d/p. As we can see in Fig. 3.10**(a)**, we numerically observe a very strong modulation of the θ-transmission response when d/p varies. In fact, with the help of Eqs. (3.14) and (3.15), we can distinguish two contrasting cases:

1. When $u^2 = 1$ which is equivalent to $d = m\lambda/2$ where m is a natural integer, we observe an infinitely narrow angle Malus' Law where $HWHM \ll \pi/4$. Precisely, the transmitted electric intensity drops to 0 for this particular value of d/p when $\theta \neq 0°$. Indeed, this is explained by the fact that the term γ in eq. (3.15) diverges when $\theta \neq 0^o$ and therefore $|\alpha|$ tends to 0. For $\theta = 0^o$, we clearly see that $\gamma = 1$. This implies that $\alpha = \alpha_T^2(\lambda)/\alpha_R^2(\lambda)$ approximately equals to 1 at maxima of α_T ($I_{out} \approx 1$). For clarity, the Malus' Law is shown in fig. 3.10(b) for $d/p = 1.435$ (red line) and not exactly at $d/p = 1.434$ ($u^2 = 1$ for $m = 2$) for which the transmission results in a Kronecker function:

$$\alpha(\theta) = \delta_{\theta,0} \tag{3.20}$$

2. When $u^2 = -1$, which is equivalent to $d = \lambda/4 + m'\lambda/2$ where m' is a natural integer, we observe a broad angle Malus' Law. The transmitted electric intensity remains high for a wide range of θ. The transmission as a function of θ is shown in Fig. 3.10**(b)** (blue curve) for $L/p = 1.793$ ($u^2 = -1$ for $m' = 2$). Such a transmission can be seen as a complementary Airy-like function ($HWHM > \pi/4$) with a near-unity value for small θ. The following equation gives the simple expression of α for the

blue line in fig. 3.10 (b), assuming that $\alpha_R = 1$ (the computed value being exactly equal to $1.0077 + i0.1307$):

$$\alpha(\theta, \lambda) = i(-1)^{m'} \frac{\alpha_T^2(\lambda)}{1 - \frac{1}{2}\sin^2\theta} \tag{3.21}$$

Consequently, both narrow and broad angle EML can be achieved by tuning d.

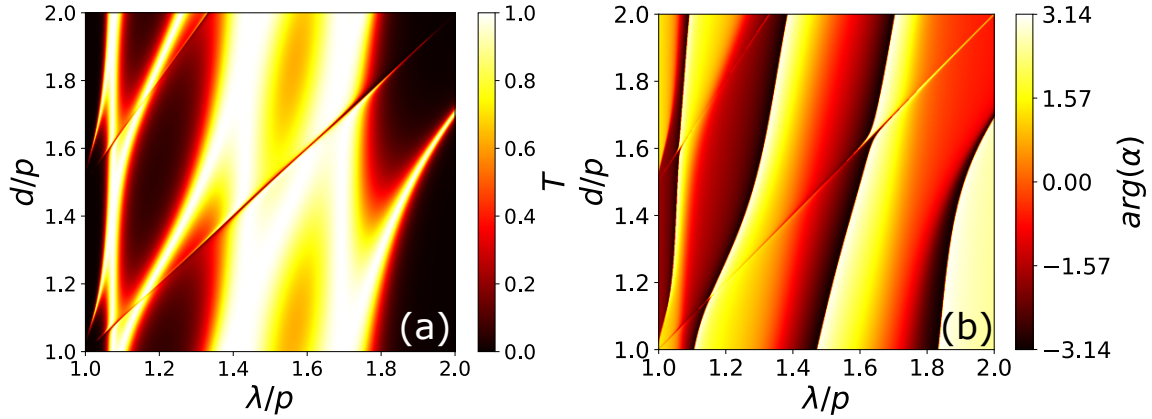

Figure 3.11: **(a)** Transmission spectrum as a function of the separation distance d/p and for $\theta = 10°$. **(b)** Evolution of the spectral phase with the distance d/p for $\theta = 10°$.

Figure 3.11**(a)** shows the evolution of the transmission spectrum as a function of the of the separating distance d for a rotation angle $\theta = 10°$. As we can observe, sharp transmission dips appear and are located at $\lambda/p = m\frac{d/p}{2}$. It actually to corresponds to a FP interference condition for a light in normal incidence. This shows the important role of the multiple reflections and confirms the ”cavity effect” interpretation mentioned in some recent papers [105–107]. By comparison of Fig. 3.11 to Fig. 3.7**(b)**, we can also remark that the rest of the spectra is not affected by the rotation of the analyzer. Figure 3.11**(b)** shows the corresponding evolution of the phase of the modulation term α. We also see additional sharp branches at the condition $\lambda/p = m\frac{d/p}{2}$ and for which $arg(\alpha) = -\pi$. As for the transmission spectrum, the rest of the spectral phase is not modified by the rotation of the analyzer.

Figure 3.12**(a)** shows three transmission spectra at a fixed separation distance $d/p = 1.69$, which coincide with the cut-off wavelength resonance of the TE_{01} guided mode in the metallic metamaterial. The three transmission spectra are obtained for different values of θ. As we can conclude from Fig. 3.12**(a)**, the transmission dip width can be controlled by θ. The quality factor Q of the transmission dip as a function of θ is shown in log-scale in Fig. 3.12**(b)**. We mention that the quality factor is computed in free oscillation regime for the Fig. 3.12**(b)**. It is striking to see that the quality factor Q theoretically diverges when θ tends to $0°$. We also observe that, in log-scale, the relation between Q and θ is linear.

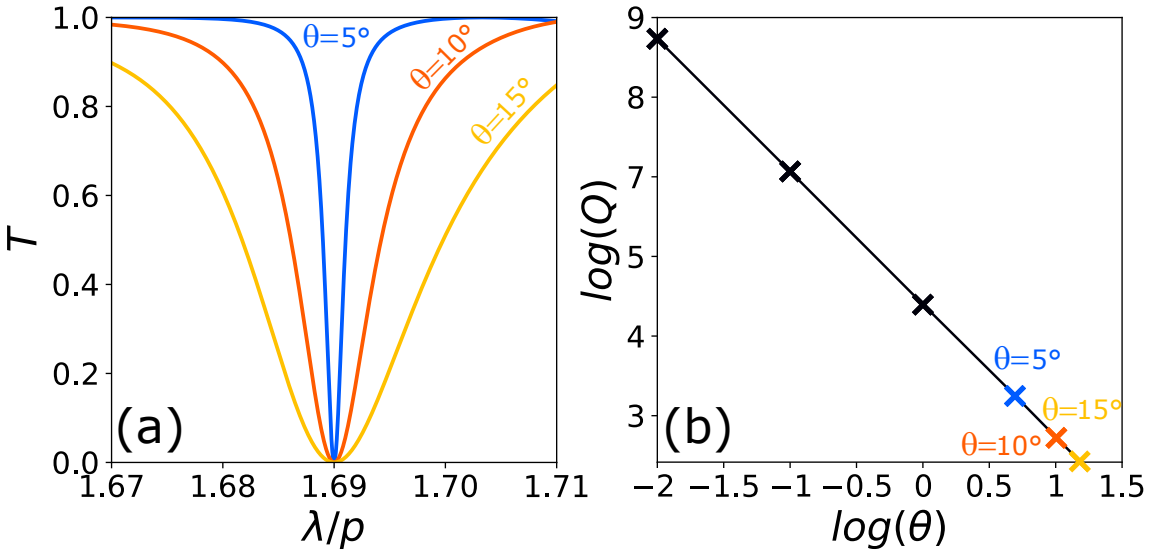

Figure 3.12: **(a)** Thee transmission spectra taken at $d/p = 1.69$ in blue, orange and yellow for $\theta = 5°$, $\theta = 10°$ and $\theta = 15°$ respectively. **(b)** Quality factor Q as a function of the angle θ in degree (where both axes are in log-scale).

Such linearity of the curve allows us to write:

$$Q = \frac{mA_m}{\theta^{B_m}}, \quad \forall \theta \neq 0° \tag{3.22}$$

where A and B are two empirical and positive parameters, and θ is expressed in degree. We have deduced that $B = 2$, and $A = 1.25 \times 10^4$ degrees^2, for $m = 2$.

Such phenomenon could be used for the design of tunable notch filter where the position and the width of the transmission dip is controlled by the relative position and rotation of the analyzer. An important point to mention is that such tunability does not originate from an active medium but from the relative arrangement of the structure itself (i.e. the angle and the distance between the metallic polarizers). In the next section, we propose some applications based on this transmission dip effect.

3.5/ APPLICATIONS - ENGINEERING THE MULTIPLE REFLECTIONS FOR ELECTRO-OPTICAL SENSING

We would like to take advantage of the sharp transmission dip previously observed in Fig. 3.11**(a)**. Instead of shifting the position of the analyzer, one can imagine the middle homogeneous layer to be composed of a dispersive medium. For example, one can think of a piezo-electric medium or an electro-optical medium for designing compact electric field sensors. Furthermore, the metallic polarizer and analyzer can simultaneously play

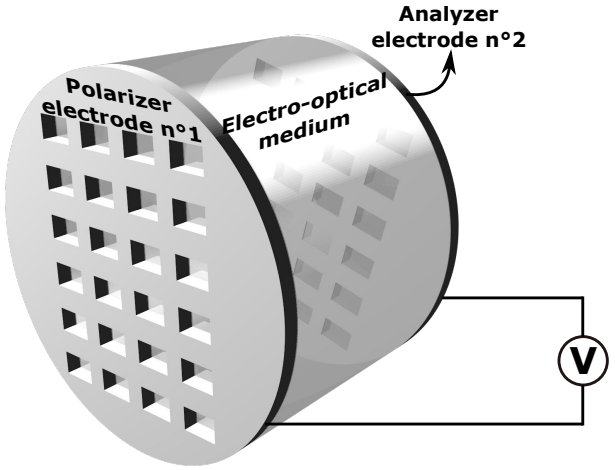

Figure 3.13: 3D rendered view of the principle of an electro-optically sensitive device. An electro-optical medium is sandwiched by the polarizer and the analyzer that are also playing the role of electrode 1 and 2 respectively.

the role of electrode and an electric voltage V can be applied in order to tune the refractive index of the material. Such design is summarized in Fig. 3.13.

We first define $L = n_{hom}d$ as the optical path length separating the polarizer and the analyzer. In the configuration depicted in Fig. 3.13, d is the electro-optical medium thickness and n_{hom} its refractive index. Contrary to the previous section, d is now fixed while n_{hom} is the variable via the electro-optical effect of the middle medium. Second, we want to define the sensitivity S of the structure, expressed in $\mu m/RIU$ (Refractive Index Unit). On the sharp transmission dip branches, the sensitivity is given by

$$S = \frac{\Delta\lambda}{\Delta n_{hom}}, \quad \forall\theta \neq 0^\circ. \tag{3.23}$$

However, there is a major difference between tuning the distance d (as we did in the previous section) and tuning its corresponding refractive index n_{hom}. Indeed, when the refractive index n_{hom} varies, it provokes a proportional shift of the cut-off wavelength of the TEM Floquet modes $\lambda_{TEM}/p = n_{hom}$. This is illustrated by Fig. 3.14**(a)** which shows the evolution of the transmission spectrum with the refractive index n_{hom} for the same geometrical parameters, with $\theta = 10^\circ$ and for $d/p = 1.0$. The dashed purple line denotes the TEM Floquet mode cut-off wavelength λ_{TEM}. If we compare it to Fig. 3.11 **(a)**, we do not observe a sharp transmission dip any more because, for $m = 2$, the FP resonance condition $\lambda/p = L/p = n_{hom}d/p = n_{hom}$ matches the TEM Floquet mode cut-off condition $\lambda_{TEM}/p = n_{hom}$. In other words, the transmission dip is superimposed to the TEM Floquet modes cut-off and is therefore not exploitable. This is confirmed by Fig. 3.14**(b)** giving the transmission spectrum for $n_{hom} = 1.69$ where we can clearly see the very low transmission

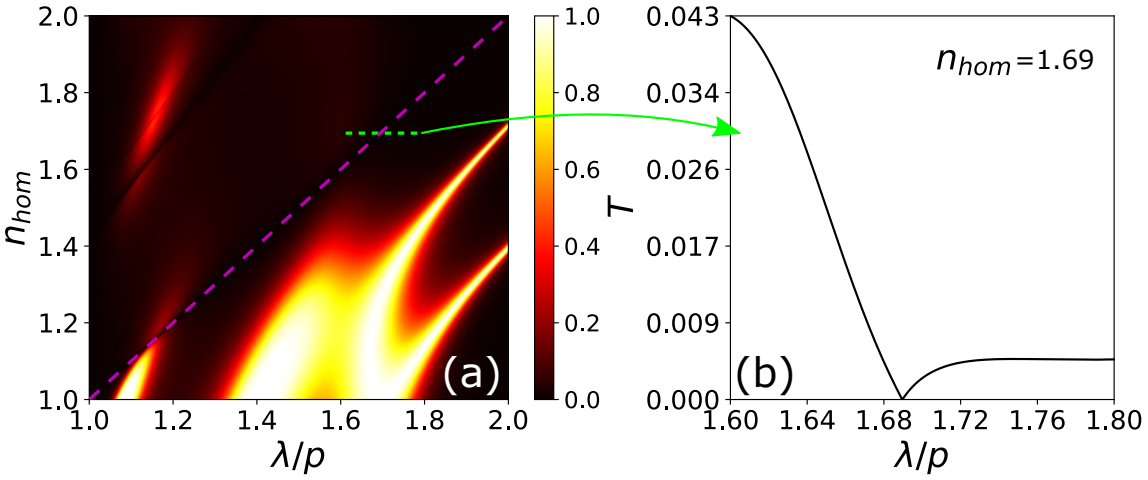

Figure 3.14: **(a)** Evolution of the transmission spectrum with the variation of the refractive index n_{hom} of middle layer with $p_x = p_y = p$ and $\theta = 10°$. The dashed diagonal line denotes the TEM Floquet mode cut-off wavelength $\lambda_{TEM}/p = n_{hom}$. **(b)** Corresponding transmission spectrum at $n_{hom} = 1.69$.

values around the dip located at $\lambda/p = 1.69$ and it therefore not exploitable for the sensing application.

In order to circumvent this superimposition, we design another subwavelength unit cell to offset the TEM Floquet mode cut-off wavelength toward shorter values. We first consider two different periods along the x and y axes. Therefore we now consider p_x and p_y and we keep p_y as a reference to normalize all geometrical values. A simple solution to offset λ_{TEM} is to reduce p_x without modifying any other geometrical parameters. Knowing that $a_x/p_y = 0.45$, we choose $p_x/p_y = 0.5$ and keep the same value for the other geometrical parameters - with the same distance $d/p_y = 1.0$ and the same angle $\theta = 10°$ - in order to analyze the influence of p_x only. By doing so, we reduce, almost to the maximum possible, the size of the bi-periodic cell to the size of its rectangular aperture.

Figure 3.15**(a)** shows the transmission spectrum as a function of the refractive index. We can note that the transmission dips reappears following the FP condition $L = m\lambda/2$. This is explained by the fact that the higher order Floquet modes polarized along the x-axis are now evanescent in considered spectral region. We note however that the sharpness of the dips is slightly reduced compared to the dip observed in Fig. 3.11 and Fig. 3.12. For example, Fig. 3.15**(b)** shows the transmission spectrum when $n_{hom} = 1.5$ and we observe that the dip sharpness is degraded compared to Fig. 3.12**(a)**. For example, in Fig. 3.15**(b)** the transmission maxima located around the dip (at $\lambda/p = 1.5$) are not reaching unity any more. Indeed, by reducing p_x we only reduce the cut-off wavelength of the higher-order Floquet modes polarized along the x axis only. The first higher order Floquet mode polarized along the y axis is still propagative between the metallic plates.

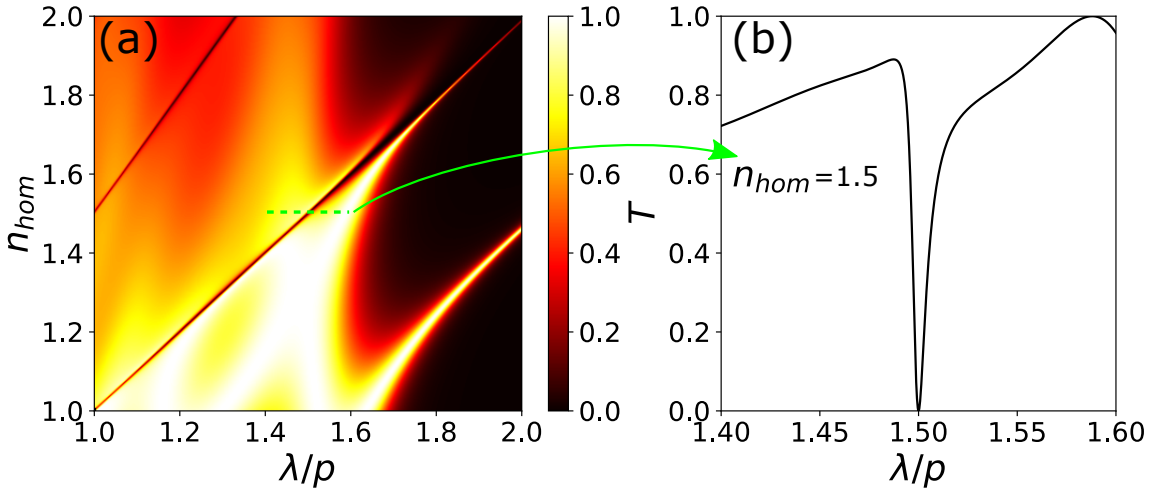

Figure 3.15: **(a)** Evolution of the transmission spectrum with the variation of the middle layer refractive index n_{hom} for $p_x/p_y = 0.5$, $d/p = 1.0$ and $\theta = 10°$. **(b)** Corresponding transmission spectrum when $n_{hom} = 1.5$

Nonetheless, such dip would be exploitable in view of sensing application.

More drastic designs of the unit cell geometry could improve the sharpness of the dip, but it would be detrimental to the bandwidth and the refractive index range on which the dips appear. It leads to a compromise between the working bandwidth - and the refractive index range - and the dip sharpness. We remind that Maxwell's equations are scale invariant and it directly implies that such design can be applied for any electromagnetic regions, from the visible to the microwave domain.

We choose to study this configuration in the THz domain because metals in this region can be considered as pec [112] and it thus perfectly satisfies the EJF framework. For this spectral region, the refractive index of most of the materials is between 3 and 4 [113]. Unfortunately, the bi-periodic metamaterials is not suitable for designing a PAC exhibiting a transmission dip branch for such range of refractive indices. Indeed, as it can be deduced from Fig. 3.15, the sharpness of the branch matching the refractive indices located between 3 and 4 is very low. It is therefore not optimized for high quality sensing. This is due to the cutoff wavelength of the fundamental cavity mode which limits the working bandwidth of the device. In other words, it means that the working bandwidth is between the TEM Floquet mode cut-off wavelength and the cutoff wavelength of the TE_{01} mode. Therefore, by reducing the period p_x to push backward the TEM Floquet mode cut-off wavelength, we also reduce greatly the transmission bandwidth of the PAC.

Fortunately, there is a simple alternative to the bi-periodic metamaterial limitation which is the mono-periodic metamaterial. We recall from the previous chapter that mono-periodic metamaterials exhibit a TEM mode with a corresponding cutoff wavelength which is lo-

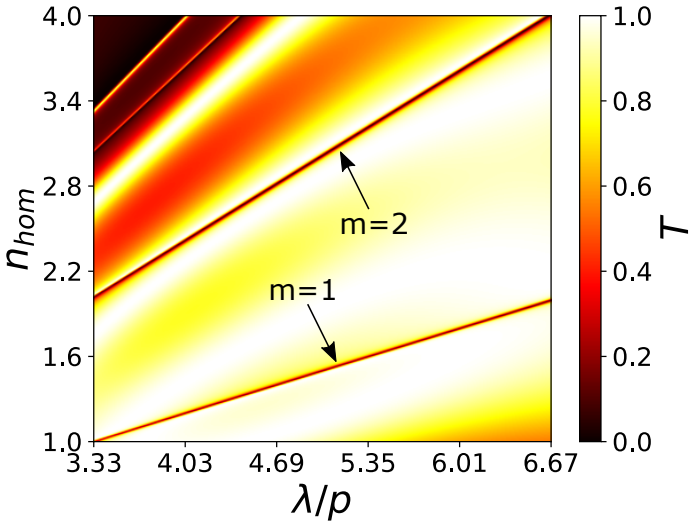

Figure 3.16: Transmission spectrum as a function of n_{hom} for mono-periodic metamaterial where the thickness is $h/p = 5/3$, the aperture width is $a/p = 2/3$ and the distance between the polarizer and the analyzer is $d/p = 5/3$ and $\theta = 10°$.

cated at infinity: $\lambda_{\text{cut-off}} \to \infty$. Then it is possible to shift the rayleigh anomaly by reducing the value of the period without limiting the working bandwidth. However, mono-periodic polarizers are characterized by only 3 parameters (a, p and h) - compared to 5 for the bi-periodic case (a_x, a_y, p_x, p_y and h) - and it limits the possibilities for the design.

As an example, we propose the following design using mono-periodical metamaterials. The thickness is $h/p = 5/3$, the aperture width is $a/p = 2/3$ and the distance between the polarizer and the analyzer is $d/p = 5/3$. We keep an angle $\theta = 10°$.

Fig. 3.16 shows the transmission spectrum of the PAC as a function of the refractive index n_{hom}. As we can see, transmission dip branches with high sharpness appears. We can also notice the influence of the TEM Floquet mode cut-off shift at the top left corner of Fig. 3.16. In fact, the dip branches are superimposed to the FP-like resonances that are established between the two metamaterials. We propose to focus on the middle branch $m = 2$ since it has a working refractive index range n_{hom} located between 2 and 4 with a very sharp dip. Note that the device can be adapted lower refractive index range by considering the branch below ($m = 1$).

For a detector working, for example, between 1 THz ($\lambda/p = 6.67$) and 2 THz ($\lambda/p = 3.37$), we deduce that $p = 45$ μm and $\Delta\lambda = 150$ μm. It follows that $S = 75$ μm/RIU. Finally, we are interested in finding a suitable value of θ to obtain a quality factor matching the resolution of THz spectrometers under the Rayleigh criterion. Hence, we deduce the minimum variation of the refractive index $(\Delta n_{hom})_{min}$ which can be detected by the device. Heterodyne detectors in THz domain offer spectral resolution [114] ($R = \Delta\lambda/\lambda$) equal to

3.3×10^{-6}. Thus, according to Eq. (3.22), to reach $Q = 1/R = 3 \times 10^5$, θ must be equal to $0.4°$. With such a quality factor, we derive from Eq. (3.23) that $(\Delta n_{hom})_{min} = \lambda/(S.Q) = 1.33 \times 10^{-5}$.

In this section, we have designed a very efficient system for THz applications ($S = 75\mu m/RIU$, $Q = 3.10^5$). Ranjan Singh *et al.* [115] has experimentally proposed a metasurface reaching $S = 57\mu m$/RIU and $Q = 28$. We have to keep in mind that our numerical results are obtained from a theory which assumes rigorously identical apertures and infinite periodicity of the metallic polarizers, in addition to a perfect parallelism between the polarizer and the analyzer. We also assume an isotropic and lossless EO material. Breaking these assumptions may affect the performances of the proposed system.

3.6/ STUDY OF THE INFLUENCE OF THE EVANESCENT WAVEGUIDE MODES

So far, we have studied the polarizer-analyzer configuration with an efficient and analytical formalism. We have established that the polarizer-analyzer structure can exhibit sharp and tunable transmission dips. However, in the EJF framework, we make the assumption that the evanescent waveguide modes are negligible in far-field propagation. We have seen that the numerically observed sharp dip originates from a complex multiple reflections process. We should now confirm the presence of those dips when the evanescent waveguide modes are included in the simulation. To this aim, we apply the S-matrix algorithm on larger scattering matrices that take into account a larger number of waveguide mode. For this multi-modal simulation, we take into account 8 waveguide mode in total, i.e. the fundamental TE_{01} guided mode and the following 7 evanescent waveguide modes, the higher order modes being totally negligible.

Figure 3.17**(a)** shows the evolution of the transmission spectrum with the distance d/p for $\theta = 10°$ and for 8 waveguide modes. It is to be compared with Fig. 3.11**(a)**. We can still remark the sharp transmission dips appearing in the spectra. We can also notice that the dips are shifted toward larger wavelengths. To clearly study the influence of the evanescent waveguide modes in the PAC, we give two comparisons between the Extended Jones Formalism simulation and the multimodal simulation in Fig. 3.17**(b)** and **(c)**. In Fig. 3.17**(b)** the polarizer and analyzer are aligned ($\theta = 0°$) and no transmission dip appears. We can observe a very good agreement for the two spectrum and validates the far-field approximation. In Fig. 3.17**(c)**, however, when the analyzer is rotated by an angle $\theta = 10°$, we can clearly notice that the dip strongly shifts while the remaining part

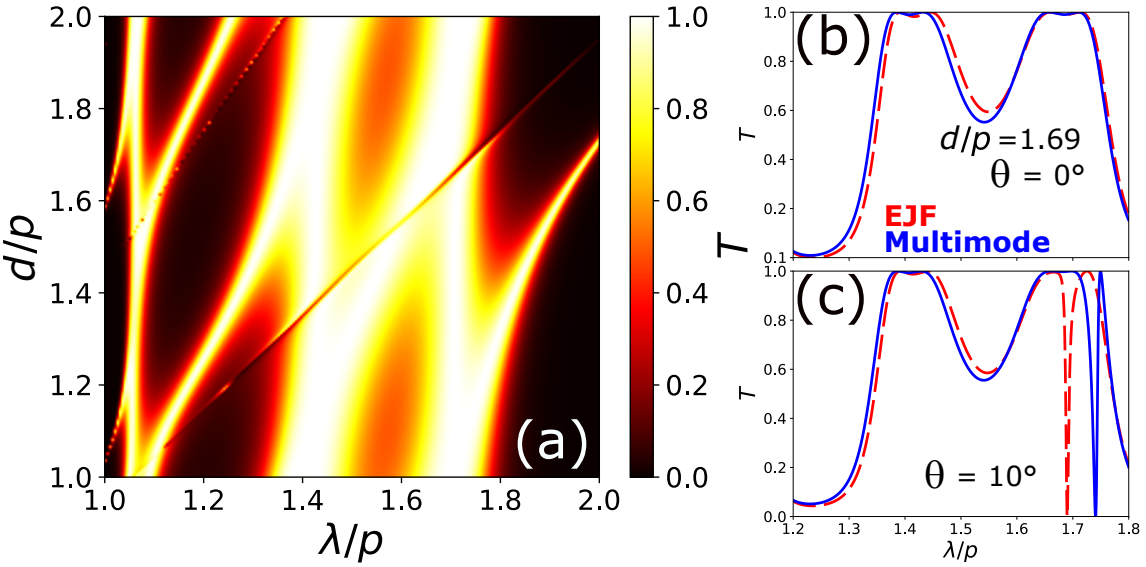

Figure 3.17: **(a)** Evolution of the transmission spectrum with the separation distance d/p, for $\theta = 10°$ and when the evanescent waveguide modes are taken into account. **(b)** Comparison of the EJF and multimodal-simulated transmission spectra when the polarizer and analyzer are aligned and **(c)** when the analyzer is rotated by $\theta = 10°$ at $d/p = 1.69$.

of the two spectra are still in good agreement. It seems surprising to see that only the transmission dip is strongly dependent on the number of considered waveguide mode. This intriguing results is not so trivial to explain and deserves a thorough study in the future.

Now we would like to compare the extended Jones formalism with the near-field simulation when we break the far-field approximation made in Sec. 3.3.1. For the next simulation, we do not consider anymore that $L > \lambda/2$. We again consider the structure free-standing in air so that only the distance d varies and $d < \lambda$.

Figure 3.18 shows the evolution of transmission spectrum for d/p varying from 0.1 to 1.0 for $\theta = 10°$. Fig. 3.18**(a)** corresponds to the EJF-simulated transmission spectra and Fig. 3.18**(b)** is the simulation taking into account the near-field propagation of the evanescent waveguide modes. As in Fig. 3.17 we can clearly notice that the transmission dip are shifted if we consider the near-field or not. In addition to the shift, we also remark discrepancies in the overall transmission spectra for $d/p < 0.6$. It is of course expected since the near-field becomes more and more impacting for shorter distance between the polarizer and the analyzer. Nonetheless, it is still possible to exploit the transmission dip which corresponds to $d \approx \lambda/2$ $(m = 1)$. This would lead to a structure with a smaller distance between polarizer and analyzer and thus, a more compact device for sensing. Moreover, the sensitivity $S = \dfrac{\Delta\lambda}{\Delta d}$ would be larger than the one we have used in Sec. 3.5.

We can conclude that the spectral shift due to the evanescent waveguide modes has to

be taken into account when designing sensitive device working at a precise wavelength for the transmission dip. The impact of the near-field is, however, rather small on the remaining part of the transmission spectra, and the dip's width - i.e the quality factor - is not affected as well. Consequently, the near-field is not detrimental to the design of sensitive device based on transmission dips. It even allows the design of more compact and more sensitive structure by reducing. In the next section, we will neglect again the near-field in order to exclusively focus on another aspect: the finite conductivity of the metal.

3.7/ METAL WITH FINITE CONDUCTIVITY

We have considered metamaterials made of metal having an infinite electrical conductivity ($\sigma \to \infty$). While this assumption is very close to reality for spectral regions such as the THz or the radio frequencies, it is however not in perfect agreement with the visible or the near infrared domains (NIR). In this section, we propose to compare our analytical formalism with a homemade RCWA (Rigorous Coupled Wave Analysis) code which account for the high but finite conductivity of a concrete metal: silver. The dispersion of the silver is then given by a Drude-Lorentz model [116]. We mention that this homemade RCWA code allows us to model monoperiodic metamaterials only. From the RCWA computation we extract the corresponding transmission and reflection Jones matrices of the monoperiodic metamaterial and we use the S-matrix algorithm to model the stacked structure. As for the EJF, the extracted far-field Jones matrices enables the rotation of the analyzer.

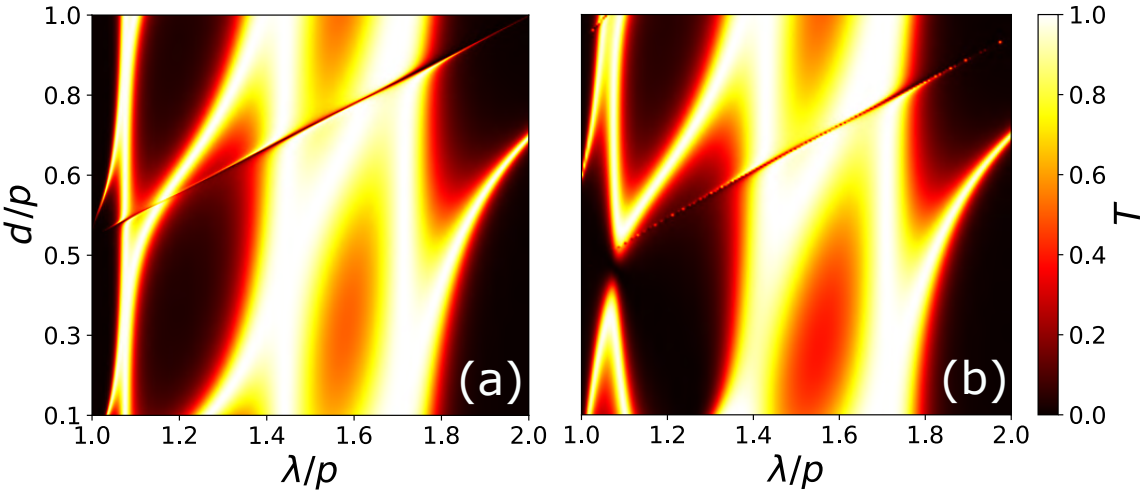

Figure 3.18: **(a)** EJF simulated transmission spectra when d/p varies from 0.1 to 1.0 and for $\theta = 10°$ **(b)** Multimodal simulated transmission spectra for the same configuration.

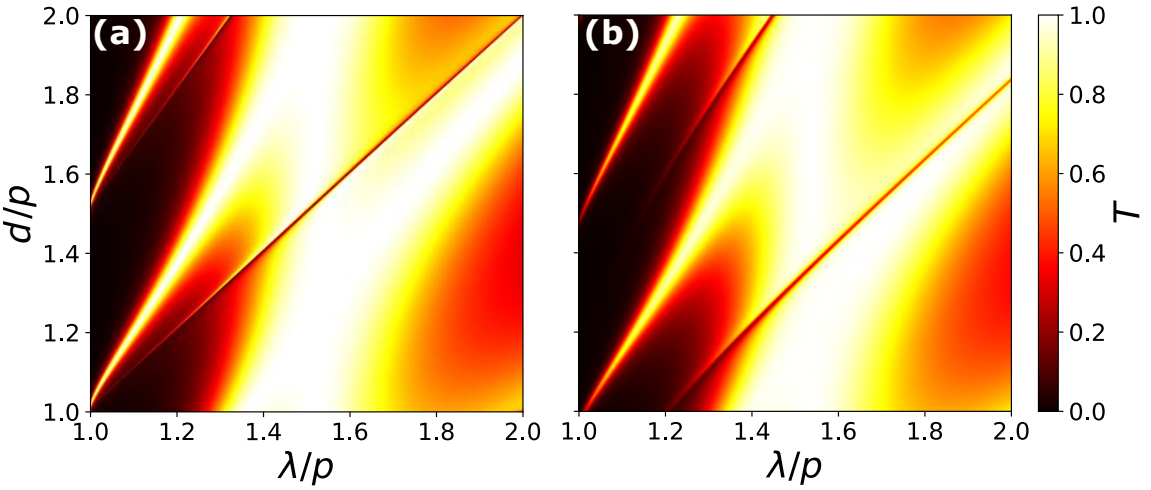

Figure 3.19: **(a)** EJF-simulated transmission spectra as a function of d/p for $\theta = 10°$ with mono-periodic PEC metallic metamaterials. **(b)** RCWA simulated transmission spectra with mono-periodic silver metamaterials.

To illustrate our study, we would like to give a basic example of transmission dips working around the telecommunication window at $\lambda = 1.55\ \mu m$. We propose the following design for the geometry of the mono-periodic metamaterials. The period is $p = 1\ \mu m$, the thickness is $h/p = 0.555$ and the aperture's width is $a/p = 0.5$ in order to get a resonance peak around $1.55 \mu m$ (due to the first FP harmonic established along the polarizers thickness). We consider the polarizer and the analyzer to be freestanding in air so that $n_{hom} = 1.0$ and $\theta = 10°$.

Figure 3.19 gives the transmission spectra as a function of the distance d/p simulated by **(a)** the extended Jones formalism and **(b)** the homemade RCWA for finite conductivity metallic metamaterials. As for the the near-field comparison in Sec. 3.6, the transmission dips are shifted towards larger wavelength when taking into account the finite conductivity of the metal. This is explained by an additional phase shift at each reflection in the cavity formed by the two metamaterial polarizers. The dip is shifted toward the higher wavelength because the finite conductivity induces a "skin effect" at each reflection and it thus increases the cavity size. The same tendency is observed for the FP resonances located between both polarizers since they also undergo the same skin effect at each reflection. However, the peak located at $\lambda/p = 1.55$ does not suffer a noticeable shift since the skin effect does not influence the FP harmonics established along the polarizers thickness. Unlike the previous section however, the dip sharpness seems to be altered by the finite conductivity.

Figure 3.20 shows **(a)** EJF-simulated and **(b)** RCWA simulated transmission spectrum with a transmission dip located at $\lambda = 1.55\ \mu m$. It highlights the impact of conductivity on

the sharpness of the transmission dip. This is actually due to the absorption of the metal which directly limits the multiple reflection effects in the structure.

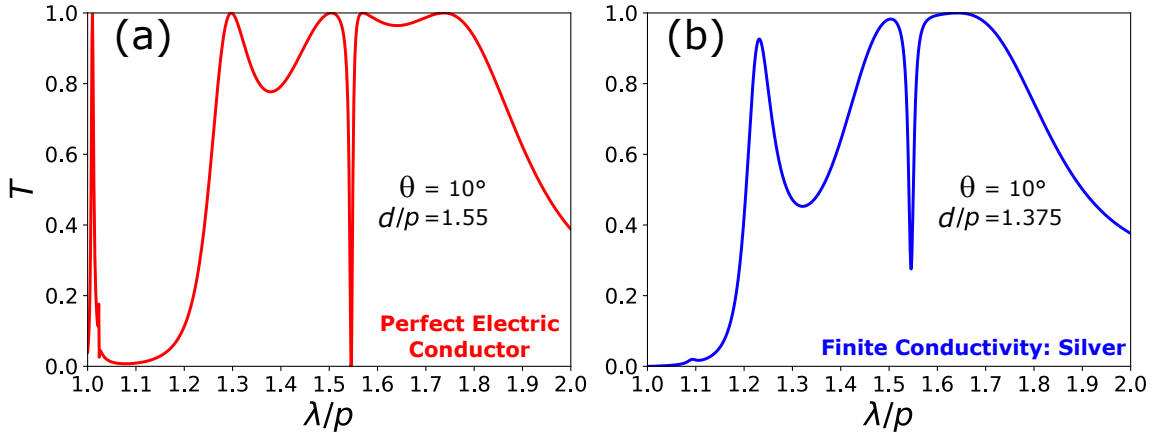

Figure 3.20: **(a)** EJF computed transmission spectrum for $\theta = 10°$ and $d/p = 1.55$ **(b)** RCWA computed transmission spectrum for $\theta = 10°$ and $d/p = 1.375$ and for a finite conductivity of silver

A brief summary of the previous section and this present section mainly point out that spectral shift has to be expected for practical fabrication. As expected, taking into account the metal finite conductivity leads to a dip sharpness decrease. For the future, it would be interesting to combine several imperfections to further study the potential degradations of the excited resonant dip. In the next chapter, we give more details on the observed spectral shift and on the transmission dip degradation.

3.8/ CONCLUSION AND DISCUSSION

In summary, we have given an analytical formalism of an extended Malus' Law with metallic polarizers for the terahertz regime. Our theoretical investigation highlights the important discrepancies with the classical Malus' Law. This is due to the θ dependency of the modulation factor as well as the multiple reflections inside the PAC which are tunable via the optical path L. Indeed, for specific values of L one can obtain broad angle or narrow angle Malus' Law. Then, we designed a structure with high sensitivity and high quality factor for characterizing the EO response of terahertz an EO material based on an extremely narrow angle Malus' Law. This analytical model of a two-layer stack of subwavelength structures provide new theoretical insights into the interactions between polarizing metamaterials. This simple structure can be seen as the basic component for multi-layered and more complex structures. In future works, we will use our analytical model as a platform to propose other applications such as high efficiency polarization

conversion, high-Q filtering, and ultra-sensitive polarimetry. It is important to note that we have given only an analytical explanation of the appearance of the transmission dip. We have not however give a complete description of its physical origin. We have studied the multiple reflection process which is - without any doubt - a key element to the transmission dips, but we have not given a precise physical model that fully explains this phenomenon.

As a final remark for this conclusion, Fig. 3.21 shows transmission spectra for different locations of the dip and for $\theta = 15°$. For Fig. 3.21**(a)** and **(b)**, the dips are located at the resonance of the single metamaterials, either at $\lambda/p = 1.434$ or at $\lambda/p = 1.69$. In this configuration, we observe that the dip has a inverted Lorentzian shape. The reader can also refer to Fig. 3.12**(a)** to have better view on this Lorentzian dip. In Fig. 3.21**(c)** and **(d)**, the dips are not located at metamaterials resonances. In this case, we can clearly notice an important variation in the shape of dip. Indeed the transmission dip are directly preceded or followed by a sharp maximum. In other word, the dip gets a highly asymmetrical shape. It is striking to see that transmission maxima can even appear in region of the spectrum where the transmission is "supposedly" low. For example, in Fig. 3.21**(d)**, a sharp transmission maxima appears in a low-transmission part of the spectrum

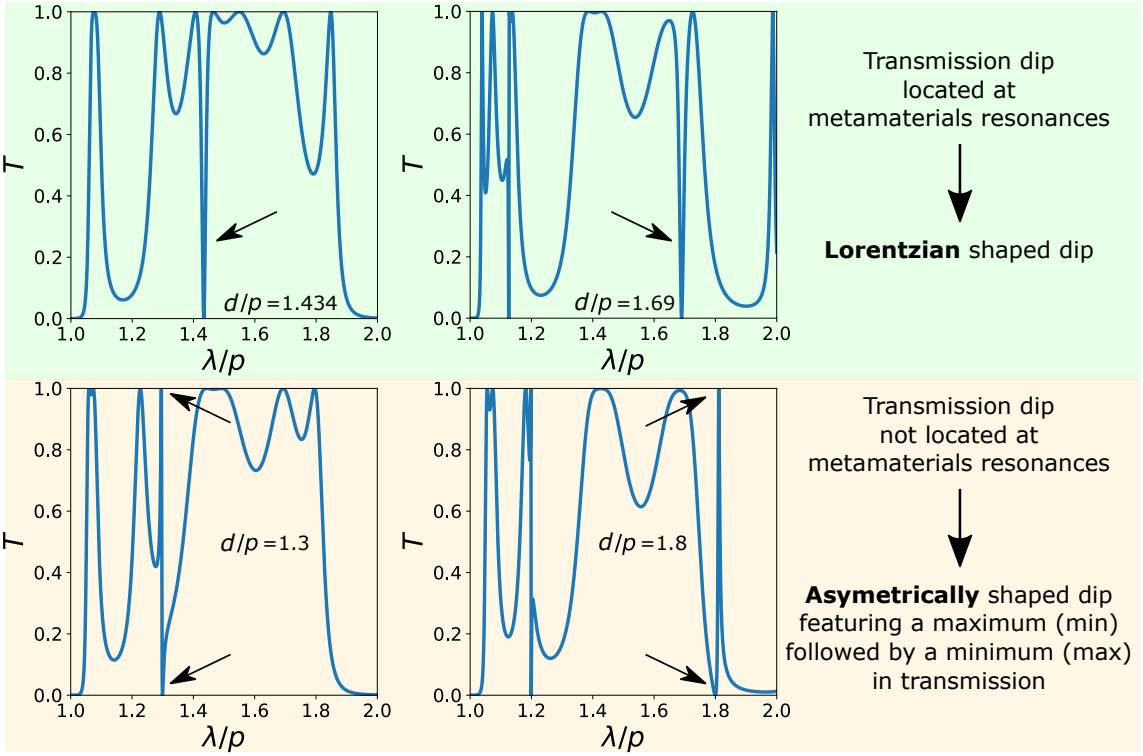

Figure 3.21: Transmssion spectra for $\theta = 15°$ and for **(a)** $d/p = 1.434$, **(b)** $d/p = 1.69$ **(c)** $d/p = 1.3$, **(d)** $d/p = 1.8$. The spectrum **(a)** and **(b)** in the green area feature symmetrical Lorentzian transmission dip while the yellow area spectrum **(c)** and **(d)** exhibit asymmetrically shaped transmission dip that are typically Fano resonance signature.

where $T < 10\%$.

This kind of sharp and asymmetric resonances belongs to the family of Fano resonances. In classical electromagnetism, Fano resonances usually arises from the coupling of a discrete state with a continuum-like state. This important insight leads us to the next chapter in which we study in detail the physical interpretation and the nature of this phenomenon. For this, we need to reconsider our point of view on the structure. Instead of considering a pile of two metallic metamaterials and focusing mainly on its transmission properties, we should now definitely adopt the point of view of a Fabry-Perot resonator which features very specific polarization properties.

4

FANO RESONANCES IN STACKED METALLIC METAMATERIALS

As the results of the previous chapter suggest, the multiple reflections between the metallic polarizers play an important role in the structure's transmission response. In some particular configuration, it even seems to lead to a special kind of resonances: the Fano resonances. If we want to deeply understand this phenomenon however, we should clarify and study in more details the multiple reflections process. Indeed, this "multiple reflections" terminology is rather vague and does not give a satisfactory answer to the excitation of Fano resonance in stacked metallic metamaterials. The goal of this chapter is to provide a simple physical model to understand Fano resonance in stacked structures and to demonstrate the potential of such structures to efficiently excite and control Fano resonances.

First, this chapter introduces the Fano resonances in electromagnetism and gives its basic underlying mechanism. It is then followed by a state of the art on Fano resonances in metamaterials and photonic structures. Second, we reconsider the polarizer-analyzer structure studied in the previous chapter as a polarized Fabry-Perot resonator. Precisely, we want to extract the resonance and polarization properties of the structure. Fortunately, we already have the required tool - the EJF - to take into account the polarization properties of this special Fabry-Perot cavity. It gives us the opportunity to develop a simple analytical model of a polarized Fabry-Perot cavity. Third, we identify the key elements that are involved in the occurrence of Fano resonances in the Fabry-Perot cavity. Besides, we specify that the Fano resonance excited in our structure follows all the basic rules of Fano resonance encountered in classical physics.

Most importantly, we emphasize that the excitation of Fano resonances in stacked metallic metamaterials has not been theoretically or experimentally reported. As we will demonstrate in this chapter, the original way (based on polarization) for exciting Fano reso-

nances in stacked structures leads to interesting possibilities. Indeed, we observe that the stacking of metallic metamaterials offers new degrees of freedom in the realization of Fano line shape. We finally conclude this chapter by mentioning that these additional and unique properties could open up new perspectives in nano-photonics and we discuss some of them.

4.1/ INTRODUCTION TO FANO RESONANCES

In 1935, Hans Beutler reported an experimental study on the absorption spectra of noble gases [117]. He observed that the absorption spectrum of Xenon featured a series of narrow absorption maxima superimposed with much wider absorption maxima. The same year, Ugo Fano gave a qualitative approach to explain this intriguing absorption lines [118, 119]. Further, in 1961, Fano gave a more complete theoretical treatment of this phenomenon and it subsequently gained in popularity [120]. Since then, this phenomenon is now known as Fano resonances. Although Fano resonances originates from atom and quantum physics, it has later spread to other domain of physics.

The principle of Fano resonances is summarized in Fig. 4.1. A continuum-like is coupled to a discrete state and leads to the excitation of a Fano resonance. We should precise what we mean when we mention continuum and discrete state. On one hand, the ”continuum” term encompasses any modes that is strongly coupled to the free-space - i.e with large radiation loss. This term is also known as ”radiant mode”, ”direct pathway” or ”bright mode”. On the other hand, the ”discrete state” encompasses any resonances that is weakly coupled to free-space - i.e. with very low radiation loss and therefore high quality factor. It is also referred as ”subradiant mode”, ”indirect pathway”, ”dark mode” or ”trapped mode”. The coupling between the ”continuum” and the ”discrete state” can be achieved in many ways but it is not the aim of this chapter to give an exhaustive summary of all the possibilities.

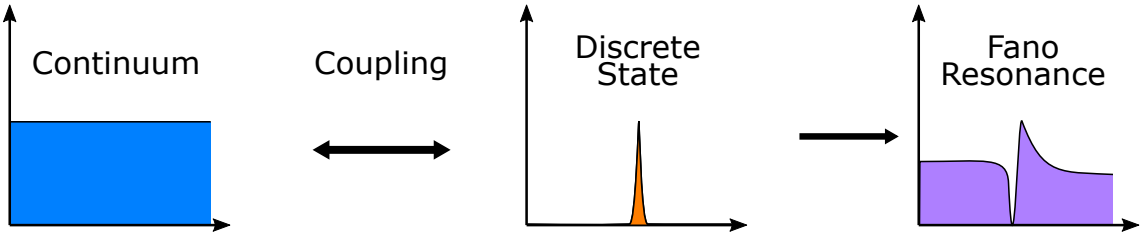

Figure 4.1: Excitation principle of a Fano resonance in electromagnetism where a continuum-like state is coupled to a discrete state.

In the early 2000’s, Shanhui Fan and co-authors made pioneering works on Fano reso-

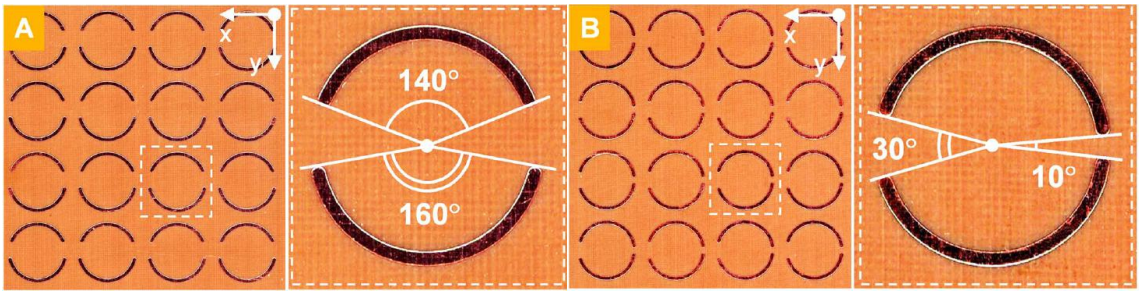

Figure 4.2: **(a)** Image of the split ring resonators with an asymmetry along the x-axis (structure A) and **(b)** along the y-axis (structure B). Images taken from [127].

nances in optics using photonic crystals [121–123]. Some other early realizations of Fano resonances were reported in 2D sonic crystal [124] or in a prism coupled to a micropillar [125]. Another paper reported Fano resonance in the framework of EOT in subwavelength diffraction gratings [126]. Few years later, the observation of Fano resonances in optical metamaterials were first reported by Fedotov *et al.* [127]. The Fano resonance phenomenon is also referred to as Electromagnetically Induced Transparency [128–133] - or EIT - but it involves the same underlying mechanisms and it is simply a matter of vocabulary [134].

The principle used in [127] for coupling the trapped mode with the continuum involves a symmetry-breaking of the metamaterial unit cell depicted in Fig. 4.2, which was inspired from [135]. They considered asymmetrically split ring resonators in two different configurations, A and B. In A, the symmetry is broken along the x-axis and in B the symmetry is broken along the y-axis.

In Fig. 4.3, the solid lines and filled circles respectively correspond to the measured and simulated response while the open circle give the response of symmetrically split ring. By breaking the ring's symmetry, it allows the coupling of the symmetric current modes - "trapped" modes - with the anti-symmetric current mode. As we can remark, the structures A and B give rise to the excitation of a symmetric current mode (II) through the coupling with an anti-symmetric current mode (I). Furthermore, the authors emphasize on the importance of the degree of asymmetry (given by the relative difference of the arc's length). They especially demonstrate that - for lossless materials - the quality factor of the sharp Fano resonance increase when the degree of asymmetry decreases. Note that for symmetrically split ring resonators, the symmetric current modes cannot be excited.

Over the past ten years, this kind of metamaterials patterned with a symmetry-breaking unit cell has been extensively used to observe and study Fano resonances. For example, asymmetrically arranged pairs of split ring resonator has been considered to precisely study the coupling between the bright and dark modes [136]. Another paper reported a

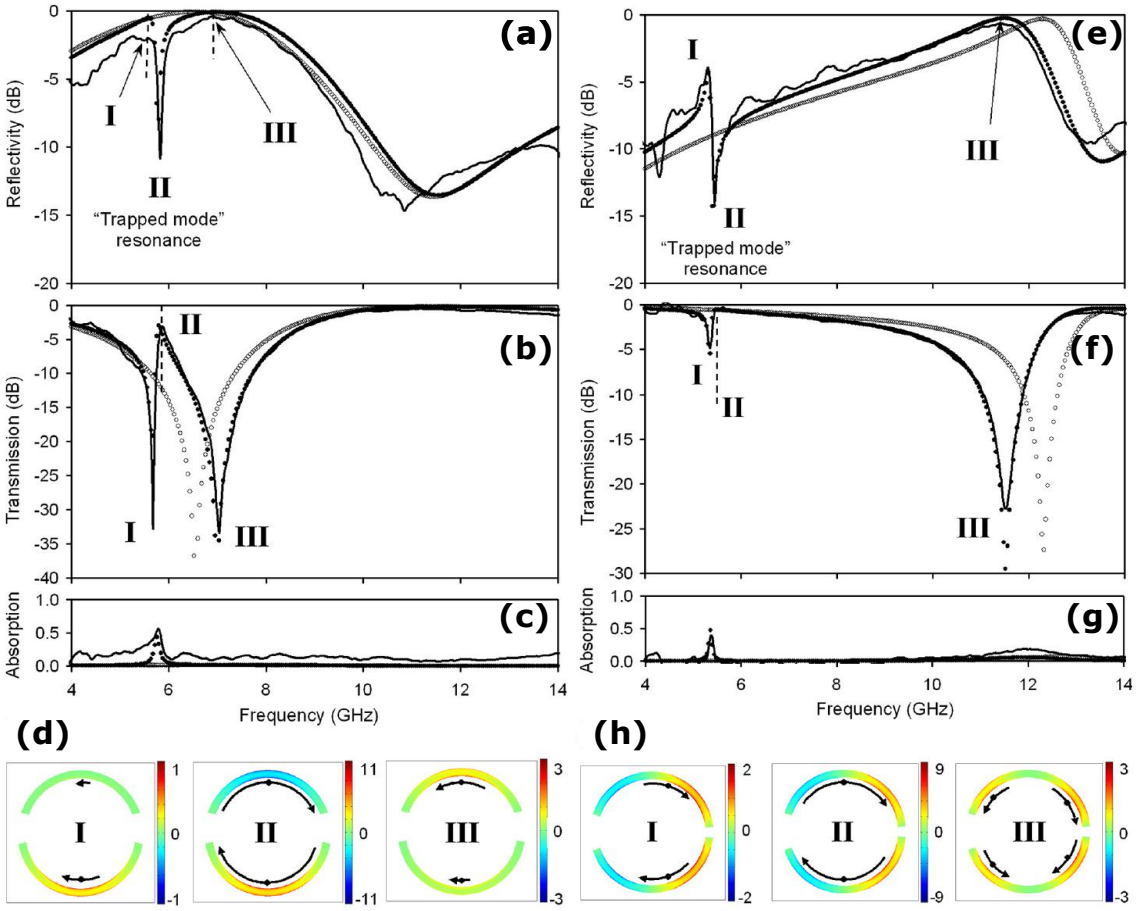

Figure 4.3: **(a)**,**(b)** and **(c)** Reflectivity, transmission and absorption spectra for the structure A with an incident light polarized along the x-axis. **(d)** Corresponding current distribution for the modes I, II and III. **(e)**,**(f)** and **(g)** Reflectivity, transmission and absorption spectra for the structure B with an incident light polarized along the y-axis. **(h)** Corresponding current distribution for the modes I, II and III. Results taken from [127].

metamaterial unit cell composed of three cut-wire arranged in an H-shape [137]. They especially highlight the EIT effect with the vertical displacement of the middle cut-wire, which therefore provokes the symmetry breaking. In 2009, Ranjan Singh *et al.* have demonstrated EIT using single split ring resonator with a pair of asymmetrically positioned gap [138]. Such structure has later been used for designing an ultrasensitive device for the THz domain [115]. The near-field coupling of dark and bright modes has also been engineered to realize Fano resonances and EIT effect [139]. In 2016, Li *et al.* have reported Fano resonances in the THz domain using symmetry-breaking of more complex unit cell [140]. More recently, asymmetrically split ring resonators either made of superconductor or made of metal have been compared in the context of Fano resonance [141].

For completeness, we also mention some other possibilities to realize Fano resonances.

Fano resonances can be achieved in plasmonic structure [142–146], or in multilayered nanoshells [147–149] or in concentric [150] and nonconcentric rings [151, 152]. It is also possible to realize Fano resonances by coupling a resonator - playing the role of the dark mode - with a waveguide [121, 153–155]. We finally mention that metamaterials supporting phase resonances [156–159] can also be used to excite Fano resonances [160, 161].

It is interesting to note that all the structure mentioned above consist of single metamaterials or single structures. They are especially designed to support both dark and bright modes as well as the coupling between them leading to Fano resonances. As we will see in the next sections, stacking metallic metamaterials featuring specific polarization properties offers another mechanism for coupling bright and dark modes. This unlocks new degrees of freedom to excite Fano resonances and it will allows us - in the last part of this chapter - to design structure with multiple and independently (or simultaneously) tunable Fano resonances.

4.2/ Polarization Induced Fano Resonance in a Polarized Fabry-Perot Resonator

In this section, we present a Fabry-Perot model extended to metamaterials with specific polarization properties. Furthermore, this model is combined to a circulating field approach - as used in lasers [162] - in order to precisely describe the Fano resonance phenomenon occurring in the structure.

4.2.1/ Polarized Fabry-Perot resonator model

In this section, we revisit the Fabry-Perot resonator. Instead of using the classical Fresnel coefficients, we use the metamaterials' Jones matrices to derive an extended Fabry-Perot model that takes into account the polarization properties of the cavity. Such attempt using matrices has already been done in the past for studying anisotropic Fabry-Perot resonators [163, 164] or chiral Fabry-Perot interferometers [165, 166]. None of these studies, however, considered mirrors with polarization dependency, they rather considered a classical Fabry-Perot cavity filled with anisotropic or optically active media. The linear-polarization dependency of the metallic metamaterials is the key difference that leads to Fano resonances excitation.

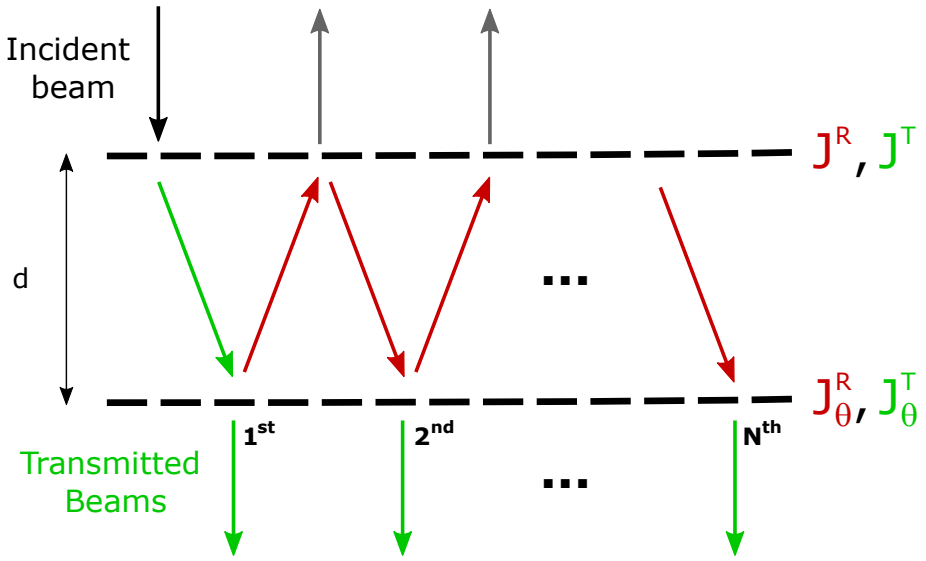

Figure 4.4: Principle of the polarized Fabry-Perot model using the extended Jones formalism. The classical Fresnel coefficients are replaced by Jones matrices to take into account the polarization properties at each interface. The first metamaterial - aligned along the x-axis - is described by its transmission and reflection Jones matrices J^T and J^R. The second metamaterials is arbitrarily rotated by an angle θ and is described by J^T_θ and J^R_θ. The homogeneous, isotropic and linear propagation from the first to second metamaterial, in the cavity, is given by the matrix U

Let us consider metallic metamaterials such as the ones we have already studied in the previous chapter. We want to describe the multiple reflections process using the Fabry-Perot resonator model. To take into account the polarization properties in transmission and reflection, we respectively consider the transmission and reflection Jones matrices derived in the first chapter. This implies to respect the same hypothesis than in the second chapter, i.e a normally incident light, only one guided mode in the subwavelength apertures and a separation distance $d > \lambda/2$. Figure 4.4 shows the basic principle of a light falling in normal incidence on the polarized Fabry-Perot resonator and undergoing the multiple reflection process. The arrows in the middle medium are deliberately inclined in order to show the multi-passes of light induced by the reflections.

The matrices J^T and J^R correspond to the transmission and reflection Jones matrices of the first metamaterials polarized along the x-axis. The matrices J^T_θ and J^R_θ are the transmission and reflection Jones matrices of the second metamaterial (identical to the first) rotated by an angle θ from the x-axis. The two metallic plates are separated by air and by a distance d. The propagation operator from the first to the second wave plate is given by $u = e^{ikd}$. The matrix that links the electric fields from the first to the second wave plate inside the cavity is $U = uI$ where I is the (2×2) identity matrix. As for the classical Fabry-Perot derivation, we sum all the transmitted beams after the second metamaterials.

For N cavity round trips, we have

$$\begin{aligned} J_{FP}^T &= J_\theta^T U J^T + J_\theta^T \left(U J^R U J_\theta^R\right) U J^T + J_\theta^T \left(U J^R U J_\theta^R\right)\left(U J^R U J_\theta^R\right) U J^T + \cdots + J_\theta^T \left(U J^R U J_\theta^R\right)^N U J^T \\ J_{FP}^T &= J_\theta^T \left[I + \left(U J^R U J_\theta^R\right) + \cdots + \left(U J^R U J_\theta^R\right)^N\right] U J^T \end{aligned} \tag{4.1}$$

where the first term $J_\theta^T U J^T$ corresponds to a single pass propagation in the structure and the other terms $J_\theta^T \left(U J^R U J_\theta^R\right)^K U J^T$ (with $K \in [1, N]$) is the propagation after a number K of cavity roundtrip. Furthermore, for any wavelength λ or angle θ, we have $det(J^R) \leq 1$, $det(J_\theta^R) \leq 1$ and $det(U) \leq 1$. Therefore, for an infinite number of cavity round trips, the series converge and we finally obtain

$$J_{FP}^T = J_\theta^T \left(I - U J^R U J_\theta^R\right)^{-1} U J^T \tag{4.2}$$

Equation 4.2 is rigorously the same as Eq. 3.10 in the second chapter derived from the S-matrix algorithm [108]. In fact, the set of recursion formulas - eqs. (15a) in [108] - forming the S-matrix algorithm can be seen as a generalized formulation of the Fabry-Perot resonator using scattering matrices.

Even though the polarized Fabry-Perot model is confirmed by the extended Jones formalism combined with the S-matrix algorithm, it does not give additional insights into the Fano resonance in the cavity. Nonetheless, in the next section we give a simple, analytical and physical model, based on a polarized Fabry-Perot cavity and a circulating field approach, that gives us more insights into the Fano resonances phenomenon in the stacked structure.

4.2.2/ CIRCULATING FIELD APPROACH

To further understand the polarization effects in the cavity, we combine the Jones formalism to a circulating field approach [162, 167]. In this way, we are able to analytically describe the resonance and polarization properties of the cavity, as well as the coupling effects that leads to the Fano resonance. As we will demonstrate, the coupling in the cavity occurs because of the specific polarization properties of the metamaterials. Thus, we introduce a new terminology: the polarization-induced Fano resonance. Furthermore, we will demonstrate that polarization-induced Fano resonances can be controlled independently or simultaneously by modifying the arrangement of the stacked structure.

To begin with, we consider metallic plates with reflection (and transmission) coefficients

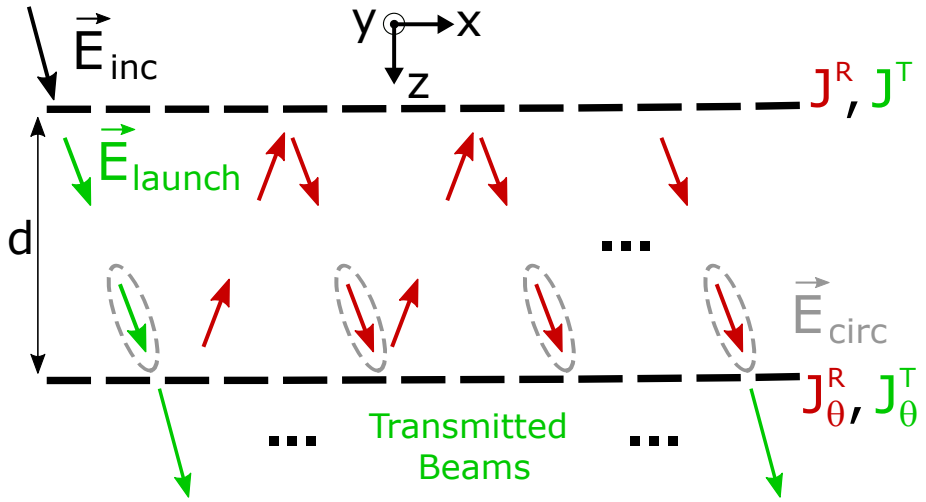

Figure 4.5: Principle of the circulating field approach where the FP resonator is made of two polarization dependent metallic plates characterized by the Jones matrices J^T,J^R and J^T_θ, J^R_θ. $\vec{E}_{launch} = J^T \vec{E}_{inc}$ is the initial electric field entering the cavity, and $\vec{E}_{circ}$ is the steady state forward circulating field.

that depend on the polarization. More precisely, this study highlights the importance of the metallic plates polarization dependency for exciting Fano resonances. We consider an electromagnetic plane wave propagating along the z-axis and falling in normal incidence on a FP cavity formed by two metallic plates. The first metallic plate serves as a reference with its main axes aligned on the x and y axes. The transmission and reflection Jones matrices which link the incident electric field $\vec{E}_{inc}$ to the transmitted or reflected electric field are given by

$$J^T = \begin{pmatrix} t_x & 0 \\ 0 & t_y \end{pmatrix} \text{ and } J^R = \begin{pmatrix} r_x & 0 \\ 0 & r_y \end{pmatrix}. \tag{4.3}$$

where t_x, t_y and r_x, r_y are respectively the transmission and reflection arbitrary coefficients along the x and y axes. The second metallic plate is described by $J^T_\theta = R(\theta)J^T R(-\theta)$ and $J^R_\theta = R(\theta)J^R R(-\theta)$. To accurately describe the resonance and polarization properties of the polarized FP cavity, we associate the Jones formalism to a circulating field approach [167], as illustrated in Fig. 4.5. The electric field $\vec{E}_{launch}$ is the initial electric field launched in the cavity, after passage through the first metallic plate. The expression of $\vec{E}_{launch}$ is given by

$$\vec{E}_{launch} = J^T \vec{E}_{inc} \tag{4.4}$$

The relation between the forward circulating electric field, $\vec{E}_{circ}$, and the electric field entering the polarized FP cavity, $\vec{E}_{launch}$, is given by

$$\vec{E}_{circ} = J_{rt} U \vec{E}_{launch} \tag{4.5}$$

where

$$J_{rt} = \left[I - U^2 J^R J_\theta^R\right]^{-1} \tag{4.6}$$

is the Jones matrix that accounts for the infinite round-trips in the polarized Fabry-Perot cavity. The expression $U^2 J^R J_\theta^R$ is the equivalent of the complex gain for a single round-trip in the cavity [162]. For more details, a scalar approach (excluding polarization properties) on the circulating field has been thoroughly investigated in [167]. For completeness, we give the transmission Jones matrix of the polarized FP cavity $J_{FP}^T = J_\theta^T J_{rt} U J^T$. More importantly, the analytical expression of the matrix J_{rt} is given by

$$J_{rt} = \frac{1}{D}\begin{pmatrix} 1 - u^2 r_y(s^2 r_x + c^2 r_y) & u^2 cs(r_x - r_y)r_x \\ u^2 cs(r_x - r_y)r_y & 1 - u^2 r_x(c^2 r_x + s^2 r_y) \end{pmatrix} = \begin{pmatrix} J_{rt}^{xx} & J_{rt}^{xy} \\ J_{rt}^{yx} & J_{rt}^{yy} \end{pmatrix} \tag{4.7}$$

where $D = det(I - U^2 J^R J_\theta^R)$, $c = cos\theta$ and $s = sin\theta$. For this complex general case, it is fundamental to note that the coupling terms J_{rt}^{yx} and J_{rt}^{xy} tends to zero when $r_x = r_y$ - as it is the case with unstructured simple mirrors. In other words, the anisotropic polarization properties of the metallic plates ($r_x \neq r_y$) brings additional polarization coupling effects - leading to Fano resonances - that are not achievable in classical FP cavities.

From now on, we choose constitutive metamaterials with a particular geometry known as wire-grid. As we will demonstrate in the next section, such basic geometry will prove very useful to excite and independently tune multiple Fano resonances over a broadband transparency window. The wire-grid geometry is similar to the mono-periodic metamaterials we have studied in Chapter 1 except that the metamaterials thickness $h/p << 1$. Such geometry has been known for decades to act as broadband linear polarizers with high transmission and high extinction ratio for the near-infrared domain [168]. Quite recently, wire-grid polarizers have also been reported for the THz range [169].

From a monomodal method combined with an extended Jones formalism [65], as described in chapter 1, we extract the corresponding transmission and reflection Jones matrices with $t_y = 0$, $r_y = -1$, and where $t_x = \alpha_T$ and $r_x = \alpha_R - 1$.

Figure 4.6 gives the wire-grid transmission spectra for two distinct geometries. In Fig. 4.6 **(a)**, we have the transmission spectrum for $a/p = 0.5$ and $h/p = 1.0$. We notice two transmission peaks at the extreme left side. They correspond to the first and second Fabry-Perot harmonic located in the lamellar apertures. This resonant phenomenon (leading to EOT) has already been discussed in chapter 2 in Sec. 2.3.4. We have not discussed however the transmission that asymptotically tends to $T = 1$ when $\lambda/p \to \infty$. This phenomenon is due to the cut-off wavelength of the TEM guided mode λ_{TEM} which tends to infinity. For the higher wavelength, the wire-grid structure act as an ultra-broadband

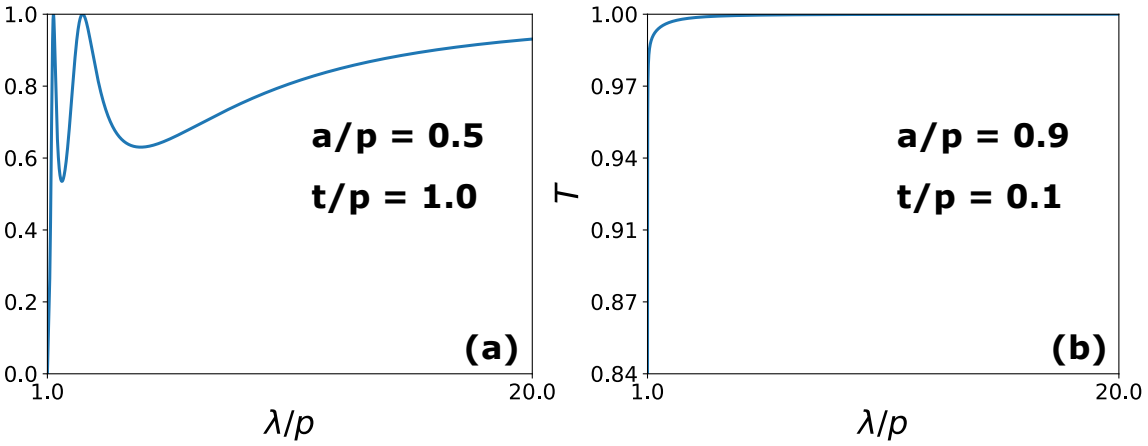

Figure 4.6: **(a)** Transmission spectrum for a monoperiodic metamaterial polarizer for $a/p = 0.5$ and $h/p = 1.0$. **(b)** Transmission spectrum for a wire-grid metasurface for $a/p = 0.9$ and $h/p = 0.1$.

polarizer with a quasi-perfect transmission ($T > 0.99$). For the second geometry, we fix $a/p = 0.9$ in order to increase the radiation loss on the x-axis, and we fix $h/p = 0.1$ in order to shift the FP resonances and the cut-off resonance toward smaller wavelength. The corresponding spectrum is given in Fig. 4.6**(b)**. As we can observe, the first FP harmonic has been shifted before the TEM Floquet mode cut-off wavelength and only the high transmission asymptote remain after this cut-off wavelength. With this particular wire-grid design, the transmission is close to 1 for any wavelength $\lambda > p$. For the rest of this study, we keep the second geometry for all metamaterials that compose the stacked structure. Nonetheless, we should keep in mind that the cut-off wavelength of the second mode TM_1, $\lambda_{\mathrm{TM}_1}/p = 2a = 1.8$. The spectral region located before $\lambda/p = 2a = 1.8$ is therefore not properly described by the EJF since a second guided mode should be taken into account for the simulation. It is however not an issue since the application we propose is demonstrated for larger wavelength where the transmission is increasingly closer to $100\ \%$.

Let us now study the structure where we consider two stacked wire-grid metasurfaces, as depicted in Fig. 4.7**(a)**. We study the spectral range where $\lambda/p \geq 2$ so that we have $h \leq \lambda/20$, and that only the fundamental transverse electromagnetic guided mode, polarized along the x-axis, is excited in the wire-grid metasurfaces. As it is expected for wire-grid polarizers, the launched electric field $\vec{E}_{launch}$ is linearly polarized along the x axis. Along the y-axis, the incident light is perfectly reflected, as indicated by the term $r_y = -1$. As we will now demonstrate, such specific polarization properties leads to polarization induced Fano resonances.

First, we assume a special case where the two wire-grids are at resonance with $\alpha_T = 1$

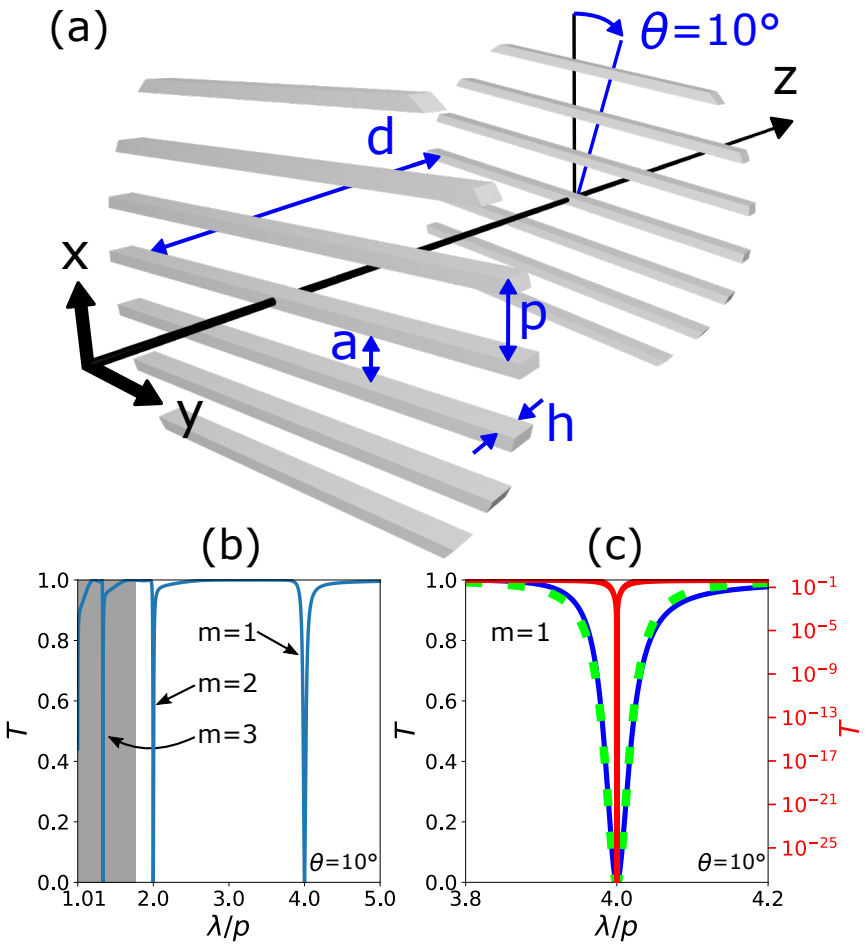

Figure 4.7: **(a)** Illustrations of two wire-grid metasurfaces stacked along the z-axis where the second metasurface is rotated by $\theta = 10°$. **(b)** Transmission spectrum for $a/p = 0.9$, $h/p = 0.1$ and $d/p = 2.0$. The integer m denotes several FP harmonics where the Fano resonances occurs. The greyed area specifies the spectral region ($\lambda/p \leq 1.8$) for which the monomodal method is not valid. **(c)** Transmission spectrum for the first FP harmonic $m = 1$. The asymmetric Fano resonance are given in linear and logarithmic scale, respectively by the blue and red curve respectively. The green curve corresponds to the inverted Lorentzian line shape, as given by Eq. (4.9).

and $\alpha_R - 1 = 0$. Though it is not totally realistic, such configuration is interesting for two reasons. First, it clearly let appear analytically the Fano resonance mechanism in the polarized FP cavity. Second, as we will show later, this kind of configuration is well adapted for exciting and tuning multiple Fano resonances over a broadband transparency window. For this case, the forward circulating electric field in the cavity is given by

$$\vec{E}_{circ} = \begin{pmatrix} 1 & 0 \\ -\dfrac{u^2 cs}{1-u^2c^2} & \dfrac{1}{1-u^2c^2} \end{pmatrix} U\vec{E}_{launch}. \tag{4.8}$$

To clearly understand the polarization-induced Fano resonance mechanism, it is now

essential to distinguish two cases:

1) For $\theta = 0°$, the cross-coupling terms are $J_{rt}^{yx} = J_{rt}^{xy} = 0$. In addition, we have $J_{rt}^{yy} = 1/(1-u^2)$ which corresponds to the Airy distribution of the electric field in a perfect y-polarized FP resonator (FP_y). Furthermore, we obtain $J_{FP}^{T} = J^T U J^T$ which simply corresponds to a single pass propagation through the structure. To summarize, the x-polarized launched electric field does not couple to the FP_y resonator and simply propagates through the structure. Therefore, the FP_y resonator is not excited or, in other word, it is "trapped" in the structure.

2) For $\theta \neq 0°$, the coupling of the x-polarized launched electric field $\vec{E}_{launch}$ with the FP_y resonator occurs via the term J_{rt}^{yx}. As we will numerically show, such coupling leads to a Fano resonance at the FP resonance condition $\lambda = 2d/m$ with $m \in \mathbb{N}$. We remind that this coupling is induced by the specific polarization properties of the wire-grids ($r_x \neq r_y$), as previously shown in Eq. (4.7). One might regard the single pass x-polarized propagation and the "trapped" FP_y resonator as an analogue of bright and dark modes, that interfere to excite Fano resonances [136].

Finally, the transmission through the structure is given by

$$T = |J_{FP}^{T,xx}|^2 + |J_{FP}^{T,yx}|^2 = \left| \frac{(1-u^2)}{1-u^2\cos^2\theta} \right|^2 u^2 \cos^2\theta \tag{4.9}$$

which is similar to the transmission expression studied in chapter 2 (see Eq. (3.14) and Eq. (3.15)) and in [95] using biperiodic metamaterials. For the FP resonance condition $\lambda = 2d/m$, we have $u = 1$ and therefore $T = 0,\ \forall\ \theta \neq 0 \pmod{\pi}$ which correspond to the Fano resonance dip. We note that for this case ($t_x = 1$), the expression of T at the FP resonance condition gives an inverted Lorentzian line shape, as predicted in Eq. (17) of ref. [123]. It is interesting to remark that the polarization-induced Fano resonance can be seen as the combination of two well known strategies for exciting Fano resonance. It associates the side-coupled cavity-waveguide concept [121] and the symmetry-breaking concept [127]. Indeed, the FP_y resonator plays the role of the side-coupled cavities while the coupling is achieved by symmetry-breaking (i.e. $\theta \neq 0 \pmod{\pi}$).

Second, we now numerically study wire-grids with realistic values for t_x (i.e. α_T) and r_x (i.e. $\alpha_R - 1$) that are extracted from the EJF [65]. In addition, the transmission Jones matrix J_{FP}^{T} is now numerically obtained by applying the S-matrix algorithm. We emphasize that, for the considered spectral region $\lambda/p > 2.0$, the wire-grids transmission along the x-axis is almost at resonance, i.e. $t_x \approx 1$ and $r_x \approx 0$. Figure 4.7**(b)** shows the transmission spectrum for two wire-grid metasurfaces separated by a distance $d/p = 2.0$ for $\theta = 10°$.

The rotation of the second metasurface provokes the excitation of polarization induced Fano resonance that are located at the FP resonance condition $\lambda = 2d/m$. The region $\lambda/p \leq 1.8$ in grey area corresponds to the region where the monomodal method is not valid and, therefore, the MMM accuracy for $\lambda/p \leq 1.8$ is not guaranteed. We choose to focus on the polarization induced Fano resonance located at the first FP harmonic $\lambda = 2d = 4.0p$ $(m = 1)$, as shown in Fig. 4.7**(c)**. For such wavelength, the thickness of the entire structure is $t_{tot} = 0.55\lambda$. Even though the structure is compact along the propagation axis (z-axis), we should mention that the dimension in the (x-y) transverse plane are directly related to the number of period (x-axis) and the invariance length (along the y-axis). To realize efficiently Fano resonances, a sufficient number of period and a large invariance length have to be considered. Thus, the dimension along the x and y axes are much higher than the wavelength. The blue curve shows the polarization induced Fano asymmetric dip. The dashed green curve shows the transmission response for the special case $t_x = 1$ showing the symmetric Lorentzian dip, as given in Eq. (4.9). The red curve shows the asymmetric Fano dip in log-scale which confirms precisely the location of the dip at $\lambda/p = 2d = 4.0$.

So far, we have considered the coupling of bright and dark mode when the wavelength matches the metamaterials resonance, but the same reasoning can be applied for any wavelength. Indeed, the transmission and reflection Jones matrices are

$$J^T = \begin{pmatrix} \alpha_T & 0 \\ 0 & 0 \end{pmatrix} \text{ and } J^R = \begin{pmatrix} \alpha_R - 1 & 0 \\ 0 & -1 \end{pmatrix}. \tag{4.10}$$

for metamaterials aligned along the x-axis. As we can observe the coupling terms are still zero if there is no rotation. The Fabry-Perot resonator along the y-axis is still ”trapped”. We notice however the difference in the term $J^{R,x,x} = \alpha_R - 1 \neq 0$ which leads to the excitation of Fabry-Perot resonance polarized along the x-axis even if the plates are aligned (see the FP_{PAC} branches in Fig. 3.7 in chapter 3). For λ close to the metamaterials resonance, it leads to a weak Fabry-Perot modulations.

As we have highlighted in Fig. 3.21 in the conclusion of the previous chapter, we can notice the asymmetric shape of the Fano resonance when the y-polarized FP resonance does not match the metamaterials aperture resonance. In refs. [170, 171], it is shown that the asymmetry factor q is proportional to $\omega_d^2 - \omega_b^2$, where the frequencies of the bright and dark modes are denoted by ω_b and ω_d. Another explanation was given by Shanhui Fan *et al.* in 2003 [123], the authors advanced that

> ”A symmetric Lorentzian line shape is reproduced only when either r or t is zero. In all other cases, the system exhibits a Fano asymmetric line shape.”

Our observations also match such a description for the Fano lineshape. Indeed, at the metamaterials resonances, the reflection coefficient falls to zero and we observe an inverted Lorentzian line shape, as shown in Fig. 3.12**(a)**. For any other wavelength, we obtain an asymmetric Fano line shape.

In this section, we have analytically and physically identified the bright and dark mode in our structures. It has been realized with the use of a polarized Fabry-Perot model in combination with the extended Jones formalism and a circulating field approach. In the next section, we demonstrate that the polarization induced Fano resonance effect can be extended for an arbitrary number N of stacked wire-grid metasurfaces. Indeed, for N wire-grid metasurfaces aligned along the x-axis, the stacked structure hosts $(N-1)$ FP_y trapped resonances that are distributed along the structure and located between the metasurfaces. The main interest in considering larger stacked structure is that each Fano resonances can be excited and tuned independently or simultaneously. Indeed, the trapped FP_y resonances are not coupled to each other, they couple only to the propagating x-polarized electric field by rotation induced symmetry-breaking.

4.2.3/ INTENSITY MAP

In this subsection, we confirm the trapped "Fabry-Perot" resonance polarized along the y-axis by plotting 2D maps of the electric field intensity for the biperiodic structure studied

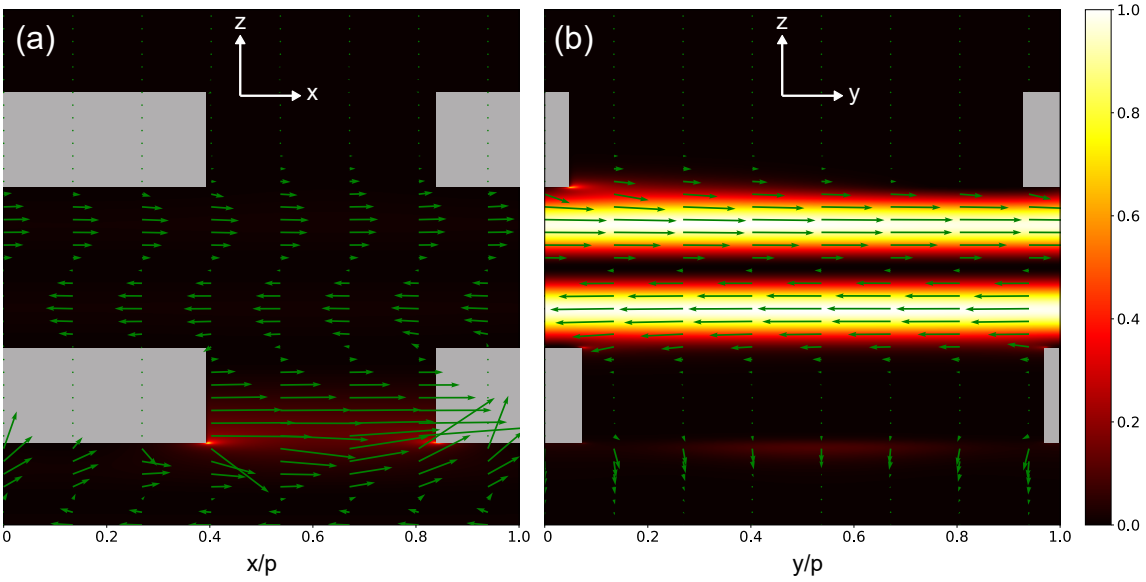

Figure 4.8: Intensity maps of the electric field computed by FDTD for the biperiodic structure of chapter 3 (polarizer-analyzer configuration). The electric field intensity is defined as **(a)** $I = |E_x|^2 + |E_z|^2$ and **(b)** $I = |E_y|^2 + |E_z|^2$ and the green arrows indicate the orientation of the electric field. The grey parts show the metamaterial.

in the chapter 3. The parameters are $a_x/p = 0.45$, $a_y/p = 0.9$, $d/p = 1.69$, $h/p = 1.0$ and the rotation of the rectangular apertures of the second metamaterials is $\varphi = 10°$. These maps are computed at $\lambda/p = 1.69$. Note that the z-axis is not at the right scale compared to the x and y axes. We choose to plot the map for the x-z and y-z cut as shown in Fig. 4.8**(a)** and **(b)** respectively. For Fig. 4.8**(a)**, the normalized intensity is given by $I = |E_x|^2 + |E_z|^2$ and for Fig. 4.8**(b)**, it is $I = |E_y|^2 + |E_z|^2$ where E_x, E_y and E_z are the components of the electric field computed by FDTD. The green arrows denote the orientation of the electric field in the x-z and y-z planes respectively. In Fig. 4.8**(a)**, we can see the destructive interference phenomenon as the electric field intensity in the cavity is almost zero. Note that we also observe the excitation of the fundamental TE_{01} guided mode inside the aperture of the first metamaterial. In the second metamaterial however, the TE_{01} mode is not excited because of the destructive interference leading to a total reflection before the first metamaterial. In Fig. 4.8**(b)**, we clearly see the "trapped" Fabry-Perot resonance polarized along the y-axis. First, we can deduce the FP harmonic number $m = 2$ as we can see two maxima. Second, the FP resonance does not couple to the metamaterials as it is cross-polarized to the fundamental TE_{01} guided mode and is "trapped" along the y-axis. The FP resonance couples only via the x axis and provokes the destructive interference - shown by Fig. 4.8**(a)** - leading to the Fano resonance.

4.3/ MULTIPLE AND INDEPENDENTLY TUNABLE FANO RESONANCES

As we have mentioned in the context section of the Introduction, the stacking of few metamaterials/metasurfaces has gain much interest in the past few years. These stacked structures are currently studied and suggested to overcome limitations faced by single metamaterials. Such structures also potentially carry exotic functionalities due to the additional interaction between each stacked metasurfaces. In the meantime, single metamaterials proved to be excellent candidate to realize Fano resonance. The interesting properties of Fano resonance drive forward the need to better control their excitation. There is currently intensive researches on tunable Fano resonances and on multiple Fano resonances excitation. In 2011, Wu *et al.* have theoretically reported Fano resonance in three-layered nanoshell that can be spectrally tuned by modifying the radii of the different layers [148]. Another study reported a dynamically tunable Fano resonance by modifying the incident beam wavelength on dual graphene nanodisk [172]. More recently, tunable Fano resonances have been theoretically proposed by modifying the opto-geometrical parameters of a stub-pair waveguide [173]. In the meantime, multiple Fano resonance

are also extensively studied. Multiple Fano resonances has been reported in a metallic metamaterial composed of an asymmetric dual-stripe unit cell [174] or made of asymmetric dual nano-bar [175]. Comb-like scattering using multiple Fano resonances has been achieved using a multilayered plamonic shell [149]. Similarly, several Fano resonance have been reported in a non-concentric core nano-shell [152]. In the terahertz, multiple Fano resonance are excited in a metallic asymmetric super cell metamaterial made of rod and U shape segments [176]. The excitation of several Fano resonances has also been theoretically reported for a surface plasmon polariton waveguide which is side-coupled with many cavities [177, 178]. Nishida *et al.* have reported multiple Fano resonance in a metallic nanoholes array via the excitation of a *multipole* surface plasmon [179]. A metasurface made of coupled T-shaped gold resonator has been shown to exhibit multiple Fano resonances as well [180]. Very recently, a study demonstrated the independent control of multiple Fano resonance in a metallic waveguide with side coupled cross shaped cavities. The precise tunability was achieved by tuning the dimension of the cross shaped cavities [181].

It is important to mention that most of the reported tunable Fano resonance are based on opto-geometrical parameters modification of the structure itself. From an experimental point of view, such real-time modification of the opto-geometrical parameters requires complicated or are simply not possible. In our case, the Fano resonance tunability is obtained by the rotation induced symmetry-breaking, as it shown in Fig. 4.7**(a)**. In addition the Fano spectral position is proportional to the optical distance between the two metamaterials. In other words, the tunability is not achieved by any unit-cell modification but rather by playing with the relative arrangement between the metallic metamaterials.

Figure 4.9 shows a summarized time lines for the Fano resonance in photonics and for the area of metamaterials. Since a decade, metamaterials have been extensively used for the excitation of Fano resonances, while stacked metamaterials/metasurfaces are developed to increase or expand the possibilities offered by metamaterials. We believe that this work is at the crossroads of the ”few layer metamaterials/metasurfaces” topic and the multiple Fano resonances engineering.

As we have mentioned in the Introduction, this PhD thesis takes part in the exploration and the study of the new possibilities offered by stacked metamaterials/metasurface. In this section, we show that larger stacks of metallic wire-grid metasurfaces can exhibit multiple and tunable Fano resonances by extending the principle described in the previous section. We show that such structures allows us to design fully reconfigurable multi-notch filter based on Fano resonances. The precise control of the multiple Fano resonance also enables to mimick EIT transmission spectra. These findings bring additional understand-

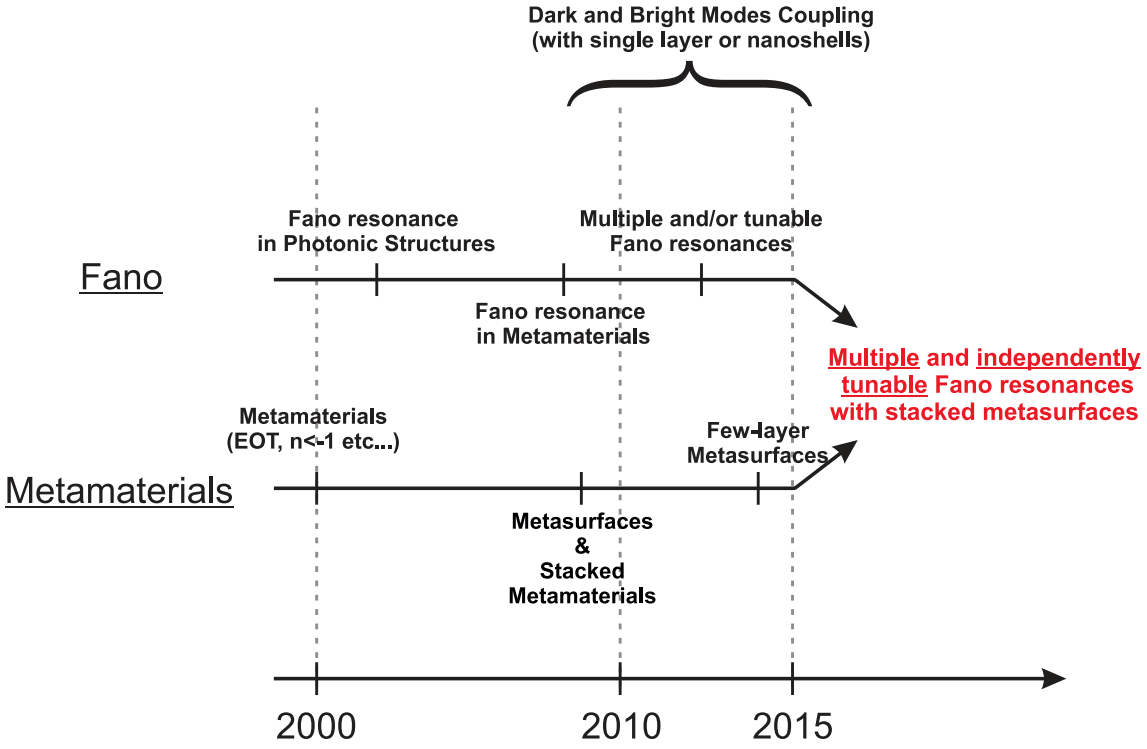

Figure 4.9: Summarized time line of the development of Fano resonances in optics and optical metamaterials.

ings and expand the perspectives of few layer metasurfaces.

First, we introduce the general studied structure and its basic principle for realizing multiple Fano resonances. Then, we choose and present a particular geometry for the constitutive metamaterial which enable Fano-based reconfigurable filtering. Second, we make a numerical study based on a specific structure made of three stacked metamaterials for filtering application. We especially show that precise re-arrangements of the stacked structure allows for tunable filters with various working regime.

4.3.1/ MULTIPLE FANO RESONANCES EXCITATION PRINCIPLE

Figure 4.10 shows the principle for realizing multiple Fano resonance with stacked metamaterials. It is based on the physical interpretation given in Sec. 4.2. If we consider a stack of N polarizing metamaterials aligned on the x-axis, then we can consider a stack of $(N-1)$ FP dark modes distributed along the y-axis and denoted by the double-head red arrows in Fig. 4.10. The green arrows oriented along the x-axis denotes the x-polarized electric field transmitted through the structure and play the role of the bright mode. The rotation of only one of the metamaterials would lead to the coupling of the FP dark modes located in its direct vicinity. It would however not affect the other dark modes. For exam-

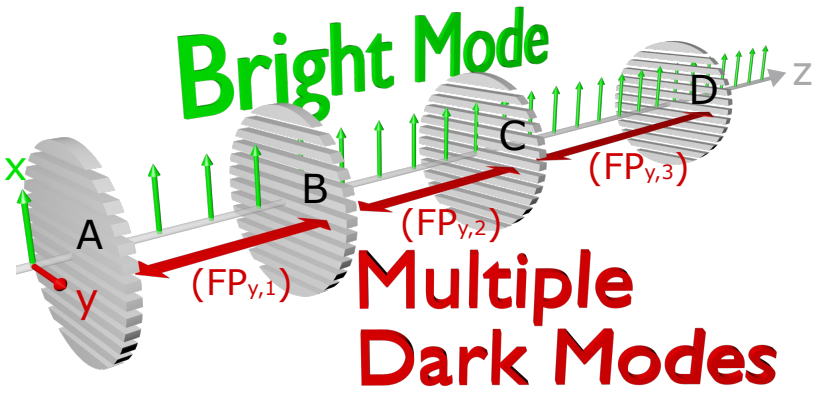

Figure 4.10: 3D-rendered schematic of stacked and aligned wire-grid polarizers. An EOT-based TEM mode polarized along the x axis propagates through the structure, and is referred as the bright mode. The stack provokes on the y axis the appearance of cascaded and perfectly trapped Fabry-Perot resonators, and are referred as the multiple dark modes.

ple, by rotating only the metasurface named D in Fig. 4.10, it authorizes the coupling of the $FP_{y,3}$ dark mode with the propagating bright mode. However, the dark modes $FP_{y,1}$ and $FP_{y,2}$ remain orthogonal and uncoupled to the bright mode. Conversely, rotating the metasurface B would permit the coupling of the dark modes $FP_{y,1}$ and $FP_{y,2}$ with the x-polarized bright mode.

4.3.2/ Application to reconfigurable and versatile filtering

With stacked wire-grid metasurface, we numerically demonstrate that it is possible to tailor one Fano resonance without affecting the other Fano line shape. We show below that it allows for flexible design of tunable dual-notch filter. We also show that a proper configuration of the structure can produce an analogue of EIT by taking advantage of the Fano line shape asymmetry. Then, we will discuss more complex configurations for comb-like filtering or arbitrary spectral shaping. We finally discuss the advantages, limits and challenges for the fabrication of such structures.

4.3.2.1/ Tunable dual-notch filter

For simplicity, we first consider a stack of 3 wire-grid metasurfaces with the geometry given above: $a/p = 0.9$, $h/p = 0.1$ and the distance between the wire-grid metasurfaces are $d_1/p = 2.0$ and $d_2/p = 2.1$. The structure induces the existence of two FP dark modes on the y-axis, as we can intuitively deduce from Fig. 4.10. The orientation of the first,

second and third metasurfaces are given by φ_1, φ_2 and φ_3 respectively.

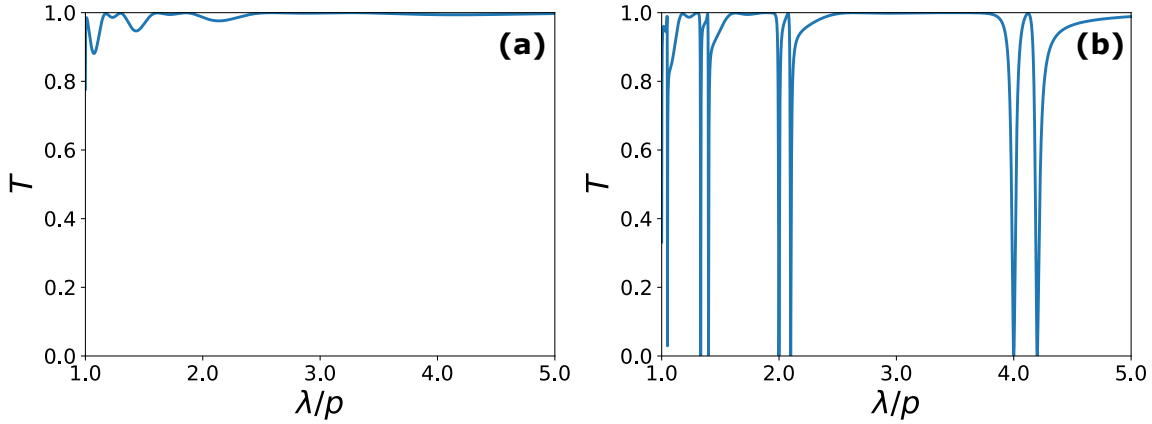

Figure 4.11: **(a)** Transmission spectrum when the three metasurface are aligned. **(b)** Transmission spectrum when the middle metasurface is rotated by 10°. The number m gives the FP harmonic number.

Figure 4.11**(a)** gives the transmission spectrum of the bright mode transmitted though the structure when the wire-grid metasurfaces are aligned. We obtain a transmission spectrum similar to the spectrum of a single plate given in Fig. 4.6**(b)**. In fact, one could expect that the transmission spectrum for two aligned wire-grids would be the squared transmission of one wire-grid, as shown in Fig. 4.6**(b)**. We notice however an additional modulation on the spectrum corresponding to the multiple reflection occurring on the x-axis. Figure 4.11**(b)** gives the transmission spectrum when only the second wire-grid metasurface is rotated by an angle $\varphi_2 = 10°$. It provokes the coupling of the bright mode with the two FP dark modes which were perfectly trapped on the y-axis before the rotation of the second plate. We can now observe the appearance of Fano lineshape pairs that are located at $\lambda = 2d_1/m$ and $\lambda = 2d_2/m$ with $m \in \mathbb{N}^*$.

For clarity, we now focus on the Fano lineshape pair found for $m = 1$. Besides, we only modify the orientation (φ_3) and the position of the third metasurface (which affects d_2) so that it only modifies the properties of the second dark modes. The parameters $d_1/p = 2.0$, $\varphi_1 = 0°$ and $\varphi_2 = 10°$ are therefore kept constant for this study. Figure 4.12**(a)** gives the transmission spectrum of the structures as a function of d_2/p. As we can see, the shift of the second Fano dip does not affect the position of the other dip. Figure 4.12**(b)** gives transmission spectra of the stack for several values of d_2/p. We remark that the bandwidth of the two dips is insensitive to the position of the second Fano resonance.

The transmission spectra as a function of φ_3 is given by Fig. 4.13**(a)** with $d_2/p = 2.1$. By modifying the orientation of the third metasurface, we modify the degree of asymmetry between the second and the third metasurface. First, it results in a increase of the bandwidth of the second dip with the increase of the asymmetry. Second, it does not

modifies the position nor the width of the other Fano dip, as shown in Fig. 4.13**(b)**. In addition, when the third metasurface is aligned with the second, i.e $\varphi_2 = \varphi_3 = 10°$, the corresponding transmission dip disappears without disturbing the remaining dip. The angular orientation of the wire-grid metasurfaces can be used as selective "on-off" Fano switch. The overall results contained in Fig. 4.12 and Fig. 4.13 shows that it is possible to achieve a reconfigurable dual-notch filter where the position and the width of the two dips can be accurately and independently controlled. It shows that it is also possible to switch from a dual-notch filter to a simple notch filter.

4.3.2.2/ TAILORING EIT-LIKE TRANSMISSION

The structure studied above for dual-notch filtering can also exhibit a EIT-like transmission response. It is possible to mimick an EIT transmission response when the two Fano resonance are very close to each other, or in other words, when $d_1/p \approx d_2/p$. Figure 4.14**(a)** gives the transmission spectra as a function of φ_2 with $\varphi_1 = \varphi_3 = 0°$, and with $d_1/p = 2.0$ and $d_2/p = 2.005$. The circled area highlight the configuration where EIT-like transmission is best achieved. Figure 4.14**(b)** gives a corresponding transmission spectra at $\varphi_2 = 2°$, $\varphi_2 = 6°$ and $\varphi_2 = 10°$ respectively with the blue, red and green lines respectively. As we can conclude, it is possible to tailor the bandwidth of the transparency window by changing the angle of rotation of the second wire-grid metasurface. The transparency windows can be attributed to the Fano resonance's maxima. In a similar way used in the previous section, the third wire-grid metasurface can be used as a switch to turn "off" the transparency window when being aligned to the second wire-grid metasurface.

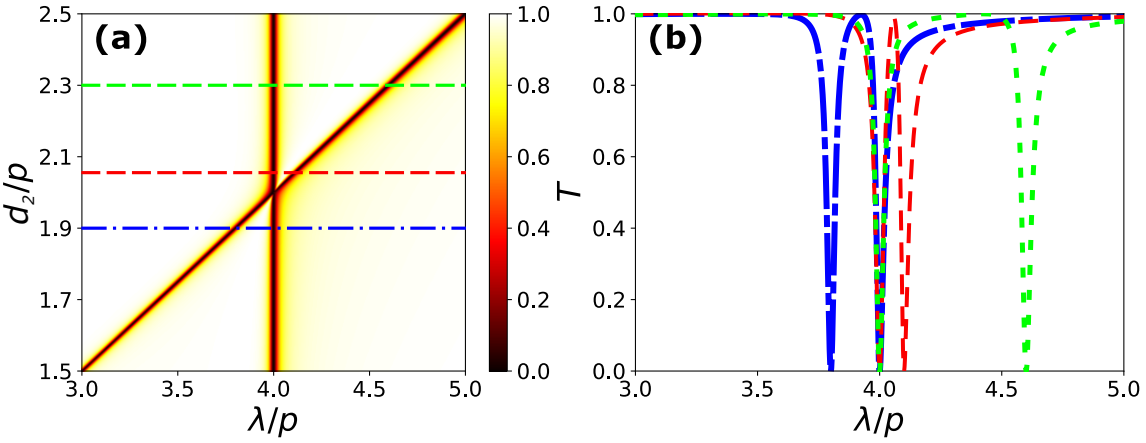

Figure 4.12: **(a)** Transmission spectra as a function of d_2/p the separation distance between the second and the third metasurface. The colored dashed lines gives the corresponding transmisssion spectra indicated in Fig. 4.12**(b)**. **(b)** Transmission spectra in blue, red and green curve respectively for $d_2/p = 1.9$, 2.1, and 2.3.

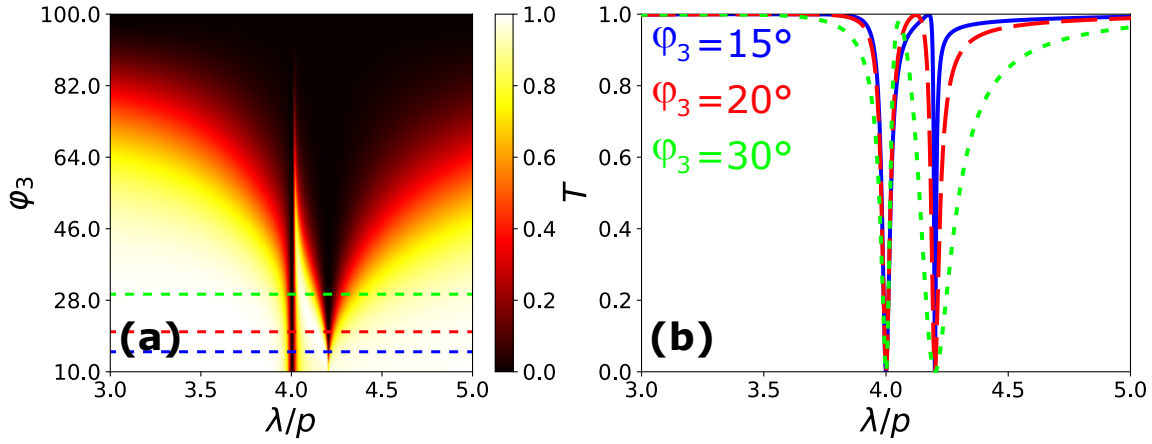

Figure 4.13: **(a)** Evolution of the transmission spectrum with the third metasurface rotation angle φ_3. **(b)** Transmission response in blue, red and green curve respectively corresponding to $\varphi_3 = 15°$, $20°$ and $30°$.

However, the obtained EIT-like transmission occurs on a very limited zero-transmission spectral band. In order to increase this spectral band, we propose to slightly change the previous design. We now set $d_2/p = 2.05$ and Fig. 4.15**(a)** gives the corresponding transmission evolution as a function of φ_2. Again, an EIT-like behavior is reproduced but on a larger zero-transmission spectral band. This is clearer in Fig. 4.15**(b)** where the transmission spectrum is plotted for $\varphi_2 = 10°$, $= 20°$ and $30°$, respectively in blue, red and green.

In the next section, we would like to briefly discuss more complex structures to demonstrate other filtering possibilities. To demonstrate the stacked structure potential, we briefly suggest two other application. In the next section we propose an inverted comb-like multi-notch filter. Then, we show in Sec. 4.3.2.4 some arbitrary spectral shaping

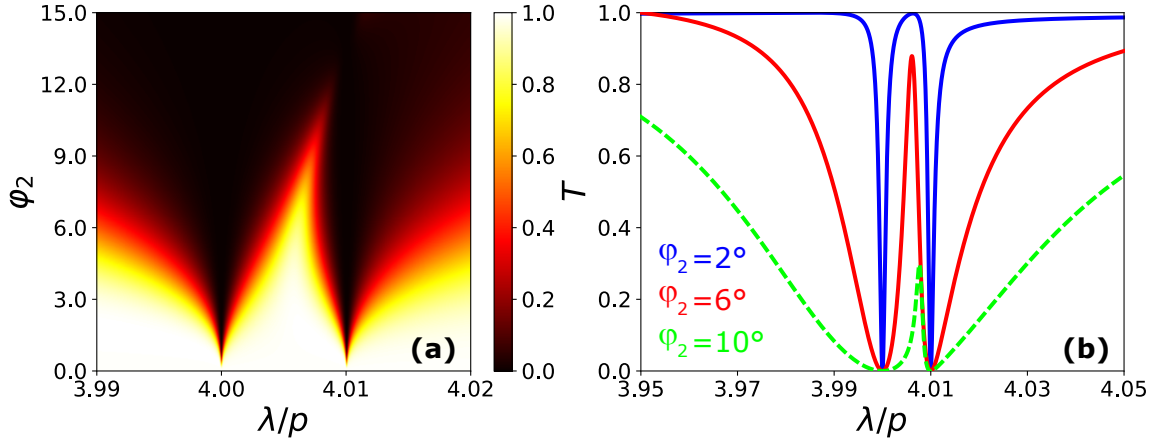

Figure 4.14: **(a)** Evolution of the transmission response with the orientation of the middle metasurface given by φ_2. **(b)** Transmission spectra in blue, red and green corresponding to $\varphi_2 = 2°$, $6°$ and $10°$ respectively.

capabilities.

4.3.2.3/ COMBLIKE MULTI-NOTCH FILTERING

We would like to briefly discuss a more complex structure that exhibits a comblike multi-notch transmission. We consider a stack made of 5 wire-grid metasurface that are progressively rotated by a constant angle $\Delta\varphi = 5°$, as depicted in Fig. 4.16**(a)**. The distances between each metasurface are linearly increased so that $d_1/p = 2.0$, $d_2/p = 2.05$, $d_3/p = 2.1$ and $d_4/p = 2.15$. The solid blue curve in Fig. 4.16**(b)** gives the corresponding transmission spectrum that shows the regularly spaced Fano dip respectively located at the resonance wavelengths of each FP dark modes. The dashed red curve shows the transmission spectrum with a progressive rotation angle $\Delta\varphi = 10°$. Increasing the degree of asymmetry between each metasurface amounts to increase the bandwidth of each dip

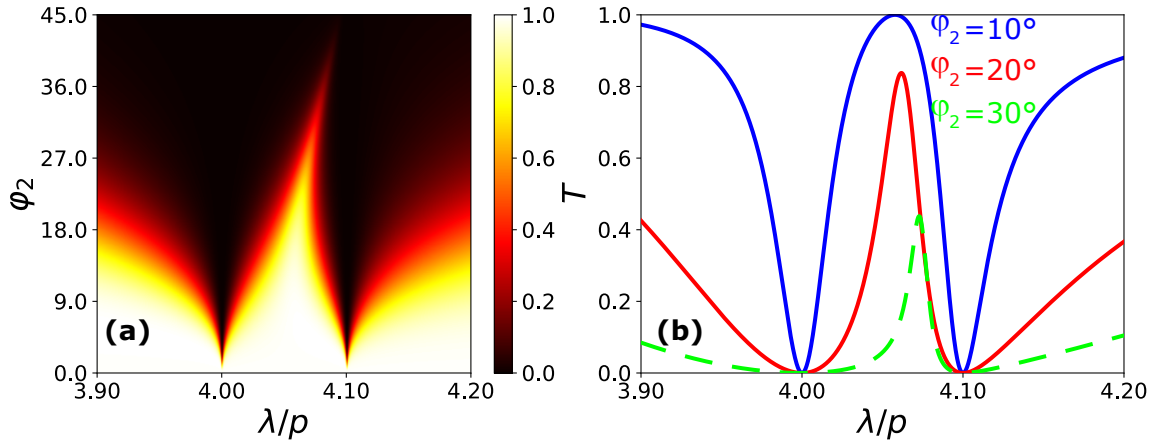

Figure 4.15: **(a)** Transmission spectrum variation as a function of φ_2. **(b)** Transmission spectra in blue, red and green corresponding to $\varphi_2 = 10°$, $20°$ and $30°$ respectively.

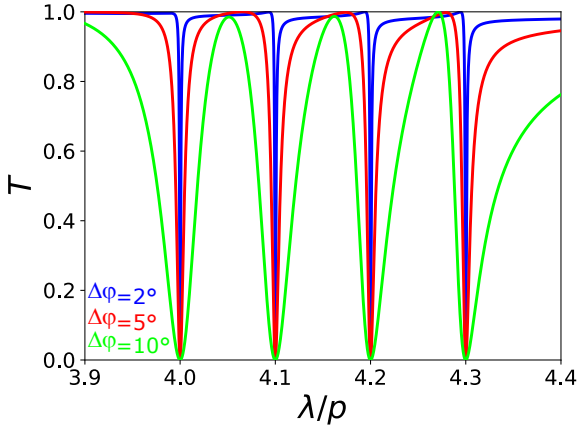

Figure 4.16: Inverted comb-like transmission spectrum for regular angle variations $\Delta\varphi = 2°$, $5°$ and $10°$ respectively depicted in blue, red and green curve.

and allows for the spectral shaping of the comblike multi-notch filter. We should however discuss the practical issues that arises from such structures in the next section.

4.3.2.4/ ARBITRARY SPECTRAL SHAPING

So far, we have demonstrated the potential of our structure for tunable and/or reconfigurable filter with Fano resonances. We have especially seen that it is possible to independently tune each Fano resonances. For large metasurface stacks, the possibilities becomes nearly infinite as we increase the complexity and the number of tunable parameters. Figure 4.17 illustrate the potential of a 4 metamaterial polarizer structure to arbitrarily shape the transmission spectrum. Fig. 4.17**(a)** shows the transmission spectrum for the following initial parameters $\varphi_1 = \varphi_3 = 0°$, $\varphi_2 = \varphi_4 = 45°$, $d_1/p = 1.75$, $d_2/p = 2.0$ and $d_3/p = 2.2$. Such configuration lead to a dual transmission peaks roughly located at $\lambda/p = 3.7$ and $\lambda/p = 4.25$. Then, by simply rotating the third metamaterial by angle $\varphi_3 = 40°$, the transmission spectrum is drastically changed, as depicted in Fig. 4.17**(b)**.

Such a drastic change in the spectrum may seem surprising. One has to keep in mind that, by rotating the third metamaterial polarizer, we modify the coupling with two dark modes simultaneously. Precisely, we change the coupling with the dark mode located between the second and third metamaterial, and the coupling between the third and fourth metamaterial. Then, tuning a single parameter can lead to dramatic change in the spectrum because of this simultaneous tuning of two Fano resonances.

An interesting perspective for the arbitrary spectral shaping could consists in developing an algorithm that could determine the optimized structure to achieve on-demand any

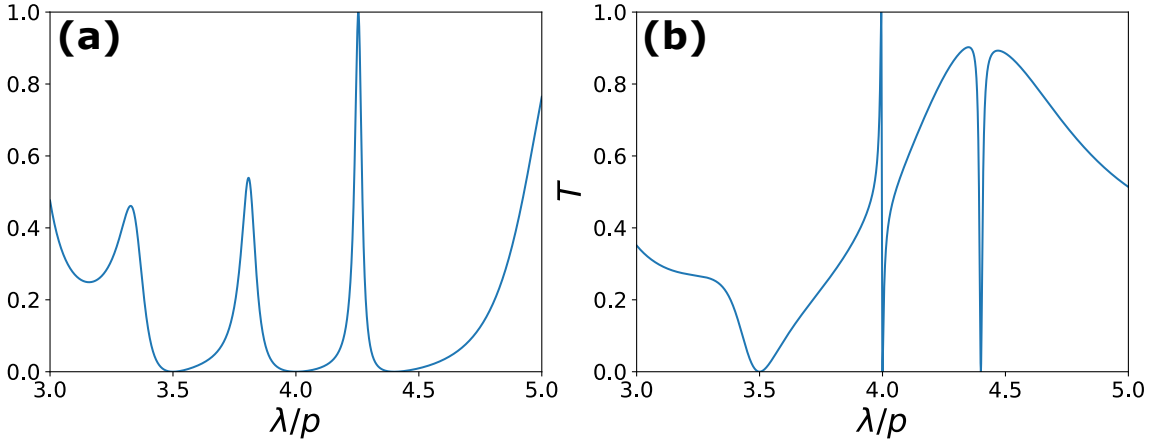

Figure 4.17: **a** Transmission spectrum for the following initial parameters: $\varphi_1 = \varphi_3 = 0°$, $\varphi_2 = \varphi_4 = 45°$, $d_1/p = 1.75$, $d_2/p = 2.0$ and $d_3/p = 2.2$. **(b)** Transmission spectrum for same parameters except $\varphi_3 = 40°$.

specific transmission spectra.

In these last subsections, we have seen that stacks of metallic wire-grid metasurfaces can be used for several applications based on polarization-induced Fano resonances. In the next section, we take advantage of our simple analytical model to further analyse the effect of the cavity round trip number N on the polarization induced Fano resonance.

4.4/ INFLUENCE OF THE NUMBER OF CAVITY ROUND TRIP

In this section, we go further by taking advantage from our efficient and analytical Jones formalism to study the influence of a limited number of cavity roundtrip: $N \neq \infty$. This configuration could be useful to model some imperfections. For example, such configuration constitutes a rough approximation for absorption in the cavity that limits the multiple reflections. A limited roundtrip number could also account for multiples reflections that could "bounce out" of a finite cavity. Such "bounce out" could be due to a incident beam slightly tilted from the normal. Instead of using the expression of transmission Jones matrix J_{FP}^{T} given by Eq. 4.2 or by Eq. 4.5, we can simply use the finite sum given by Eq. 4.1. This allows us to study the relationship between the cavity round trip number N with the dark and bright mode coupling. For this study, we consider the biperiodic structure studied in the previous chapter with $a_x/p = 0.45$, $a_y/p = 0.9$ and $h/p = 1.0$ and $d/p = 1.69$. We prefer to study the biperiodic structure since the spectral content is richer than for the wire-grid geometry. Indeed the biperiodic structure contains many resonance peaks and it is interesting to analyse the influence of a limited roundtrip number on the different resonances.

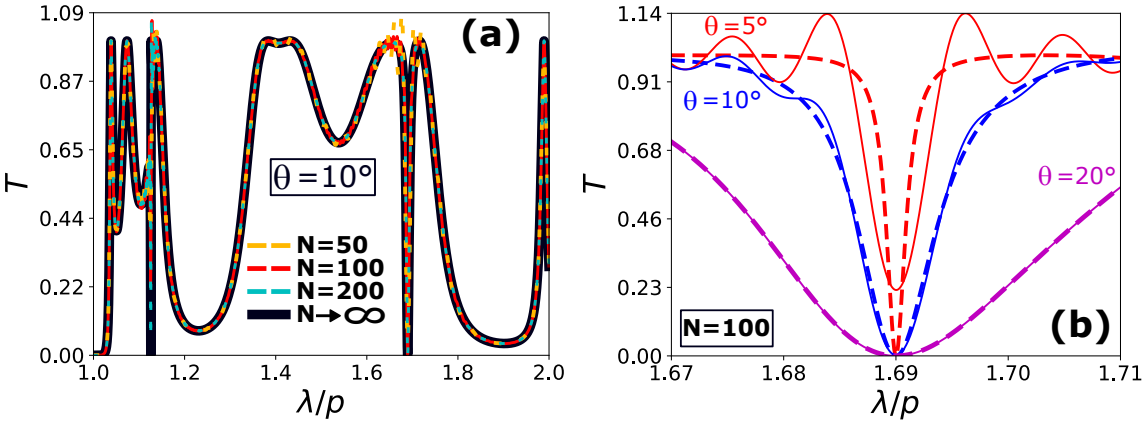

Figure 4.18: **(a)** Transmission spectra for different values of cavity round trip number N at $\theta = 10°$. **(b)** Transmission spectra for different rotation angle θ and for a fixed cavity round trip number $N = 100$ in solid lines and for $N \to \infty$ in dashed lines

Figure 4.18 **(a)** shows the influence of a finite number of cavity round trip on the transmission response. The transmission derived from the S-matrix algorithm - which corresponds to $N \to \infty$ - is given by the thick solid black line. The yellow, red and cyan dashed line respectively correspond to $N = 50$, $N = 100$ and $N = 200$ round trip in the cavity. First we can remark that N does not have a significant influence on the spectrum except at the Fano resonance wavelength. For example, at $\lambda/p = 1.69$, the transmission spectra for $N = 50$ or $N = 100$ does not exactly follows the black curve. Figure 4.18 **(b)** shows the influence of the angle θ on the transmission spectra for a fixed number $N = 100$. The solid lines corresponds to spectra obtained for $N = 100$ and the dashed lines are the extended Jones formalism counterparts. For $\theta = 20°$, the reconstructed spectrum for $N = 100$ is in perfect agreement with the EJF-simulated spectrum. For $\theta = 10°$ however, the truncation to $N = 100$ is insufficient to reconstruct the exact spectrum. We can even remark some undulations in the spectrum that reminds, for example, truncated Fourier series in signal processing. The degradation is even more important for $\theta = 5°$ where it leads to a very poor recovery of the transmitted signal.

These observations however, make perfect sense when considering θ as the coupling coefficient between the bright mode (x-polarized transmitted electric field) and the dark mode (FP_y resonator). For large values of θ, the coupling is strong and fewer cavity round trips are necessary to efficiently realize the Fano resonance. For smaller value of θ, the coupling decreases as well. Therefore, a larger number of cavity round trip are needed to efficiently couple the dark mode with the bright mode. It also explains the sharpness degradation in Fig. 3.20 when the absorption of the metal is taken into account. A rather small coupling between the dark and the bright mode ($\theta = 10°$) necessitates a large number N of cavity round trips. At each round trip, however, the Fabry-Perot dark mode is progressively absorbed in the metal and therefore limits the coupling with the bright mode.

We have studied the dark and bright mode coupling as a function of N for a Fano excitation at the resonance metamaterials. However, we should also study the coupling for an asymmetric Fano lineshape. Indeed, in Fig. 4.18 we have considered an inverted Lorentzian resonance which is a particular case of the Fano resonance linshape. It seems interesting to consider an opposite case where the lineshape asymmetry is strong. For example, we now consider $d/p = 1.8$. Figure4.19 shows recovered transmission spectra (solid lines) with $N = 100$ compared with the perfect case (dashed lines) for several values of θ. We can observe the same tendency as in Fig. 4.18. For $\theta = 5°$, the reconstructed spectrum is totally inaccurate. For $\theta = 10°$, the transmission minimum is well reproduced but the transmission maximum is much lower in amplitude and the wavelength peak is

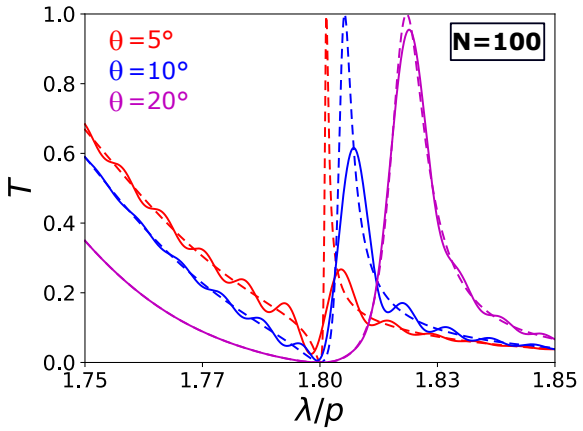

Figure 4.19: Transmission spectra for different values of θ. The solid lines correspond to transmission spectra simulated with an infinite number of cavity round trip. The dashed lines represents the same spectra for 100 cavity round trips.

slightly shifted towards larger wavelengths. For $\theta = 20°$, the transmission minimum is perfectly recovered but the transmission maximum is still slightly shifted towards higher wavelengths. Compared to the symmetric Lorentzian line shape, the coupling for an asymmetric line shape seems to be more critical. It is nonetheless interesting to note that for an asymmetric Fano resonance, the angle θ allows for a wavelength tunability of the transmission peak. This could be used to design narrowband and tunable transmission filters.

From a more general point of view, these results confirm the resonating nature - linked to the multiple reflections in the cavity - of the observed Fano resonances. Furthermore, the round trip cavity number greatly influences the Fano line shape "quality" – as it is the case for the classical Fabry-Perot resonator. In the next section, we discuss some advantages in terms of fabrication tolerances.

4.5/ FABRICATION TOLERANCES

The studied metamaterials involve rather simple geometries to fabricate, such as rectangular aperture or lamellar apertures. In addition, we have shown in this chapter that the Fano resonance excitation directly originates from the metamaterials polarization properties. We would like to briefly study the fabrication imperfection influence on the Fano excitation. For that, we consider a reference bi-periodic metamaterials where $a_x/p = 0.45$, $a_y/p = 0.9$ and $h/p = 1.0$. We consider the second metamaterial to have fabrication error and its parameters are denoted by a'_x/p, a'_y/p and t'/p. We define Δ as the relative fabrication error with the reference geometry so that $\Delta = \dfrac{a_x - a'_x}{a_x} = \dfrac{a_y - a'_y}{a_y} = \dfrac{t - t'}{t}$. The period

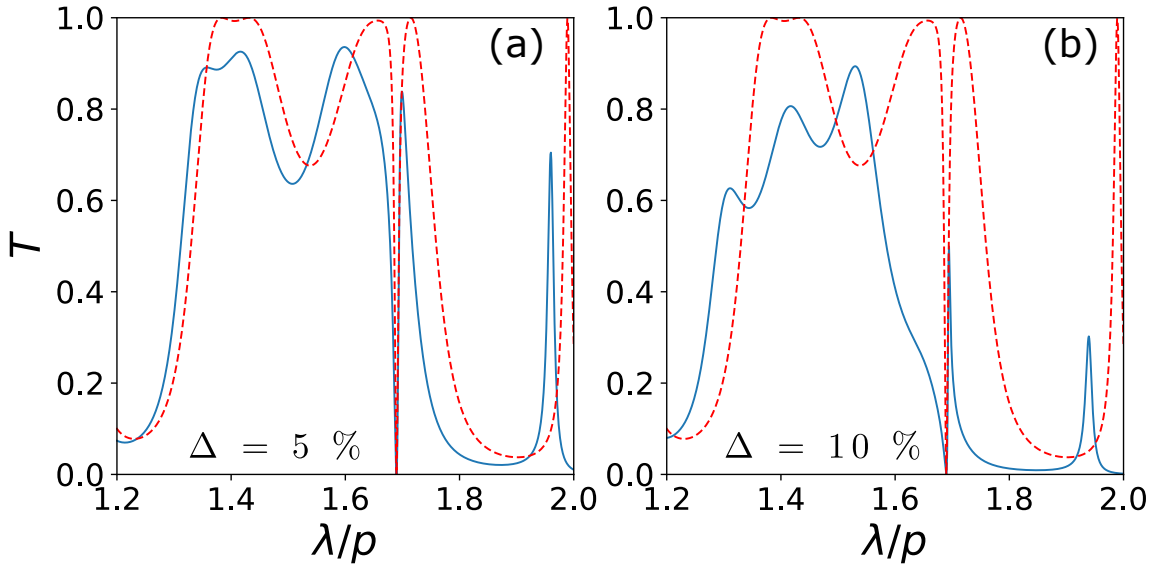

Figure 4.20: Simulated transmission spectra when a fabrication error Δ between the two metamaterial polarizers is taken into account. **(a)** Transmission spectrum for $\Delta = 5\%$. **(b)** Transmission spectrum for $\Delta = 10\%$. Both transmission spectra are compared with a reference of $\Delta = 0\%$ in dashed red line.

p is the same for both metamaterials.

Figure 4.20 shows the EJF-simulated transmission spectrum for **(a)** $\Delta = 5$ % and **(b)** $\Delta = 10\%$. For $\Delta = 5\%$, the overall transmission decreases due to a mismatch between the non-identical TE_{01} guided modes. However the Fano resonance, located at $\lambda/p = 1.69$, is still well exploitable though we can see a slight asymmetry on the Fano lineshape. For $\Delta = 10\%$, we can clearly observe an important discrepancy with the perfect case ($\Delta = 0\%$). First, the Fano resonance has a strongly asymmetric line shape. By inducing such large fabrication error, we substantially modify the spectral resonance of the second metamaterial. Hence, the dark mode resonance is superimposed to one metamaterial resonance only and it therefore leads to an asymmetric shape. Second, the Fano resonance visibility is drastically reduced but the sharp line can still be exploited for sensing application for example. On one hand, fabrication error as high as 10% in combination with absorption losses would lead to very low Fano-like excitations. On the other hand, a Δ of 10 % is very high and a configuration with $\Delta \approx 5\%$ seems objectively closer to reality. By changing the geometry of the second metamaterials aperture, it modifies the terms $J_\theta^{T,x,x}$ and $J_\theta^{R,x,x}$ only. In other words, we influence the bright mode propagation through the structure but the dark mode is not directly affected.

In this section, we have used the Jones formalism to develop a simple Fabry-Perot model for two polarizing metamaterials. We have then analytically and physically demonstrated the presence of the bright and dark modes in the cavity. When the structure presents a

mirror symmetry, the dark and bright modes are orthogonally polarized and therefore uncoupled. The coupling occurs when breaking the mirror symmetry by applying a rotation angle θ.

In the next section, we have expanded the concept of polarization-induced Fano resonances to a larger number of stacked metallic metamaterials. We especially emphasize that the additional degrees of liberty offered by the stacked structure allows for reconfigurable and versatile filtering devices.

4.6/ DISCUSSION

Although our study relies on structure with simple geometry, the different possibilities that have been shown always involve the manipulation of a freestanding wire-grid metasurfaces. Such reconfigurable structures in the visible domain would require a precise nano-positioning for each metasurfaces and could lead to complex setup. However, the results can be scaled for larger wavelengths and are probably more suitable for designs in the terahertz or microwave range. For these spectral regions, the wire-grid metasurfaces dimensions reach the millimeter scale and can be handled more easily. Furthermore, our model assumes perfect electric conductor materials, and metals in the terahertz or microwave region are good candidates to approximate this ideal case.

4.7/ SUMMARY

In this chapter, we have developed and used an analytical Fano-like model to physically interpret the sharp transmission dip observed in the second chapter. First, we have developed a simple Jones model to analytically demonstrate the presence of bright and dark modes in our polarized Fabry-Perot cavity. We have suggested that a y-polarized Fabry-Perot dark mode is located between two metamaterials. Then the FP dark mode can be coupled to the x-axis bright mode by breaking the stacked metamaterials alignment via the rotation angle θ.

Such concept of bright and dark mode coupling in stacked metallic metamaterials (or similar kind of stacked polarized structure) seems to not have been reported in the literature. In our opinion, it is important to emphasize that the dark mode is not created by a specially designed unit-cell with a particular asymmetry. In our case, the FP dark mode appears because of the stacking while the bright mode is transmitted through the structure. To be more specific, the bright mode results from the metamaterial-based enhanced optical

transmission and propagate along the x-axis. In the meantime, the orthogonally polarized dark modes arise from the aligned stacked structure and are trapped between the metamaterials. In other words, the dark modes in our structure are not occurring at the same ”location” than the bright mode, as it is the case for asymmetric unit-cell based metamaterials. In our case, it is the symmetry breaking of the overall structure that provokes the dark modes coupling.

If we look back at the mentioned bibliography, the stacked structure combines two distinct strategies for exciting Fano resonance. It associates the side-coupled cavity-waveguide concept first presented by Shanhui Fan [121] and the symmetry-breaking concept first reported in metamaterials by Fedotov *et al.* [127]. Indeed, the y-polarized Fabry-Perot resonators (FP_y) play the role of the side-coupled cavities while the coupling is achieved by symmetry-breaking. This combination is made possible in the structure because of the specific polarization properties of its constitutive stacked metamaterials. However, it is important to remind that the propagated light polarized along the x-axis is not - strictly speaking - a ”waveguide” propagation.

Furthermore, we have shown that larger stacks of freestanding metasurfaces can be used to exhibit and separately tune multiple Fano resonances. We believe that stacks of metasurfaces/metamaterials provide a new route to produce Fano resonances and an original way to design a wide variety of reconfigurable filtering devices. This high versatility also proves the structure to be a good candidate to even realize arbitrary spectral shaping. From a more general point of view, Fabry-Perot resonators made of anisotropic and twisted mirrors could reach broader applications in physics.

5

SPECTRALLY TUNABLE LINEAR POLARIZATION ROTATION USING STACKED METALLIC METAMATERIALS

In the previous chapter, we have demonstrated that stacks of metallic metamaterials can be very efficient to achieve and tune polarization-induced Fano resonances. Then, we have proposed filtering applications based on this observation. As we have seen in chapter 3, the Fano dip can also be engineered for detection such as electro-optical sensing. However, stacking metallic metamaterials can be used for totally different applications that do not necessarily involve Fano resonances. In this chapter, we propose to use stacked metamaterials to perform a spectrally tunable linear polarization rotation.

First, we give a state of the art of polarization rotation using metamaterials. We distinguish several kinds of structures that are suitable for polarization rotation. Second, we physically describe the linear polarization rotation principle that can be used with stacked metallic metamaterials. We present the general EJF form for an arbitrary metamaterials number N. Third, we numerically study the polarization rotation and show that it can operate either on a broad spectral band or on an ultra narrow spectral band. For the broadband polarization rotation, we focus on some parameters such as the separation distance between metamaterials or the rotation angle in oreder to optimize the bandwidth. We especially show that some specific configurations are efficient for cross-polarization rotation. For the ultra-narrow band polarization rotation, we show that it can be achieved only for a very particular stacked structure configuration. Besides, we propose another structure for the polarization rotation based on Fano resonance excitation and polarization induced effects. We show that in some particular configurations, it is possible to achieve a quasi cross-polarization rotation using only two metallic polarizers. We finally conclude that stacked metamaterials offers many configurations to realize polarization rotation and

we discuss the advantages of each configuration. Part of the results presented in this chapter has been published in 2017 [182].

5.1/ STATE OF THE ART

Polarization rotation with metamaterials was first reported using a metallic gammadion-shaped subwavelength unit cell [183–185], as shown in Fig. 5.1. The linearly polarized incident light was launched on the gammadion metamaterial and the 1st order diffraction reflected light was rotated by an angle $\Delta\theta$. In those studies, the polarization rotation is explained by the chirality of the structure. Another early study on reflective polarization rotation was reported using anisotropic metamaterials [55]. The polarization rotation is also sometimes referred to as polarization conversion. In this manuscript however, we prefer to use the term rotation since conversion can have another meaning, i.e., conversion of a linear polarization into a circular or elliptical polarization for example.

Studies on reflective polarization rotator with broad wavelength range and with a $90°$ rotation angle has been further developed using subwavelength unit-cell such as split wire rings [186], disk split ring resonators [187], tilted coupled split rings [188], meta

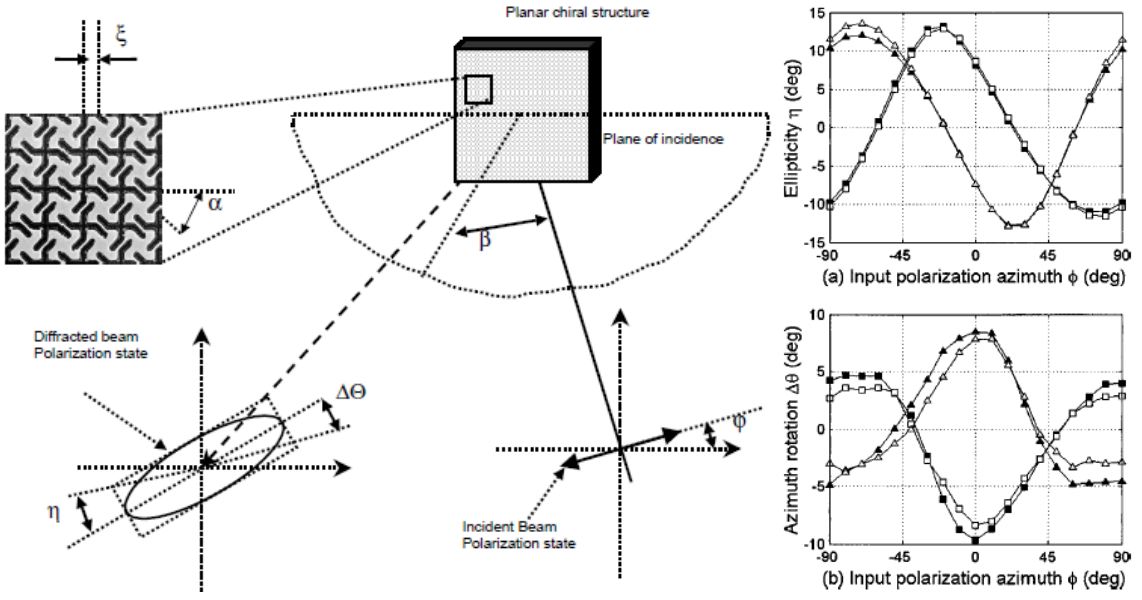

Figure 5.1: Principle of reflective polarization rotation using gammadion unit-cell metamaterial. An incident input linearly polarized beam falls on a gammadion based planar chiral metamaterial. After reflection, the output beam has been rotated by an angle $\Delta\theta$ and the beam ellipticity is given by η. Inset **(a)** Output beam ellipticity η as a function the polarization orientation (polarization azimuth ψ). Inset **(b)** Polarization rotation value $\Delta\theta$ versus ψ. Figures taken from [183]

reflect-array [189], C-shaped slits [190], Y-shaped nano-antennas [191] or elliptic plasmonic resonators [192]. More complex patterns such as array-shaped [193] or anchor-shaped [194, 195] unit-cells have also been studied. Each of these studies involved complex three-layer metamaterials composed of a metallic ground plane, a dielectric substrate and either a dielectric or metallic structured top layer. Very recently, reflective polarization rotation has been achieved by metasurface antenna for the GHz regime [196] and by cross shaped graphene metamaterial [197]. A recent interesting study reported switchable polarization rotation with a three-layers metamaterial composed of a vanadium dioxyde (VO_2) phase change materials as the intermediate layer substrate [198]. By modulating the phase-change material temperature below (or above) the threshold of $68°C$, the incident linear polarization was rotated by $+45°$ (or $-45°$) after reflection.

The main alternative to reflective polarization rotation is the transmissive polarization rotation where light polarization is rotated after its passage through the metamaterial. Early works on transmissive polarization rotation was reported using single metamaterials also composed of gammadion unit-cell [57, 199, 200]. Another recent work reported polarization rotation with a stero gammadion unit-cell [201], i.e. a gammadion shape resonator patterned on a trenched surface. Recent polarization rotation demonstrations were realized with metasurfaces composed of helices [202], asymmetrically split ring resonators [203] or metal-graphene hybrid structure with higher order symmetry pattern [204]. Tunable polarization rotation was achieved using a reconfigurable metasurface based on a micro-electro-mechanical-system actuation. [205]. Later, stacking metamaterials to realize transmissive broadband cross-polarization rotation has been extensively studied. For example, in 2010, an early demonstration of a 90° polarization rotation was realized with a pair of chiral metamaterials [206]. The same year, polarization rotation was performed with a pair of L-shaped slit patterned metallic layers [207]. The polarization rotation was enhanced by the Fabry-Perot resonances between the metallic layers which was itself coupled to a plasmonic mode. More recently, a bi-layer metallic metamaterial with connected slots exhibited efficient cross-polarization rotation [208].

Since few years, stacks of three metamaterials prove to be very efficient to achieve broadband cross-polarization rotation [209–213]. In general, it consists in progressively rotating in the transverse plane the second and the third metamaterials - or its unit-cell pattern - by $45°$. After passage in the third metamaterial, the polarization is rotated by $90°$. One schematic example is depicted in Fig. 5.2 [210] where the authors demonstrated cross-polarization rotation over a broadband THz range.

These results were achieved using three stacked mono-periodic metallic metamaterials. A very recent study used the same kind of stacked metallic metamaterials and demon-

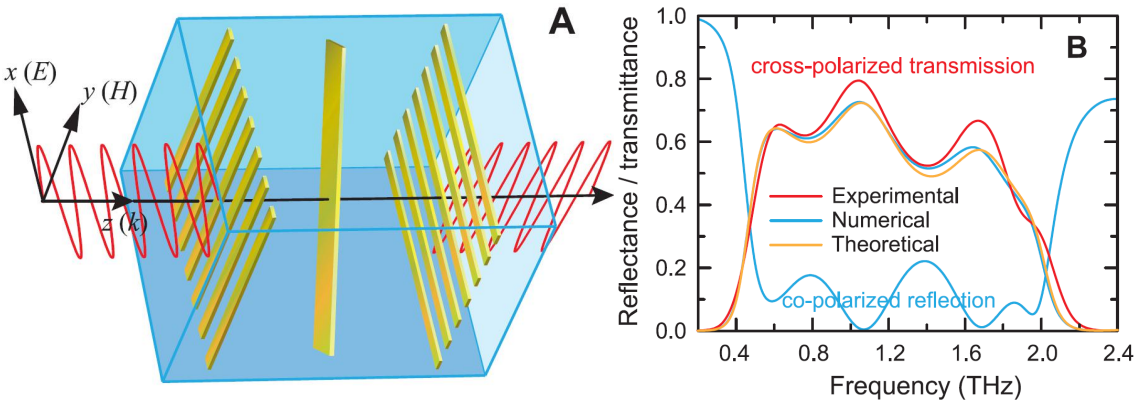

Figure 5.2: **(a)** 3D schematic principle of polarization rotation through a stack of monoperiodic metamaterials. **(b)** Compared transmission spectrum corresponding to cross polarization rotation obtained theoretically, numerically and experimentally. Figures taken from [212].

strated similar polarization rotation properties [214]. Other studies however have reported broadband cross-polarization rotation where the middle metamaterial is composed of a different unit cell such as split wire rings [215], split disks [216], T-shaped resonators [107] or disk split rings [217]. Polarization rotation was also studied for an arbitrary amount of stacked nanorods [218, 219]. It has to be noted that such stacked and progressively twisted structure can also present asymmetric transmission properties that can be used to design optical isolators [56, 104].

Nonetheless, for most of these studies, the reported cross-polarized transmissions values are significantly less than 100%. One example is shown in Fig. 5.2**(b)** where the maximum cross-polarized transmission value is 80%, at a frequency close to 1 THz, while the rest of the cross-polarized transmission spectrum reaches no more than 65%. For the structure we consider in this chapter, we will demonstrate that the transmission values reach 100% thanks to two phenomena:

1) the enhanced optical transmission (EOT) in the metamaterials apertures, covered in chapter 2

2) the multiple reflections (or FP like resonances) occurring between the metamaterials, analysed in chapter 3.

Moreover, we will show that total cross-polarization rotation is achievable in several configurations.

5.2/ LINEAR POLARIZATION ROTATION PRINCIPLE

In this section, we present the principle of Linear Polarization Rotation (LPR) which consists in rotating the x-component of the incident linear electric field $\vec{E}_{inc}$ by an angle θ - counted from the x-axis - after transmission through the last metamaterial polarizer, as shown in Fig. 5.3. Hence, the first Metallic Polarizer (MP) is oriented such that its transmitted electric electric field $\vec{E}_T$ is along the x axis (term α of J^T in eq. 2.89). In other words, the incident electric field component along the y-axis is not transmitted nor rotated but totally reflected by the first MP and is denoted by $\vec{E}_R$ (term -1 of J^R in eq. 2.89). The rotation angle of each MP uniformly changes from 0 (1^{st} MP) to θ (last MP) in the transverse Oxy-plane. We introduce φ as the uniform rotation angle between two consecutive MPs, so that

$$(N-1)\,\varphi = \theta \; mod \; \pi. \tag{5.1}$$

For more clarity on the notation and on the numerical study, we consider the stacked metamaterials to have the same unit-cell geometry so that they only differ by their transverse orientation. Furthermore, we consider a constant rotation angle φ and a constant separation distance d between the metamaterials.

We have developed a simple theoretical model which illustrates the physical principle underlying the LPR effect. This present model is a generalized form to an arbitrary MP number $N \geq 3$ of the theory previously used for two stacked MP in chapter 3. We analyti-

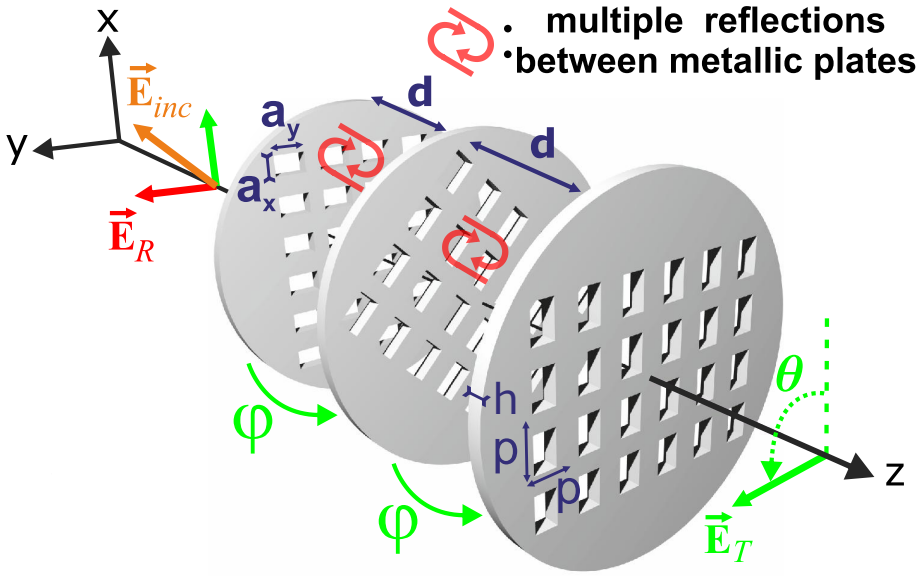

Figure 5.3: 3D rendered schematic depicting the linear polarization rotation principle. The incident field x-component - in green - is transmitted and progressively rotated by an angle θ after the transmission through the last MP.

cally deduce the expressions of the transmission and reflection Jones matrices, denoted by J_N^T and J_N^R respectively, for a stack of N MP:

$$J_N^T = \begin{pmatrix} J_{x,x}^T & 0 \\ J_{y,x}^T & 0 \end{pmatrix} = \alpha_T^{(N)} (\cos\varphi)^{N-1} \begin{pmatrix} \cos\theta & 0 \\ \sin\theta & 0 \end{pmatrix}, \tag{5.2}$$

and

$$J_N^R = \begin{pmatrix} J_{x,x}^R & 0 \\ 0 & J_{y,y}^R \end{pmatrix} = \alpha_R^{(N)} \begin{pmatrix} 1 & 0 \\ 0 & 0 \end{pmatrix} - I_d, \tag{5.3}$$

where I_d is the identity matrix. The terms $\alpha_T^{(N)}$ and $\alpha_R^{(N)}$ are the Airy-like spectrally resonant coefficients of the whole structure. Their analytical expressions are obtained by using the iterative process of the S-matrix algorithm that accounts for the MP stacking. More details can be found in chapter 3. After tedious calculations, the coefficients $\alpha_T^{(N)}$ and $\alpha_R^{(N)}$ in Eq. (5.2) and Eq. (5.3) are given by

$$\alpha_T^{(N)} = \frac{\alpha_T^{(N-1)} \alpha_T u}{\gamma_N - u^2 (1 - \alpha_R) \left(1 - \alpha_R^{(N-1)}\right)}, \tag{5.4}$$

and

$$\alpha_R^{(N)} = \alpha_T \frac{\alpha_T^{(N)}}{\alpha_T^{(N-1)}} \left(\alpha_R^{(N-1)} \delta - 1\right) u + \alpha_R, \tag{5.5}$$

with

$$\gamma_N = \frac{1 - u^2 \left(1 - \alpha_R \alpha_R^{(N-1)} \sin^2\varphi\right)}{1 - u^2}, \text{ and } \delta = \frac{\cos^2\varphi - u}{1 - u^2}, \tag{5.6}$$

where $u = \exp(ik_0 d)$ is the propagation term in the homogeneous layers separating the MPs. Equations (5.4) and (5.5) are iterative formulas where the initial terms $\alpha_T^{(1)}$ and $\alpha_R^{(1)}$ correspond to α_T and α_R, as previously presented in chapter 2.

We remind that this theory is restricted to the far-field approximation and it implies that the distance d is large enough to neglect coupling between evanescent waves at the interfaces of two consecutive MP, as discussed in chapter 3. Thus, the transmission involves only propagating electromagnetic fields which are reduced to the 0th diffracted propagative order in the considered spectral range. Nonetheless, we remind that the evanescent waves in homogeneous regions are taken into account in the transmission and reflection properties of each MP via the coupling coefficient C (given by the Eq. (2.35) in chapter 2). Besides, we remind that the studied spectral domain is chosen such that only the fundamental guided mode TE_{01} propagates inside the rectangular apertures, and therefore satisfy the monomodal criterion.

5.2.1/ TOTAL TRANSMISSION OF LINEAR POLARIZATION ROTATION

To study the transmission properties of our structure, we define the transmission coefficient T such that

$$T = \left|J^T_{N,x,x}\right|^2 + \left|J^T_{N,y,x}\right|^2 = \left|\alpha^{(N)}_T \left(\cos\varphi\right)^{N-1}\right|^2 \tag{5.7}$$

We remark that the transmission coefficient has an expression which is similar to the extended Malus' Law studied in chapter 2 (Eq. (3.16)). As for the extended Malus' Law, we have a modulation factor $\alpha^{(N)}_T$ that accounts for the multiple reflection in the structure, and the progressive rotation is given by $(\cos\varphi)^{N-1}$. It is important to remind that the transmission coefficient is an intrinsic property of the structure and do not depend on the incident light polarization.

To begin, we focus on a stack of three metamaterials aligned on the x-axis, with the following geometry $a_x/p = 0.3$, $a_y/p = 0.9$, $h/p = 1$ (see Fig. 5.3). The transmission spectrum as a function of the separation distance d is shown in Fig. 5.4 **(a)**. We can remark that the observed transmission response is similar to the transmission response of two aligned metamaterials given in Fig. 3.7**(b)**. We notice however an additional Fabry-Perot resonance. Indeed, the addition of a third metamaterial produces a FP resonator, polarized along the x-axis and located between the second and third metamaterials. It leads to degenerated resonance pairs for each Fabry-Perot harmonics.

Figure 5.4 **(b)** shows the transmission spectrum as a function of d/p when $\varphi = 45°$ - which corresponds to a cross-polarization rotation configuration. As we can remark and

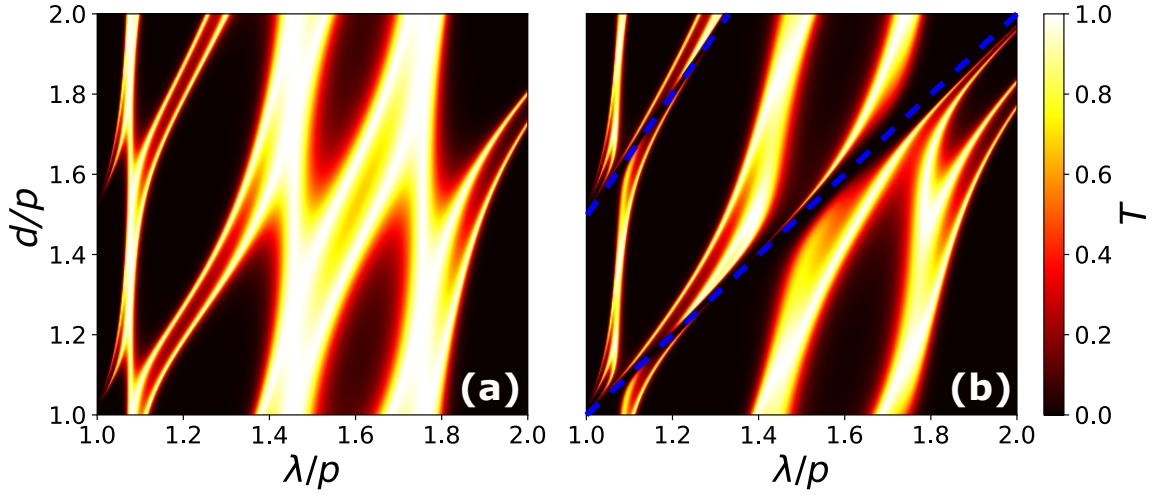

Figure 5.4: **(a)** Transmission spectrum as a function of the separation distance d for $\varphi = 0°$, i.e. three aligned polarizers. **(b)** Transmission spectrum as a function of d when $\varphi = 45°$, i.e. cross polarization configuration. The blue dotted line denotes the polarization induced Fano resonances dip.

expect, Fano transmission dips appear for the condition $\lambda = 2d/m$. As we have seen in the previous chapter discussing polarization-induced Fano resonances, it is due to the metamaterials rotation which allows for the coupling of the FP_y resonance and leads to Fano dips. Unfortunately, to realize cross-polarization rotation with three metamaterials, the rotation angle is $\varphi = 45°$ which implies a strong coupling of the FP_y dark mode and therefore leads to a transmission dip with a large bandwidth. Such broad Fano dip is detrimental to broadband cross-polarization rotation. Nonetheless, we show later that such configuration can be optimized to achieve broadband cross-polarization rotation. From now on, we concentrate our study on the spectral range where $\lambda/p \in [1.2,\ 2.0]$.

The separation distance d/p is thereafter chosen equal to 1, i.e such that, at least, two distinct resonant transmission peaks occur in $\lambda/p \in [1.2, 2.0]$. The configuration with such parameter values is labelled as **A** in Fig. 5.5**(a)** marked by the horizontal white dotted line.

It may be surprising to get total transmission at resonances by simply interposing one linear polarizer at $45°$ between two crossed ones. According to eq. (5.2), it means that $T = |\alpha_3|^2 [\cos(\pi/4)]^4 = 1$ at resonances. We expect that this total transmission is due to the multiple reflections between the metamaterial polarizers, as suggested in the previous chapters. In particular, the enhanced transmission is mainly due to the x-polarized Fabry-Perot resonance (as shown in Fig. 3.7). For cascaded dichroic polarizers, where the multiple reflections vanish, $T = \left|(\cos\varphi)^{N-1}\right|^2$ which is equivalent to eq. (5.7) with $|\alpha_N| = 1$ $\forall \lambda/p$. In this case and for $N = 3$, the transmission reaches only 25% for dichroic polarizers instead of 100% at resonance of PMP, as numerically demonstrated in Fig. 5.4. This perfectly agrees with the extended Malus' Law and demonstrates that the multiple reflections between the MP are responsible for the observed total transmission at resonance.

We may also expect that the peak positions largely depend on the homogeneous layer's thickness d because of these multiple reflections. However, the transmission spectra for different values of d/p shown in Fig. 5.4**(b)** exhibit peaks with positions that roughly coïncide with the ones of a single PMP ($\lambda/p \approx 1.4$ and 1.68), except when the Fano dips of the cavity, formed by two consecutive PMP, intersect the PMP own resonances (see oblique blue dotted line in Fig. 5.4**(b)**). For more details on such complex transmission phenomenon, the reader can refer to the the chapter 4 where the polarization induced Fano resonance phenomenon is investigated.

5.3/ LINEAR POLARIZATION ROTATION WITH TUNABLE QUALITY FACTOR

In this section, we show that the arrangement of the structure, as well as the holes geometry, are playing a crucial role to control the LPR quality factor $Q = \frac{\lambda_0}{\Delta\lambda}$, where λ_0 is the central wavelength in the transmission bandwidth, and $\Delta\lambda$ is the bandwidth measured at FWHM (i.e., -3 dB in log-scale). However, the rotated output field polarization direction, given by θ, and the quality factor, which is influenced by φ cannot be arbitrarily and simultaneously fixed. Hence, we first focus on the angle φ with no consideration for θ.

From now on, we restrict our study to the peak close to $\lambda/p = 1.68$ which is related to the cut-off of the TE_{01} guided mode inside the rectangular holes. However, the cut-off wavelength of the TE_{01} mode is equal to $2a_y$. This implies to keep the same value of a_y in order to avoid important peak shifts. In section 5.3.1, the study is led to design Broadband LPR (BPR) which corresponds to low quality factors (Q < 10). Then, we discuss the limitations of the BPR. Conversely, in section 5.3.2 we design a Narrowband LPR (NPR) which corresponds to ultra-high quality factors (Q $> 10^5$).

5.3.1/ BROADBAND LINEAR POLARIZATION ROTATION

First, a_x/p must be chosen as large as possible (in order to increase the radiation losses of the apertures) to obtain BPR. Nevertheless, the value of a_x/p must be chosen such

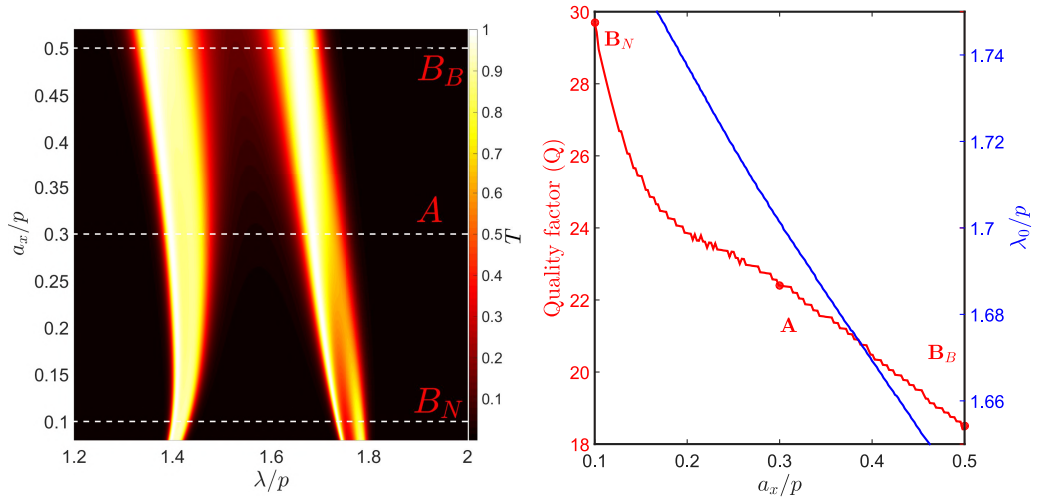

Figure 5.5: **(a)** Evolution of the transmission spectrum for configuration **A** ($N = 3$ and $\varphi = 45°$) when the aperture width a_x/p decreases to 0.1 or increases up to 0.5. **(b)** The red curve gives the quality factor Q as function of a_x/p. The blue curve shows the corresponding shift of the central wavelength λ_0/p.

that the cut-off wavelength of the second mode TE_{10} $(2a_x)$ remains smaller than the TEM Floquet mode cut-off wavelength so that $2a_x \leq p$. Therefore, the maximum value of a_x/p is 0.5 in order to satisfy the monomodal criterion. Results shown in Fig. 5.5**(a)** confirm that the width of transmission peaks increases when a_x/p grows. Precisely, Fig. 5.5**(b)** shows the quality factor Q computed for the peak close to $\lambda/p = 1.68$. It particularly shows that Q decreases when the rectangle's width, a_x/p, increases. Thereafter, we fix $a_x/p = 0.5$ for BPR. The BPR with such parameter values is labelled as $\mathbf{B}_B$ in Fig. 5.5**(b)** with $Q = 18.4$.

Figure 5.6**(a)** shows the variation of Q with respect to φ, for different values of N and for a separation distance $d/p = 1.0$. As expected, the quality factor decreases when φ decreases. Similarly to photonic crystal band gaps broadening, quality factors tend to one limit for a fixed value of φ when the number N of cascaded PMP increases. We also remark that a BPR with $N = 3$ reaches identical performances at $\varphi = 0.5^o$ than a BPR with $N = 15$. Hence, for polarization rotation with small angle, a limited number of metamaterials N $(N = 3)$ is sufficient to achieve the best performance. This configuration is labelled as $\mathbf{C}_B$ in Fig. 5.6**(a)** for which $Q = 7.9$. The inset graph in Fig. 5.6**(a)** reveals that the peak position remains almost constant near $\lambda_0 \approx 1.65$.

Another way to broaden the bandwidth is to merge 2 (or more) peaks by shifting the peak centered at $\lambda/p \approx 1.4$ toward the one centered to $\lambda/p \approx 1.68$ for example. The peak close to $\lambda/p = 1.4$ is related to a Fabry-Perot-like resonance of the TE_{01} cavity mode

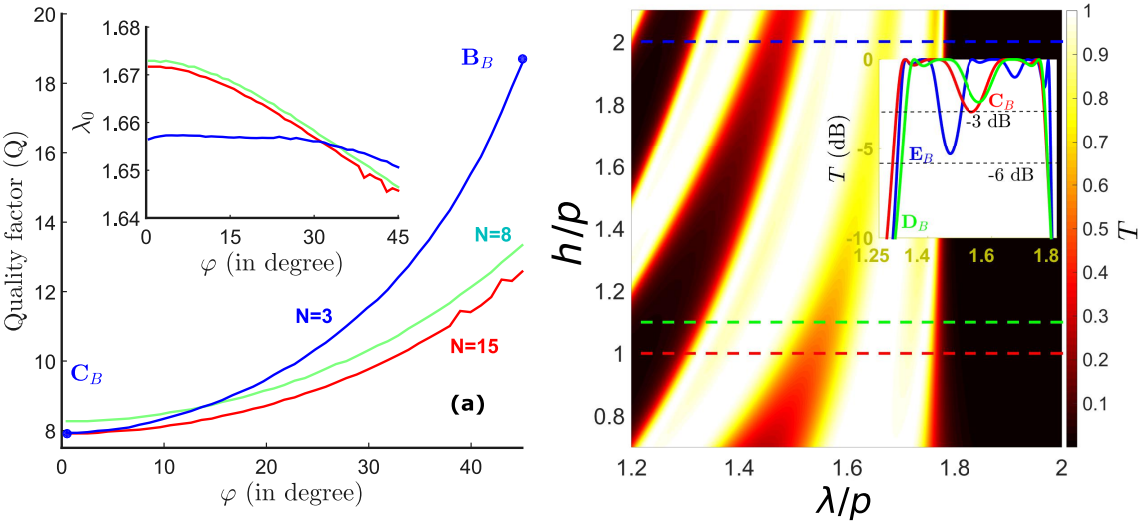

Figure 5.6: **(a)** Quality factor versus the rotation angle φ for different metamaterial polarizer number N. The inset graph gives the corresponding shift of the central wavelength. **(b)** Transmission spectrum versus the polarizer metamaterials thickness h/p.

and its resonance wavelength changes with the metal thickness h. The position of the peak near $\lambda/p = 1.68$, related to the cut-off of TE_{01} cavity mode, is not affected by h/p values because it only depends on a_y ($\lambda^{\mathrm{TE}_{01}}_{cut-off} = 2a_y$). Figure 5.6**(b)** depicts transmission spectra for different values of h/p. As expected, we see that the two peaks merge but the bandwidth of each peak narrows when h/p increases. The spectra shown in the inset of Fig. 5.6**(b)** computed for a BPR with $h/p = 2$, and labelled as $\mathbf{D}_B$, reveals a relatively low quality factor: $Q = 3.29$. As we can observe in the inset spectra of Fig. 5.6**(b)**, it is possible to modulate the spectral bandwidth, or in other words, the quality factor Q, at a -3dB threshold while the bandwidth at -6dB is barely affected with the variation of h. Those results show that it is possible to lower the quality factor by increasing the rectangle's width, by reducing the angle φ and by carefully choosing the metamaterials thickness h. In the same time, they demonstrate that Q converges to a limit value. These multilayered devices present transmission properties close to cascaded nanobars structure studied in [219]. It features similar broadband range with a very efficient LPR obtained by twisting. Until now, the overall results demonstrate that it possible to optimize (or tune) the bandwidth while preserving a very high transmission coefficient ($T \approx 100\%$).

However, as mentioned above, the relation between φ and θ given by eq. (5.1) does not allow to choose an accurate quality factor Q and an arbitrary angle θ simultaneously. This issue is especially crucial for the achievement of a low Q and tunable LPR. For example, in the case of a cross-polarization rotation where $\theta = 90°$ and with $N = 3$, the angle φ is therefore equal to $45°$ since we consider a progressive rotation. Such a value of φ is not optimized to obtain a low Q cross-polarization rotation. In this case, the corresponding quality factor is $Q = 11.3$ for $\lambda_0 \approx 1.68$. Thus, we discuss two options to overcome this limitation.

The first option simply consists in increasing N in order to reduce φ and therefore lower the quality factor. Figure 5.7**(a)** shows the transmission spectra for different values of N

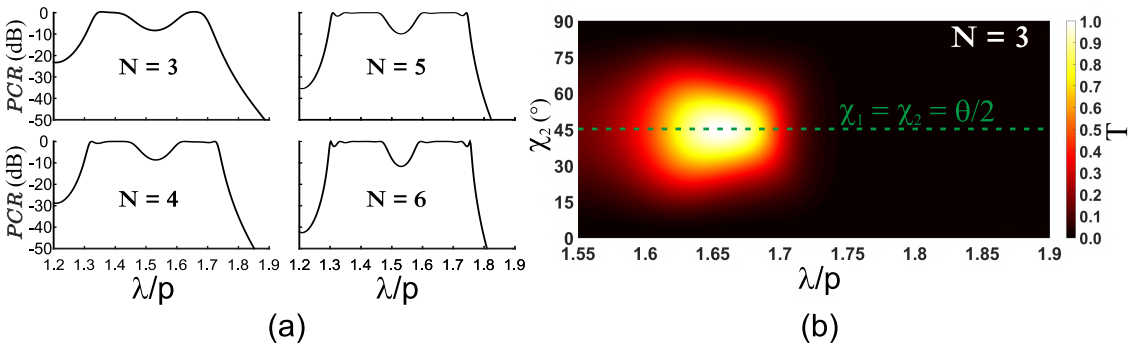

Figure 5.7: **(a)** Cross polarization rotation spectra given for $N \in [3, 6]$ metamaterial polarizers number. **(b)** Transmission spectrum as a function of χ_2 for $N = 3$.

for $\theta = 90°$. As expected from Fig. 5.6**(a)**, we observe a broadening of the transmission spectra when N increase. However, Fig. 5.6**(a)** and 5.7**(a)** shows that such a broadening is limited and converges to a finite spectral bandwidth (convergence of Q when $\varphi \to 0°$). Consequently, a reasonable number of polarizers should be chosen to achieve a good trade-off between a large bandwidth and a realistic device easy to fabricate.

The second possibility is to consider a non-uniform angle χ between each plate for a stack of N polarizers such that $\sum_{i=1}^{N-1} \chi_i = \theta$ with $i \in \{1, 2, \ldots, N-1\}$. Precisely, we study the simple case of $N = 3$ with $\chi_1 + \chi_2 = 90°$, and Fig. 5.7**(b)** shows the transmission spectra as a function of χ_2. One note that the transmission spectrum is optimized when $\chi_1 = \chi_2 = 45°$ featuring a perfect transmission with the broadest band (lowest Q). Thus, breaking the intermediate rotation angle φ into different values χ_i is not efficient for achieving a total and low-Q LPR. Nevertheless, Fig. 5.7**(b)** also shows that the structure exhibits an angular tolerance within which its performances are barely affected.

Another possibility is to consider different values for each separation distances between the metamaterials. Again, we focus on a three metamaterials stacked structure with a constant angle $\varphi = 45°$ and two different separation distances values denoted by d_1 and d_2. The value of d_1 is fixed to $d_1/p = 1.0$ while we analyse the transmission spectrum as a function d_2/p, as shown in Fig. 5.8. For more relevance, such results have to be compared with Fig. 5.4**(b)**, where both distances are varied at the same time ($d_1 = d_2 = d$). As we can see, considering different separation distance values does not increase the bandwidth nor the overall transmission. However, as for the previous study, such results indicates that the structure is also robust against metamaterials positioning errors and preserves a transmission coefficient equal or close to 100%.

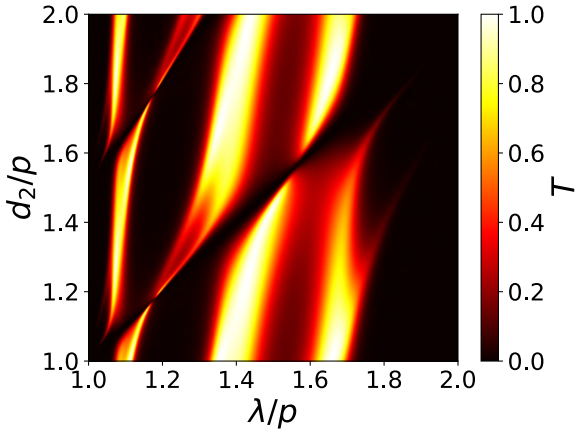

Figure 5.8: Transmission spectrum as a function of d_2/p, the distance separating the second and third (last) metamaterials.

5.3.2/ NARROWBAND LINEAR POLARIZATION ROTATION

Contrary to BPR, a_x/p must be chosen as small as possible in order to reduce the radiation losses and thus to realize NPR. Hence, the value of a_x/p is fixed to 0.1 which corresponds to the polarization rotation labelled as $\mathbf{B}_N$ in Fig. 5.5. For this value of a_x/p and for $N = 3$, the peak close to $\lambda/p = 1.75$ shown in Fig. 5.5**(a)** splits into two peaks. The quality factor plotted in Fig. 5.5**(b)**, equal to 29.7 at $\mathbf{B}_N$, is computed for the whole peak. We assume that this effect is due to resonance degeneracy. The whole structure may be seen as a stack of 5 cascaded and coupled resonators. Indeed, for $N = 3$, there are 3 resonating MPs coupled to 2 multiple reflections resonances located in the two homogeneous regions. This complex behaviour deserves a thorough analysis in a future work. The narrow peaks are indicated by dark arrows in Fig. 5.9**(a)**. Precisely, we see in the graph on the left of Fig. 5.9**(a)** that the most narrow peak is increasingly being thin when φ tends to 90^o while the other ones disappear. More generally, for N stacked metamaterials, there are $(N-1)$ transmission peaks corresponding to the $(N-1)$ FP resonances distributed along the structure. One of the peak features a relatively broad spectral bandwidth with $T < 1$, while the $(N-2)$ remaining peaks are very narrow with $T = 1$ at resonances. It is interesting to see that, for fixed values of N, all narrow peaks

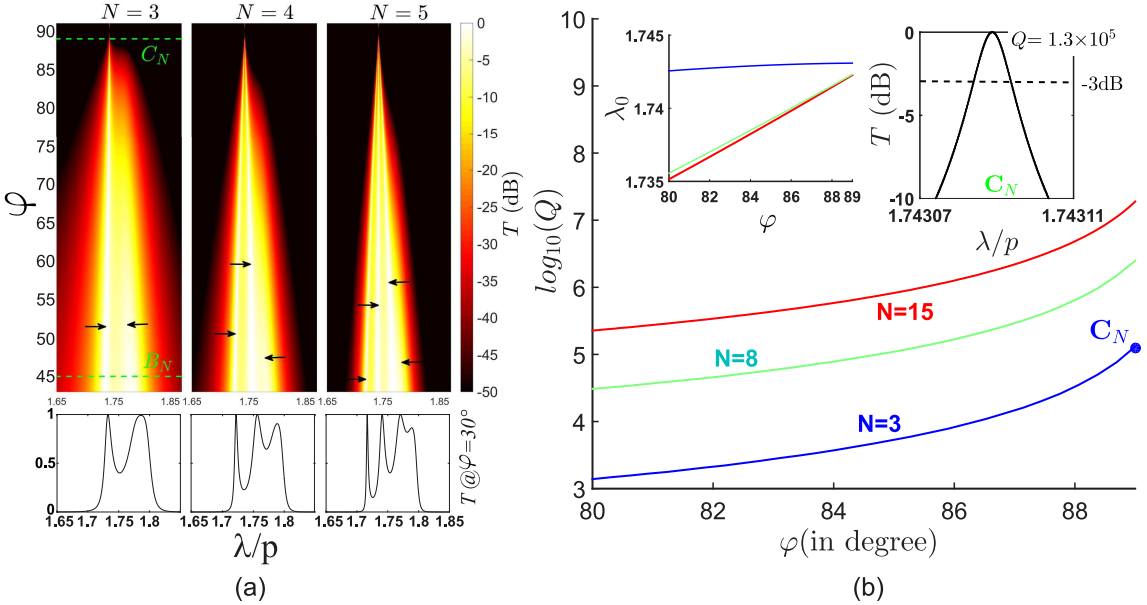

Figure 5.9: **(a)** Transmission spectra as a function of φ for a stack of 3, 4 and 5 metamaterials polarizers respectively shown in the left, center and right graph. The inset below are the corresponding transmission spectrum at $\varphi = 30°$. **(b)** Quality factor Q versus φ for different polarizer number N. The left inset graph shows the corresponding variation of the central wavelength λ/p. The right inset spectrum shows a narrow transmission peak obtained for $\varphi = 89°$ and the corresponding quality factor is $Q = 1.3 \times 10^5$.

seem to converge to a unique value of λ/p when φ increases. Such intriguing behavior is not well understood for the moment and is under investigation and we suspect that complex polarization induced effects are involved. In order to distinguish the peaks more easily, the peaks are also depicted in the lower inset spectra in Fig. 5.9**(a)** for $\varphi = 30°$. For such value of φ, the peaks appear more clearly. For $\varphi > 45°$ the peaks start merging and they cannot be individually located. Thereafter, we study in particular the nearest peak to $\lambda/p = 1.68$.

We are now interested in the variation of the quality factor of the chosen transmission peak when φ tends to 90^o. The results are depicted in Fig. 5.9(b) and reveal that the quality factor drastically diverges when φ tends to $90°$, regardless the value of N. As an example, the NPR with $\varphi = 89°$ and $N = 3$ is labelled as $\mathbf{C}_N$. For this case, Q reaches 1.3×10^5, and the transmission spectra is plotted in the inset graph on the right of Fig. 5.9**(b)**. In the inset graph on the left, we remark that peak positions converge to a unique value of λ/p when φ increases and it confirms the observation made in Fig. 5.9(a). This interesting result could be used for the design of high quality filters for the THz spectral band. Nevertheless, in view of experimental demonstration, the robustness of the structure with respect to the fabrication imperfections should be discussed. However, the latter greatly depends on the manufacturing process that is not already established. Such parametric study involving pure numerical methods, such as the FDTD, must be applied to take into account the real geometry of the structure [22].

5.4/ DARK-MODE-BASED TUNABLE POLARIZATION ROTATION WITH EVANESCENT METASURFACES

Until now in this manuscript, we have studied several applications where the constituent metamaterials systematically work at wavelength values located at - or close to - the sub-wavelength aperture's resonance. It leads to the direct consequence that an enhanced transmission occurs for the light polarized along the rectangle's width ($\alpha_T \approx 1$), and thus the metamaterials played the role of polarizers. In this section however, we would like to investigate polarization rotation when the constituent metamaterials work after the cut-off wavelength of the fundamental mode (evanescent regime). In other words, we consider the spectral region where α_T falls to zero ($\alpha_R - 1 \approx -1$). To simplify the notation, we pose

$$\alpha'_R = \alpha_R - 1 \tag{5.8}$$

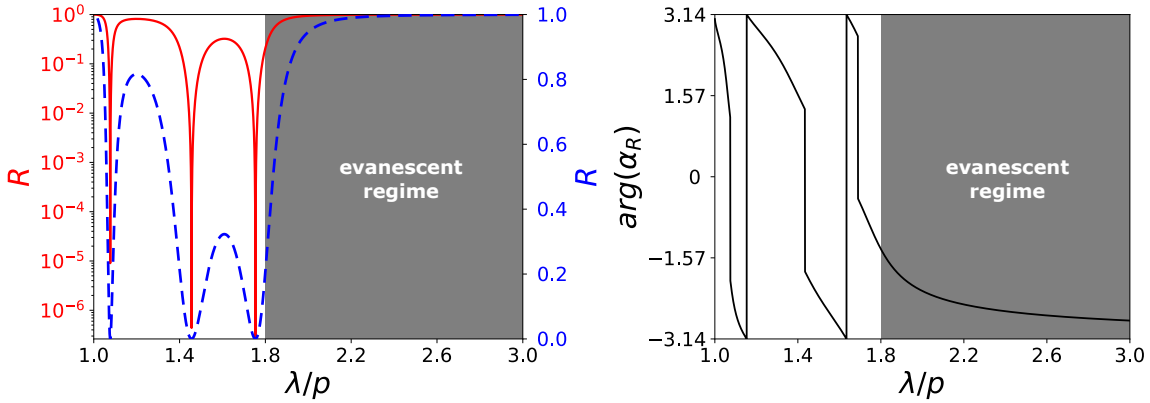

Figure 5.10: **(a)** Reflection versus λ/p given in linear and logarithmic scale, respectively shown in blue and red. **(b)** Wrapped phase value of the reflection coefficient α'_R as function of λ/p. The greyed area denotes the spectral region after the fundamental mode TE_{01} cut-off wavelength.

Furthermore, we remind that the reflection along the y axis is -1. To summarize, the metamaterials do no act as polarizers but as reflective metallic plates with polarization dependency, as initially presented in chapter 4. Nonetheless, it is crucial to note that the fundamental evanescent mode is still the dominant mode in the aperture and that it does not affect the validity of the theory. Now, we focus on the x-axis reflection coefficient β of the metamaterials and we consider the incident light $\vec{E}_{inc}$ to be lineary polarized along the x-axis. Figure 5.10**(a)** shows the reflection spectrum of a bi-periodic metamaterials with rectangular apertures where $a_x/p = 0.45$, $a_y/p = 0.9$ and $h/p = 1.0$, aligned on the x-axis. The reflection spectrum is shown in linear scale (blue dashed curve) and in logarithmic scale (red solid curve). The region where the fundamental mode becomes evanescent is for $\lambda/p > 2a_y = 1.8$ and is represented by the grey area. For $\lambda/p > 1.8$, the reflection $R = |\alpha'_R|^2$ tends to be total. Figure 5.10**(b)** gives the phase of the x-axis reflection coefficient α'_R. We can see that the phase of α'_R asymptotically tends to $-\pi$ when $\lambda/p \to \infty$. It indicates that, as λ/p increases, the corresponding phase tends to the value of a perfect mirror. In other words, as λ/p increases, the light tends to be less coupled to the evanescent fundamental mode and thus the reflection term α'_R get closer to the perfect electric conductor reflection ($\alpha'_R \to -1$). One note that, for $\lambda/p \to \infty$, we obtain $\alpha'_R = -1$ which correspond to a perfect mirror with no polarization dependency.

From now on, we focus on a stack of two metamaterials working in evanescent regime in the spectral range $\lambda/p \in [1.8, 2.4]$. To better understand the underlying physics in this structure, we study the circulating field, given by Eq. (4.8), presented in the previous chapter. More precisely, we consider the two metamaterials to be aligned ($\theta = 0°$) so that

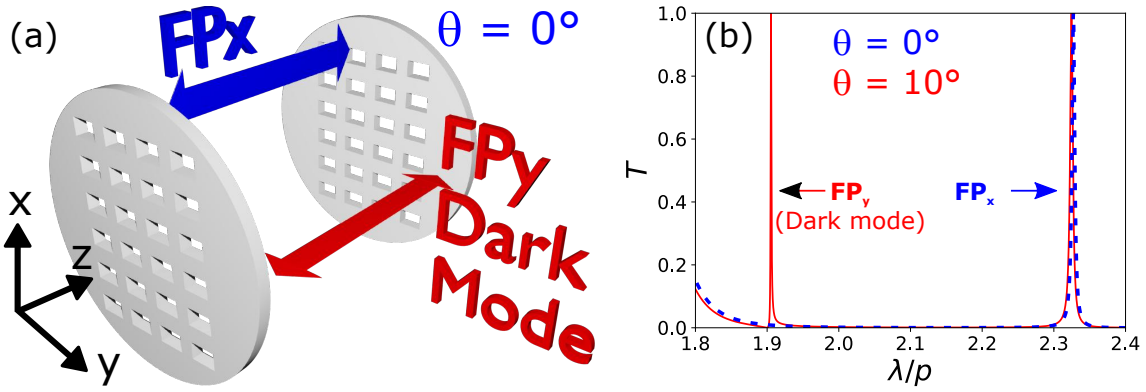

Figure 5.11: **(a)** 3D-rendered schematic of the dark-mode based tunable polarization rotation principle. **(b)** Dashed blue line: transmission spectrum when the two wire-grid metasurface are aligned ($\theta = 10°$). Solid red line: Transmission spectrum for $\theta = 10°$.

the circulating electric field $\vec{E}_{circ}$ is given by

$$\vec{E}_{circ} = \begin{pmatrix} \frac{1}{1-u^2\alpha_R'^2} & 0 \\ 0 & \frac{1}{1-u^2} \end{pmatrix} U\vec{E}_{launch}. \tag{5.9}$$

We remind that $\vec{E}_{launch}$ is the electric field that has just entered the cavity: $\vec{E}_{launch} = J^T\vec{E}_{inc}$. As we can see, for two metamaterials aligned along the x-axis, the circulating field in the cavity corresponds to two FP resonators that are orthogonally polarized, as depicted in Fig. 5.11**(a)**. More precisely, one FP resonance is polarized along the x-axis (FP_x) and the other FP resonance (FP_y) is trapped (i.e. not excited for $\theta = 0°$) on the y-axis.

The FP_y resonance found in this is configuration is, in fact, the same FP_y resonance previously studied in chapter 4 for explaining the polarization induced Fano resonance. The main difference with the previous chapter is, the presence of another FP resonance polarized on the x-axis instead of an optically enhanced guided mode transmitted through the structure. As we will show, this main difference will lead to a substantially different behavior where the structure acts as a dual polarized FP resonator.

As we can expect, the FP_y resonator is excited only for $\theta \neq 0°$ as shown in Fig. 5.11**(b)**. As we can see, the FP_y Fano transmission dip is exactly located at $\lambda/p = 2d/p = 1.9$ while its corresponding transmission peak is very close to it. The FP_x resonance, however, is shifted towards higher wavelength and located approximately at $\lambda/p = 2.33$. This shift is explained by the coupling of the FP_x resonance with the fundamental evanescent mode which leads to a phase value for the reflection different than $-\pi$, as already shown in Fig. 5.10**(b)**. Thus, a small rotation angle induces the excitation of the additional FP_y resonance located at a different wavelength without affecting the FP_x resonance.

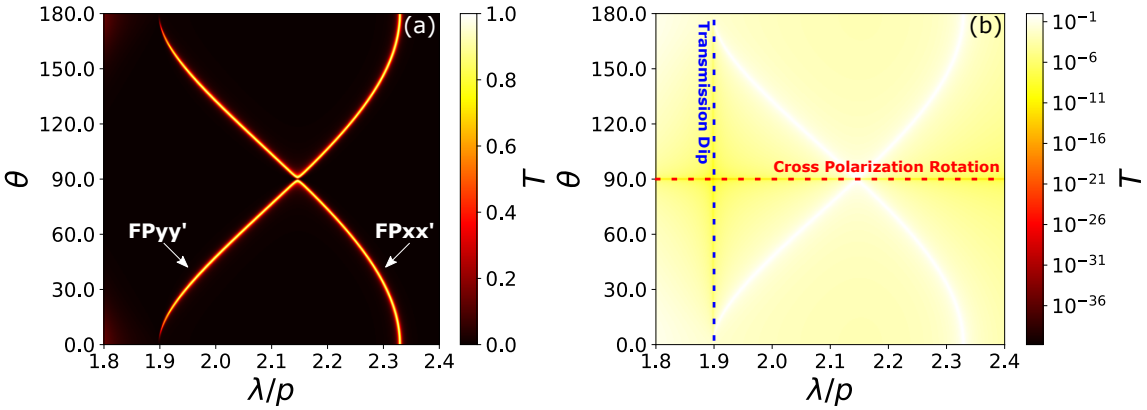

Figure 5.12: **(a)** Evolution of the transmission spectrum with the angle θ. The arrows denotes the two orthogonally polarized FP fundamental harmonics FP_x and FP_y that are excited in the hybridized cavity. **(b)** The logarithmic scale counterpart. The dashed blue line highlight the fano-type transmission dip exactly located at $\lambda/p = 1.9$. The dashed red line denotes the cross-polarization case where the transmission drops to zero.

Figure 5.12**(a)** and **(b)** gives the transmission spectrum as a function of the angle θ in linear and logarithmic scale respectively. It shows the general tendency of the FP resonance according to θ. For small rotation angle ($\theta < 10°$), the FP$_y$ dark mode coupling is low and therefore, its bandwidth is narrow as well. We also note that the transmission peak position barely affected. However for $\theta \in [10°, 89°]$, the spectral shift for both FP resonances is clearly noticeable. In addition, we note that the dark mode's bandwidth becomes constant after $\theta = 30°$. Such spectral shift suggest the emergence of a coupling between the two FP resonances. Indeed, when θ is sufficiently large, the FP standing waves are partially reflected on the two reflection axes at each interface. In other words, for the FP $_y$ (FP$_x$) resonance, the reflection on the x axis (y axis) is not negligible any more. Therefore, the rotation angle provokes a hybridization of the FP cavity. In particular, for $\theta = 89.1°$ the two FP resonances merges with each other at $\lambda/p = 2.145$. For $\theta = 89.1°$, the reflection axes are almost superimposed with their orthogonal counterpart, i.e. the x-axis (y-axis) is almost superimposed with the rotated y-axis (x-axis). Such configuration therefore rotates by almost $90°$ the incident x-polarized light. A structure proposed in [103] also achieved cross-polarization rotation using only two metamaterials polarizers where surface plasmon polaritons - located between the two polarizers - are responsible for the high transmission. In our case however, it purely involves a cavity enhanced transmission, which was - to our knowledge - never reported for only two metamaterial polarizers.

Another interesting possibility would be to reduce the metamaterials thickness to obtain metasurface structure, i.e. a compact structure with a total thickness h_{total} smaller than the transmitted wavelength: $h_{\text{total}} < \lambda$. To this aim, we propose the following geometry:

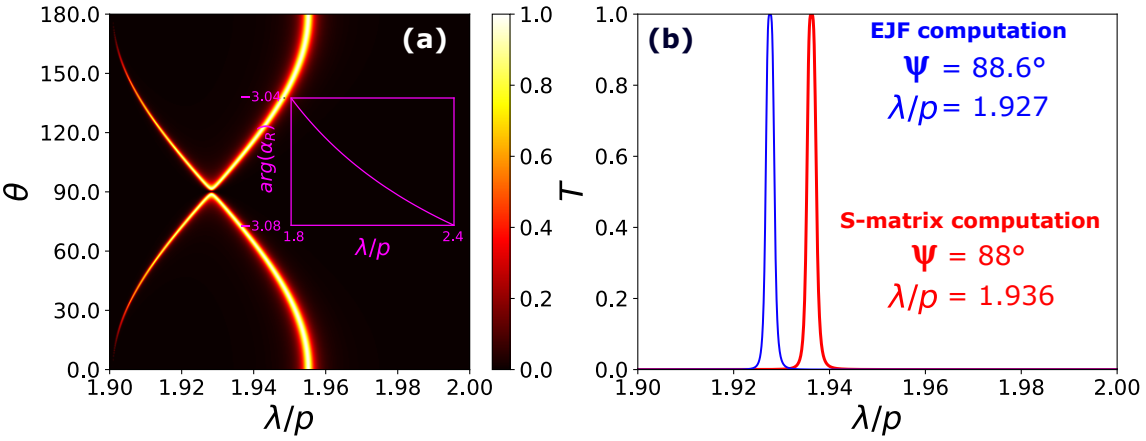

Figure 5.13: **(a)** Evolution of the transmisssion spectrum as a function of θ for $a_x/p = 0.2$, $a_y/p = 0.5$ and $h/p = 0.1$. The inset graph gives the corresponding reflection coefficient phase value for a single metasurface. **(b)** Transmission spectrum for quasi-cross polarization rotation. EJF simulation shows a perfect transmission for $\Psi = 88.6°$ at $\lambda/p = 1.927$ while the S-matrix simulation shows an optimized transmission for Ψ.

$a_x/p = 0.2$, $a_y/p = 0.5$ and $h/p = 0.1$. The separation distance is kept at the same value $d/p = 0.95$. The transmission response as a function of θ is shown in Fig. 5.13**(a)**. As we can see, the transmission response is similar to Fig. 5.12. The main difference is the shift of the spectral position of the FP_x resonance branch. This difference is explained by the new value of $a_y/p = 0.5$ which leads to a cut-off wavelength for the fundamental mode $\lambda_c^{TE_{01}}/p = 2a_y = 1.0$. Since the fundamental mode cut-off is located at a much lower wavelengths compared to the working wavelength, the evanescent fundamental mode is weakly coupled to the FP_x resonance. It results that the reflection phase value is much closer (between -3.04 and -3.08, as shown in the inset purple graph) to that of a perfect reflection phase value (π for a pec). As a consequence, the FP_x resonance at $\theta = 0°$ tends to get closer to the ideal case $\lambda/p = 2d = 1.9$.

In order to validate our model, we compare our EJF-simulated transmission response with an S-matrix computation that takes into account 7 evanescent waveguide modes for the computation. The homemade near-field simulation code does not allows us to directly rotate the second metasurface by an angle θ because the Bravais lattices of each metasurfaces have to remain aligned. However, it is possible to rotate by an angle Ψ the subwavelength aperture inside its own Bravais lattice. For the EJF simulation, a quasi-cross-polarization rotation with perfect transmission is obtained for $\Psi = 88.6°$ at $\lambda/p = 1.927$. For the S-matrix computation, the quasi-cross polarization rotation is achieved for $\Psi = 88°$ at $\lambda/p = 1.936$. This difference between the Bravais lattice and the pattern rotation was discussed in [67]. At this working wavelengths, the thickness of the entire structure is $h_{tot} \approx 0.6\lambda$.

5.5/ SUMMARY

In the first part of this chapter, we have focused on polarization rotation application using large stacked structure ($N \geq 3$). Principally, we have theoretically investigated LPR with an extremely tunable spectral bandwidth and a total transmission. More specifically, the polarizing devices consisted in stacks of MP separated by homogeneous dielectric layers. The numerical results are supported by a new and efficient model from which the Jones matrices of such stacked structures are analytically expressed. The optimized LPR is achieved by regularly rotating the successive MP to mimic a chiral structure. Furthermore, we have underlined the influence of the rectangular holes' width and, more importantly, the angle φ to selectively achieve a broadband or narrowband LPR. Precisely, we have shown that low quality factor ($Q < 10$) and high quality factor ($Q > 10^5$) can be obtained. Most importantly, for the different proposed configurations, the structure ensures a total (or near-total) transmission in the working wavelength range. Besides, the results suggest that the structure is robust against fabrication imperfections or positioning errors. In the second part, we have proposed an original polarization rotation principle based on Fabry-Perot trapped resonance. Based on the model presented in the previous chapter, we have designed a structure, comprising two metamaterials only, that is able to achieve LPR up to $\theta \approx 88^\circ$ on a narrow spectral band. The different proposed configuration could be applied for the design of broadband linear cross-polarization rotators or high-Q filters, which represent important cornerstones in optical communications.

6

CONCLUSIONS

For the conclusions, we first give a summary of the presented work and the main results obtained during this thesis. The general results shown in the manuscript raise some issues and potential ideas for the future. We address the main issues that are crucial for the future fabrication and experiments. We especially emphasize that the potential experimental problems that can be encountered depend on the considered spectral region - from visible to terahertz domain. Then we further discuss some ideas and perspectives from a more theoretical point of view. Principally, we show that more potential applications could be considered by incorporating additional features to the stacked structure, either by considering more bulk properties for the substrate - such as absorption, anisotropy etc... - or by engineering more complex unit cell to the constitutive metamaterials.

6.1/ SUMMARY OF THE WORK

This work is based on a Jones formalism extended to metamaterials extracted from a well-known modal method. It has been recently developed in our team since 2014. During this thesis we have validated this new formalism by comparing it with a rigorous full S-matrix computation for single metallic metamaterials. The assumptions and approximation used have thus been validated. As we already mentioned, these assumptions are judicious and do not greatly influence the accuracy of the results. We remind however that this monomodal formalism is analytical only for certain kind of unit-cell geometry. We have also shown that the EJF agrees very well with rigorous S-matrix algorithm for stacked structure. This Jones formalism could be further applied to metamaterials with more complex shape or to structure that could exhibit imperfections or additional properties. However, for such configuration, the EJF validity should be confirmed again.

Based on this appropriate and efficient model, we have studied many possibilities and

explored interesting physical effects. We have demonstrated that stacked metallic metamaterials can be used for a wide variety of applications such as in sensing, filtering or polarization rotation. We think that our works open new ways to use stacked metallic metamaterials and offer new degrees of freedom compared to single metallic metamaterials. Overall, it suggests that our structure shows high versatility and that probably more application could be considered such as optical switching.

Besides, we have basically revealed that Fano resonances can be induced by the specific polarization properties of metallic metamaterials. First, we have numerically observed the Fano resonances. Second, thanks to the EJF we have simply and analytically demonstrated in our structures the presence of bright and dark modes which are essential for the

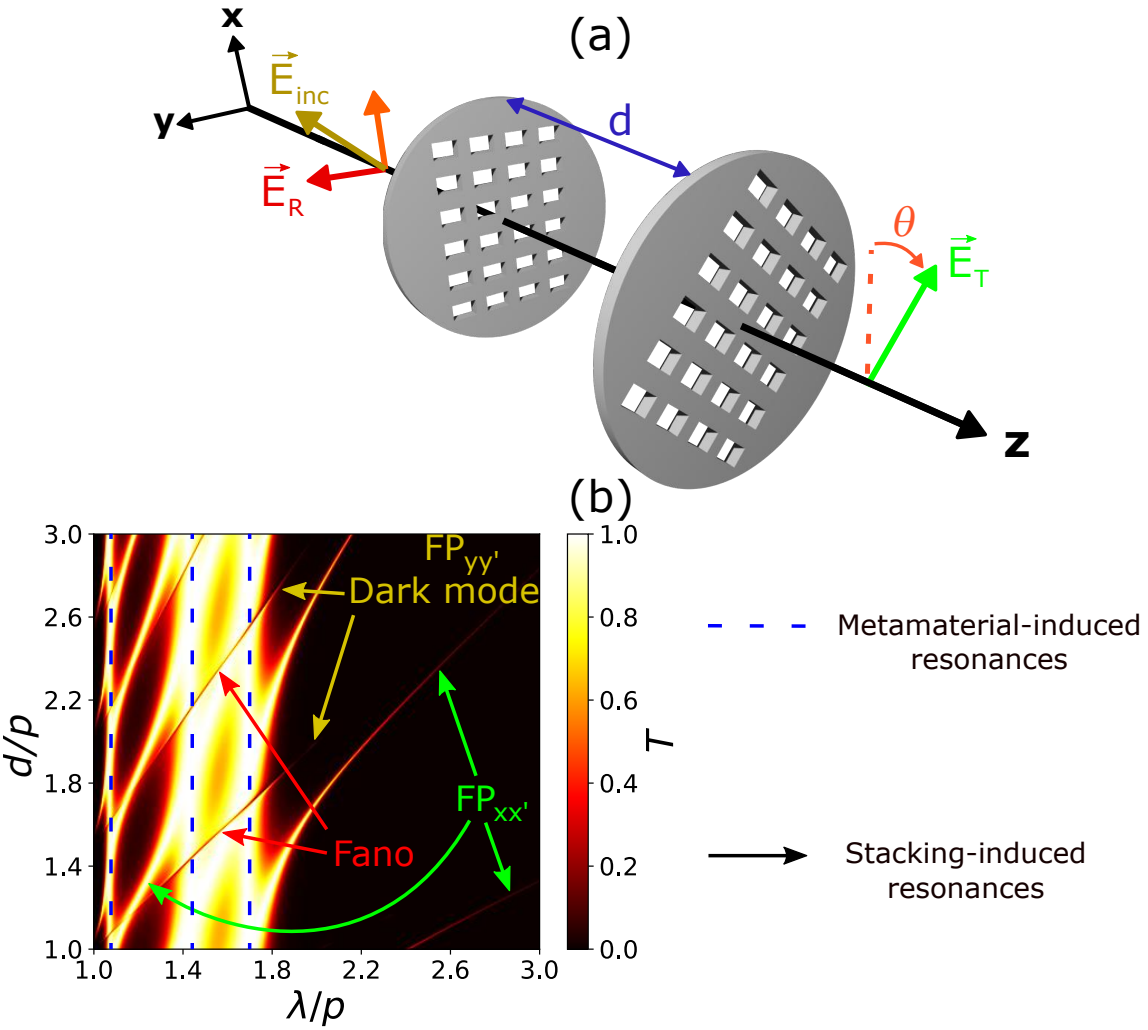

Figure 6.1: **(a)** Reminder on the principle scheme of a stack of two metamaterials separated by a distance d. **(b)** Schematic summary of the resonant behavior of stacked metamaterial polarizers. The dashed vertical blue lines outline the resonance originating from the constitutive metamaterials. The several colored arrows point out the several kind of resonance that arises from the stacking.

Fano resonance formation. Third, we have developed a basic and clear physical model of the polarization-induced Fano resonance process. This overall study gives us a precise, clear and rather simple method to design structure based on Fano resonance.

Figure 6.1**(b)** summarizes the different effects and resonances that have been studied in this thesis. It shows more clearly the complexity of stacked metamaterials and the diversity of phenomena that can occur in such structure. It shows the transmission spectrum as a function of the distance between 2 biperiodic metallic polarizers, as depicted in Fig. 6.1**(a)**. The parameters are $a_x/p = 0.45$, $a_y/p = 0.9$, $h/p = 1.0$ and $\theta = 10°$.

The resonance marked by the dashed vertical lines are due to the resonant properties of the metallic metamaterials. The resonances highlighted by the colored arrows originates from the metamaterials stacking.

There are however some numerical results in the fourth chapter which have not been completely clarified. Indeed, in Fig. 5.6 (now plotted below in Fig. 6.2**(b)**), we numerically showed the spectral narrowing of the transmission response when $\varphi \to 90°$ for $N \geq 3$. The corresponding comment for these results does not give a complete and satisfactory explanation as it does not provide the underlying origin of this phenomenon. It is even more intriguing to see that in chapter 2, this spectral narrowing is not observed when using only 2 metamaterial polarizers (see Fig. 6.2**(a)**). The comparison between $N = 2$ and $N = 3$ is given in Fig. 6.2. The discrepancy between these two distinct configurations - $N = 2$ and $N = 3$ - can been seen as a clue and is the starting point of a future analysis. For now, we suspect that a kind of Fano-like resonance is involved.

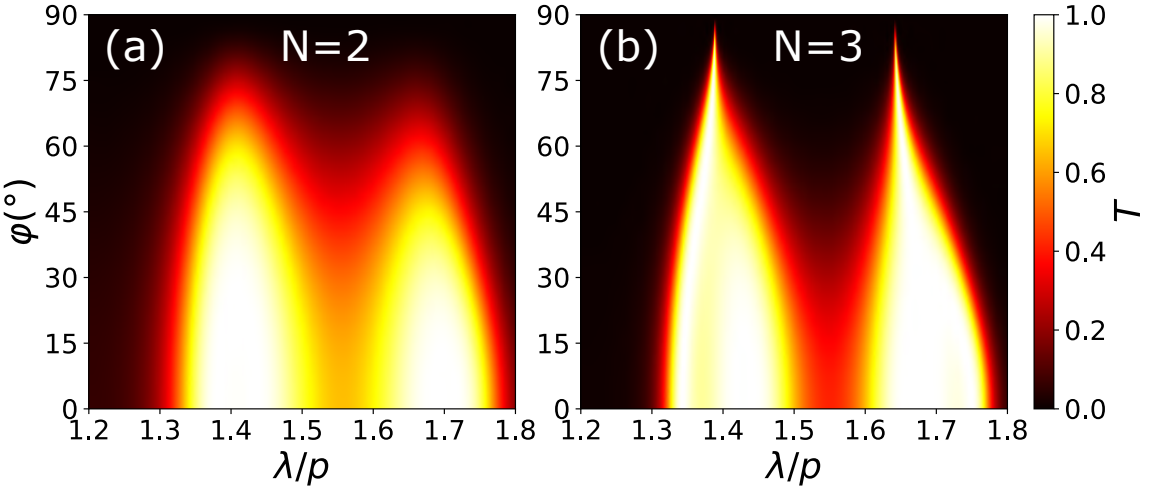

Figure 6.2: **(a)** Transmission spectrum through a stack of 2 metamaterials as a function of φ, the progressive rotation angle. **(b)** For 3 stacked metamaterials.

6.2/ EXPERIMENTAL PERSPECTIVES

As we mentioned in the chapter 2 that covers the theoretical modelling, the EJF can be arbitrarily scaled to any spectral range. For each region come specific challenges or issues for fabrication and experiments. This is mainly due to the spectral dependency of the materials properties and the overall dimension of the fabricated sample. In this section, we present some of the main problems that will be encountered for future fabrication and experiments. We also discuss some solutions to overcome or solve those problems.

From our standpoint, the visible and near-infrared spectral domain are the most challenging area for the fabrication. First, the metal absorption is larger than for THz or microwaves and is not at all negligible. When considering application with high sensitivity, the metal absorption will impose a limit to the quality factor values. Even highly conducting metals exhibit few percent of absorption that are detrimental to efficiently achieve a cavity effect. Special coating will have to be considered in order to increase the metamaterials reflectivity. Second, the sub-micron structure dimensions requires the use of dielectric substrates to deposit and engineer the metal. This essential step also induces more limitations. The air-dielectric and dielectric-metal interface implies unwanted Fresnel reflections and a TEM Floquet mode cut-off wavelength shifts (as seen in chapter 3). Furthermore, the substrate can also exhibit losses, anisotropy etc... In addition, we have to keep in mind that increasing the number of stacked metamaterials also cascade the losses and imperfections (inhomogeneity, absorption and so on) ”seen” by the light as it propagates through the structure. Therefore, some of the studied applications including a large number of stacked metamaterial seems highly complicated to achieve without important performance degradation. Finally, one has to keep in mind that if two metamaterials are deposited at each substrate facet, we permanently loose the angular tunability between them.

Nonetheless, there are some positive counterparts in the visible that has also to be mentioned. First, dielectric substrates naturally feature higher refractive indices than air or vacuum. It implies that placing a substrate between two metamaterials allows us to proportionally reduce its thickness to excite Fano and/or Fabry-Perot resonances at the same spectral position. It then permits the design of more compact devices. Second, the absorption of the substrate is not necessarily detrimental to the cavity effect. Indeed, the propagation losses could be neglected since the propagation distance is very small, even after a large number of cavity round trips. Third, the finite conductivity of metal can be beneficial for broadband application since it increases the metamaterials radiation losses. It would be for example, interesting for broadband cross-polarization rotation.

For the terahertz domain, the fabrication and experimental aspects are drastically different from the visible and near-infrared. First, for most metals, the reflectivity is very close to 100% and the pec approximation thus very close to reality. It makes the high-Q Fano based application possible and easier to be designed. Second, given the considered wavelength, the overall studied structures are much larger and the metamaterials unit-cell dimensions reach the order of tens or hundreds of micrometers or even millimeters. Therefore, the use of a substrate could be avoided and the stacked metamaterials could be ”freestanding” in air or vacuum. However, a mechanical device for the alignment and the structure tunability would then be necessary. More generally, the fabrication process is likely to be cheaper, easier and less time consuming.

Even though the structure are handled more easily than in visible, they are also obviously much larger in dimensions, thus less compact. The necessary mechanical maintaining device also increase the final size of the structure. The overall volume occupied by the device is likely to reach few millimeter or centimeter cubes. Such volume may be important depending on the desired integrability. Compared to the optical domain, the terahertz domain has also much less technological maturity. Characterizing these structures in the THz will highly depend on the available sources and detectors. Note that stacked metallic metamaterials could also be used to develop new tools for the THz and participate to cover the so called ”THz gap” [220–222].

Metals in the microwave domain shares the same specificity as for the THz, i.e. very high electrical conductivity. For the microwaves however, the structures dimensions can reach very large values, up to meter size which is simply not practical. For this domain, the relevance of stacked metallic metamaterials has to be discussed and such structures should be compared with the already available technologies.

For all spectral regions, the metamaterials parallelism is critical to obtain good performances and good cavity effect. The parallelism is however more easy to control and adjust for larger metamaterials dimensions. If a substrate is needed, the substrate thickness variation has also to be taken into account. We remind that the model developed during this thesis considers metamaterials with infinite periodicity. The finite metamaterials dimension should also be considered for ultimate practical design. In the theory, the misalignments between infinitely periodic metamaterials does not lead to a substantial degradation of the cavity effect. It merely shifts the Fabry-Perot and Fano resonances in the cavity. From the experimental point of view however, finite and not parallel metamaterials could cause the light to ”go out” of the polarized cavity after enough multiple reflections.

As we have seen in this section, many aspects and issues have to be considered for the

practical fabrication and experimental demonstrations. To conclude this discussion, we think that the terahertz domain offers the best compromise between fabrication, compactness and performance.

6.3/ THEORETICAL PERSPECTIVES

In the last section, we discussed the main issues and key points to experimentally apply the concepts and applications we have presented in the manuscript. Nonetheless, we have not yet envisioned a more general interpretation of the studied structure nor the potential implications of the main results.

Our theoretical model considers metamaterials that are surrounded and separated by homogeneous, linear, isotropic and lossless layers. Nonetheless, we have developed an original formalism on stacked metamaterials that could help us to incorporate different layers. For example, taking into account an anisotropic separation layer would probably imply a phase difference between the bright mode and the dark mode. This could be exploited further to fine tune Fano resonances excited in the structure. In the same manner, carefully designed inhomogeneous layers could bring more functionalities to stacked metamaterials. Furthermore, separation layers featuring optical activity would be another way to couple the bright and dark mode in our structure. It has to be noted that, from a purely mathematical point of view, the matrix representing a chiral layer would be equivalent to the rotation of one metamaterials via the rotation matrix $R(\theta)$. One could expect the same results and performances by including a chiral layer instead of rotating the metamaterials. There is currently a trend on phase change materials such as VO_2 [198, 223] which could be studied in order to add more functionalities to stacked structures. Finally, the Fabry-Perot dark mode could also be used to progressively absorb light at precise wavelengths, either by relying on the metal absorption or by inserting an absorptive material.

Another aspect that has not been considered yet is the field enhancement that occurs in between the metamaterials because of the multiple reflections. The cavity effect we have studied could be also used to achieve optical nonlinearities in a purposefully inserted nonlinear medium. More generally, the inclusion of a gain medium could be considered to propose laser cavity with special polarization effects.

The possibilities we have just mentioned above rely on additional bulk properties of the separation layers. However, a second main possibility has to be considered, that is to say, adding more ”complexity” to the metamaterial itself. A direct option would be to use

the EJF to model unit-cell featuring two orthogonally polarized modes (bimodal method) to design and stack artificial anisotropic metallic metamaterial. Such structure could allow the control of Fano resonance in an original way. Another direct option would be to consider stacked metamaterials with different unit-cell in order to add more degree of freedom for controlling the Fano resonance excitation. More complex unit-cell shape could also be envisaged. In this case, other simulation techniques - such as FDTD, FEM etc... - will be necessary to model the metamaterials properties. Furthermore, we have not thoroughly studied the possibilities offered by the near-field yet. It would be nonetheless interesting to analyse stacked structures with separation distances that are much smaller than the wavelength to analyse the influence of the evanescent waveguide mode and their near-field propagation.

We have mentioned in the introduction that stacked metamaterials are proposed because of the higher degree of freedom (metamaterials position and rotation) and the new possibilities they can offer. As we have suggested, the main outcome of this PhD thesis can serve as a basis to further study more complex structures. The combination of separation layers having specific properties - such as anisotropy or nonlinearity - together with metamaterials having more complex unit-cell would probably allow for even more degrees of freedom while the number of configurations and possibilities grows exponentially.

As a final remark of this manuscript, we would like to stand back and try to give a more general description of these structures. If we look back at the first studied stack (made of two metamaterials), we could simply summarize it as a polarized Fabry-Perot cavity that hosts a Fabry-Perot dark mode. This exotic feature arises from the interdependency between the polarization properties and the reflection properties of the structure. More specifically, if the metamaterial are considered in transmission regime ($p < \lambda < \lambda_{TE_{01}}$), the stacked structures combine a ”single pass” bright mode on the transmission x-axis and stacked ”multi pass” dark mode on the y-axis. It is very important to remind that such physics originates from very simple and basic polarization properties of the constitutive metamaterials. It would be interesting to seek materials - other than metamaterials - that could exhibit the same basic polarization properties. From a more general perspective, Fabry-Perot cavities are widely used in optics and therefore, this present work could find use in a large diversity of device and application in optics.

BIBLIOGRAPHY

[1] ABBOT, B. P., AND OTHERS. **Observation of Gravitational Waves from a Binary Black Hole Merger**. *Physical Review Letters 116*, 6 (Feb. 2016), 061102.

[2] HECHT, J. **Understanding fiber optics**. Prentice Hall, 2002.

[3] AGRAWAL, G. P. **Fiber-Optic Communication Systems**. John Wiley & Sons, Feb. 2012.

[4] TUCHIN, V. **Tissue Optics: Light Scattering Methods and Instruments for Medical Diagnosis**. SPIE, 2015.

[5] MOORE, G. E. **Cramming more components onto integrated circuits**. *Electronics 38*, 8 (1965).

[6] NOVOTNY, L., AND HECHT, B. **Principles of nano-optics**. Cambridge university press, 2006.

[7] JOANNOPOULOS, J. D., JOHNSON, S. G., WINN, J. N., AND MEADE, R. D. **Photonic Crystals: Molding the Flow of Light, Second Edition**. Princeton University Press, Oct. 2011.

[8] QIU, W., NDAO, A., VILA, V. C., SALUT, R., COURJAL, N., BAIDA, F. I., AND BERNAL, M.-P. **Fano resonance-based highly sensitive, compact temperature sensor on thin film lithium niobate**. *Optics Letters 41*, 6 (Mar. 2016), 1106.

[9] QIU, W., LU, H., BAIDA, F. I., AND BERNAL, M.-P. **Ultra-compact on-chip slot Bragg grating structure for small electric field detection**. *Photonics Research 5*, 3 (June 2017), 212.

[10] PENDRY, J. B. **Negative refraction makes a perfect lens**. *Physical review letters 85*, 18 (2000), 3966.

[11] LEONHARDT, U. **Optical Conformal Mapping**. *Science 312*, 5781 (June 2006), 1777–1780.

[12] PENDRY, J. B. **Controlling Electromagnetic Fields**. *Science 312*, 5781 (June 2006), 1780–1782.

[13] ALÙ, A., SILVEIRINHA, M. G., SALANDRINO, A., AND ENGHETA, N. **Epsilon-near-zero metamaterials and electromagnetic sources: Tailoring the radiation phase pattern**. *Physical Review B 75*, 15 (Apr. 2007).

[14] LANDY, N. I., SAJUYIGBE, S., MOCK, J. J., SMITH, D. R., AND PADILLA, W. J. **Perfect Metamaterial Absorber**. *Physical Review Letters 100*, 20 (May 2008).

[15] PLUM, E., LIU, X.-X., FEDOTOV, V. A., CHEN, Y., TSAI, D. P., AND ZHELUDEV, N. I. **Metamaterials: Optical Activity without Chirality**. *Physical Review Letters 102*, 11 (Mar. 2009).

[16] CAI, W., AND SHALAEV, V. **Optical Metamaterials**. Springer New York, New York, NY, 2010.

[17] HOLLOWAY, C. L., KUESTER, E. F., GORDON, J. A., O'HARA, J., BOOTH, J., AND SMITH, D. R. **An Overview of the Theory and Applications of Metasurfaces: The Two-Dimensional Equivalents of Metamaterials**. *IEEE Antennas and Propagation Magazine 54*, 2 (Apr. 2012), 10–35.

[18] YU, N., GENEVET, P., KATS, M. A., AIETA, F., TETIENNE, J.-P., CAPASSO, F., AND GABURRO, Z. **Light Propagation with Phase Discontinuities: Generalized Laws of Reflection and Refraction**. *Science 334*, 6054 (Oct. 2011), 333–337.

[19] NI, X., ISHII, S., KILDISHEV, A. V., AND SHALAEV, V. M. **Ultra-thin, planar, Babinet-inverted plasmonic metalenses**. *Light: Science & Applications 2*, 4 (Apr. 2013).

[20] SMITH, D. R., PENDRY, J. B., AND WILTSHIRE, M. C. K. **Metamaterials and negative refractive index**. *Science 305*, 5685 (2004), 788–792.

[21] KILDISHEV, A. V., BOLTASSEVA, A., AND SHALAEV, V. M. **Planar Photonics with Metasurfaces**. *Science 339*, 6125 (Mar. 2013), 1232009–1232009.

[22] NDAO, A., BELKHIR, A., SALUT, R., AND BAIDA, F. I. **Slanted annular aperture arrays as enhanced-transmission metamaterials: Excitation of the plasmonic transverse electromagnetic guided mode**. *Applied Physics Letters 103*, 21 (Nov. 2013), 211901.

[23] GANSEL, J. K., THIEL, M., RILL, M. S., DECKER, M., BADE, K., SAILE, V., VON FREYMANN, G., LINDEN, S., AND WEGENER, M. **Gold Helix Photonic Metamaterial as Broadband Circular Polarizer**. *Science 325*, 5947 (Sept. 2009), 1513–1515.

[24] EBBESEN, T. W., LEZEC, H. J., GHAEMI, H. F., THIO, T., AND WOLFF, P. A. **Extraordinary optical transmission through sub-wavelength hole arrays**. *Nature 391*, 6668 (Feb. 1998), 667–669.

[25] BETHE, H. A. **Theory of Diffraction by Small Holes**. *Physical Review 66*, 7-8 (Oct. 1944), 163–182.

[26] RITCHIE, R. H., ARAKAWA, E. T., COWAN, J. J., AND HAMM, R. N. **Surface-plasmon resonance effect in grating diffraction**. *Physical Review Letters 21*, 22 (1968), 1530.

[27] MAIER, S. A. **Plasmonics: Fundamentals and Applications**. Springer Science & Business Media, May 2007.

[28] PORTO, J. A., GARCÍA-VIDAL, F. J., AND PENDRY, J. B. **Transmission Resonances on Metallic Gratings with Very Narrow Slits**. *Physical Review Letters 83*, 14 (Oct. 1999), 2845–2848.

[29] POPOV, E., NEVIÈRE, M., ENOCH, S., AND REINISCH, R. **Theory of light transmission through subwavelength periodic hole arrays**. *Physical Review B 62*, 23 (Dec. 2000), 16100–16108.

[30] CAO, Q., AND LALANNE, P. **Negative Role of Surface Plasmons in the Transmission of Metallic Gratings with Very Narrow Slits**. *Physical Review Letters 88*, 5 (Jan. 2002), 057403.

[31] ASTILEAN, S., LALANNE, P., AND PALAMARU, M. **Light transmission through metallic channels much smaller than the wavelength**. *Optics Communications 175*, 4–6 (Mar. 2000), 265–273.

[32] BAIDA, F. I., AND VAN LABEKE, D. **Light transmission by subwavelength annular aperture arrays in metallic films**. *Optics Communications 209*, 1–3 (Aug. 2002), 17–22.

[33] BAIDA, F. I., AND VAN LABEKE, D. **Three-dimensional structures for enhanced transmission through a metallic film: Annular aperture arrays**. *Physical Review B 67*, 15 (Apr. 2003), 155314.

[34] BAIDA, F., VAN LABEKE, D., GRANET, G., MOREAU, A., AND BELKHIR, A. **Origin of the super-enhanced light transmission through a 2-D metallic annular aperture array: a study of photonic bands**. *Applied Physics B 79*, 1 (July 2004), 1–8.

[35] MOREAU, A., GRANET, G., BAIDA, F., AND VAN LABEKE, D. **Light transmission by subwavelength square coaxial aperture arrays in metallic films**. *Optics Express 11*, 10 (May 2003), 1131–1136.

[36] POUJET, Y., ROUSSEY, M., SALVI, J., BAIDA, F. I., VAN LABEKE, D., PERENTES, A., SANTSCHI, C., AND HOFFMANN, P. **Super-transmission of light through subwavelength annular aperture arrays in metallic films: Spectral analysis and near-field optical images in the visible range**. *Photonics and Nanostructures - Fundamentals and Applications 4*, 1 (Feb. 2006), 47–53.

[37] POUJET, Y., SALVI, J., AND BAIDA, F. I. **90% Extraordinary optical transmission in the visible range through annular aperture metallic arrays**. *Optics Letters 32*, 20 (Oct. 2007), 2942–2944.

[38] BOYER, P., AND VAN LABEKE, D. **Analytical study of resonance conditions in planar resonators**. *Journal of the Optical Society of America A 29*, 8 (Aug. 2012), 1659–1666.

[39] CHANDEZON, J., RAOULT, G., AND MAYSTRE, D. **A new theoretical method for diffraction gratings and its numerical application**. *Journal of Optics 11*, 4 (July 1980), 235–241.

[40] CALOZ, C., AND TATSUO, I. **Electromagnetic Metamaterials Transmission Line Theory**. 2005.

[41] AZNAR, F., GIL, M., BONACHE, J., AND MARTÍN, F. **Modelling metamaterial transmission lines: a review and recent developments**. *Opto-Electronics Review 16*, 3 (Jan. 2008).

[42] ANTONAKAKIS, T., BAIDA, F. I., BELKHIR, A., CHEREDNICHENKO, K., COOPER, S., CRASTER, R., DEMÉSY, G., DESANTO, J., GRANET, G., GRALAK, B., GORAY, L., LI, L., MAYSTRE, D., STOUT, B., ZOLLA, F., SCHMIDT, G., SKELETON, E., GUENNEAU, S., NICOLET, A., POPOV, E., AND VIAL, B. **Gratings: Theory and Numeric Applications, Second Revisited Edition**. AMU, (PUP), CNRS, ECM, Nov. 2014.

[43] LI, J., AND HUANG, Y. **Time-Domain Finite Element Methods for Maxwell's Equations in Metamaterials**, vol. 43 of *Springer Series in Computational Mathematics*. Springer Berlin Heidelberg, Berlin, Heidelberg, 2013.

[44] KOLUNDŽIJA, B. M., AND DJORDJEVIĆ, A. R. **Electromagnetic modeling of composite metallic and dielectric structures**. Artech House antennas and propagation library. Artech House, Boston, 2002.

[45] MOHARAM, M. G., AND GAYLORD, T. K. **Rigorous coupled-wave analysis of planar-grating diffraction**. *Journal of the Optical Society of America 71*, 7 (July 1981), 811–818.

[46] POMP, A. **The Integral Method for Coated Gratings: Computational Cost**. *Journal of Modern Optics 38*, 1 (Jan. 1991), 109–120.

[47] BOYER, P. **Elaboration d'une méthode différentielle pour l'étude des fibres optiques microstructurées**. PhD thesis, Aix-Marseille, 2006.

[48] PETIT, R., Ed. **Electromagnetic Theory of Gratings**, vol. 22 of *Topics in Current Physics*. Springer Berlin Heidelberg, Berlin, Heidelberg, 1980.

[49] DEGIRON, A., LEZEC, H., YAMAMOTO, N., AND EBBESEN, T. **Optical transmission properties of a single subwavelength aperture in a real metal**. *Optics Communications 239*, 1-3 (Sept. 2004), 61–66.

[50] SARRAZIN, M., AND VIGNERON, J.-P. **Polarization effects in metallic films perforated with a bidimensional array of subwavelength rectangular holes**. *Optics Communications 240*, 1-3 (Oct. 2004), 89–97.

[51] DIMAIO, J. R., AND BALLATO, J. **Polarization-dependent transmission through subwavelength anisotropic aperture arrays**. *Optics express 14*, 6 (2006), 2380–2384.

[52] GORDON, R., BROLO, A. G., MCKINNON, A., RAJORA, A., LEATHEM, B., AND KAVANAGH, K. L. **Strong Polarization in the Optical Transmission through Elliptical Nanohole Arrays**. *Physical Review Letters 92*, 3 (Jan. 2004).

[53] STRELNIKER, Y. M. **Theory of optical transmission through elliptical nanohole arrays**. *Physical Review B 76*, 8 (Aug. 2007).

[54] ELSER, J., WANGBERG, R., PODOLSKIY, V. A., AND NARIMANOV, E. E. **Nanowire metamaterials with extreme optical anisotropy**. *Applied Physics Letters 89*, 26 (Dec. 2006), 261102.

[55] HAO, J., YUAN, Y., RAN, L., JIANG, T., KONG, J. A., CHAN, C. T., AND ZHOU, L. **Manipulating Electromagnetic Wave Polarizations by Anisotropic Metamaterials**. *Physical Review Letters 99*, 6 (Aug. 2007).

[56] FEDOTOV, V. A., MLADYONOV, P. L., PROSVIRNIN, S. L., ROGACHEVA, A. V., CHEN, Y., AND ZHELUDEV, N. I. **Asymmetric Propagation of Electromagnetic Waves through a Planar Chiral Structure**. *Physical Review Letters 97*, 16 (Oct. 2006).

[57] VALLIUS, T., JEFIMOVS, K., TURUNEN, J., VAHIMAA, P., AND SVIRKO, Y. **Optical activity in subwavelength-period arrays of chiral metallic particles**. *Applied Physics Letters 83*, 2 (July 2003), 234–236.

[58] BAIDA, F. I., BOUTRIA, M., OUSSAID, R., AND VAN LABEKE, D. **Enhanced-transmission metamaterials as anisotropic plates**. *Physical Review B 84*, 3 (July 2011), 035107.

[59] DAHDAH, J., HOBLOS, J., AND BAIDA, F. I. **Nanocoaxial Waveguide Grating as Quarter-Wave Plates in the Visible Range**. *IEEE Photonics Journal 4*, 1 (Feb. 2012), 87–94.

[60] SHEN, B., WANG, P., POLSON, R., AND MENON, R. **Ultra-high-efficiency metamaterial polarizer**. *Optica 1*, 5 (Nov. 2014), 356.

[61] PELZMAN, C., AND CHO, S.-Y. **Polarization-selective optical transmission through a plasmonic metasurface**. *Applied Physics Letters 106*, 25 (June 2015), 251101.

[62] PFEIFFER, C., AND GRBIC, A. **Controlling Vector Bessel Beams with Metasurfaces**. *Physical Review Applied 2*, 4 (Oct. 2014), 044012.

[63] MENZEL, C., ROCKSTUHL, C., AND LEDERER, F. **Advanced Jones calculus for the classification of periodic metamaterials**. *Physical Review A 82*, 5 (Nov. 2010).

[64] KRUK, S. S., PODDUBNY, A. N., POWELL, D. A., HELGERT, C., DECKER, M., PERTSCH, T., NESHEV, D. N., AND KIVSHAR, Y. S. **Polarization properties of optical metasurfaces of different symmetries**. *Physical Review B 91*, 19 (May 2015).

[65] BOYER, P. **Jones matrices of perfectly conducting metallic polarizers**. *Journal of the Optical Society of America A 31*, 6 (June 2014), 1226.

[66] CHENG, H., LIU, Z., CHEN, S., AND TIAN, J. **Emergent Functionality and Controllability in Few-Layer Metasurfaces**. *Advanced Materials 27*, 36 (Sept. 2015), 5410–5421.

[67] BOUTRIA, M., OUSSAID, R., VAN LABEKE, D., AND BAIDA, F. I. **Tunable artificial chirality with extraordinary transmission metamaterials**. *Physical Review B 86*, 15 (Oct. 2012).

[68] ASKARPOUR, A. N., ZHAO, Y., AND ALÙ, A. **Wave propagation in twisted metamaterials**. *Physical Review B 90*, 5 (Aug. 2014), 054305.

[69] MENZEL, C., SPERRHAKE, J., AND PERTSCH, T. **Efficient treatment of stacked metasurfaces for optimizing and enhancing the range of accessible optical functionalities**. *Physical Review A 93*, 6 (June 2016).

[70] RANJBAR, A., AND GRBIC, A. **Analysis and synthesis of cascaded metasurfaces using wave matrices**. *Physical Review B 95*, 20 (May 2017).

[71] PFEIFFER, C., ZHANG, C., RAY, V., GUO, L. J., AND GRBIC, A. **High Performance Bianisotropic Metasurfaces: Asymmetric Transmission of Light**. *Physical Review Letters 113*, 2 (July 2014).

[72] PFEIFFER, C., AND TOMASIC, B. **Linear-to-Circular Polarizers for Multi-Octave Bandwidths and Wide Scan Angles at MM-Wave Frequencies Using Rotated Anisotropic Layers**. *Progress In Electromagnetics Research C 79* (2017), 49–64.

[73] LIN, Z., GROEVER, B., CAPASSO, F., RODRIGUEZ, A. W., AND LONČAR, M. **Topology Optimized Multi-layered Meta-optics**. *arXiv:1706.06715 [physics]* (June 2017). arXiv: 1706.06715.

[74] TIERNEY, B. B., AND GRBIC, A. **Controlling Leaky Waves with 1-D Cascaded Metasurfaces**. *IEEE Transactions on Antennas and Propagation* (2018), 1–1.

[75] BHATTACHARYYA, A. K. **Phased Array Antennas: Floquet Analysis, Synthesis, BFNs, and Active Array Systems**. John Wiley & Sons, Inc., Hoboken, NJ, USA, Dec. 2005.

[76] MUNK, B. A. **Frequency Selective Surfaces, Theory and Design**. Wiley, 2000.

[77] LOEWEN, E. G., AND POPOV, E. **Diffraction Gratings and Applications**. CRC Press, May 1997.

[78] AMITAY, N., AND GALINDO, V. **The analysis of circular waveguide phased arrays**. *The Bell System Technical Journal 47*, 9 (Nov. 1968), 1903–1932.

[79] CHAO-CHUN CHEN. **Transmission through a Conducting Screen Perforated Periodically with Apertures**. *IEEE Transactions on Microwave Theory and Techniques 18*, 9 (Sept. 1970), 627–632.

[80] KANTOROVIČ, L. V., AKILOV, G. P., AND SILCOCK, H. L. **Functional analysis**, 2. ed ed. Pergamon Pr, Oxford u.a, 1982.

[81] HARRINGTON, R. F. **Field Computation by Moment Methods**. Wiley-IEEE Press, 1968.

[82] AMITAY, N., AND GALINDO, V. **On energy conservation and the method of moments in scattering problems**. *IEEE Transactions on Antennas and Propagation 17*, 6 (Nov. 1969), 747–751.

[83] CHAO-CHUN CHEN. **Transmission of Microwave Through Perforated Flat Plates of Finite Thickness**. *IEEE Transactions on Microwave Theory and Techniques 21*, 1 (Jan. 1973), 1–6.

[84] MCPHEDRAN, R. C., AND MAYSTRE, D. **On the theory and solar application of inductive grids**. *Applied physics 14*, 1 (1977), 1–20.

[85] JACKSON, J. D. **Classical electrodynamics**. John Wiley & Sons, 2012.

[86] LALANNE, P., HUGONIN, J. P., ASTILEAN, S., PALAMARU, M., AND MÖLLER, K. D. **One-mode model and Airy-like formulae for one-dimensional metallic gratings**. *Journal of Optics A: Pure and Applied Optics 2*, 1 (Jan. 2000), 48.

[87] MUNK, B. **Finite antenna arrays and FSS**. IEEE Press ; Wiley-Interscience, Hoboken, N.J, 2003.

[88] GANS, M. **A General Proof of Floquet's Theorem (Correspondence)**. *IEEE Transactions on Microwave Theory and Techniques 13*, 3 (May 1965), 384–385.

[89] KITTEL, C. **Introduction to solid state physics**, 8th ed ed. Wiley, Hoboken, NJ, 2005.

[90] WOOD, R. W. **On a Remarkable Case of Uneven Distribution of Light in a Diffraction Grating Spectrum**. *Proceedings of the Physical Society of London 18*, 1 (June 1902), 269.

[91] RAYLEIGH, L. **On the Dynamical Theory of Gratings**. *Proceedings of the Royal Society of London. Series A, Containing Papers of a Mathematical and Physical Character 79*, 532 (Aug. 1907), 399–416.

[92] POZAR, D. M. **Microwave Engineering**. Wiley, Feb. 2004.

[93] HAUS, H. A., AND MELCHER, J. R. **Electromagnetic fields and energy**. Prentice Hall, 1989.

[94] De Feijter, J. A., Benjamins, J., and Veer, F. A. **Ellipsometry as a tool to study the adsorption behavior of synthetic and biopolymers at the air-water interface**. *Biopolymers 17*, 7 (July 1978), 1759–1772.

[95] Romain, X., Baida, F., and Boyer, P. **Extended Malus law with terahertz metallic metamaterials for sensitive detection with giant tunable quality factor**. *Physical Review B 94*, 4 (July 2016).

[96] Maxwell, J. C. **A Treatise on Electricity and Magnetism**. *Cambridge Core* (June 2010).

[97] Huygens, C. **Treatise on Light**. Echo Library, 1690.

[98] Malus, E. L. **Mémoire sur la mesure du pouvoir réfringent des corps opaques**. *Nouveau Bulletin des Sciences par la Société Philomaiques de Paris*, 4 (Jan. 1808), 77 – 81.

[99] Hart, M., and D. Rodrigues, A. R. **Optical activity and the Faraday effect at X-ray frequencies**. *Philosophical Magazine B 43*, 2 (Feb. 1981), 321–332.

[100] Li, W., Lu, X., and Lin, Y. **Novel Absolute Displacement Sensor with Wide Range Based on Malus Law**. *Sensors 9*, 12 (Dec. 2009), 10411–10422.

[101] Brukner, C., and Zeilinger, A. **Malus' law and quantum information**. *acta physica slovaca 49* (1999), 647–652.

[102] Vallet, M., Bretenaker, F., Le Floch, A., Le Naour, R., and Oger, M. **The Malus Fabry–Perot interferometer**. *Optics Communications 168*, 5-6 (1999), 423–443.

[103] Huang, C.-p., Wang, Q.-j., Yin, X.-g., Zhang, Y., Li, J.-q., and Zhu, Y.-y. **Break Through the Limitation of Malus' Law with Plasmonic Polarizers**. *Advanced Optical Materials 2*, 8 (Aug. 2014), 723–728.

[104] Zhang, C., Pfeiffer, C., Jang, T., Ray, V., Junda, M., Uprety, P., Podraza, N., Grbic, A., and Guo, L. J. **Breaking Malus' law: Highly efficient, broadband, and angular robust asymmetric light transmitting metasurface: Breaking Malus' law**. *Laser & Photonics Reviews* (Aug. 2016).

[105] Liu, D.-Y., Li, M.-H., Zhai, X.-M., Yao, L.-F., and Dong, J.-F. **Enhanced asymmetric transmission due to Fabry-Perot-like cavity**. *Optics Express 22*, 10 (May 2014), 11707.

[106] XIAO, Z.-Y., LIU, D.-J., MA, X.-L., AND WANG, Z.-H. **Multi-band transmissions of chiral metamaterials based on Fabry-Perot like resonators**. *Optics Express 23*, 6 (Mar. 2015), 7053.

[107] WANG, H.-B., ZHOU, X., TANG, D.-F., AND DONG, J.-F. **Diode-like broadband asymmetric transmission of linearly polarized waves based on Fabry–Perot-like resonators**. *Journal of Modern Optics* (Nov. 2016), 1–10.

[108] LI, L. **Formulation and comparison of two recursive matrix algorithms for modeling layered diffraction gratings**. *Journal of the Optical Society of America A 13*, 5 (May 1996), 1024–1035.

[109] REDHEFFER, R. **On the relation of transmission-line theory to scattering and transfer**. *Studies in Applied Mathematics 41*, 1-4 (1962), 1–41.

[110] MONTIEL, F., AND NEVIERE, M. **Perfectly conducting gratings: a new approach using infinitely thin strips**. *Optics Communications 144*, 1-3 (Dec. 1997), 82–88.

[111] BOYER, P., AND VAN LABEKE, D. **Analytical scattering matrix of subwavelength infinitely conducting metallic gratings in TM polarization**. *arXiv:1303.4189 [physics]* (Mar. 2013). arXiv: 1303.4189.

[112] NAFTALY, M., AND DUDLEY, R. **Terahertz reflectivities of metal-coated mirrors**. *Applied optics 50*, 19 (2011), 3201–3204.

[113] WU, Q., AND ZHANG, X.-C. **Design and characterization of traveling-wave electrooptic terahertz sensors**. *Selected Topics in Quantum Electronics, IEEE Journal of 2*, 3 (1996), 693–700.

[114] COUTAZ, J.-L. **Optoélectronique térahertz**. EDP Sciences, 2012.

[115] SINGH, R., CAO, W., AL-NAIB, I., CONG, L., WITHAYACHUMNANKUL, W., AND ZHANG, W. **Ultrasensitive terahertz sensing with high-Q Fano resonances in metasurfaces**. *Applied Physics Letters 105*, 17 (Oct. 2014), 171101.

[116] RAKIĆ, A. D., DJURIŠIĆ, A. B., ELAZAR, J. M., AND MAJEWSKI, M. L. **Optical properties of metallic films for vertical-cavity optoelectronic devices**. *Applied Optics 37*, 22 (Aug. 1998), 5271.

[117] BEUTLER, H. **Über Absorptionsserien von Argon, Krypton und Xenon zu Termen zwischen den beiden Ionisierungsgrenzen 2 P 3 2/0 und 2 P 1 2/0**. *Zeitschrift für Physik A Hadrons and Nuclei 93*, 3 (1935), 177–196.

[118] FANO, U. **Sullo spettro di assorbimento dei gas nobili presso il limite dello spettro d'arco**. *Il Nuovo Cimento (1924-1942) 12*, 3 (1935), 154–161.

[119] FANO, U., PUPILLO, G., ZANNONI, A., AND CLARK, C. W. **On the absorption spectrum of noble gases at the arc spectrum limit**. *Journal of research of the National Institute of Standards and Technology 110*, 6 (1935), 583.

[120] FANO, U. **Effects of Configuration Interaction on Intensities and Phase Shifts**. *Physical Review 124*, 6 (1961), 1866–1878.

[121] FAN, S. **Sharp asymmetric line shapes in side-coupled waveguide-cavity systems**. *Applied Physics Letters 80*, 6 (Feb. 2002), 908–910.

[122] FAN, S., AND JOANNOPOULOS, J. D. **Analysis of guided resonances in photonic crystal slabs**. *Physical Review B 65*, 23 (June 2002).

[123] FAN, S., SUH, W., AND JOANNOPOULOS, J. **Temporal coupled-mode theory for the Fano resonance in optical resonators**. *JOSA A* (2003).

[124] GOFFAUX, C., SÁNCHEZ-DEHESA, J., YEYATI, A. L., LAMBIN, P., KHELIF, A., VASSEUR, J. O., AND DJAFARI-ROUHANI, B. **Evidence of Fano-Like Interference Phenomena in Locally Resonant Materials**. *Physical Review Letters 88*, 22 (May 2002).

[125] LEE, H.-T., AND POON, A. W. **Fano resonances in prism-coupled square micropillars**. *Optics letters 29*, 1 (2004), 5–7.

[126] SARRAZIN, M., VIGNERON, J.-P., AND VIGOUREUX, J.-M. **Role of Wood anomalies in optical properties of thin metallic films with a bidimensional array of subwavelength holes**. *Physical Review B 67*, 8 (Feb. 2003).

[127] FEDOTOV, V. A., ROSE, M., PROSVIRNIN, S. L., PAPASIMAKIS, N., AND ZHELUDEV, N. I. **Sharp Trapped-Mode Resonances in Planar Metamaterials with a Broken Structural Symmetry**. *Physical Review Letters 99*, 14 (Oct. 2007).

[128] PAPASIMAKIS, N., FEDOTOV, V. A., ZHELUDEV, N. I., AND PROSVIRNIN, S. L. **Metamaterial Analog of Electromagnetically Induced Transparency**. *Physical Review Letters 101*, 25 (Dec. 2008).

[129] ZHANG, S., GENOV, D. A., WANG, Y., LIU, M., AND ZHANG, X. **Plasmon-Induced Transparency in Metamaterials**. *Physical Review Letters 101*, 4 (July 2008).

[130] CHIAM, S.-Y., SINGH, R., ROCKSTUHL, C., LEDERER, F., ZHANG, W., AND BETTIOL, A. A. **Analogue of electromagnetically induced transparency in a terahertz metamaterial**. *Physical Review B 80*, 15 (Oct. 2009).

[131] LIU, N., LANGGUTH, L., WEISS, T., KÄSTEL, J., FLEISCHHAUER, M., PFAU, T., AND GIESSEN, H. **Plasmonic analogue of electromagnetically induced transparency at the Drude damping limit**. *Nature Materials 8*, 9 (Sept. 2009), 758–762.

[132] PAPASIMAKIS, N., FU, Y. H., FEDOTOV, V. A., PROSVIRNIN, S. L., TSAI, D. P., AND ZHELUDEV, N. I. **Metamaterial with polarization and direction insensitive resonant transmission response mimicking electromagnetically induced transparency**. *Applied Physics Letters 94*, 21 (May 2009), 211902.

[133] TASSIN, P., ZHANG, L., KOSCHNY, T., ECONOMOU, E. N., AND SOUKOULIS, C. M. **Low-Loss Metamaterials Based on Classical Electromagnetically Induced Transparency**. *Physical Review Letters 102*, 5 (Feb. 2009).

[134] TASSIN, P., KOSCHNY, T., AND SOUKOULIS, C. M. **Field Enhancement with Classical Electromagnetically Induced Transparency**. In *Nonlinear, Tunable and Active Metamaterials*, I. V. Shadrivov, M. Lapine, and Y. S. Kivshar, Eds., vol. 200. Springer International Publishing, Cham, 2015, pp. 303–319.

[135] PROSVIRNIN, S., AND ZOUHDI, S. **Resonances of closed modes in thin arrays of complex particles**. In *Advances in electromagnetics of complex media and metamaterials*. Springer, 2002, pp. 281–290.

[136] SINGH, R., ROCKSTUHL, C., LEDERER, F., AND ZHANG, W. **Coupling between a dark and a bright eigenmode in a terahertz metamaterial**. *Physical Review B 79*, 8 (Feb. 2009).

[137] LIU, N., WEISS, T., MESCH, M., LANGGUTH, L., EIGENTHALER, U., HIRSCHER, M., SO?NNICHSEN, C., AND GIESSEN, H. **Planar Metamaterial Analogue of Electromagnetically Induced Transparency for Plasmonic Sensing**. *Nano Letters 10*, 4 (Apr. 2010), 1103–1107.

[138] SINGH, R., AL-NAIB, I. A., YANG, Y., ROY CHOWDHURY, D., CAO, W., ROCKSTUHL, C., OZAKI, T., MORANDOTTI, R., AND ZHANG, W. **Observing metamaterial induced transparency in individual Fano resonators with broken symmetry**. *Applied Physics Letters 99*, 20 (2011), 201107.

[139] HAN, S., SINGH, R., CONG, L., AND YANG, H. **Engineering the fano resonance and electromagnetically induced transparency in near-field coupled bright**

and dark metamaterial. *Journal of Physics D: Applied Physics 48*, 3 (Jan. 2015), 035104.

[140] LI, X., BIAN, X., MILNE, W. I., AND CHU, D. **Fano resonance engineering in mirror-symmetry-broken THz metamaterials**. *Applied Physics B 122*, 4 (Apr. 2016).

[141] SRIVASTAVA, Y. K., AND SINGH, R. **Impact of conductivity on Lorentzian and Fano resonant high- *Q* THz metamaterials: Superconductor, metal and perfect electric conductor**. *Journal of Applied Physics 122*, 18 (Nov. 2017), 183104.

[142] ARTAR, A., YANIK, A. A., AND ALTUG, H. **Directional Double Fano Resonances in Plasmonic Hetero-Oligomers**. *Nano Letters 11*, 9 (Sept. 2011), 3694–3700.

[143] ARTAR, A., YANIK, A. A., AND ALTUG, H. **Multispectral Plasmon Induced Transparency in Coupled Meta-Atoms**. *Nano Letters 11*, 4 (Apr. 2011), 1685–1689.

[144] FRANCESCATO, Y., GIANNINI, V., AND MAIER, S. A. **Plasmonic Systems Unveiled by Fano Resonances**. *ACS Nano 6*, 2 (Feb. 2012), 1830–1838.

[145] FORESTIERE, C., DAL NEGRO, L., AND MIANO, G. **Theory of coupled plasmon modes and Fano-like resonances in subwavelength metal structures**. *Physical Review B 88*, 15 (Oct. 2013).

[146] LOVERA, A., GALLINET, B., NORDLANDER, P., AND MARTIN, O. J. **Mechanisms of Fano Resonances in Coupled Plasmonic Systems**. *ACS Nano 7*, 5 (May 2013), 4527–4536.

[147] MUKHERJEE, S., SOBHANI, H., LASSITER, J. B., BARDHAN, R., NORDLANDER, P., AND HALAS, N. J. **Fanoshells: Nanoparticles with Built-in Fano Resonances**. *Nano Letters 10*, 7 (July 2010), 2694–2701.

[148] WU, D., JIANG, S., AND LIU, X. **Tunable Fano Resonances in Three-Layered Bimetallic Au and Ag Nanoshell**. *The Journal of Physical Chemistry C 115*, 48 (Dec. 2011), 23797–23801.

[149] MONTICONE, F., ARGYROPOULOS, C., AND ALÙ, A. **Multilayered Plasmonic Covers for Comblike Scattering Response and Optical Tagging**. *Physical Review Letters 110*, 11 (Mar. 2013).

[150] YIN, L.-Y., HUANG, Y.-H., WANG, X., NING, S.-T., AND LIU, S.-D. **Double Fano resonances in nanoring cavity dimers: The effect of plasmon hybridization between dark subradiant modes**. *AIP Advances 4*, 7 (July 2014), 077113.

[151] FU, Y. H., ZHANG, J. B., YU, Y. F., AND LUK'YANCHUK, B. **Generating and Manipulating Higher Order Fano Resonances in Dual-Disk Ring Plasmonic Nanostructures**. *ACS Nano 6*, 6 (June 2012), 5130–5137.

[152] ZHANG, J., AND ZAYATS, A. **Multiple Fano resonances in single-layer nonconcentric core-shell nanostructures**. *Optics Express 21*, 7 (Apr. 2013), 8426.

[153] HE, Z., LI, H., ZHAN, S., LI, B., CHEN, Z., AND XU, H. **Oscillator Model Analysis for Slow Light in Bright-Dark-Dark Waveguide Systems**. *IEEE Photonics Technology Letters 27*, 22 (Nov. 2015), 2371–2374.

[154] HE, Z., LI, H., ZHAN, S., LI, B., CHEN, Z., AND XU, H. **Tunable Multi-switching in Plasmonic Waveguide with Kerr Nonlinear Resonator**. *Scientific Reports 5*, 1 (Dec. 2015).

[155] TU, Z., GAO, D., ZHANG, M., AND ZHANG, D. **High-sensitivity complex refractive index sensing based on Fano resonance in the subwavelength grating waveguide micro-ring resonator**. *Optics Express 25*, 17 (Aug. 2017), 20911.

[156] FANTINO, A. N., GROSZ, S. I., AND SKIGIN, D. C. **Resonant effects in periodic gratings comprising a finite number of grooves in each period**. *Physical Review E 64*, 1 (June 2001).

[157] SKIGIN, D. C., AND DEPINE, R. A. **Transmission Resonances of Metallic Compound Gratings with Subwavelength Slits**. *Physical Review Letters 95*, 21 (Nov. 2005).

[158] HIBBINS, A. P., HOOPER, I. R., LOCKYEAR, M. J., AND SAMBLES, J. R. **Microwave Transmission of a Compound Metal Grating**. *Physical Review Letters 96*, 25 (June 2006).

[159] BENDOYM, I., GOLOVIN, A. B., AND CROUSE, D. T. **The light filtering and guiding properties of high finesse phase resonant compound gratings**. *Optics Express 20*, 20 (2012), 22830–22846.

[160] CHEN, S., JIN, S., AND GORDON, R. **Subdiffraction Focusing Enabled by a Fano Resonance**. *Physical Review X 4*, 3 (Aug. 2014).

[161] CHEN, S., JIN, S., AND GORDON, R. **Super-transmission from a finite subwavelength arrangement of slits in a metal film**. *Optics Express 22*, 11 (June 2014), 13418.

[162] SIEGMAN, A. E. **Lasers**. University Science Books, 1986.

[163] DOYLE, W. M., AND WHITE, M. B. **Properties of an anisotropic Fabry–Perot resonator**. *JOSA 55*, 10 (1965), 1221–1225.

[164] MAMAEV, Y. A., AND KHANDOKHIN, P. A. **Nonorthogonal polarisation eigenstates in anisotropic cavities**. *Quantum Electronics 41*, 6 (June 2011), 571–576.

[165] SILVERMAN, M. P., AND BADOZ, J. **Interferometric enhancement of chiral asymmetries: ellipsometry with an optically active Fabry–Perot interferometer**. *JOSA A 11*, 6 (1994), 1894–1917.

[166] TIMOFEEV, I. V., GUNYAKOV, V. A., SUTORMIN, V. S., MYSLIVETS, S. A., ARKHIPKIN, V. G., VETROV, S. Y., LEE, W., AND ZYRYANOV, V. Y. **Geometric phase and o -mode blueshift in a chiral anisotropic medium inside a Fabry-Pérot cavity**. *Physical Review E 92*, 5 (Nov. 2015).

[167] ISMAIL, N., KORES, C. C., GESKUS, D., AND POLLNAU, M. **Fabry-Perot resonator: spectral line shapes, generic and related Airy distributions, linewidths, finesses, and performance at low or frequency-dependent reflectivity**. *Optics Express 24*, 15 (July 2016), 16366.

[168] BIRD, G. R., AND PARRISH, M. **The wire grid as a near-infrared polarizer**. *JOSA 50*, 9 (1960), 886–891.

[169] TAKANO, K., YOKOYAMA, H., ICHII, A., MORIMOTO, I., AND HANGYO, M. **Wire-grid polarizer sheet in the terahertz region fabricated by nanoimprint technology**. *Optics letters 36*, 14 (2011), 2665–2667.

[170] GALLINET, B. **Fano Resonances in Plasmonic Nanostructures: Fundamentals, Numerical Modeling and Applications**. PhD thesis, EPFL, 2012.

[171] GALLINET, B., LOVERA, A., SIEGFRIED, T., SIGG, H., AND MARTIN, O. J. F. **Fano resonant plasmonic systems: Functioning principles and applications**. pp. 18–20.

[172] ZHANG, Z., SU, X., FAN, Y., YIN, P., ZHANG, L., AND SHI, X. **Dynamically tunable Fano resonance in planar structures based on periodically asymmetric graphene nanodisk pair**. *Physica B: Condensed Matter 473* (Sept. 2015), 7–10.

[173] DENG, Y., CAO, G., YANG, H., LI, G., CHEN, X., AND LU, W. **Tunable and high-sensitivity sensing based on Fano resonance with coupled plasmonic cavities**. *Scientific Reports 7*, 1 (Dec. 2017).

[174] CHEN, Y.-T., CHERN, R.-L., AND LIN, H.-Y. **Multiple Fano resonances in metallic arrays of asymmetric dual stripes**. *Applied Optics 49*, 15 (May 2010), 2819–2826.

[175] MORITAKE, Y., KANAMORI, Y., AND HANE, K. **Demonstration of sharp multiple Fano resonances in optical metamaterials**. *Optics Express 24*, 9 (May 2016), 9332.

[176] AMARLOO, H., HAILU, D. M., AND SAFAVI-NAEINI, S. **Multiple Fano Resonances Structure for Terahertz Applications**. *Progress In Electromagnetics Research Letters 50* (2014), 1–6.

[177] CHEN, Z., SONG, X., DUAN, G., WANG, L., AND YU, L. **Multiple Fano Resonances Control in MIM Side-Coupled Cavities Systems**. *IEEE Photonics Journal 7*, 3 (June 2015), 1–10.

[178] LI, C., LI, S., WANG, Y., JIAO, R., WANG, L., AND YU, L. **Multiple Fano Resonances Based on Plasmonic Resonator System With End-Coupled Cavities for High-Performance Nanosensor**. *IEEE Photonics Journal 9*, 6 (Dec. 2017), 1–9.

[179] NISHIDA, M., HATAKENAKA, N., AND KADOYA, Y. **Multipole surface plasmons in metallic nanohole arrays**. *Physical Review B 91*, 23 (June 2015).

[180] KHAN, A. D., AND AMIN, M. **Polarization Selective Multiple Fano Resonances in Coupled T-Shaped Metasurface**. *IEEE Photonics Technology Letters 29*, 19 (Oct. 2017), 1611–1614.

[181] YANG, J., SONG, X., YANG, S., CUI, L., AND YU, L. **Independently controllable multiple Fano resonances in side-coupled MDM structure and its applications for sensing and wavelength demultiplexing**. *Journal of Physics D: Applied Physics 50*, 32 (Aug. 2017), 325107.

[182] ROMAIN, X., BAIDA, F. I., AND BOYER, P. **Spectrally tunable linear polarization rotation using stacked metallic metamaterials**. *Journal of Optics 19*, 8 (Aug. 2017), 085102.

[183] ZHELUDEV, N. I., PAPAKOSTAS, A., POTTS, A. W., COLES, H. J., AND BAGNALL, D. M. **Layered chiral metallic meta-materials**. *Complex Mediums III: Beyond Linear Isotropic Dielectrics 4806* (2002), 112–118.

[184] PAPAKOSTAS, A., POTTS, A., BAGNALL, D. M., PROSVIRNIN, S. L., COLES, H. J., AND ZHELUDEV, N. I. **Optical Manifestations of Planar Chirality**. *Physical Review Letters 90*, 10 (Mar. 2003).

[185] ZHANG, W., POTTS, A., PAPAKOSTAS, A., AND BAGNALL, D. M. **Intensity modulation and polarization rotation of visible light by dielectric planar chiral metamaterials**. *Applied Physics Letters 86*, 23 (June 2005), 231905.

[186] SINGH, R., PLUM, E., ZHANG, W., AND ZHELUDEV, N. I. **Highly tunable optical activity in planar achiral terahertz metamaterials**. *Optics Express 18*, 13 (2010), 13425–13430.

[187] CHENG, Y. Z., WITHAYACHUMNANKUL, W., UPADHYAY, A., HEADLAND, D., NIE, Y., GONG, R. Z., BHASKARAN, M., SRIRAM, S., AND ABBOTT, D. **Ultrabroadband reflective polarization convertor for terahertz waves**. *Applied Physics Letters 105*, 18 (Nov. 2014), 181111.

[188] WEN, X., AND ZHENG, J. **Broadband THz reflective polarization rotator by multiple plasmon resonances**. *Optics Express 22*, 23 (Nov. 2014), 28292–28300.

[189] YANG, Y., WANG, W., MOITRA, P., KRAVCHENKO, I. I., BRIGGS, D. P., AND VALENTINE, J. **Dielectric Meta-Reflectarray for Broadband Linear Polarization Conversion and Optical Vortex Generation**. *Nano Letters 14*, 3 (Mar. 2014), 1394–1399.

[190] HE, J., XIE, Z., WANG, S., WANG, X., KAN, Q., AND ZHANG, Y. **Terahertz polarization modulator based on metasurface**. *Journal of Optics 17*, 10 (Oct. 2015), 105107.

[191] VEYSI, M., GUCLU, C., BOYRAZ, O., AND CAPOLINO, F. **Thin anisotropic metasurfaces for simultaneous light focusing and polarization manipulation**. *Journal of the Optical Society of America B 32*, 2 (Feb. 2015), 318–323.

[192] ZHANG, Z., LUO, J., SONG, M., AND YU, H. **Large-area, broadband and high-efficiency near-infrared linear polarization manipulating metasurface fabricated by orthogonal interference lithography**. *Applied Physics Letters 107*, 24 (Dec. 2015), 241904.

[193] CHEN, H., WANG, J., MA, H., QU, S., XU, Z., ZHANG, A., YAN, M., AND LI, Y. **Ultra-wideband polarization conversion metasurfaces based on multiple plasmon resonances**. *Journal of Applied Physics 115*, 15 (Apr. 2014), 154504.

[194] YIN, J. Y., WAN, X., ZHANG, Q., AND CUI, T. J. **Ultra Wideband Polarization-Selective Conversions of Electromagnetic Waves by Metasurface under Large-Range Incident Angles**. *Scientific Reports 5* (July 2015), 12476.

[195] DONG, G., SHI, H., XIA, S., ZHANG, A., XU, Z., AND WEI, X. **Ultra-broadband perfect cross polarization conversion metasurface**. *Optics Communications 365* (Apr. 2016), 108–112.

[196] NI, C., CHEN, M. S., ZHANG, Z. X., AND WU, X. L. **Design of Frequency-and Polarization-Reconfigurable Antenna Based on the Polarization Conversion Metasurface**. *IEEE Antennas and Wireless Propagation Letters 17*, 1 (Jan. 2018), 78–81.

[197] LUO, S., LI, B., YU, A., GAO, J., WANG, X., AND ZUO, D. **Broadband tunable terahertz polarization converter based on graphene metamaterial**. *Optics Communications 413* (Apr. 2018), 184–189.

[198] EARL, S. K., JAMES, T. D., GÓMEZ, D. E., MARVEL, R. E., HAGLUND, R. F., AND ROBERTS, A. **Switchable polarization rotation of visible light using a plasmonic metasurface**. *APL Photonics 2*, 1 (Jan. 2017), 016103.

[199] KUWATA-GONOKAMI, M., SAITO, N., INO, Y., KAURANEN, M., JEFIMOVS, K., VALLIUS, T., TURUNEN, J., AND SVIRKO, Y. **Giant Optical Activity in Quasi-Two-Dimensional Planar Nanostructures**. *Physical Review Letters 95*, 22 (Nov. 2005).

[200] KWON, D.-H., WERNER, P. L., AND WERNER, D. H. **Optical planar chiral metamaterial designs for strong circular dichroism and polarization rotation**. *Optics express 16*, 16 (2008), 11802–11807.

[201] ZHANG, W., ZHU, W. M., CHIA, E. E. M., SHEN, Z. X., CAI, H., GU, Y. D., SER, W., AND LIU, A. Q. **A pseudo-planar metasurface for a polarization rotator**. *Optics Express 22*, 9 (May 2014), 10446–10454.

[202] FANIAYEU, I., KHAKHOMOV, S., SEMCHENKO, I., AND MIZEIKIS, V. **Highly transparent twist polarizer metasurface**. *Applied Physics Letters 111*, 11 (Sept. 2017), 111108.

[203] HU, S., YANG, S., LIU, Z., LI, J., AND GU, C. **Broadband cross-polarization conversion by symmetry-breaking ultrathin metasurfaces**. *Applied Physics Letters 111*, 24 (Dec. 2017), 241108.

[204] OTTOMANIELLO, A., ZANOTTO, S., BALDACCI, L., PITANTI, A., BIANCO, F., AND TREDICUCCI, A. **Symmetry enhanced non-reciprocal polarization rotation in a terahertz metal-graphene metasurface**. *Optics Express 26*, 3 (Feb. 2018), 3328.

[205] ZHANG, M., ZHANG, W., LIU, A. Q., LI, F. C., AND LAN, C. F. **Tunable Polarization Conversion and Rotation based on a Reconfigurable Metasurface**. *Scientific Reports 7*, 1 (Dec. 2017).

[206] YE, Y., AND HE, S. **90 polarization rotator using a bilayered chiral metamaterial with giant optical activity**. *Applied Physics Letters 96*, 20 (May 2010), 203501.

[207] LI, T., WANG, S. M., CAO, J. X., LIU, H., AND ZHU, S. N. **Cavity-involved plasmonic metamaterial for optical polarization conversion**. *Applied Physics Letters 97*, 26 (2010), 261113.

[208] WOO, J. M., HUSSAIN, S., AND JANG, J.-H. **A terahertz in-line polarization converter based on through-via connected double layer slot structures**. *Scientific Reports 7* (Feb. 2017), 42952.

[209] WEI, Z., CAO, Y., FAN, Y., YU, X., AND LI, H. **Broadband polarization transformation via enhanced asymmetric transmission through arrays of twisted complementary split-ring resonators**. *Applied Physics Letters 99*, 22 (Nov. 2011), 221907.

[210] XU, J., LI, T., LU, F. F., WANG, S. M., AND ZHU, S. N. **Manipulating optical polarization by stereo plasmonic structure**. *Optics express 19*, 2 (2011), 748–756.

[211] CONG, L., CAO, W., ZHANG, X., TIAN, Z., GU, J., SINGH, R., HAN, J., AND ZHANG, W. **A perfect metamaterial polarization rotator**. *Applied Physics Letters 103*, 17 (Oct. 2013), 171107.

[212] GRADY, N. K., HEYES, J. E., CHOWDHURY, D. R., ZENG, Y., REITEN, M. T., AZAD, A. K., TAYLOR, A. J., DALVIT, D. A. R., AND CHEN, H.-T. **Terahertz Metamaterials for Linear Polarization Conversion and Anomalous Refraction**. *Science 340*, 6138 (June 2013), 1304–1307.

[213] FAN, R.-H., ZHOU, Y., REN, X.-P., PENG, R.-W., JIANG, S.-C., XU, D.-H., XIONG, X., HUANG, X.-R., AND WANG, M. **Freely Tunable Broadband Polarization Rotator for Terahertz Waves**. *Advanced Materials 27*, 7 (Feb. 2015), 1201–1206.

[214] FAN, R.-H., LIU, D., PENG, R.-W., SHI, W.-B., JING, H., HUANG, X.-R., AND WANG, M. **Broadband integrated polarization rotator using three-layer metallic grating structures**. *Optics Express 26*, 1 (Jan. 2018), 516.

[215] LIU, D.-J., XIAO, Z.-Y., MA, X.-L., AND WANG, Z.-H. **Broadband asymmetric transmission and multi-band 90 polarization rotator of linearly polarized wave based on multi-layered metamaterial**. *Optics Communications* (2015).

[216] CHENG, Y., GONG, R., AND WU, L. **Ultra-Broadband Linear Polarization Conversion via Diode-Like Asymmetric Transmission with Composite Metamaterial for Terahertz Waves**. *Plasmonics* (Aug. 2016).

[217] CHENG, Y., ZHAO, J.-C., MAO, X., AND GONG, R. **Ultrabroadband Diode-Like Asymmetric Transmission and High-Efficiency Cross-Polarization Conversion Based on Composite Chiral Metamaterial**. *Progress In Electromagnetics Research 160* (2017), 89–101.

[218] ZHAO, Y., BELKIN, M., AND ALÙ, A. **Twisted optical metamaterials for planarized ultrathin broadband circular polarizers**. *Nature Communications 3* (May 2012), 870.

[219] WANG, Y.-H., SHAO, J., LI, J., ZHU, M.-J., LI, J., AND DONG, Z.-G. **Unidirectional cross polarization rotator with enhanced broadband transparency by cascading twisted nanobars**. *Journal of Optics 18*, 5 (May 2016), 055004.

[220] LEE, Y.-S. **Principles of terahertz science and technology**, vol. 170. Springer Science & Business Media, 2009.

[221] SONG, H.-J., AND NAGATSUMA, T. **Handbook of terahertz technologies: devices and applications**. CRC press, 2015.

[222] ROUT, S., AND SONKUSALE, S. **Active Metamaterials**. Springer International Publishing, Cham, 2017.

[223] BORN, N., CRUNTEANU, A., HUMBERT, G., BESSAUDOU, A., KOCH, M., AND FISCHER, B. M. **Switchable THz Filter Based on a Vanadium Dioxide Layer Inside a Fabry-Perot Cavity**. *IEEE Transactions on Terahertz Science and Technology 5*, 6 (Nov. 2015), 1035–1039.

LIST OF FIGURES

Document generated with LaTeX and:
the LaTeX style for PhD Thesis created by S. Galland — http://www.multiagent.fr/ThesisStyle
the tex-upmethodology package suite — http://www.arakhne.org/tex-upmethodology/

école doctorale **sciences pour l'ingénieur et microtechniques**

Title: Study of the polarization of light through a stack of metallic metamaterials

Keywords: Nano-optics, Metallic metamaterials, Polarization, Fano/Fabry-Perot resonances

Abstract:

This PhD thesis deals with the theoretical study of stacked metallic metamaterials. Such structures are currently investigated to extend the functionalities offered by single metallic metamaterials. We especially focus on the specific polarization properties of the stacked metallic metamaterials.

We first present the type of metamaterial that we consider, and we describe the modal method that is used to model its electromagnetic properties. We outline the linear polarization properties characterizing the metamaterial thanks to an Extended Jones Formalism (EJF) recently developed by our team.

In combination with the EJF, we apply the S-matrix algorithm to the study of a stack of two metallic metamaterials in a polarizer-analyzer configuration. We derive an analytical expression for the transmission response of the stacked structure: the Extended Malus' Law. Mainly, it highlights the Fabry-Perot-like resonances located between the metamaterials.

Using larger stacked structures, we demonstrate that spectrally tunable and low loss polarization rotation can be achieved owing to these Fabry-Perot-like resonances.

In essence, we reveal a new way of realizing Fano resonances which are induced by the specific polarization properties of the metamaterials. We show that such resonances can be engineered for sensing or filtering applications. Moreover, the polarization-induced Fano resonances expand the possibilities of stacked metallic metamaterials.

Titre : Study of the polarization of light through a stack of metallic metamaterials

Mots-clés : Nano-optique, Métamatériaux métalliques, Polarisation, Résonances Fano/Fabry-Perot

Résumé :

Cette thèse a pour but l'étude théorique de métamatériaux métalliques empilés. Ces structures sont actuellement proposées pour améliorer et élargir les fonctionnalités des métamatériaux métalliques. Nous portons un intérêt particulier aux propriétés de polarisation de ces structures métalliques empilées.

En premier lieu, nous précisons le type de métamatériaux que nous étudions et nous présentons la méthode modale qui nous permet de décrire les propriétés électromagnétiques de la structure. A l'aide d'un Formalisme de Jones Etendu (FJE), développé récemment dans notre équipe, nous faisons ressortir les principales propriétés de polarisation linéaire de ces métamatériaux métallique.

En alliant le FJE à l'algorithme de propagation de la matrice S, nous étudions un empilement de deux métamatériaux vus comme un montage polariseur-analyseur. Nous établissons ensuite une expression de la transmission de la structure: la loi de Malus étendue. Cela nous permet notamment de démontrer les résonances de type Fabry-Perot qui ont lieu entre les métamatériaux.

Pour des structures plus conséquentes, nous montrons qu'il est possible de réaliser une rotation de la polarisation, à très faible perte et spectralement agile, grâce aux résonances de type Fabry-Perot.

Fondamentalement, nous révélons une nouvelle façon d'exciter des résonances Fano qui sont induites par les propriétés de polarisation des métamatériaux. Ces résonances peuvent être utilisées pour des applications de capteur ou de filtrage. De plus, ces résonances Fano induites par la polarisation ouvrent de nouvelles possibilités d'applications pour les empilements de métamatériaux métalliques.

UBFC UNIVERSITÉ BOURGOGNE FRANCHE-COMTÉ

Université Bourgogne Franche-Comté
32, avenue de l'Observatoire
25000 Besanon, France